

Refraction Interference Elimination Employing Smart Arrays at VHF

**A project submitted to Middlesex
University in partial fulfilment of the
requirements for the degree of
Doctor of Professional Studies**

Antonios Constantinides

Middlesex University, June 2017

Acknowledgements

I would like to express my gratitude to my supervisor Dr. John Howard and my adviser Dr. Annette Fillery Travis for their help and guidance throughout my years of research. I would also like to thank Dr. Savvas Kontos for the perfect coordination of the programme and for his valuable assistance in regards to all administrative issues concerning my Doctorate.

List of Contents

ACKNOWLEDGEMENTS	I
LIST OF CONTENTS	II
LIST OF FIGURES.....	VI
LIST OF TABLES	X
GLOSSARY OF SYMBOLS AND ABBREVIATION.....	XI
ABSTRACT.....	1
THE PROFESSIONAL ELEMENTS OF THE PROJECT	3
CHAPTER 1: INTRODUCTION	5
1.1. Introduction to the proposed system	5
1.2. Brief Thesis Outline:	7
CHAPTER 2: HISTORICAL OVERVIEW.....	8
2.1 Basic Interference Concepts	9
2.2 Special Cases of Abnormal Radio Signals Propagation	11
2.2.1 Japan	11
2.2.2 South Korea	12
2.2.3 Channel Islands	12
2.2.4 United Kingdom	13
2.3 The Role of Antennas in Terms of Interference	14
2.3.1 Basic Concepts and Theorems	15
2.3.2 Conventional Antennas	15
2.3.3 Advanced Antenna Topologies, Collinear & Phased Arrays	17
2.3.4 Chapter Conclusion	18
CHAPTER 3: ANALYSIS OF VHF PROPAGATION MECHANISMS THAT CAUSE INTERFERENCE WITHIN THE SOUTHERN COASTAL REGIONS OF CYPRUS.....	21

3.1 Statement of the Problem	21
3.2 Interference Testing Methodology	23
3.2.1 Line of Sight	24
3.2.2 Diffraction	24
3.2.3 Tropospheric Scatter	24
3.2.4 Surface Ducting	25
3.2.5 Elevated Layer Reflection and Refraction	25
3.2.6 Hydrometeor Scatter	25
3.3 Location and Instrumentation Set Up	25
3.4 The Importance of the RX Antenna Polarization Sense	26
3.5 Vertical Polarization	27
3.5.1 Advantages and Disadvantages of Linear Vertical Polarization in the Context of FM Broadcasting	27
3.5.2 Discussion of Circular Polarization Antennas in FM Broadcasting.....	29
3.5.3 Linear Versus Circular Polarization	30
3.6 Rigorous Analysis of the Voltage Standing Wave Ratio (VSWR) and Insertion Loss of the Testing Equipment Topology	31
3.6.1 True Antenna Gain-Overall Signal Losses-Compensation	34
3.7 Monitoring Unwanted Overseas Transmissions	35
3.7.1 The Path Length Calculations of the Detected Signals	35
3.7.2 Measurements of 102.5MHz, 95.5MHz and 94.8MHz performed at 1:00 PM between June 17 th and September 2 nd , 2015.....	38
3.7.3 Measurements of the 95.5 MHz and 94.8 MHz Signals Between June 17 th and September 2th, 2015, made at 1:00 PM & 9:00 PM.....	41
3.7.4 Short Term Measurements of the 95.5MHz and 94.8 MHz Signals Conducted between June 17 th and September 2th, 2015, from 11:00 AM to 7:00 PM	42
3.7.5 Discussion and Results of measurements	43
3.8 Analysis of the Monitored Signals	45
3.8.1 Line of Sight Interference Analysis.....	45
3.8.2 Diffraction Interference.....	48
3.8.3 Tropospheric Scattering.....	49
3.8.3 Refraction Interference	51
3.8.5 Normal Conditions	52
3.8.6 Sub-Refraction	52
3.8.7 Super Refraction.....	52
3.8.8 Trapping.....	53
3.9 The Climate of the Southern Coast of Cyprus	54
3.9.1 Air Temperature.....	54

3.9.2 Sea Temperature	55
3.9.3 Soil Temperature.....	56
3.9.4 Relative Air Humidity	56
3.9.5 Wind.....	57
3.10 Results and Discussion	57
3.11 Very Strong Signal Intensity	59
3.11.1 Results pertaining to measurements made on June 18 th 2015	59
3.11.2 Results pertaining to the measurements performed on July 7 th 2015.....	61
3.11.3 Results pertaining to the measurements performed on July 11 th 2015.....	62
3.11.4 Results pertaining to the measurements performed on July 21 st 2015	64
3.12 Results pertaining to Medium Field Intensity.....	65
3.12.1 Results pertaining to the measurements performed on July 12 th 2015.....	66
3.12.2 Results pertaining to the measurements performed on July 31 st 2015.....	67
3.13 Results pertaining to Low Field Intensity	68
3.13.1 Results pertaining to the measurements performed on June 20 th 2015	68
3.13.2 Results pertaining to the measurements performed on June 30 th 2015	70
3.13.3 Results pertaining to the measurements performed on August 30 th 2015.....	71
3.14 The Type of Ducts along the Limassol Coast	73
3.15 Chapter Conclusion	75
CHAPTER 4: PHASED ARRAYS-THE SOLUTION TO THE PROBLEM OF INTERFERENCE	77
4.1 Directivity, Gain & Effective Aperture	78
4.2 Radiation Pattern	80
4.3 The Effect of Physical Dimensions on the Antenna Performance.....	80
4.4 The Short Dipole Antenna	83
4.5 The Short Monopole Antenna	86
4.6 The Normal Mode Helical Antenna (NMHA).....	88
4.7 Real Conditions measurements of the NMHA	89
4.8 The Quarter-wavelength Monopole versus the NMHA	91
4.9 The Gain of the NMHA versus that of the Quarter-wavelength Monopole Antenna.....	93
4.10 Optimization of the Normal Mode Helical Antenna.....	94

4.11	The Final Design of the NMHA	96
4.12	Uniform Linear Arrays.....	99
4.13	Application of Circular Arrays.....	102
4.14	The Smart Antenna Design	103
4.15	Final Construction and Assessment of the Smart Antenna	106
4.16	Interface between the Array and a Dedicated Commercial Receiver	110
4.16.1	The Phase Locked Loop (PLL).....	112
4.16.2	The Liquid Crystal Display (LCD) Monitor Circuit	115
4.16.3	The Control Circuit	117
4.17	Key Equipment Used for the Research	122
 CHAPTER 5: CONCLUSION AND FUTURE WORK.....		123
 REFERENCES		126
 APPENDICES.....		130
APPENDIX 1: GOVERNMENT MEASUREMENTS OF LEBANON 92.1 MHz FROM 1/9/14 to 14/9/14.....		129
APPENDIX 2: UPPER AIR DATA OBTAINED BY WRF-ARW VERSION 3.4.....		182
APPENDIX 3: L.C.D MONITOR PROGRAMMING CODE		188
APPENDIX 4: CONTROL SYSTEM PROGRAMMING CODE		216
APPENDIX 5: BASIC CONVERTED FROM LOGICATOR FOR PICAXE FLOWCHART		217
APPENDIX 6: PRESENTATIONS CONFERENCES RELATED TO THE RESEARCH PROJECT		221
APPENDIX 7: PUBLICATIONS RELATED TO THE RESEARCH PROJECT		222

LIST OF FIGURES

Figure 1 The Area Affected by Interference from the Middle East	21
Figure 2 Spectrum Analyzer Readings of the Local Radio Services in Limassol	22
Figure 3 Spectrum Analyzer Readings during Motion	23
Figure 4 Testing Equipment Arrangement.....	26
Figure 5 Linear Vertical and Horizontal Incident Waves.....	28
Figure 6: Azimuth and Elevation Planes of E field of a Half-wave Linearly Polarized Dipole	29
Figure 7 The Rotation of a Circular Polarization Incident Wave.....	30
Figure 8 The Testing Antenna.....	31
Figure 9 Scattering Parameters of One Port System	33
Figure 10 VSWR Analyzer	33
Figure 11 Return Loss versus Signal Loss (dB).....	34
Figure 12 Overall Signal Losses.....	35
Figure 13 Path Length between Limassol and Israel, 376 km, Height 860 m	37
Figure 14 Path Length between Limassol and Lebanon, 271 km, Height 2995 m	37
Figure 15 Path Length between Limassol and Olympus, 29 km, Height 1549 m.....	38
Figure 16 The Field Strength Variations in the 102.5 MHz Signal.....	39
Figure 17 The Field Strength Variations in the 95.5 MHz Signal.....	39
Figure 18 The Field Strength Variations in the Local CYBC 94.8 MHz Radio Signal.....	40
Figure 19 The Field Strength Intensity of the Three Signals under Study	40
Figure 20 The Field Strength Variations in the 95.5 MHz and 94.8 MHz Signal, as Measured at 1:00 and 9:00 PM.....	42
Figure 21 The Field Strength Variations of the 95.5 MHz and 94.8 MHz Signals, as measured between 11:00 and 7:00 PM.....	42
Figure 22 The Average Strength of the 95.5 MHz Signal Arriving from Israel During the Summer Months	44
Figure 23 The Average Signal Strength of the 102.5 MHz Signal Arriving from Lebanon during Summer Months	45
Figure 24 Radio versus Visual Horizon.....	46
Figure 25 Diffraction by Spherical Earth –Effect of Distance.....	49
Figure 26 The Four Classifications of Refraction.....	52
Figure 27 The Three Types of Ducts: (a) Surface, (b) Surface-based, and (c) Elevated ducts.	53
Figure 28 Mean Monthly Air Temperature in Limassol	55
Figure 29 Mean Monthly Sea Temperature near Limassol	56

Figure 30 The coordinates under investigation for the radio signals emitted at frequencies of 95.5 and 102.5 MHz	59
Figure 31: Temperature versus height measured on 18-06-2015 at Point 3	60
Figure 32: N-units per meter versus height measured on 18-06-2015 at Point 3	60
Figure 33: Temperature versus height measured on 18-06-2015 at Point 2	60
Figure 34: N-units per meter versus height measured on 18-06-2015 at Point 2	60
Figure 35: Temperature versus height measured on 18-06-2015 at Point 1	61
Figure 36: N-units per meter versus height measured on 18-06-2015 at Point 1	61
Figure 37: Temperature versus height measured on 7-7-2015 at Point 3.	61
Figure 38: N-units per meter versus height measured on 7-7-2015 at Point 3.....	61
Figure 39: Temperature versus height measured on 07-07-2015 at Point 2.....	62
Figure 40: N-units per meter versus height measured on 07-07-2015 at Point 2.....	62
Figure 41: Temperature versus height measured on 07-07-2015 at Point 1.....	62
Figure 42: N-units per meter versus height measured on 07-07-2015 at Point 1.....	62
Figure 43: Temperature versus height measured on 11-07-2015 at Point 3.....	63
Figure 44: N-units per meter versus height measured on 11-07-2015 at Point 3.....	63
Figure 45: Temperature versus height measured on 11-07-2015 at Point 2.....	63
Figure 46: N-units per meter versus height measured on 11-07-2015 at Point 2.....	63
Figure 47: Temperature versus height measured on 11-07-2015 at Point 1.....	64
Figure 48: N-units per meter versus height measured on 11-07-2015 at Point 1.....	64
Figure 49: Temperature versus height measured on 21-07-2015 at Point 3.....	64
Figure 50: N-units per meter versus height measured on 21-07-2015 at Point 3.....	64
Figure 51: Temperature versus height measured on 21-07-2015 at Point 2.....	65
Figure 52: N-units per meter versus height measured on 21-07-2015 at Point 2.....	65
Figure 53: Temperature versus height measured on 21-07-2015 at Point 1.....	65
Figure 54: N-units per meter versus height measured on 21-07-2015 at Point 1.....	65
Figure 55: Temperature versus height measured on 12-07-2015 at Point 3.....	66
Figure 56: N-units per meter versus height measured on 12-07-2015 at Point 3.....	66
Figure 57: Temperature versus height measured on 12-07-2015 at Point 2.....	66
Figure 58: N-units per meter versus height measured on 12-07-2015 at Point 2.....	66
Figure 59: Temperature versus height measured on 12-07-2015 at Point 1.....	67
Figure 60: N-units per meter versus height measured on 12-07-2015 at Point 1.....	67
Figure 61: Temperature versus height measured on 31-07-2015 at Point 3.....	67
Figure 62: N-units per meter versus height measured on 31-07-2015 at Point 3.....	67
Figure 63: Temperature versus height measured on 31-07-2015 at Point 2.....	68
Figure 64: N-units per meter versus height measured on 31-07-2015 at Point 2.....	68
Figure 65: Temperature versus height measured on 20-06-2015 at Point 3.....	69
Figure 66: N-units per meter versus height measured on 20-06-2015 at Point 3.....	69
Figure 67: Temperature versus height measured on 20-06-2015 at Point 2.....	69
Figure 68: N-units per meter versus height measured on 20-06-2015 at Point 2.....	69
Figure 69: Temperature versus height measured on 20-06-2015 at Point 1.....	70

Figure 70: N-units per meter versus height measured on 20-06-2015 at Point 1.	70
Figure 71: Temperature versus height measured on 30-06-2015 at Point 3.	70
Figure 72: N-units per meter versus height measured on 30-06-2015 at Point 3.	70
Figure 73: Temperature versus height measured on 30-06-2015 at Point 2.	71
Figure 74: N-units per meter versus height measured on 30-06-2015 at Point 2.	71
Figure 75: Temperature versus height measured on 30-06-2015 at Point 1.	71
Figure 76: N-units per meter versus height measured on 30-06-2015 at Point 1.	71
Figure 77: Temperature versus height measured on 30-08-2015 at Point 3.	72
Figure 78: N-units per meter versus height measured on 30-08-2015 at Point 3.	72
Figure 79: Temperature versus height measured on 30-08-2015 at Point 2.	72
Figure 80: N-units per meter versus height measured on 30-08-2015 at Point 2.	72
Figure 81: Temperature versus height measured on 30-08-2015 at Point 1.	72
Figure 82: N-units per meter versus height measured on 30-08-2015 at Point 1.	72
Figure 83: Surface Based Duct measurements made on 18-06-15 at Point 3.	73
Figure 84: Surface Based Duct measurements made on 06-08-15 at Point 3.	74
Figure 85: Surface Based Duct measurements made on 24-06-15 at Point 3.	73
Figure 86: Surface Based Duct measurements made on 07-07-15 at Point 3.	73
Figure 87: Surface Duct measurements made on 11-07-15 at Point 3.	73
Figure 88: Surface Based Duct measurements made on 12-07-15 at Point 3.	73
Figure 89: Surface Based Duct measurements made on 23-07-15 at Point 3.	73
Figure 90: Elevated Duct measurements made on 24-07-15 at Point 3.	73
Figure 91: Surface Based Duct measurements made on 28-07-15 at Point 3.	73
Figure 92: Surface Duct measurements made on 31-07-15 at Point 3.	73
Figure 93: Surface Based Duct measurements made on 08-08-15 at Point 3.	74
Figure 94: Surface Duct measurements made on 16-08-15 at Point 3.	73
Figure 95: Dielectric loss tangent diagram.	81
Figure 96: The short dipole.	83
Figure 97: Equivalent circuit of the small dipole's impedance network.	83
Figure 98: The Q factor of a small dipole.	85
Figure 99: The impedance of the small dipole.	86
Figure 100: The monopole.	87
Figure 101: Radiation resistance as a function of wavelength.	87
Figure 102: The Normal Mode Helical Antenna (NMHA).	90
Figure 103: The radiation resistance of the NMHA.	91
Figure 104: The VSWR response of the NMHA.	91
Figure 105: The radiation resistance of the quarter-wavelength monopole antenna.	92
Figure 106: The VSWR response of the monopole antenna.	92
Figure 107: The field strength intensity of the NMHA versus the monopole.	93
Figure 108: The NMHA mounted in series with the planar helix.	94
Figure 109: The VSWR response of the modified helix.	95
Figure 110: The field strength intensity of the modified and unmodified helix.	96

Figure 111: The modified NMHA	96
Figure 112: The VSWR response of the modified NMHA.....	97
Figure 113: Real conditions field strength measurements of the modified NMHA	98
Figure 114: A three-element uniform antenna array with an element separation d and at the plane meeting the $\theta = \pi/2$ criterion	99
Figure 115: Two-element phased array	100
Figure 116: Radiation pattern of two-element phased array	101
Figure 117: The radiation pattern of two-element phased array with the excitation phase of 108°	101
Figure 118: The circular array geometry	102
Figure 119: The circular array design	103
Figure 120: Cardioid radiation pattern of the four-element circular array at 270° HPBW = 90°	104
Figure 121: Cardioid radiation pattern of the four-element circular array at 90° , HPBW = 90°	105
Figure 122: Cardioid radiation pattern of the four-element circular array at 180° , HPBW = 90°	105
Figure 123: Cardioid radiation pattern of the four-element circular array at 0° , HPBW = 90°	106
Figure 124: Four-element circular array	106
Figure 125: Four-port zero-degree splitter	107
Figure 126: The quarter-wavelength monopole under test.....	107
Figure 127: The reception of the quarter-wavelength monopole antenna	108
Figure 128: The circular Array under test.....	109
Figure 129: Monitoring “on air” radio services using the circular array	110
Figure 130: The spectrum analyzer readings of the null	110
Figure 131: Receiver circuit diagram	111
Figure 132: The receiver circuit board	111
Figure 133: Circuit diagram of the phase-locked loop circuitry	113
Figure 134: The PLL board	114
Figure 135: The PLL low-pass filter response	115
Figure 136: The monitor LCD circuit diagram.....	116
Figure 137: The JSPHS-150+ data sheet.....	117
Figure 138: Control system under test	118
Figure 139: The control system circuit diagram.....	119
Figure 140: The four-character LCD	120
Figure 141: The complete receiver with the circular array.....	120
Figure 142: The laboratory in which the research was conducted	121
Figure 143: The key testing equipment employed in the present study	121

List of Tables

Table 1 The Interaction of Linear and Circular Polarization Antennas.....	30
Table 2: Specifications of circular polarized dipole.....	31
Table 3: The RG213 Specifications	32
Table 4: Technical Specifications of the Monitored Transmissions	36
Table 5 : The Technical Specifications of the Transmitting Points.....	37
Table 6: The Field Strength Variations in the 95.5 MHz and 94.8 MHz Signals, as Measured at 1:00 and 9:00 PM	41
Table 7: Very Strong Field Strength Intensity	59
Table 8: Medium Field Strength Intensity	65
Table 9: Low Field Strength Intensity.....	68
Table 10: Field strength of the NMHA and the monopole.....	93
Table 11: The field strength intensity of the modified and unmodified helix	95
Table 12: Real conditions field strength measurements of the modified NMHA	98
Table 13: The weights of the circular array at 270 degrees	104
Table 14: The weights of the circular array at 90°	104
Table 15: The weights of the circular array at 180°	105
Table 16: The weights of the circular array at 0°	105
Table 17: The phase arrangement	108
Table 18: The JSPHS-150+ performance data	117

Glossary of symbols and abbreviations

Abbreviation	Explanation
A_0	Propagation attenuation
A_{eff}	Effective Aperture
ADC	Analog to Digital Converter
AGC	Automatic Gain Control
Ψ	Incident Angle
AGND	Analog Ground
A_r	The receiving antenna effective aperture
β_n	Excitation Phase
c	Speed of Light 3×10^8 ms
CYBC	Cyprus Broadcasting Corporation
d	Distance
dLOS	Line of Sight Distance
D_n	Normalized path length
DAB	Digital Audio Broadcasting
DVB-T	Digital Video Broadcasting Terrestrial
DRM	Digital Radio Mondiale
δ	Skin depth
ϵ	Relative permittivity
e	Water vapour pressure (mb)
e_a	Actual water vapour pressure (mb)
E	Electric field

ERP	Effective Radiated Power
F,f	Frequency
FM	Frequency Modulation
G	Gain
h	Height
H	Magnetic field
HF	High Frequency
Hz	Hertz
I/P	Input
IEE	Institute of Electrical Engineers
ITU	International Telecommunication Union
K	Effective ray curvature (k factor)
KF	Fresnel Zone Layer
λ	Wavelength
γ	Rayleigh Roughness
LOS	Line of Sight
Ld	Diffraction path loss (dB)
Lp	Total path attenuation
LCD	Liquid crystal display
M	Modified refractivity
NMHA	Normal Mode Helical Antenna
N	Refractivity

n	Radio refractive index
σ	Conductivity
PCB	Prototype circuit board
PLL	Phase Locked Loop
RX	Receiver
r	earth radius
S	Power flux density
SIR	Signal to interference ratio
SNR	Signal to noise ratio
TX	Transmitter
UHF	Ultra-high frequency
VCO	Voltage Controlled Oscillator
VHF	Very high frequency
VSWR	Voltage standing wave ratio

Refraction Interference Elimination Employing Smart Arrays at VHF

By

Antonios Constantinides

Abstract

Radio interference from the Middle East is one of the most significant problems plaguing the local radio services in Cyprus today. The issue is particularly noticeable on the highway, where it affects in-car tuners in all coastal areas of the island when the weather is hot and humid. In this work, the problem of interference from the Middle East was explored in the context of field strength variations versus the type of propagation mechanism favouring the radio waves in Band II, allowing them to travel from the Middle East to beyond the horizon in Cyprus. This problem was significant, since no line of sight exists between the two regions. After in-depth analysis adhering to the ITU (International Telecommunications Union) Recommendations, it was demonstrated that interference is caused by “Tropospheric Ducting”, i.e., trapping of the overseas transmitted signals between two layers of the troposphere at different heights. The upper air data were obtained using the Weather Research Forecasting (WRF-ARW version 3.4) model. The results yielded by the present study confirm that this model provides accurate prediction of interference for up to five days in advance. The interference problem is widely recognized, and therefore many attempts have been made to explicate its causes and provide solutions. The aim of the present study was to present a robust solution based on an innovative receiving antenna design. The antenna is a receiver’s component that collects electromagnetic waves from various directions. The rationale behind focusing on a circular array topology is that its tuning ensures that the receiver processes the desired signal only, while rejecting the unwanted interference. This can presently only be achieved by a large directional external antenna that must be steered mechanically in the desired direction. As this arrangement is not practical, an innovative smart antenna was proposed as an alternative. A circular phased array is a very compact antenna that produces a predicted radiation pattern, whereby it receives maximum energy from the desired direction without

the need for mechanical control. Circular arrays exhibit high gain as well as immunity to interference, making them ideal for use in high interference environments. This combination allows the antenna to be incorporated into a commercial deck receiver or installed on vehicles.

The Professional Elements of the Project

The project “Refraction Interference Elimination Employing Smart Arrays at VHF” is closely linked to my professional background as a chartered radio engineer. I gained extensive experience in the field while working in the US and European industry in the capacity of radio transmitter and antenna designer. This is evidenced by the two separately funded research projects, which I have successfully implemented while also conducting my research for the doctorate degree. Particularly, the first research project was endorsed by the Research Promotion Foundation, with the goal of optimizing Digital Video Terrestrial Transmitters (DVB-T) in terms of efficiency and linearity of the final stage. The second project was initiated by the Ministry of Communication and Works, as a part of which I undertook the design and development of a dual-band solid state laterally diffused metal oxide semiconductor (LDMOS) amplifier that enables operation in Band II (87.5–108 MHz) by analog FM, Digital Radio Mondiale (DRM+) excitors and in band III (174-240MHz) for Digital Audio Broadcasting (DAB+) radio. Both projects commenced in October 2013 and were successfully completed in June of 2015. I have reported on the outcomes of these projects in international conferences and publications, the details of which are given in the appendices.

As a part of these initiatives, I was involved in many practical of engineering tasks, one of which pertained to the testing of RF apparatus in order to ascertain compliance with European standards, namely the Low Voltage Directive (LVD), Electromagnetic Compatibility (EMC) and Radio and Telecommunication Terminal Equipment (R&TTE). The main objective was to ensure that radio transmitters and receivers are certified with the European CE conformity for marking purpose. In addition to these activities, I utilized the laboratory equipment of ET Broadcast to conduct experimental research pertaining to my doctorate degree.

The rationale behind my doctorate research is based on my professional experience and the gaps in the knowledge I could glean through my activities and practical expertise. Going forward, I will benefit from not only the skills gained working as an engineer, but also my study findings. As the director of ET Broadcast LTD, I am confident that I can provide significant contribution to the field, as I will develop and realize in practice many FM radio transmitting projects aimed at mitigating the problem of interference from the overseas Middle East radio services. My appreciation of these issues has prompted me to, in

collaboration with the Cyprus Government, embark on this journey of academic research. The ultimate aim of my doctorate dissertation was to assist in finding the most optimal solution to the overseas interference, and use the results for the current and future radio plans in terms of the Middle East radio station frequency allocation. Furthermore, in the world of communication engineering, the implementation of a smart antenna that blocks the interference is valuable practical contribution to the field of engineering with a wide scope of applications. The project was also endorsed by my mentor, Dr. John Howard, the President of ET Industries INC, a firm that specializes in the design and manufacturing of phased arrays and intelligence antennas. With his full support, I was successful in developing this type of antenna ensuring that it operates in Band II. Hence, I envisage that the same solution can be applied by other practitioners in other sectors benefiting from commercial and military communication systems that can be compromised by interference. Its utilization will result in enhanced system performance, as discussed in the future work and conclusion chapters.

Chapter 1: Introduction

1.1. Introduction to the proposed system

Radio interference is presently the most serious issue affecting the operation of terrestrial radio stations in Cyprus. This problem has become particularly acute in recent years because of the high demand for new local and national radio services internationally. The interference examined in the present study is caused by a plethora of radio services that broadcast from the Middle East. Although VHF radio waves propagate under line of sight conditions, when the temperature rises, i.e., during the summer months, numerous and very strong Middle Eastern radio signals reach Cyprus and thus conflict with the local radio services, resulting in a complete loss of the desired signal. While the cause of this problem is presently not well understood, various attempts to mitigate it have been proposed over the years. As a solution, the Cypriot government mandates that the radio station owners install repeaters along the southern coast of Cyprus, where this issue is most prominent. However, introduction of new repeaters necessitates having a broader spectrum due to which the commercial band FM has become saturated. The worsening interference problem, which is expected to escalate further in the future, has motivated this doctorate dissertation, the aim of which is to analyze the problem of radio interference along the southern coast of Cyprus and offer a solution that can be utilized both in Cyprus and elsewhere in the world, as this issue is becoming prevalent in other regions. For example, in 2002, an abnormal propagation case was reported in South Korea by Son and Lee (2012), who analyzed the interference caused by ‘CPS’ (Cellular Phone System) in the ‘TRS’ (Trunked Radio System) due to the non-line overseas radio signals from Japan. In their comprehensive work, Sim and Warrington (2003) examined abnormal atmospheric conditions that enable VHF/UHF signals to travel beyond the horizon and cause interference in the Channel Islands. In Japan, Shin, Nishi and Yoshida (2011) conducted a study during 2005–2010, aiming to elucidate the causes of abnormal VHF-UHF signal propagation, which caused interference in the local radio and TV services. These and similar cases are discussed in more detail in the following chapters. They confirm that abnormal interference is an international problem, recognized by the International Telecommunications Union (ITU), prompting introduction of standards that can guide identification and assessment of abnormal propagation mechanisms arising due to meteorological conditions, which is the focus of the present study.

More specifically, the aim of this research was to investigate the characteristics of overseas signals arriving to Cyprus in terms of propagation mechanisms defined by the ITU, such as

the tropospheric refraction of radio waves and ducting propagation, along with the radio refractive index, its formulae and refractivity data, as well as the prediction procedures for the evaluation of microwave interference between stations on the Earth's surface at frequencies above 0.7 GHz which can be applied also for the VHF band as it has been used successfully by Son and Lee (2002). In order to achieve these objectives, real world measurements in Band II (87.5–108 MHz) were utilized in analyses, based on current overseas radio transmissions monitored in the southern coast of Cyprus beyond the horizon in a clear interference free spectrum during the hot dry summer months. The focus was specifically on the field strength variations in terms of the types of ducts that enhance the radio waves from the Middle East in Band II, allowing them to travel beyond the horizon and reach Cyprus.

The Department of Meteorology in Cyprus was instrumental in this research, as it provided all the upper air data needed to evaluate the problem on specific dates and times along the points that were selected based on the path of the selected radio signals arriving from the Middle East to the coast of Limassol. A particularly important contribution of the present study stems from the innovative calculations performed using the Weather Research Forecasting (WRF-ARW Version 3.4) model that, based on this implementation, enables accurate forecast of the interfering signal strength for the future period of up to five days.

Although the interference problem is widely recognized, and many attempts have been made to explicate its causes and provide solutions, at present the focus is on tuning the receiving antenna. The antenna is a receiver's component that collects electromagnetic waves from various directions. The rationale behind focusing the solution on the antenna is that its tuning ensures that the receiver processes the desired signal only, while rejecting the unwanted interference. This can only be achieved by a directional antenna that, when operating in VHF Band II, is large in size and must be steered mechanically in the desired direction. As this arrangement is not practical, smart antennas have been proposed as an alternative. These phased arrays have been used for years in radars. A phased array can produce a predicted radiation pattern, whereby it radiates its maximum energy in the desired direction (Malahias and Zagos, 1998) without the need for mechanical control. Owing to these characteristics, phased arrays exhibit high gain as well as immunity to interference, making them ideal for use in high interference environments. Howard and Fung have also developed the Clever Dumb Antenna that enables dividing up to 360° cell site into several high gain sectors. Benefiting from the phased array principles, the aim of the present study was to apply this technology in Band II by overcoming the physical

constraints imposed by the long signal wavelength characterizing this band. One of the most significant problems that have been addressed in this research is the size of the antenna, which must be relatively small to be employed in practice, while not compromising its performance. This combination would ensure that it can be incorporated into a commercial deck receiver or installed on vehicles. This aim was achieved by investigating the performance of popular small antennas operating in Band II, such as the small dipole, the short stub, as well as the Normal Mode Helical Antenna (NMHA), whereby the latter was shown to provide the best performance. Although NMHA is a narrow band antenna, its performance was optimized in this work, ensuring that it provides the best possible VSWR response across the entire Band II while keeping its dimensions small. Finally, the topology of the phased array designed as a part of this study is based on the circular array, as it can operate with a very small diameter and provide a directional pattern without distortion near the end-fire direction as explained in chapter 4. This design choice has been justified in practice, since the circular array can detect signals in all directions, successfully rejecting the interference coming from the Middle East coast.

1.2. Brief Thesis Outline:

Historical Overview and Critical Analysis: The thesis begins with a comprehensive literature review, which helps place the present study in the context of extant work in the field, as well as identify gaps in the current knowledge of interference, abnormal interference in particular. The studies reviewed in this chapter pertain to special cases of abnormal interference recorded around the world and the causes of radio interference, such as tropospheric refraction and ducting. This is followed by the discussion of methodologies that have been adopted to date in the assessment of interference. In addition, the historical development of antennae is briefly discussed, elucidating the key differences between conventional and smart antennae in the treatment of interference. The chapter ends with the discussion of the existing smart antenna designs, along with their application in telecommunications sectors as a means of mitigating the interference issue.

Analysis of VHF Propagation Mechanisms that Cause Interference within the Southern Coastal Regions of Cyprus: This chapter describes the methodology adopted in the present study in order to detect and evaluate the interference affecting the Southern coast of Limassol, which is caused by the Middle Eastern radio services. Furthermore, it discusses the measurements performed on the existing Middle Eastern radio services that arrive to Cyprus with strong signal density during the summer months, as well as the variation in these signals based on specific meteorological changes. In this evaluation, the ITU

standards were followed, as explained in this chapter. As previously noted, close collaboration with the Department of Meteorology was instrumental to the success of this project, since it has provided all meteorological data needed to meet the ITU Recommendations. Thus obtained meteorological data were combined with intensity measurements pertaining to the interference, allowing detailed examination of all propagation mechanisms permitting the electromagnetic waves to travel beyond the horizon.

Phased Arrays – A Robust Solution to the Problem of Interference: This chapter provides justification for using a phased array as the solution to the interference problem in Cyprus and other regions of the world. It commences with a discussion of key antenna theory principles pertinent to the implementation of the smart antenna and its specifications. This is followed by an examination of the behaviour of small antennas, such as the Hertzian dipole, the short stub and the Normal Mode Helical Antenna (NMHA), in order to justify performing laboratory experiments using individual array elements. In this evaluation, great emphasis was placed on the NMHA because of its superior performance and very small physical dimensions, allowing it to be modified in order to overcome the narrow band response issues and low efficiency of all small antennas. As a result, in this work, the bandwidth of the NMHA was optimized by testing several new topologies in order to obtain the best VSWR response and gain with the smallest permissible size. In addition, according to phased array theory, circular array is the best topology for this application, which was designed in this study by employing four modified NMHA. Because the array must be interfaced with a commercial receiver, a compatible receiver was also designed and constructed successfully in order to support the project.

Conclusion and future work: In this chapter, the most important findings and contributions yielded by the present study are summarized, along with the directions in which the research presented here can be expanded in the future. For instance, by applying additional measurements of the overseas transmissions, it will be possible to determine the probability of enhanced VHF (30–300 MHz) signals reaching the coast of Cyprus as a function of season, month, and time of day. Furthermore, applications of circular arrays in other commercial bands, such as Band III (174 to 240 MHz) for Digital Audio Broadcasting (DAB+), and digital video broadcasting terrestrial TV (DVB-T) that broadcasts in UHF Band in the channels 21–69 (i.e., in the 512–800 MHz frequency range) should also be investigated.

Chapter 2: Historical overview

2.1 Basic Interference Concepts

The problem of interference in radio communications, as indicated below, has been considered a significant global issue since the establishment of the first generation wireless technology. According to Marriott (1923), the first case of interference was reported in the USA, in 1901. In his view, ‘at the time, there was unintentional and intentional interference between radio stations in New York harbour’. This was when the Marconi Company, the American Wireless Telephone, Telegraph Company, and the De Forest Company tried to report the International “Yacht Races” at the same time. The above mentioned, was an object lesson that proved the need for avoiding radio interference and interference fights, and caused experiments and development in tune and in etheric diplomacy’ (P.375-388).

Jackson (1987) commented on case of interference, which was appointed in 1933 by the Council of the IEE. ‘The representative committee has reviewed the matters of interference to radio reception in order to make recommendations on methods of suppression and incorporation of suppression requirements in specifications for electrical equipment and also on the need for legislation’ (P.244-250).

Since then, as the incidences of interference became more prevalent, the global research interest on the issue grew, focusing mainly on ways to overcome the problem of interference by exploring new properties of electromagnetic waves. More specifically, the propagation properties in different wavelengths, new and/or upgraded modulation schemes and antenna topologies were explored, and some of these efforts are discussed below.

The first radio modulation scheme was designed with the focus on amplitude modulation, whereby a constant carrier was employed, the amplitude of which changed with respect to the modulated signal. Since the noise usually affects the amplitude of the received signal, it becomes an integral part of the demodulated information and is thus perceived as a product of interference (Greb et al 2003:220-221).

However, in 1930, Armstrong invented FM radio, which had superior performance compared to the AM, in terms of interference and noise immunity. FM radio utilizes the frequency modulation scheme, whereby its carrier frequency changes according to the amplitude of the modulation signal. As a result, the FM radio scheme is less susceptible to noise, as it demodulates only the frequency variations, without affecting the noise, typically treated an amplitude modulation component.

On the other hand, interference in terms of the antenna properties has been investigated by Dr. John Kraus, the inventor of the helical antenna and the corner reflector. In his work, Kraus (1988) presents crucial antenna parameters, such as the directive gain, as well as the front to back ratio, both of which play a key role in the enhancement of the signal to noise ratio (SNR). These factors are analyzed in his book “Antennas”, where the author also discusses the benefits of the phased arrays and their performance with respect to specific geometric shapes.

Owing to the considerable research effort in this field, the approaches in dealing with the problem of interference have been significantly improved since these early initiatives. However, it has not yet been eliminated, perhaps because of the growing demand for new radio services. In this regard, the International Telecommunication Union (ITU) has proposed specific regulations pertaining to certain technical aspects of radio communications manufacturing that cause interference. For example, recommendation “ITU-R BS.412-9” titled ‘Planning standards for terrestrial FM sound broadcasting at VHF’ governs the design and development of commercial Band FM radio transmitters. Its objective is to suggest the optimal technical specifications, targeting the maximum level of harmonic and spurious emissions, as well as the deviation limits, which prevents introducing interference to other radio services within the service area.

Although VHF/UHF electromagnetic waves travel on a straight line, under certain conditions, this may not be the case. These special mechanisms of propagation have been also demonstrated by the recommendation “ITU-R P.452-11” that designates the special properties of VHF/UHF electromagnetic waves that enable the transmitted signal to travel above high obstacles by diffraction or beyond the horizon by refraction or scattering. According to Recommendation ITU-RP.844-1* (1994) ‘Sporadic-E ionization appears as intensification in ionization in the form of a horizontal sheet of about 1km average thickness and a horizontal dimension of the order of 100 km. The height is commonly 100 to 120 km. Such sporadic-E layers can cause abnormal VHF propagation for periods lasting for several hours. The occurrence of sporadic-E propagation decreases with increasing frequency, but can be a significant cause of interference at frequencies up to about 135 MHz’. Consequently, under non-line of sight conditions, the aforementioned issues could cause interference between two different radio service areas, if the radio planning service has not been designed properly.

* Radiocommunication Study Group 3 made editorial amendments to this Recommendation in 2000 in accordance with Resolution ITU-R 44.

In this regard, beyond the Cyprus problem of interference, which concerns the Middle East radio services and was discussed in detail in chapter 1, several other non-line of sight special cases of interference have been registered throughout the world and are discussed as a part of the literature review. Due to the fact that they were introduced by signals transmitted beyond the horizon, every individual case is considered as an abnormal propagation. This phenomenon has been reported in several regions, including Japan, Korea, Channel Islands, and the UK. These individual cases are examined in more detail in subsequent sections.

2.2 Special Cases of Abnormal Radio Signals Propagation

2.2.1 Japan

Shin, Nishi and Yoshida (2011:1-4) present the ‘Classification method for reflection and duct propagation of FM radio waves observed at Hiroshima and Aso in Japan’. In their work, the authors focus on the issues of non-line of sight signals that caused interference to local radio and television services. The study lasted for five years, spanning the 2005-2010 period, and its primary aim was to detect the main cause of this abnormal propagation, as well as to examine its behaviour during specific seasons and weather conditions. Furthermore, the research was extended to identify a specific point of time at which the phenomenon reached its peak levels. The classification method the authors applied for the detection of the FM signal was implemented in frequencies in the 76-90 MHz range that, according to the ITU, it is the permissible frequency allocation of the commercial FM band in Japan. Furthermore, a Phased Locked Loop (PLL) synthesized receiver and an UDA-YAGI antenna were used for reception purposes, providing data acquisition during the day and night. The research findings, however, indicated that the interference was caused by two principal components, which have been reported as the ‘Reflection’ and ‘Ducting’. The Modelling of Tropospheric ducting effects on VHF/UHF propagation issues has also been reported by Slingsby (1991), who conducted a study that explored the extensive range in VHF/UHF transmissions, due to anomalous propagation conditions. The impact of such phenomenon, in the author’s view, ‘causes volatile problems of inter-service interference’. The author stated that ‘A reliable prediction of such anomalous propagation effects is therefore important in the planning of broadcasting services’. Furthermore, in publishing the paper, the author aimed to introduce to the broadcasting community ‘an effective

technique for determining the effects of troposphere ducts on signal coverage which is known as the ‘parabolic equation method Concepts’ (P.25-34).

2.2.2 South Korea

In 2002, an abnormal propagation case was reported as a study focusing on the coastal region of South Korea (Son and Lee, 2002). This case pertained to the interference of ‘CPS’ (Cellular Phone System) and ‘TRS’ (Trunked Radio System) due to the non-line of sight interference, which was caused in 1994 by overseas radio signals from Japan. The analysis performed as a part of the study focused on the field strength variations of the interference signal. The required data were collected from March to November in order to facilitate the path loss calculations pertaining to an assigned reference signal. The study findings suggest that the interference arose due to ‘Ducting’ which is discussed later. In this regard, the authors presented a new method (not relying on the parabolic equation) to predict the propagation loss in the lower atmosphere, which they termed the ‘APM’ (Advanced Propagation Model). The method is based on real measurements of field strength that are subsequently compared to a calculated model based on the ‘predicted propagation loss values’. In addition, as a part of this investigation, the authors also explored the reception antenna parameters that reduce the effect of interference. According to their report, ‘the technique, method which can protect from harmful interference are antennas tilt angle adjustment or antennas height adjustment or antennas diversity or base station position, displacement, etc’. Furthermore, the authors noted ‘As an effective way to reduce interference is to tilt an antenna main beam pattern downward at a certain angle, but this method reduces the service coverage region’. They concluded that ‘The radio ducting signal is varied as duct height, transmitting antenna height, receiving antenna height. ‘Thus, interference can be mitigated by adjusting the antenna height’ (P.502-505).

2.2.3 Channel Islands

In their renowned work, Sim and Warrington (2003:800-803) demonstrate ‘Measurements of the propagation characteristics of VHF/UHF radio waves over two over-sea paths in the Channel islands’. Their research focus on the atmospheric conditions, as well as the propagation principles that enable the VHF/UHF signals to travel beyond the horizon. According to the authors, ‘special propagation characteristics are defined as diffraction around the earth’s curvature, refraction within the atmosphere, and scattering within the troposphere’. Another crucial aim of the study was to determine the characteristics of antenna height, which was, according to their findings, ‘appropriate to inter-ship communications on VHF and UHF frequencies at ranges beyond the direct line of sight’.

The experiment was performed over a period of 17 months and 248 and 341 MHz were the selected frequencies under investigation.

In order to explore the aforementioned phenomena, two different sets of transmitting/receiving equipment were used to detect field strength variations over specific weather and non-line of sight conditions. In conclusion, the authors highlighted the significance of the outcome of their investigation, in particular the ‘enhancement of the interference field strength during warm summer days’.

2.2.4 United Kingdom

More recently, in his work titled ‘Statistics of Anomalous Atmospheric Propagation at UHF Frequencies’, Rudd (2009:3862-3864) explored short-term interference across the English Channel and the North Sea. The study was performed due to the lack of information on the short-term interference, given that most data was outdated and was provided by ‘the broadcasters in the decade of 1950-1960’. According to the author, ‘although the past studies provided a very good understanding of the annual statistics of the path loss between frequencies from 40 MHz to 40 GHz, have not, however, provided detailed statistical data about seasonal, diurnal and night time broadcast measurements’. In this respect, the new approach was necessary, in order to extend the knowledge of the short-term interference, in particular the phenomena affecting the terrestrial Digital TV services in the United Kingdom. One of the study objectives was to better understand the nature of the short-term interference, which has been considered as a ‘major destructive factor in reception quality for the terrestrial services in coastal regions, due to ducting overseas paths which do not exist over land’. Therefore, the investigation focused on the area encompassing the English Channel, including the French coast, as well as parts of the North Sea, from Belgium to Holland.

In this work, the field strength data collection technique from Holland and Belgium was implemented by the use of one receiver, and a log periodic antenna, which was installed in the coast of Southwold, where it was employed as a 24-hour monitoring system, as well as for annual measurements. Furthermore, the experiments conducted as a part of this investigation yielded results suggesting that, during the ducting event, ‘the power received for every individual transmitter were very stable’. In contrast, in the case of a ‘single frequency network (SFN) a fast fading pattern of + 2dB was detected’. It is worth noting here that propagation predictions have also been calculated on theoretical basis by utilizing the ITU-R Recommendations (P.370) and (P.452), which aim to contribute to the frequency planning and coordination. According to the author, ‘The algorithm of the new

revised ITU-R models (P.1546) has been revised to the ITU-R P.1812. The statistical results were found to be identical in both ways, like utilizing ITU-R recommendation models as well as from real measurements’.

Based on the models of propagation discussed above, it can be concluded that all investigations conducted in this field thus far have utilized antenna measurements in order to determine the field strength variations over the interference under specific conditions. As a result, it can be concluded that antenna likely plays a key role in understanding the entire propagation issue. It is therefore vital to examine the role of antennas in terms of interference and reception quality. This is achieved by exploring the past researchers’ work, in the literature review presented in the subsequent chapters.

2.2.5 Nigeria

In 2007, Adediji and Ajewole (2008) examined the vertical radio refractivity profile in Akure (southwestern Nigeria) at a height of 0, 50, 100, 150 and 200 m, because all previous studies conducted in the area aimed to investigate the surface refractivity gradient only. The meteorological data were obtained using five Wireless weather stations (Integrated Sensor Suite, ISS) installed at the aforementioned heights. In contrast, authors of previous studies conducted in Nigeria utilized radiosonde to obtain extrapolated data that lack the spatial and temporal resolutions necessary for the measurement of small-scale variations, particularly in the lower atmosphere. Furthermore, according to Adediji and Ajewole (2008) ‘radiosonde data do not provide a sufficiently high degree of accuracy to be completely acceptable for use in observing changes in the degree of stratification of the very lowest layers of the atmosphere’. The authors conducted the study between January and December 2007 and plotted the data in 30-minute intervals during this period. The obtained results indicated the occurrence of sub-refractive conditions observed to be prevalent between January and July, while super-refraction and ducting were observed mostly between August and December.

Because the aforementioned stations cannot obtain radiosonde data based on the coordinates in Figure 30, and the data are observed only once a day, the prognostic model WRF-ARW Version 3.4 was used in the present study because it is a special weather forecasting software that enables upper air data simulation at any fixed coordinates and hour in the day.

2.3 The Role of Antennas in Terms of Interference

2.3.1 Basic Concepts and Theorems

According to Balanis (2012:5-7), ‘antennas are the eyes and ears of wireless radio communications’. Moreover, ‘antennas dated back to Marconi’s days in 1901’. However, historically, antennas have primarily been used as an integrated part of every wireless communication system. According to Straw (2000), an antenna consists of at least one active element, which acts as the source of a resonant circuit, and it is known as the driven element. When operating as a transmitting source, the antenna radiates electromagnetic energy to the free space. In contrast, when used as a receiving source, it operates in exactly the opposite manner, as it collects electromagnetic energy radiated by the transmitters into the free space. For the aforementioned modes of operation, the reciprocity in antennas has been also demonstrated by John Giannopoulos (1963) in his work focusing on ‘the antennas for TV reception’. As the author stated, antennas exhibit equal properties, whether operating as transmitters or receivers, in terms of the radiation pattern, impedance, and bandwidth. The above reciprocity theorems have been justified by Lorentz Rayleigh-Carson in the 19th century, and later by Green, who demonstrated the relation between the ‘interchange of electric potential and electric charge density’.

Antennas are sources of electromagnetic energy and thus play a very significant role in the determination of the SNR value in wireless communication systems. This is discussed by Olsson, Brostrom and Craig (2004:1968-1702), who presented the method of elimination pertaining to interference as the ‘single antenna interference rejection in GSM/EDGE Networks’.

Furthermore, Mouhamadou et al (2006:251-265) provide additional information regarding the importance of the antennas in wireless radio and mobile cellular networks, by demonstrating ‘the Interference Suppression of the Linear Antenna Arrays controlled by phase with the use of the SQP algorithm’. In their view, ‘the performance of mobile cellular radio networks is limited by the level of co channel interference’. Therefore, ‘the use of antenna arrays is very helpful in enhancing the performance and capacity of the wireless communication system’.

2.3.2 Conventional Antennas

Before proceeding with an in-depth literature review regarding the advanced antenna topologies, which are described later, it is important to demonstrate why a simple antenna unit has been developed in other superior models and how this improvement has

contributed to interference control. For instance, according to Lee (1984), in theory, in its simplest form, an antenna is a short-sized (hertzian) dipole. However, the author also presented a literature review regarding the antenna design development, indicating that the hertzian dipole is not adequate for being used in real world applications, mainly because of its low efficiency and inadequate matching impedance response. In practice, however, the monopole antenna has been considered adequate, and is presently used by most of the commercial radio receivers in stationary and mobile applications, as indicated below.

According to Khan, Azim and Islam (2014:339-342), a monopole antenna provides an omnidirectional pattern and its performance depends strictly on the ground plane's conductivity. This claim was justified by applying the method of images. However, over the years, the antenna research has explored the combination of active and passive elements, as well as complete antenna systems in various geometric shapes, in order to achieve superior specifications over the traditional monopole. For example, the main focus on the research conducted by Kraus (1988) was the compromise among the crucial antenna's parameters, such as the radiation pattern, gain, efficiency, matching and bandwidth. As a part of the study, he assessed the effect of the antenna's physical size. It was evaluated as a function of the antenna's efficiency versus the operating wavelength, as well as its construction conductive material. More recently, Gorbachev et al (2010:177-179) presented a printed Yagi, directional antenna with significant lower physical size operating at a frequency of 1.8 GHz. In this, the main objective was to develop and explore the antenna, via a two-phase methodology. First, the research team designed and implemented the antenna based on the traditional approach, after which it was enhanced using a thick " ϵ_r " substrate material in order to compare the characteristics and performance of the two designs. It has been reported that the use of a thick substrate beyond the antenna's size affects the antenna's matching and directivity.

In relation to this study, it is worth noting that the Yagi is a linear polarized antenna comprising one active element as well as a number of passive elements defined as reflectors and directors (Yeo and Lee, 2016). Empirical evidence indicates that Yagi antennas provide high gain as well as a directional radiation pattern in order to operate as a lens. According to extant research, they are capable of increasing the power density of a selected signal within a specific angle defined as the beam width, whereas their performance degrades when operating outside the aforementioned range. As a result, Yagi antennas are mostly used in stationary receiving applications, where the desired signal and the interference are arriving from two different directions (Neelgan and Raju, 2011:115-

130). According to Kraus (1988), among other directional antennas commonly used in VHF/UHF wireless communications, most notable are the Corner Reflector, the Helical, as well as the log-periodic models. Under special circumstances, the dish antennas are also used in some UHF link wireless applications.

2.3.3 Advanced Antenna Topologies, Collinear & Phased Arrays

Literature review conducted as a part of this study has revealed that a single antenna is unable to provide unlimited high gain. For instance, according to Lee (1984), the maximum gain that can be provided by a single Yagi antenna is currently 15 dBi. Thus, two or more antennas, mounted side by side or stacked, must be used, in order to increase the total gain of the system. Such an arrangement is known as collinear arrays. According to the extant data, collinear broadside and end-fire active radiators provide high performance specifications in advanced applications, such as terrestrial broadcasting services. For example, Mappatao (2010:222-225) reports that 'FM antennas manufactured by most antenna manufacturers have an omnidirectional pattern in the horizontal plane, radiating signals equally well in all directions'. The author further states that 'These antennas, when used by radio stations, commonplace in high rise structures to obtain full coverage of the desirable areas within the service area of the station'. In such applications, 'Several bays are often side mounted along the top portion of a tower to achieve a higher gain' (Mappatao, 2010:222-225). Furthermore, according to Straw (2002), a collinear array is one-dimensional phased array that provides the benefit of the beam tilt in the desired direction of the incident wave. This arrangement is achieved by providing the required space and phase parameters of the active radiators. Other important aspects of collinear arrays have also been investigated by Delfino, Procopio and Rossi (2004:1480-1483), who assessed the effects of mutual coupling between the bays comprising the array. Thus, the current research has filled the gap in the extant knowledge in this field. In particular, it has contributed useful technical information on 'Phased Arrays, which beyond cellular communications are used in areas such as satellite communications and radars'.

Furthermore, Phased Arrays consist of a certain number of active radiators, side mounted vertically and horizontally, forming geometric shapes that resemble squares, rectangles or circles (Ndt.net, 2017). Among the many benefits of this system, the most notable one is that it provides very high gain that depends on the single antenna parameters, its architecture as well as the total number of active radiators that constitute the aforementioned array system. As a result, by ensuring the correct spacing among the active radiators, as well as the desired phase and amplitude, a Phased Array can produce a

predicted radiation pattern, whereby radiates its maximum energy in the desired direction (Malahias and Zagors, 1998:161-164). According to these characteristics, Phased Arrays exhibit high gain as well as immunity performance within a high interference environment. These advantages are due to the ability to program the main beam's directivity and Front to Back Ratio in advance. Howard and Fung conducted their study, focusing on an antenna, which they labelled 'Clever Dumb Antenna' in reference to its ability to derive the great benefits of the multi-beam antennas interfaced by a beamformer. According to the authors, 'the great benefit of such antennas enables dividing up to 360 degree cell site into several high gain sectors'. It is important to note that a beamformer the authors refer to is a signal processing technique based on a network comprised by phase shifters that enable programming of the adequate phase shift of the radiators in order to produce an optimum radiation pattern as well as beam tilt. In a different study, Vedula Paladuga and Prithvi, (2015) present a circular phased array, referring to it as a smart antenna, due to its ability to provide a low side lobe response for scanning purposes. As the side lobes are minor beams, scanning antennas enable reception from different angles of the main beam. Owing to these properties, low side-lobe response arrays are primarily aimed for use in a high interference environment. Winters (1998) and Gil (2005) extended the aforementioned research by examining the parameters of the two major categories of smart antennas, namely the phased and adaptive arrays. The adaptive arrays' radiation pattern, as the author's state, 'it is auto adjusted according to the move of interference, whereas the phased arrays' radiation pattern are not. They further explained that 'it is steered or different beams are selected as the desired user moves'. According to this view, smart antennas are highly recommended for new generation wireless communications. Consequently, they are presently being extensively researched in 'Europe in order to be applied in GSM networks as well as in Japan for satellite communications'. In this regard, the use of smart antennas is justified, given that they provide great benefits against interference. Presently, they are being applied experimentally in 4G/5G wireless radio communication systems and it is likely that their range of applications will expand in the future, given that this promising area of research will be explored for many years to come.

2.3.4 Chapter Conclusion

The literature reviewed in this chapter has confirmed that the problem of interference has influenced the global research of wireless radio communications. In this work, this phenomenon will be explored in two main phases. The first phase concerns the detection as well as the scientific analysis of the interference, whereas the second phase pertains to

upgrading the existing hardware technology in order to improve the operations of wireless communications, enabling quality operations within an interference environment. The review of the extant literature has further indicated that the interference is caused by the interaction of unwanted wireless radio signals with the useful ones. Moreover, while it typically occurs in direct line of sight, under certain circumstances, it can arise in abnormal propagation conditions. For example, in several regions of the world, including Japan, South Korea, Channel Islands, and the UK, the abnormal propagation has been investigated due to the fact that it has caused serious interference problems in different sectors of local wireless services.

For instance, in Japan interference primarily affected radio and television services, whereas in South Korea, cellular phone services suffered the greatest effects. In addition, in the Channel Islands, the investigation focused on non-line of sight signals in VHF/UHF bands, as this was the phenomenon that caused interference. This was also the case in the UK, where the interference was explored on behalf of terrestrial digital television services due to short-term interference affecting their performance. In order to model the behaviour of the interference, many studies have been conducted so far. However, most such investigations have been based on statistical analysis and data acquisition techniques, along with different data fitting methods, such as the parabolic equation and the 'Advanced Propagation Models'. As was shown in the discussions presented in previous sections, abnormal propagation is based mainly on refraction, diffraction or scattering, and it strictly depends on weather conditions prevalent in the region under investigation. In this respect, no scholarly articles have been published about abnormal propagation that caused the interference in Cyprus, or more generally the Eastern Mediterranean Sea.

Furthermore, based on Kraus (1988) and Balanis (2012:5-7), the findings reported in the reviewed literature have indicated that antenna is still the most effective weapon against interference. Due to the fact that antennas are the eyes and ears of wireless communications, they can be designed to control interference. Recent studies have indicated that the advanced antenna topologies, such as the phased and adaptive arrays, can be utilized as smart antenna configurations capable of auto-adjusting the main beam's direction according to the interference movements. The aforementioned technology has been applied experimentally in GSM, beyond satellite and radar systems. However, no scientific or scholarly articles have been identified as a part of this literature review, where the authors provide information on the application of smart antennas in either FM radio or the Digital Audio Broadcasting (D.A.B). In particular, no work has been conducted on

smart antennas that operate in Band II and Band III, perhaps because of the significant physical size requirements in the aforementioned frequency range which is discussed in chapter 4.

Chapter 3: Analysis of VHF Propagation Mechanisms that Cause Interference within the Southern Coastal Regions of Cyprus

3.1 Statement of the Problem

This chapter explores the type of propagation mechanism in the VHF Band II (87.5-108MHz), which favours the overseas transmissions from the Middle East, allowing them to cause a strong destructive interference in the local radio services along the southern coast of Cyprus. The co-channel and adjacent-channel interference degrades the reception quality in major service areas within the cities of Paphos, Limassol, Larnaca and their suburbs, as illustrated on the map presented in Figure 1.



Figure 1: The area affected by interference from the Middle East

The interference also adversely affects the "in car listening" quality across the main highway that connects the aforementioned cities. This phenomenon can be better understood by noting that, according to preliminary measurements in Band II, the national radio services' field strength intensity in Limassol ($34^{\circ}42'26.66''N$, $33^{\circ} 1'24.35''E$) lies between 55 and 60 dB μ V/m, as indicated by the spectrum analyzer readings shown in Figure 2. Furthermore, measurements during motion, across the highway, have indicated that the field of the national services fluctuates in the 35-52 dBuV/m range, as confirmed by the spectrum analyzer readings shown in Figure 3. (These measurements were conducted by the use of a 0 dB monopole antenna at one meter height above the ground and at a speed of 75 km/h). Thus, the Carrier-to-Interference-Ratio (SIR)¹ of the local radio services to the undesired overseas transmissions determines the co-channel interference² at any random point of reception within the southern coast of Cyprus. The co-channel and adjacent channel interference only occur when the level of these

¹ It is the quotient between the average received modulated carrier power to the average received co-channel interference power.

² Co-channel interference is crosstalk from two different radio transmitters using the same frequency

unwanted signals exceeds that of the local services. This occurs at random locations where the automobile receiver demodulates an unwanted signal, rather than the desired program to which it has been tuned. Empirical evidence indicates that this phenomenon is more pronounced in motion due to multipath fading (K. Chy, 2015).

According to the Cyprus government, the monthly average field strength intensity of unwanted overseas transmissions fluctuates. However, under the conditions investigated in this study, these effects, must exceed the free space level of the local radio transmissions in order to produce interference in band II. Furthermore, the field strength intensity of these unwanted transmissions may depend on the weather conditions, and thus varies with the season and the time of reception. For instance, the phenomenon appears weak during the spring and peaks during the hot, dry summer months.

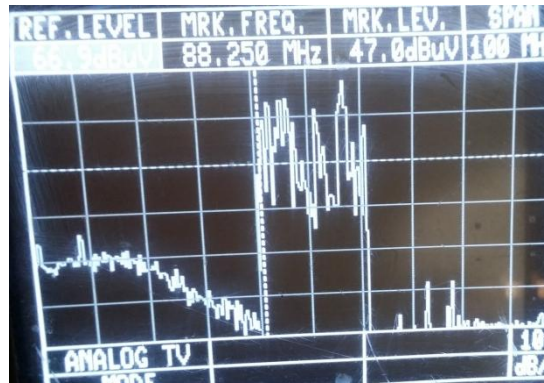


Figure 2 : Spectrum analyzer readings of the local radio services in Limassol

During the autumn, the effect weakens again and vanishes completely in the winter. The extant Tropospheric case studies conducted in Korea, Nigeria, Japan, etc. (presented in the literature review chapter) revealed that a non-line of sight interference is attributed to abnormal mechanisms of propagation. Hence, one of the aims of the present study is to reveal the propagation mechanisms affecting the signal quality in Cyprus.

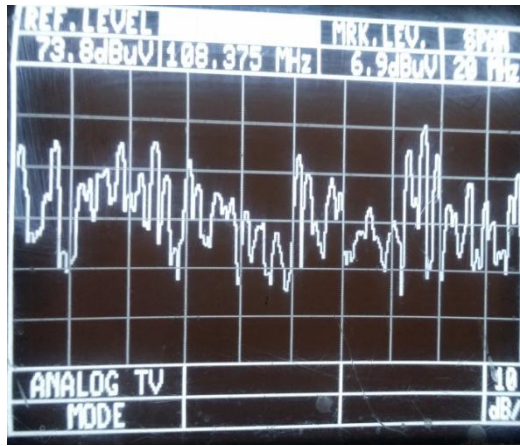


Figure 3: Spectrum analyzer readings during motion

The focus is specifically on those favouring the radio waves in Band II, allowing them to travel from the Middle East beyond the horizon in Cyprus, since line of sight conditions do not exist between the two regions as it will be investigated in the following chapters. The aims and objectives of the study are presented below in this chapter and in the remaining chapters.

3.2 Interference Testing Methodology

The methodology adopted in this study for determining the type of interference propagation mechanism is based on experimental research (real condition measurements) as well as applied theory of propagation mechanisms. In performing the measurements, the goal was to plot the field intensity variations of the unwanted overseas signals versus various weather parameters. Furthermore, the aim was to investigate their characteristics in terms of all types of propagation mechanisms. A vital part of the research has been based on the implementation of a path profile analysis, which focuses on the detection of overseas radio waves as they have been monitored in Cyprus in clear spectrum during the summer of 2015. They arrive to Cyprus from two different directions, Israel and Lebanon, and will be discussed thoroughly later. This assertion is confirmed by the measurements that were conducted from June to September 2015 by utilizing dedicated test equipment, described in the subsequent sections. A vital part of the path profile analysis was based on the Recommendations ITU-R 452, 453, and 834. These recommendations provide the testing procedures and mathematical expressions incorporating the meteorological parameters that affect the radio refractivity of the Troposphere that permits the overseas radio waves to travel beyond the horizon and cause interference (more details on this phenomenon are provided below).

Specifically, in this work, the Recommendation ITU-R P.834 was adopted, as it pertains to the effects of tropospheric refraction on radio wave propagation' and Tropospheric Ducting propagation. For the same purpose, the ITU-R P.453 was also considered in order to demonstrate the radio refractive index, its formulae and refractivity data. Finally, the ITU-R P.452 pertains to the prediction procedures for the evaluation of microwave interference between stations on the surface of the Earth at frequencies above about 0.7 GHz. It has been utilized in this study, as it pertains to all possible cases of propagation mechanisms that enable interference.

The main objective of this research is to explore each type of these propagation mechanisms on individual basis by considering the two major categories, as demonstrated by the Recommendation ITU-R 452, which indicates that the long-term mechanisms incorporate the line of sight, diffraction and tropospheric scatter. The short-term mechanisms, on the other hand, include ducting, elevated layer reflection, as well as hydrometeor scatter (Son, 2002). More details pertaining to the scientific properties of each of the aforementioned propagation mechanisms are defined by the ITU and are presented in the following paragraphs, because they constitute the foundation of this study.

3.2.1 Line of Sight

‘The most straightforward interference propagation case occurs when a line-of-sight transmission path exists under normal (i.e. well-mixed) atmospheric conditions. However, an additional complexity is introduced when sub-path diffraction causes a slight increase in the signal level above that normally expected. In addition, on all but the shortest paths (i.e. paths longer than about 5 km), signal levels can often be significantly enhanced for short periods of time by multipath and focusing effects resulting from atmospheric stratification’

3.2.2 Diffraction

‘Beyond line-of-sight and under normal conditions, diffraction effects generally dominate wherever significant signal levels exist. For services that are unaffected by anomalous short-term problems, the accuracy to which diffraction can be modelled generally determines the density of systems that can be achieved. However, the diffraction prediction capability must have sufficient utility to cover smooth-Earth, discrete obstacle and irregular (unstructured) terrain situations’.

3.2.3 Tropospheric Scatter

‘This mechanism defines the “background” interference level for longer paths (e.g. those exceeding 100-150 km in length) where the diffraction field becomes very weak. However,

except for a few special cases involving sensitive Earth-based stations or very high power interferers (e.g. radar systems), interference arising from troposcatter will be at a level that it too low to be of practical significance’.

3.2.4 Surface Ducting

‘This is the most important short-term interference mechanism over water and in flat coastal land areas, and can give rise to high signal levels over long distances over the sea (exceeding 500 km). Such signals can exceed the equivalent “free-space” level under certain conditions’.

3.2.5 Elevated Layer Reflection and Refraction

‘The treatment of reflection and/or refraction from layers at heights up to a few hundred meters is of major importance, as these mechanisms enable signals to overcome the diffraction loss arising from the terrain very effectively under favourable path geometry conditions. Again, the impact can be significant over quite long distances (up to 250-300 km)’.

3.2.6 Hydrometeor Scatter

‘Hydrometeor scatter can be a potential source of interference between terrestrial link transmitters and Earth-based stations because it may act virtually omnidirectional, and can therefore have an impact in directions off the great-circle interference path. However, the interfering signal levels are quite low and do not usually represent a significant problem’.

3.3 Location and Instrumentation Set Up

The equipment described in this section was used for monitoring the field strength intensity of the undesirable signals from the Middle East in order to study their properties. However, it is not practically possible to conduct field strength measurements at every single reception point within the southern coast of Cyprus. Consequently, it was important to identify a reference point that can serve as a permanent and reliable source of measurements of field strength intensity of the unwanted overseas transmissions on a daily basis. This was achieved by utilizing the testing equipment of the company “ET Broadcast LTD”, located in the northern part of Limassol (34°42'37.14"N, 33° 1'15.26"E). The location is at 313 ft above sea level (asl) and has an absolute line of sight with the coast of Limassol. For reception purposes, a broadband response, circular polarized dipole antenna has been installed outdoors, on a mast, one meter above the ground in order to represent the height of a typical commercial receiver’s antenna. The testing *equipment* arrangement is illustrated in Figure 4 and all its components are described below.

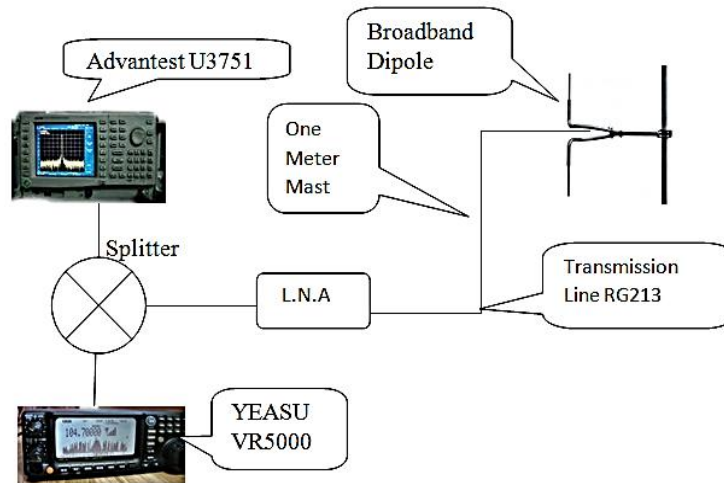


Figure 4: Testing equipment arrangement

The Advantest U3751 is a professional spectrum analyzer that is used to provide field strength measurements of the monitored unwanted transmissions. The YEASU receiver VR5000 was employed in the present study in order to provide the audio information of the unwanted signals during testing. Furthermore, the circularly polarized dipole antenna was used as the major receiving antenna of the testing chain. The low noise amplifier was included into the equipment chain in order to compensate for the signal losses arising from impedance mismatch, as well as insertion losses due to the wiring among the testing components.

In addition to these measurements, additional data was obtained from the Department of Electronic Communications, which is the official body of the Cyprus Government responsible for radio signal measurements and monitoring. The department has official access to the sophisticated system “THALIS” that enables field strength data from all major regions of Cyprus to be displayed on a continuous basis for a long period of time. The system comprises of a chain of omnidirectional antennas that provide the field strength information to a central computer unit in Nicosia. Finally, the radiosonde data required for the present study were sourced from the Meteorological Department of Cyprus.

3.4 The Importance of the RX Antenna Polarization Sense

Monitoring antenna polarization sense³ is essential for obtaining accurate readings of the unwanted transmissions’ detection. The importance of this key issue in radio communications discipline stems from the fact that the air interface between the transmitting and receiving antennae must exhibit an identical polarization sense in order to achieve a maximum Signal to Noise Ratio (SNR) of the received signals (Wang, Lv and

³ The polarization of an antenna is the direction of the radiated fields produced by the antenna.

Li, 2014). The aforementioned case is described by two principal equations representing the electric field's vector orientation of the radiated or received electromagnetic waves (Kraus, 1988):

$$E_x = E_1 (\sin(\omega t - \beta z)) \quad (1)$$

$$E_y = E_2 (\sin(\omega t - \beta z + \delta)) \quad (2)$$

Where:

E_1 = amplitude of the wave in x direction

E_2 = amplitude of the wave in y direction

$$\beta = 2\pi/\lambda$$

δ = time phase angle by which E_y precedes E_x

Considering these equations, the two major antenna polarizations utilized by radio industry in Band II are discussed below.

3.5 Vertical Polarization

A linearly polarized antenna Electric field phasor is only in one plane, which can be either vertical or horizontal. Hence, utilizing a linear vertically polarized antenna ensures that the electric field vector (E) is perpendicular to the Earth's surface, whereas the magnetic field (H) vector oscillates at 90 degrees angle compared to the Electric field as illustrated in Figure 5. However, despite its horizontal polarization, this arrangement is not applied in FM radio services, which rely on a linear horizontal polarization antenna, and thus benefits from vertical polarization. In practice, the polarization state of linearly polarized antennae is determined by the orientation of the antenna's wire with respect to the Earth's surface. In theory, these arrangements are described by Eq. 1 and 2, i.e. when $E_1 = 0$, the wave is linearly polarized in the Y direction and vice versa (Kraus, 1988).

3.5.1 Advantages and Disadvantages of Linear Vertical Polarization in the Context of FM Broadcasting

Vertical antenna polarization is predominantly used in FM radio broadcasting, as it provides many benefits. For example, a vertically polarized monopole antenna is found in most automobiles for reception purposes (Fanning, 2009). As a result, a vertically

polarized transmitting antenna will provide the maximum possible SNR in the received signals during driving.

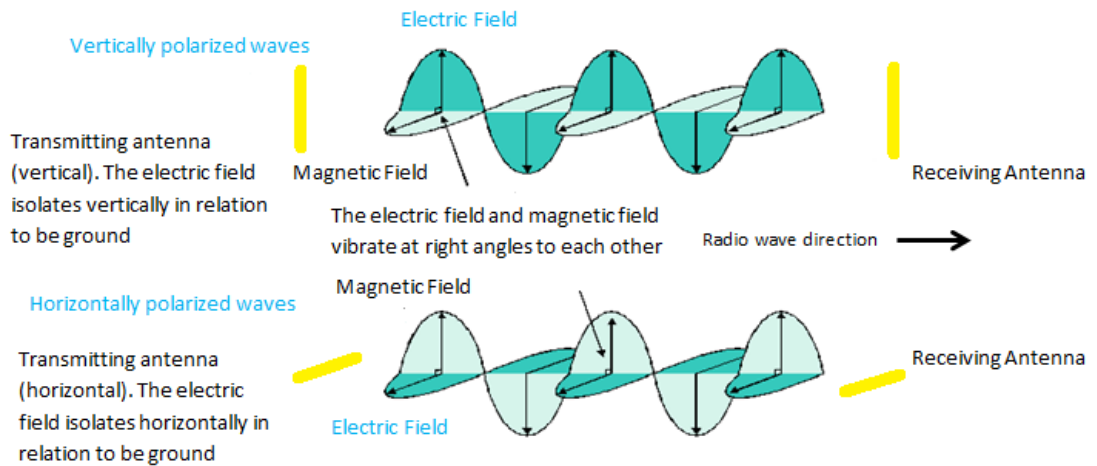


Figure 5: Linear vertical and horizontal incident waves

Another important factor that has prompted the broadcasting industry to adopt linear vertical polarization antennae in many applications is the omnidirectional radiation pattern⁴ that is obtained by a vertically polarized half-wave dipole (Straw, 2002). In this respect, the E and H plane patterns of a linear vertically polarized half-wave dipole antenna have been simulated by the use of EZNEC software, as demonstrated in Figure 6. The magnetic field (H) represents the horizontal plane (Azimuth), whereas the electric field (E) is perpendicular, i.e. lies in the vertical plane (Elevation). The expression describing the half-wave dipole's electric field is given by (Kraus, 1988):

$$E = \frac{\cos \left[\left(\frac{\pi}{2} \right) \cos \theta \right]}{\sin \theta} \quad (3)$$

Where θ is the angle of direction of the E Field

Despite the aforementioned benefits of linear polarization, its major drawback arises from the reflections of a linear polarized wave that occur from buildings in densely built urban areas, such as cities, or from the hills in rough terrain. This phenomenon results in a change from the linear, vertical polarization to a random polarization state.

⁴ The radiation pattern is a graphical depiction of the relative field strength transmitted from or received by the antenna.

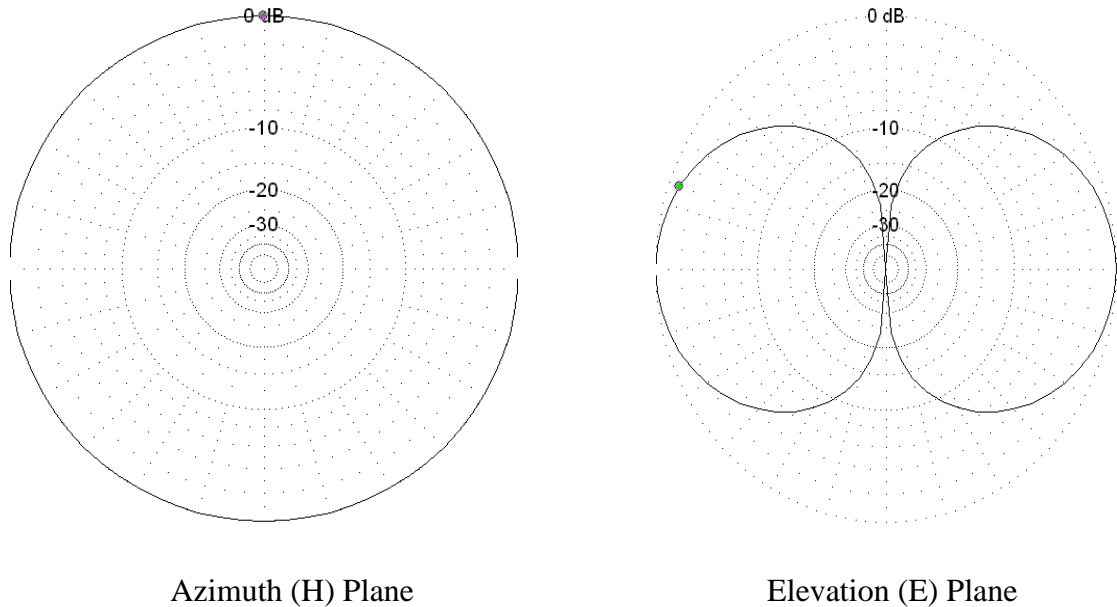


Figure 6: Azimuth and elevation planes of E field of a half-wave linearly polarized dipole

In case of a receiver's vertically polarized antenna, as installed on an automobile, signal will not be received properly due to the random polarization, and will cause nulls.

3.5.2 Discussion of Circular Polarization Antennas in FM Broadcasting

Although dual linear polarization was considered, the processing of the signal was more complex and therefore circular polarization was chosen for ease of signal processing. A circular polarized antenna enables radiation or reception equally well, in all planes, and across 360 degrees, as it contains both vertical and horizontal linear components. However, it should be noted that the planes are always out of phase by $\frac{1}{4} \lambda$ (denoting signal wavelength). Consequently, there is always a 3 dB loss when a circularly polarized incident wave is received by a linear polarization antenna and vice versa (Lee, 1984). Based on the Eq. 1 and 2, the circular polarization (CP) state occurs when $E_1 = E_2$ and $\delta = \pm 90$. The CP ability to operate in all planes equally well is defined as the axial ratio of a circularly polarized antenna, which becomes a crucial factor when the linear polarization of an incident wave is unknown. In this respect, the electric field of a circularly polarized antenna rotates perpendicular to the axis, and according to the sign of the time phase angle δ , it rotates clockwise or counter clockwise, as illustrated in Figure 7.

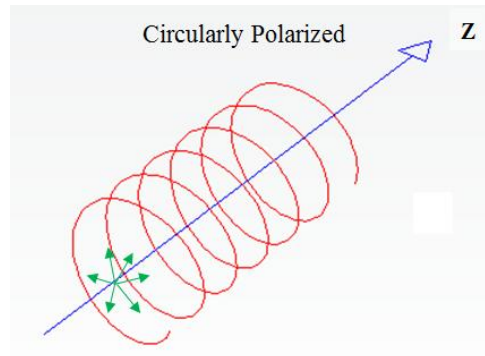


Figure 7: The rotation of a circular polarization incident wave

One important benefit of a circular polarization incident wave is that, although its rotation changes direction due to reflections from clockwise to counter clockwise and vice versa, it always incorporates the linear polarization components in any rotational direction. Thus, from the perspective of a receiver’s linear monopole antenna, this change will not be noticeable in terms of the received signal’s field intensity (Green, 1983). However; an important disadvantage of the circular polarized antennas concerns the 3 dB loss that occurs in reception when the receiver has been installed with a linear polarization antenna.

3.5.3 Linear Versus Circular Polarization

The interaction of linear and circular polarization antennae is illustrated in Table 1.

	Horizontal	Vertical	RHCP	LHCP
Horizontal	0	30	3	3
Vertical	30	0	3	3
RHCP	3	3	0	30
LHCP	3	3	30	3

Table 1: The interaction of linear and circular polarization antennas

Based on the above, the following conclusions can be reached:

1. As a circularly polarized receiving antenna enables reception in all planes, it will provide a superior performance in cases where the incident wave is affected by a random linear polarization.
2. When the receiving antenna is LHCP, a circularly polarized RHCP wave will introduce significant losses, which are typically in the order of 30 dB.
3. A vertically polarized receiving antenna will provide a maximum SNR when the incident wave is only vertically polarized; however, due to reflections, polarization may be random and exhibit losses.

4. A vertically polarized antenna enables a good reception when the incident wave is circularly polarized in either RHCP or LHCP mode and vice versa.

Considering the above parameters, in this study, a circularly polarized antenna was employed for monitoring the unwanted transmissions under the condition that they utilize linearly polarized antennas. This is elaborated on in the subsequent chapters. Briefly, circular polarized dipole provides a better SNR than a linearly polarized one, i.e. it eliminates the need to align the antenna.

The specifications of the selected circular polarized dipole are presented in Table 2.

Freq. range: 87.5 – 108 MHz
Impedance: 50 Ohm
V.S.W.R.: <1.4:1
Gain: -1.5 db
Bandwidth: 300 KHz
Connector: “N”
Weight: 5 Kg
Max Power: 500 W
Polarization: Circular
Dimension: 580 x 350 x 850 mm

Table 2: Specifications of circular polarized dipole



Figure 8: The testing antenna

3.6 Rigorous Analysis of the Voltage Standing Wave Ratio (VSWR) and Insertion Loss of the Testing Equipment Topology

The true operating conditions of the testing equipment’s topology should be computed before commencing the monitoring of the unwanted transmissions arriving from the Middle East. This task must be accomplished in order to avoid inaccurate results in measurements concerning the field intensity of the monitored signals, especially those pertaining to the weak ones. In this regard, the SNR of the received signals at the input port

of the “Advantest spectrum analyzer” (Fig. 4) is determined according to their signal density, the receiving antenna’s “Gain” and from the Voltage Standing Wave Ratio (VSWR), as well as the “insertion losses” of each element in the test equipment chain, as expressed by Eq. 4 and 5 below (S.Laverghetta, 1996):

$$SNR(dB) = \left(\frac{P(Signal)}{P(Noise)} \right) = 10 \log_{10}(signal) - 10 \log_{10}(Noise) \quad (4)$$

$$PdB(signal) = Antenna(GaindB) - \{\sum(VSWR + Insertion Losses)\} \quad (5)$$

Based on Eq. 5, the antenna is considered the most vital component of the chain, as it determines the SNR of the entire system. Furthermore, the reflection losses from the antenna’s VSWR and the transmission line’s insertion losses will be combined, resulting in a reduction of the antenna’s Gain, as expressed by equation 5. Therefore, the field intensity readings of the received signals will not be accurate. Consequently, the reflection and insertion losses must be compensated for, properly, by the use of a Low Noise Amplifier, as will be discussed at the end of this chapter. The major loss of the system is expected to be caused by the transmission Line RG213, the computation of which is described below.

Step 1: Calculations of the Coaxial Cable Length Insertion Losses

The attenuation in dB per unit length of the transmission line RG213 can be derived from the factory specifications given in table 3. It is computed based on a simple cross-multiplication using Eq. 6 below:

$$Loss (dB)15 meters = \frac{6.89}{100} \times 15 = 1.0335 dB \text{ or } 21.18\% \quad (6)$$

1. Inner Conductor Material and Plating: Copper
2. Dielectric Type: PE
3. Shield Material: Copper Braid
4. Impedance: 50 ohm
5. Velocity of Propagation: 0.66
6. Length: 15 meters
7. Testing Frequency: 100 MHz
8. Attenuation (dB/100 m) = 6.89

Table 3: The RG213 specifications

Step 2: Calculations of Antenna's VSWR Losses

The VSWR losses of the antenna arise due to the impedance mismatch between the coaxial cable characteristic impedance (50Ω), the source and the antenna's impedance arising due to the change from purely resistive function to complex impedance. This is a very important consideration in practical measurements,

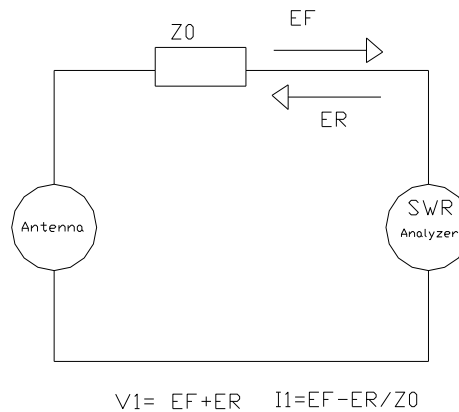


Figure 9: Scattering parameters of one port system

as the antenna has been installed on a metallic mast, very close to the Earth's surface. Thus, the mutual coupling of the surrounding objects, including the mast and the Earth's surface, will ultimately affect the 50Ω default impedance indicated by the antenna's factory specifications, changing it to an unknown value that must be established based on new measurements (Hon Tat Hui, 2010). The VSWR measurements are conducted at the input of the 15-meter-long transmission line RG213, as illustrated in Figure 10. The VSWR can be expressed via scattering parameters in terms of one port system (e.g. S_{11}), as illustrated in Figure 10 (HEWLETT PACKARD, APPLICATION NOTE 95-1, 1995)

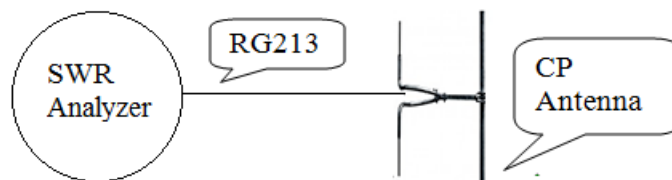


Figure 10: VSWR analyzer

The mathematical expression describing the VSWR in one port system is given by:

$$VSWR = \frac{1+S_{11}}{1-S_{11}} \tag{7}$$

S_{11} = Reflection coefficient given by S parameters

The return loss characteristics can thus be calculated using the expression below (Eq. 8) with the results provided in Figure 11.

$$\text{Return Loss (dB)} = 20 \cdot \log \frac{VSWR+1}{VSWR-1} \quad (8)$$

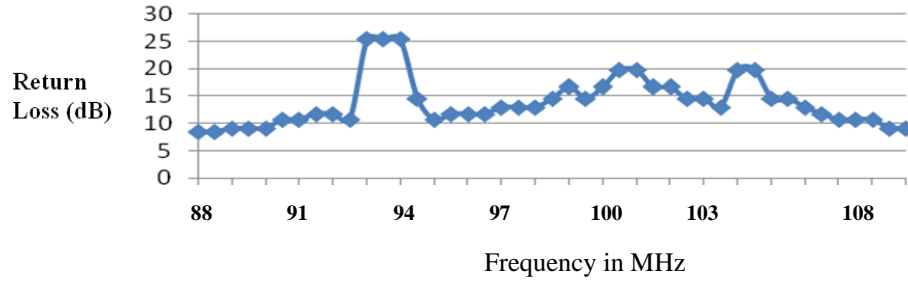


Figure 11: Return loss versus frequency

3.6.1 True Antenna Gain-Overall Signal Losses-Compensation

The transmission line RG213 losses based on its 15-meter length were calculated at 1.0335 dB using Eq. 6. The information pertinent to the return loss characteristics of the antenna response were illustrated in Figure 11 as well. Thus, the overall losses comprise of two components—the VSWR and insertion losses—which are combined. These phenomena are described by Eq. 9 and 10, respectively:

$$VSWR \text{ Loss}(dB) = 20 \cdot \log \left[\frac{VSWR+1}{VSWR-1} \right] - 1.0335 \text{ dB} \quad (9)$$

$$P(\text{signal}) = \text{Antenna}(\text{Gain dB}) - [\sum(VSWR + \text{Insertion Losses})] \quad (10)$$

Finally, the true signal losses are given in Figure 12, which indicates that the losses range between 1 and 1.5 dB, according to the testing frequency. Furthermore, these additional losses will reduce the circularly polarized antenna's gain by -2.5 to -3 dB. However, these losses can be compensated by the use of a Low Noise Amplifier, which is installed on the mast in a close proximity to the antenna, in order to restore the gain of the antenna back to -1.5 dB. The amplifier has a variable gain (0-10 dB), and illustrated in Figure 4.

The VSWR and insertion losses of the splitter and the connectors are negligible and have thus been excluded from the above calculations.

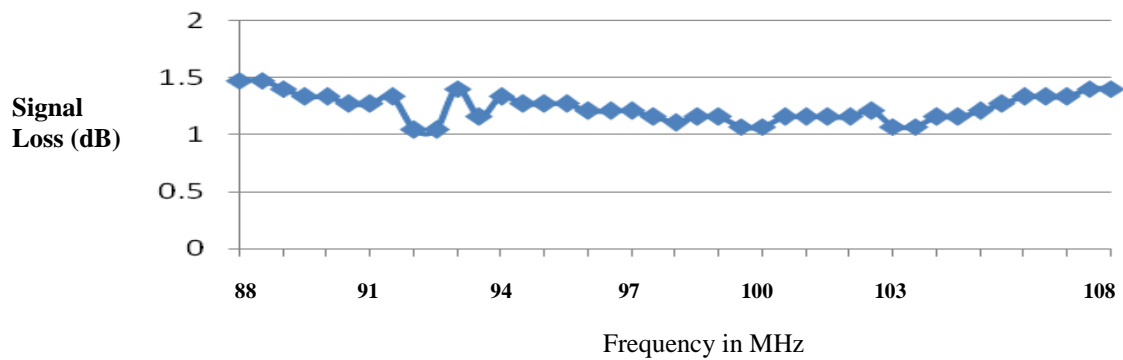


Figure 12: Overall signal losses versus frequency

3.7 Monitoring Unwanted Overseas Transmissions

This section focuses on the behaviour of the overseas signals arriving from the Middle East in clear spectrum. It also provides their technical specifications, followed by the long- and short-term field strength intensity measurements made by the 30 kW main transmitter of the Cyprus Broadcasting Corporation (CYBC) that is installed on Olympus Mountain, Troodos. The CYBC’s field intensity measurements in Limassol are also included, as they are adopted in the present study as the reference values for all other national radio services in Cyprus because they all exhibit similar specifications. It should, however, be noted that, although many unwanted overseas transmissions have been monitored in Band II, as they overlap with the local radio services, their behaviour could not be studied. Nonetheless, two overseas signals could be detected in a very clear spectrum in Limassol, namely The Lebanon “Radio Libran Libre” 102.5 FM, broadcast from Lebanon, and the “Tel Aviv” 95.5 MHz, broadcast from Jerusalem, Israel. In this work, these two signals served as the reference overseas transmissions, i.e. their behaviour represents all other unwanted transmissions in Band II that arrive from the Middle East to Cyprus. This decision was made as all incoming unwanted signals arriving from that direction are transmitted from the same region and exhibit similar technical properties. The technical specifications of the aforementioned overseas signals, as well as the national radio “CYBC” have been obtained by the I.T.U. and are illustrated in table 4.

3.7.1 The Path Length Calculations of the Detected Signals

The path length from the aforementioned regions to the coast of Limassol must be determined, as it is subsequently utilized for the line-of-sight calculations, performed in the next chapter. Therefore, by the use of Google Earth professional software tools, the path length between Israel and Limassol, as well as Lebanon and Limassol, has been calculated based on the coordinates given in Figure 13. The transmitting point’s altitude of the 95.5

MHz signal from Israel is 860 m, and the path length to Limassol is 376 km. Similarly, the path length of the Lebanese 102.5 MHz signal to Limassol is illustrated in Figure 14, and is measured at 271 km, whereby the transmitter point is located at 2295 m asl. Finally, the path length between Limassol and Olympus Mountain, as it concerns the service area of the national radio station CYBC 94.8 MHz signal, is illustrated in Figure 15 and is measured at 29 km only, with the transmitting point altitude of 1549 m (i.e. the transmitting point has absolute line of sight with Limassol).

ITU country code	LBN	ITU country code	ISR	ITU country code	CYP
Location	Farayar/Mzaar	Location	Jerusalem/Eitanim	Location	Mount Olympos
Coordinates	35e50/33n58	Coordinates	35e06/31n47	Coordinates	32e52/34n56
Longitude	33°50'24.80"	Longitude	35°05'50.40"	Longitude	32°51'38.15"
Latitude	33°57'55.80"	Latitude	35°46'39.60"	Latitude	34°56'18.70"
Longitude decimal	35.840222	Longitude decimal	35.097333	Longitude decimal	32.860597
Latitude decimal	33.965389	Latitude decimal	31.777667	Latitude decimal	34.938528
Coordinates precision	3	Coordinates precision	3	Coordinates precision	3
Frequency	102.5000000	Frequency	95.5000000	Frequency	94.8000000
Language	ar	Language	He	Language	El
Program	Loubnan al-Horr=R.Liban Libre	Program	IBA 2 Reshet Bet	Program	CyBC-RIK Trito Prog.
Modulation	m	Modulation	S	Modulation	S
Power	50.0000000	Power	40.0000000	Power	30.0000000
		Directional	D		
Polarisation	v	Polarisation	V	Polarisation	c
		Antenna relative height	90		
		Effective relative height	860		
RDS-PS	noRDS	RDS-PS	BET_E__	RDS-PS	_AKOYTE_TO_TPITO TOY_PIK_94,8_MHz 94.0_MHz 96.0_MHz 106.7MHZ HH:MM:SS
RDS-PI	noPI	RDS-PI	4202	RDS-PI	2203
		Remarks	May/June 2010 at Balaton/Hungary	PTY	99

Table 4: Technical specifications of the monitored transmissions

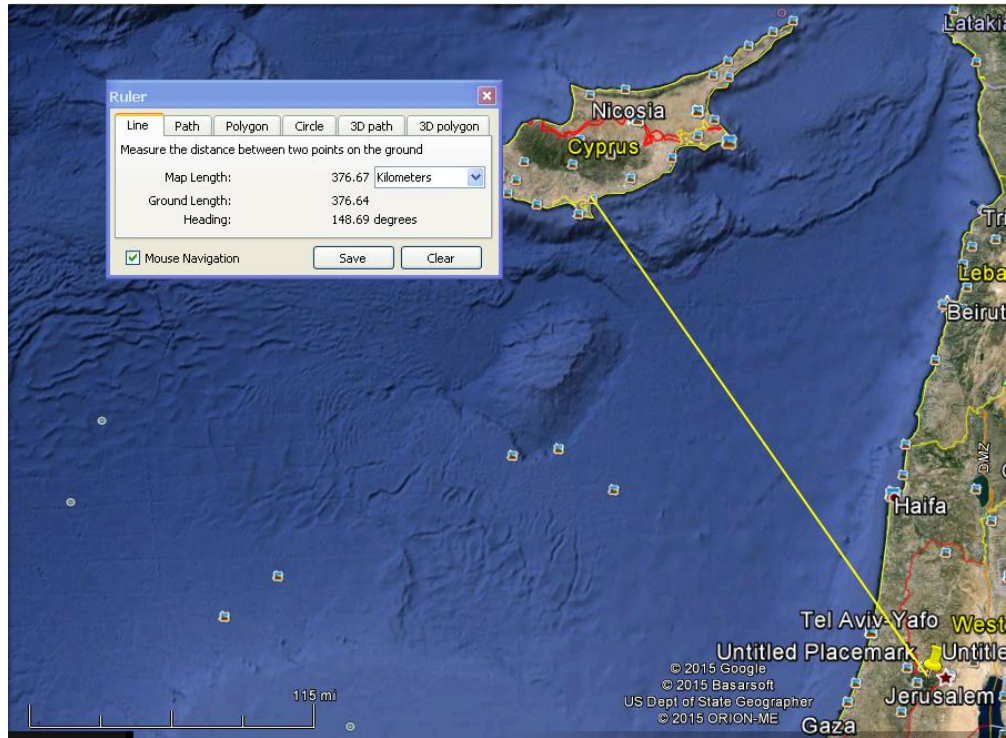


Figure 13: Path length between Limassol and Israel, 376 km, height 860 m

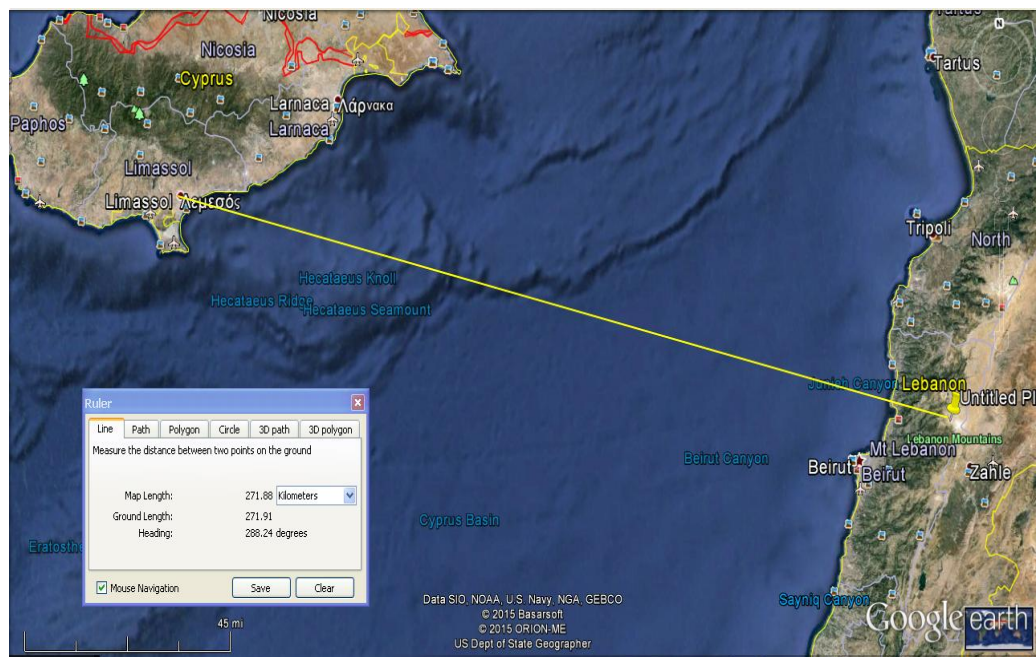


Figure 14: Path length between Limassol and Lebanon, 271 km, height 2995 m

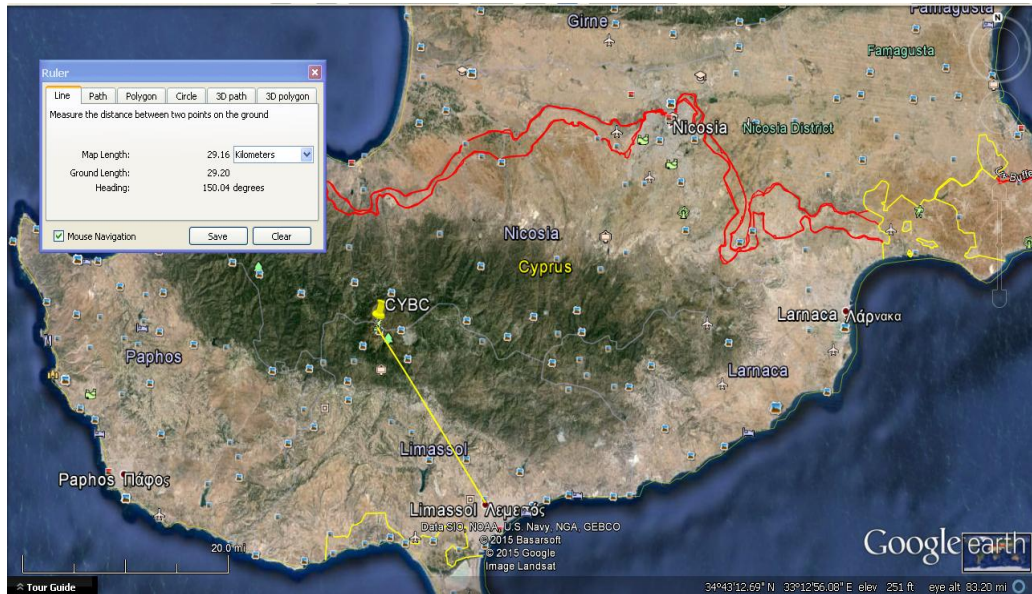


Figure 15: Path length between Limassol and Olympus, 29 km, height 1549 m

The crucial technical specifications of the signals under consideration are demonstrated in table 5, as they are used in the analysis of the propagation mechanisms that cause the interference in Cyprus, which is provided in the next chapter.

Frequency	Location	Path Length	Height	ERP
102.5 MHz	Lebanon	271 km	2995 m	50 kW
95.5 MHz	Israel	376 km	860 m	40 kW
94.8 MHz	Cyprus	29 km	1549 m	30 kW

Table 5: The technical specifications of the transmitting points

3.7.2 Measurements of 102.5MHz, 95.5MHz and 94.8MHz performed at 1:00 PM between June 17th and September 2nd, 2015

The short-term field strength variations in the 102.5 MHz signal from Lebanon are demonstrated in Figure 16. The measurements have been conducted from June 17th until September 2nd, 2015, at 1:00 PM. During this period, the average field strength intensity of 102.5 MHz was measured at 30 dBuV, and ranged from 10 dBuV to 48 dBuV, with the fluctuations essentially comprising of noise. The field strength variation of the aforementioned signal was in the order of 38 dBuV.

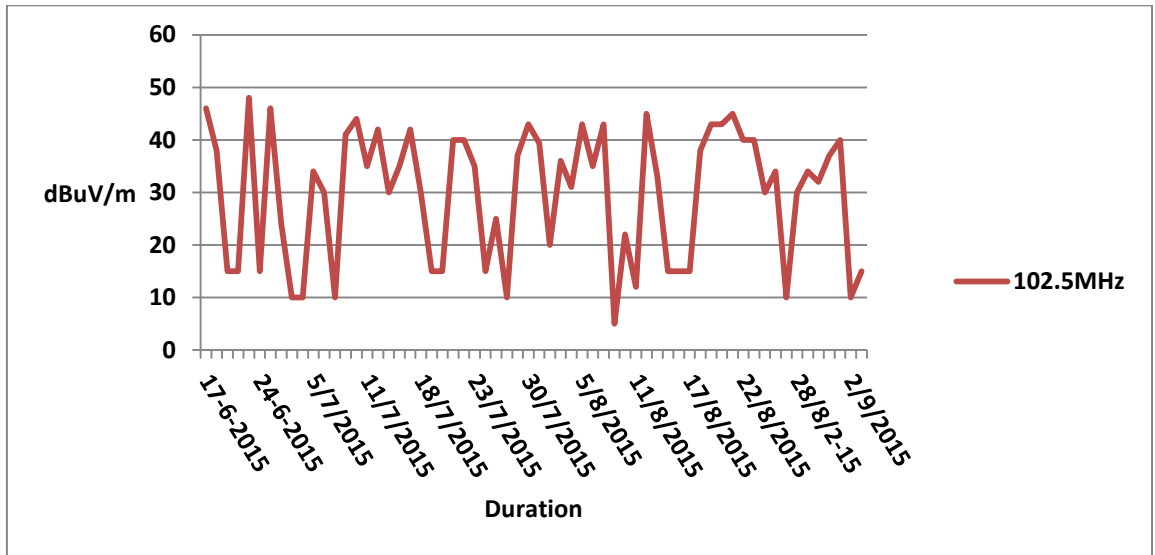


Figure 16: The field strength variations in the 102.5 MHz signal

Similarly, the field strength intensity of the 95.5 MHz signal arriving from Israel was measured between June 17th and September 2nd, 2015, at 1:00 PM, with the data illustrated in Figure 17. The average field strength was 45 dBuV, with 10 dBuV and 71 dBuV denoting the minimum and maximum, respectively. The ripple in the signal was measured at 61 dB.

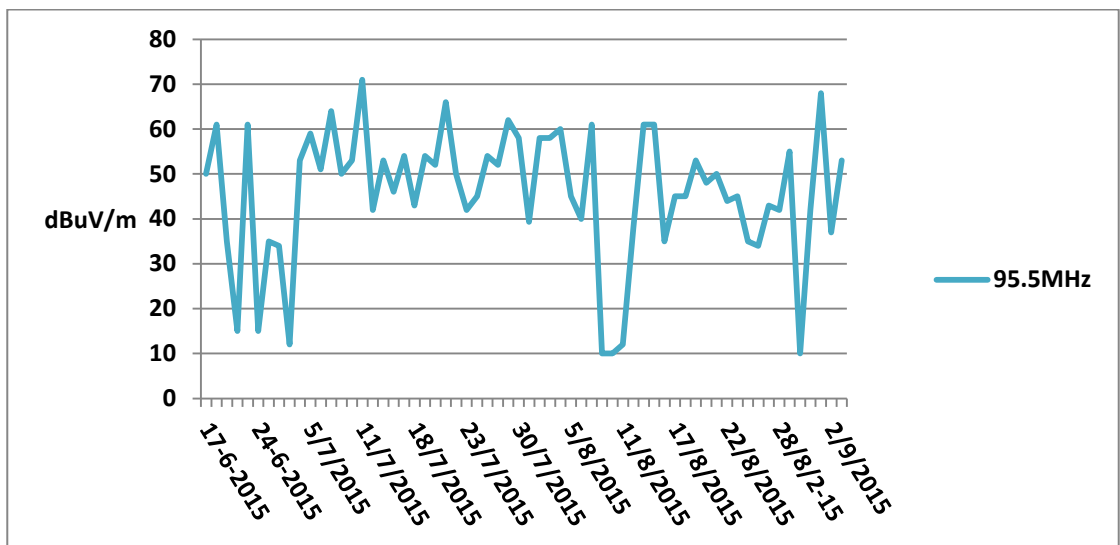


Figure 17: The field strength variations in the 95.5 MHz Signal

The measurements pertaining to the local national radio CYBC signal were performed within the same period and are illustrated in Figure 18. The graph is almost linear and the ripple is only 2 dB.

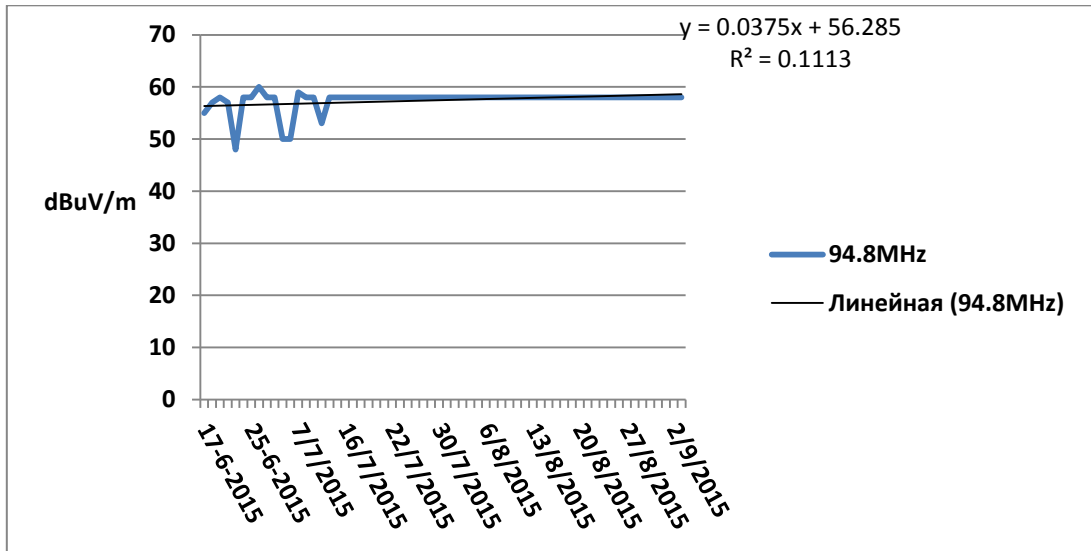


Figure 18: The field strength variations in the local CYBC 94.8 MHz radio signal

The field strength variations of the three signals under study are merged on the graph depicted in Figure 19. The green colour represents the field strength intensity of the local 94.8 MHz radio signal, whereas the red and blue lines correspond to the overseas signals at 102.5 MHz and 95.5 MHz, respectively. According to Figure 19, the field strength of the 95.5 MHz prevails over the local radio 94.8 MHz on the specific dates depicted on the graph. Therefore, the cause of co-channel interference has been established, and is evident from Figure 19, which reveals that the peaks of the 95.5 MHz signal are above the green line that represents the field strength of the local services.

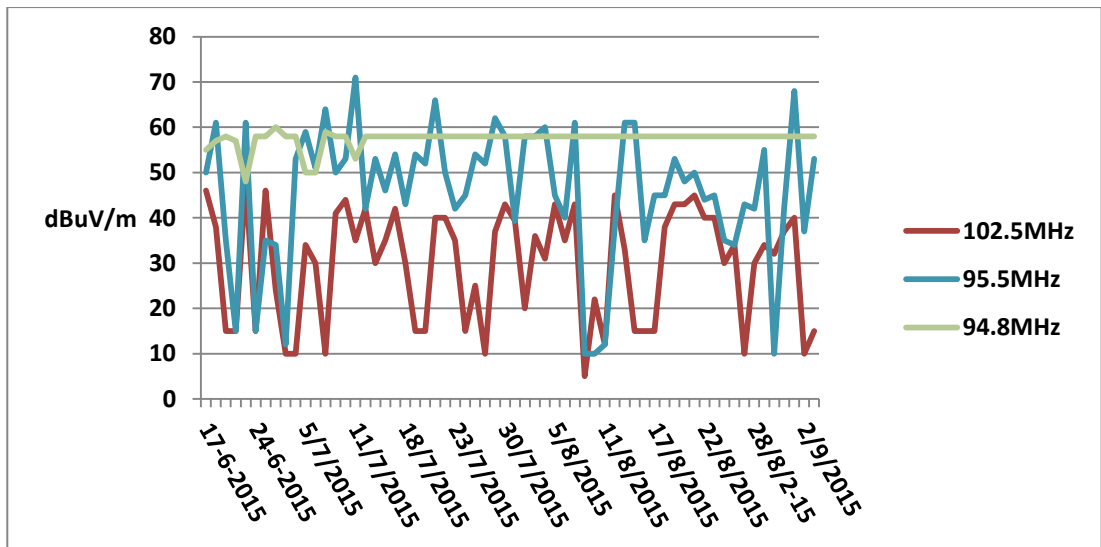


Figure 19: The field strength Intensity of the three signals under Study

3.7.3 Measurements of the 95.5 MHz and 94.8 MHz Signals Between June 17th and September 2th, 2015, made at 1:00 PM & 9:00 PM

Figure 20 illustrates field strength variations of the 95.5 MHz signal arriving from Israel and the local CYBC 94.8 MHz radio signal, noted on specific dates. The measurements were conducted at 1:00 PM and 9:00 PM. According to Figure 20, the overseas signal's field intensity is unstable relative to the local channel CYBC radio signal. Another important observation is that the average field of the overseas 95.5 MHz signal was higher in the evening compared to the levels measured during the day.

Figure 20 illustrates the variations in this phenomenon and elucidates the cause of co-channel interference, which would occur in the evening on the given dates, provided that the local radio services used the same spectrum as that adopted by the overseas signals.

Date	95.5 MHz (dBuV) 1:00 PM Israel	95.5 MHz (dBuV) 9:00 PM Israel	94.8 MHz (dBuV) 9:00 PM Cyprus
6/8/2015	40	68	58
7/8/2015	61	61	58
8/8/2015	10	51	58
10/8/2015	10	41	58
11/8/2015	12	43	58
12/9/2015	38	45	58
13/8/2015	61	67	58
14/8/2015	61	56	58
16/8/15	35	10	58
17/8/2015	45	53	58
18/8/2015	48	65	58
20/8/2015	50	67	58
21/8/2015	44	70	58
Average	39.61538462	53.61538462	58
Maximum	61	70	58
Minimum	10	10	58

Table 6: The field strength variations in the 95.5 MHz and 94.8 MHz signals, as measured at 1:00 and 9:00 PM

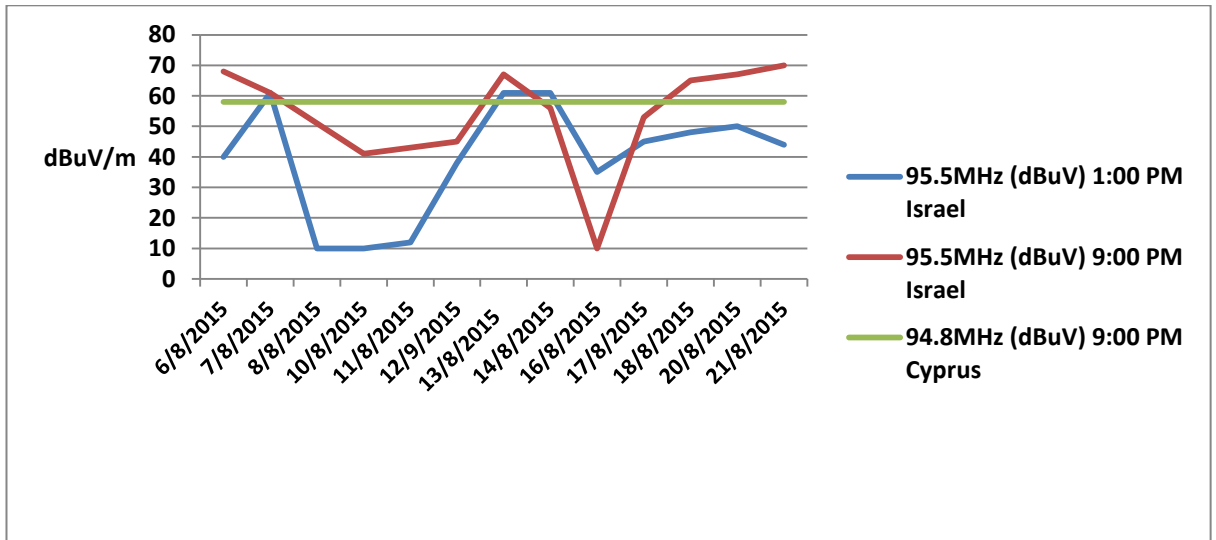


Figure 20: The field strength variations in the 95.5 MHz and 94.8 MHz signal, as measured at 1:00 and 9:00 PM

3.7.4 Short Term Measurements of the 95.5MHz and 94.8 MHz Signals Conducted between June 17th and September 2th, 2015, from 11:00 AM to 7:00 PM

The field strength variations in the Israel radio service 95.5 MHz signal between 11:00 AM and 7:00 PM, based on the measurements conducted on August 24th and 25th, 2015 is illustrated in figure 21. These measurements revealed that the field strength intensity of the overseas signal was sporadic, i.e. comprised of various values. An important observation is that its intensity measured on August 24th at 4:00 PM exceeded the free space value of the local national radio services CYBC, whereas the values were below the reference value at all other times.

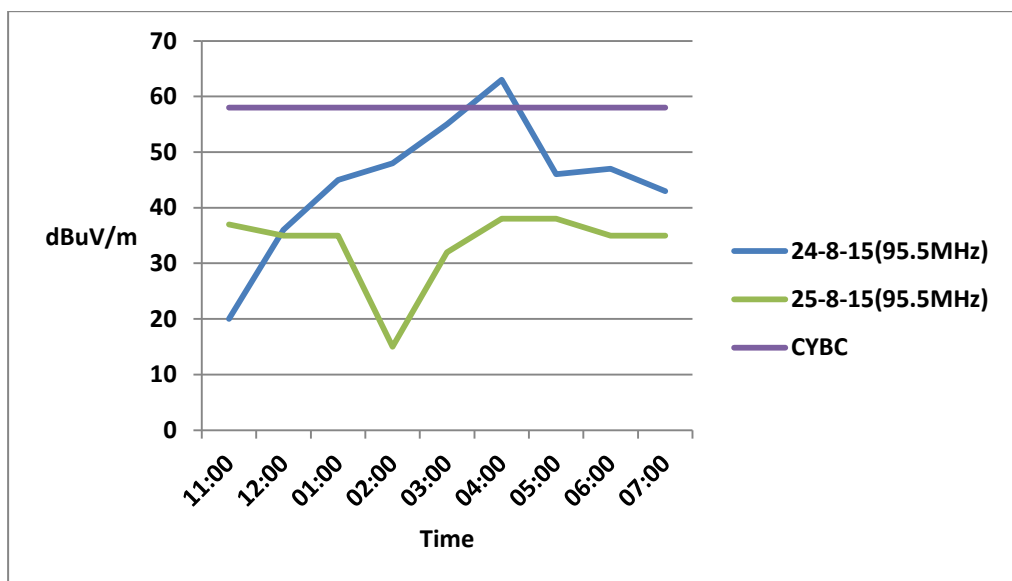


Figure 21: The field strength variations of the 95.5 MHz and 94.8 MHz signals, as measured between 11:00 and 7:00 PM

3.7.5 Discussion and Results of measurements

The measurements described in preceding sections have elucidated the manner in which the field strength intensity of the overseas transmissions could cause co-channel interference in Limassol during the summer months of 2015. It could be established that this phenomenon occurs as the monitored signals' field strength intensity varies with the month, day and time of the reception, causing the unwanted signals to prevail over the local radio services. The average field intensity measurements of the monitored 95.5 MHz signal from Israel during the summer months (June, July and August) are illustrated in Figure 22. According to the data, the average signal strength was 33 dBuV/m in June, increasing to 53 dBuV/m in July, before declining to 42 dBuV/m in August. Therefore, the signal is weakest in July. Furthermore, the strength of the 95.5 MHz signal arriving from Israel exceeded that of the local CYBC radio service in certain periods of summer, as well as during some parts of the day, despite the difference in the frequency designated for these two signals. Moreover, as the propagation losses increase with distance, it would be expected that signals arriving from Jerusalem (located is 376 km away from Limassol) would be weaker than those arriving from Olympus (at only 29 km distance). As a result, the expected field strength intensity of the 95.5 MHz signal should be considerably lower than that of the CYBC signal, as justified by the path loss equation (Eq. 11) given by (Debus, 2006) .

$$L_{bf} = 32.4 + 20 \log f + 20 \log d \quad dB \quad (11)$$

Particularly, under line of sight conditions, the path loss between Jerusalem and Limassol can be estimated using the following data and Eq. 12:

Distance from Jerusalem to Limassol: 370 km

Frequency: 95.5 MHz

Altitude: 860 m asl

ERP: 40 kW

$$Path Loss = 32.4 + 20 \log(95.5) + 20 \log(370) \rightarrow 123dB \quad (12)$$

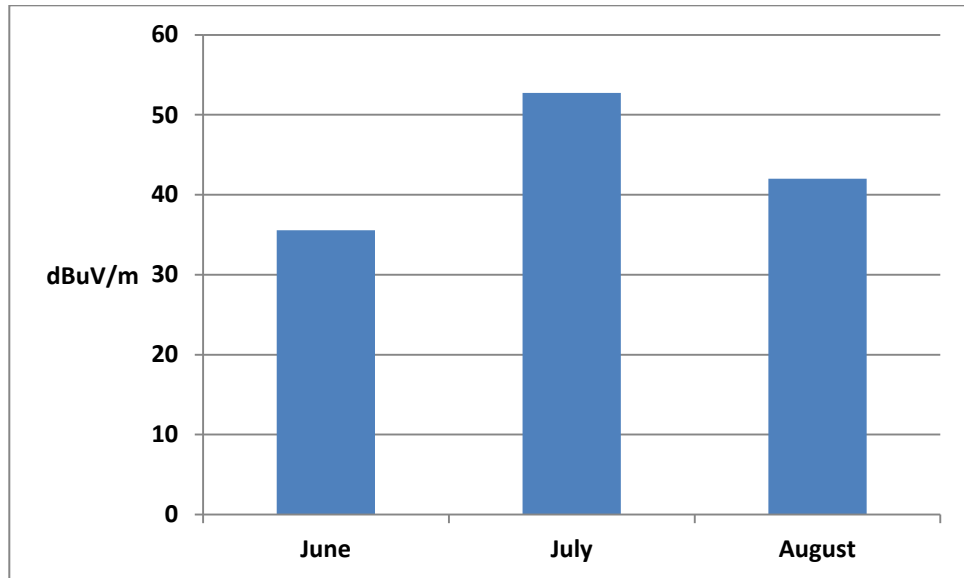


Figure22: The average strength of the 95.5 MHz signal arriving from Israel during the summer Months

According to Eq. 12, the path loss between Jerusalem and Limassol is 123 dB. Since the effective radiated power of the 95.5 MHz signal is 40 kW (table 5), it corresponds to the signal strength in Limassol of approximately 0.02 uW or 60 dBuV at a 50 Ω antenna. However, according to the measurements, the maximum intensity of the 95.5 MHz signal was 71 dBuV/m, exceeding its free space value by 10 dB.

It should also be noted that the field strength intensity of the national radio CYBC signal was almost constant in all measurements.

On the other hand, the path loss calculations of the CYBC 94.8 MHz signal are presented below:

Distance from Olympus to Limassol: 29 km

Frequency: 94.8 MHz

Altitude: 1549 m asl

ERP: 30 kW

$$Path Loss = 32.4 + 20 \log(94.8) + 20 \log(29) \rightarrow 101dB \quad (13)$$

As can be seen from the above, the loss is 101 dB. Since the power is 30 kW, the attenuation of 101 dB corresponds to 2.38 uW or 80 dBuV at a 50 Ω antenna. According to the measurements, the maximum field strength of the CYBC signal was 58 dBuV/m, most likely due to the fact that the monitored antenna is installed on a 1-meter mast, adversely affecting the line of sight to the point of transmission.

However, it is noteworthy that the average field intensity of the 102.5 MHz signal arriving from Lebanon (illustrated in Figure 23) is different from the 95.5 MHz signal. The field has an average intensity of 13 dBuV in June, after which it increases to 31 dBuV in July,

before declining to 30 dBuV in August. The path loss calculations pertaining to the path from Lebanon Limassol are given below.

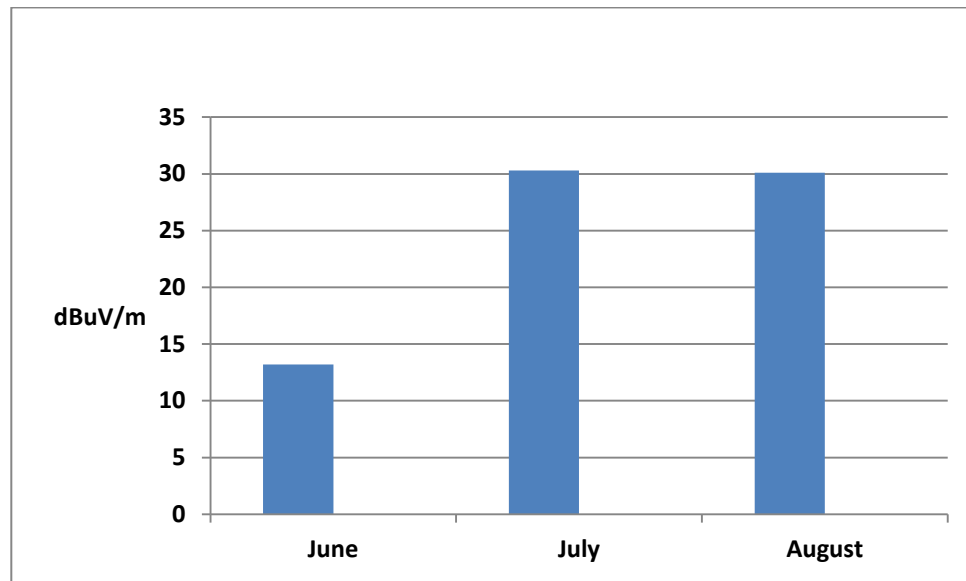


Figure 23: The average signal strength of the 102.5 MHz signal arriving from Lebanon during summer months

Distance from Lebanon to Limassol: 271 km

Frequency: 102.5 MHz

Altitude: 2995 m asl

ERP: 50 kW

$$Path\ Loss(dB) = 32.4 + 20 \log(102.5) + 20 \log(270) \rightarrow 121dB \quad (14)$$

According to Eq. 14, the path loss between Lebanon and Limassol is 121 dB. However, although Lebanon is closer to Limassol than Jerusalem, according to the measurements, the maximum field intensity for the signal arriving from Lebanon was 49 dBuV/m, corresponding to 13 dBuV/m below its maximum free space value.

The measurement instability of the overseas signals under study indicated that the signal propagation in Limassol is affected by an abnormal propagation mechanism. In order to understand the behaviour of the monitored overseas signals, a scientific analysis was performed, as described in the next section.

3.8 Analysis of the Monitored Signals

In order to better understand the phenomena affecting foreign radio signals that can be detected in Limassol, the propagation mechanism of the 95.5 MHz signal broadcast from Israel and 102.5 MHz signal arriving to Cyprus from Lebanon.

3.8.1 Line of Sight Interference Analysis

Line of sight interference occurs when a transmitted electromagnetic wave travels in a straight line from the transmitting antenna to the receiver, i.e. there are no obstructions that

could block the propagation. In the case of interest for this study, the line-of-sight analysis pertains to the transmitting origin of the signals monitored in Limassol. As no obstructions (other than the Mediterranean Sea) exist between Limassol and the Middle Eastern regions considered in this work, the line-of-sight analysis is limited to the radio horizon illustrated in Figure 24. The radio horizon is given as a function of the effective Earth radius, the elevation of the transmitting and receiving points, and the distance between them. In this analysis, it is essential to distinguish between the visual and radio horizon, due to the refraction of the radio waves, discussed below.

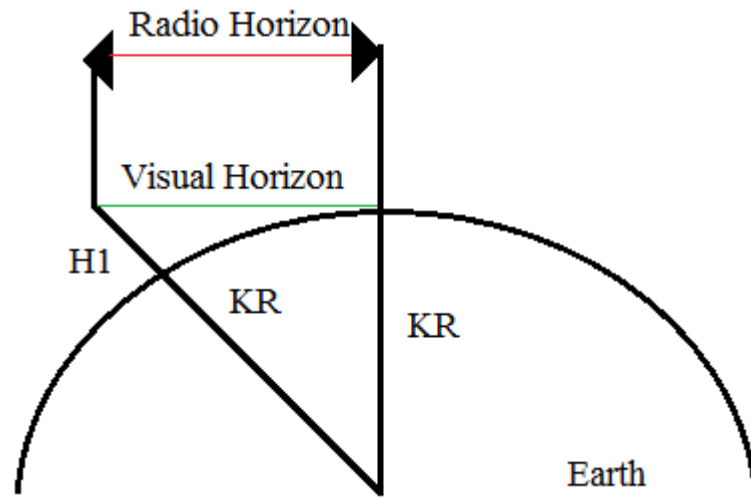


Figure 24: Radio versus visual horizon

The geometric horizon is defined as the visual field limit imposed by the Earth's curvature. However, under normal atmospheric conditions, the path length of the radio horizon in the VHF/UHF frequency domains appears to extend beyond the visual horizon, as the incident wave bends downwards. This phenomenon is described in the Recommendation ITU-834 and can be expressed by Eq.15 below:

$$\frac{1}{\rho} = -\frac{\cos\phi}{n} \frac{dn}{dh} \quad (15)$$

Where:

ρ = radius of the ray path curvature

n = refractive index of the atmosphere

dn/dh = vertical gradient of the refractive index

h = the point elevation above the Earth surface in km

φ = angle of the ray path measured from the horizontal plane

Under normal conditions, the refractive index is equal to unity and the angle φ is equal to zero. Thus, Eq. 15 can be simplified, as shown in Eq. 16 below:

$$\frac{1}{\rho} = - \frac{dn}{dh} \quad (16)$$

In practice, Eq. 16 is used for terrestrial line of sight calculations, whereby Earth is considered to be perfectly spherical.

Thus, based on the Earth's geometric radius of 6370 km, its effective radius can be then calculated by taking into account a constant coefficient k' which is approximately 1.33 under normal atmospheric conditions. Incorporating this into Equation 17 yields:

$$\text{Effective Earth Radius} = \sqrt{(KR + H)^2 - (KR)^2} \quad (17)$$

$$\text{Where } KR = 6370 \text{ km} \times \frac{4}{3} = 8500 \text{ m}$$

The radio horizon between the Middle Eastern regions and Limassol can be then calculated by applying the Pythagorean Theorem on the right-angled triangle, as shown in Figure 28 and presented below.

Paths Lengths:

1) Jerusalem – Limassol: Distance = 376 km, Height = 860 m Frequency: 95.5 MHz

$$\text{Radio Horizon (Jerusalem – Limassol)} = \sqrt{(8500000 + 860)^2 - (8500000)^2} = 120 \text{ km} \quad (18)$$

According to the results yielded by Equation 18, the path length between Limassol and Jerusalem is 376 km, thereby the 95.5 MHz signal is not arriving to Limassol by a line-of-sight propagation mechanism.

2) Beirut-Limassol: Distance 271 km, Height = 2995 m Frequency: 102.5 MHz

Height (H) = 3083 Meters

$$\text{Radio Horizon (Beirut – Limassol)} = \sqrt{(8500000 + 2995)^2 - (8500000)^2} = 224 \text{ km} \quad (19)$$

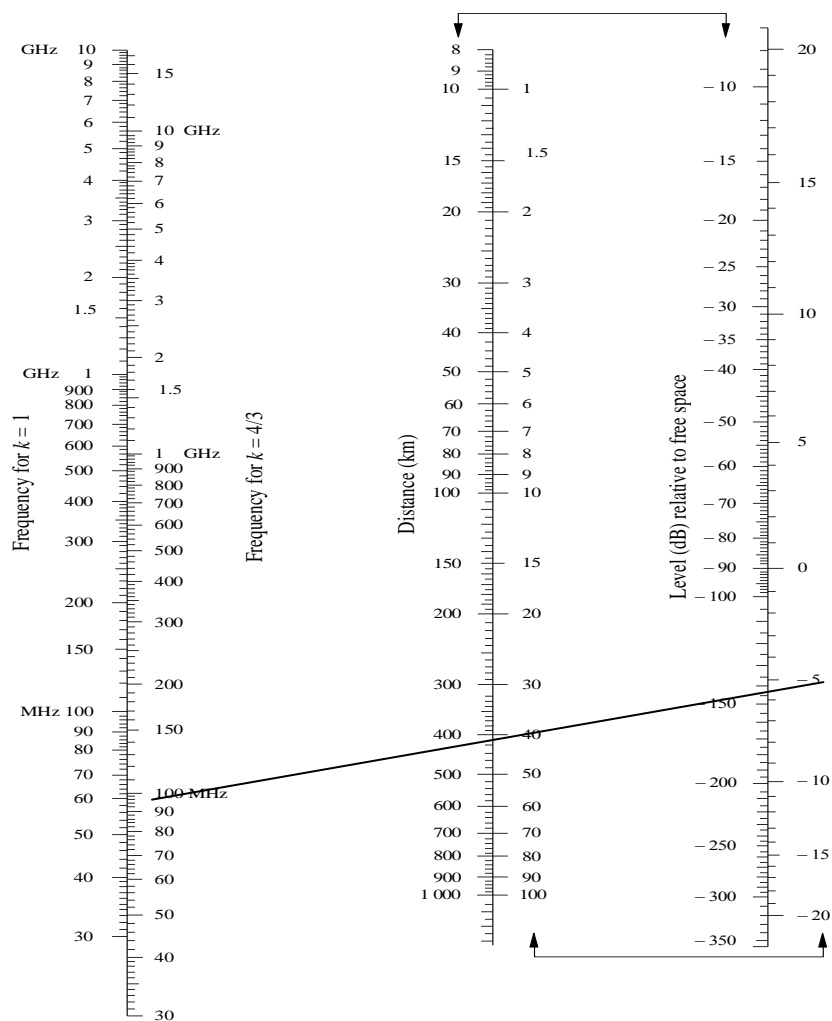
Equation 19 reveals that the path length between Beirut and Limassol is 271 km. Thereby the 102.5 MHz signal is not arriving to Cyprus by a line-of-sight propagation mechanism.

It should be noted that, beyond the radio horizon, the signals will either attenuate rapidly or propagate away from the Earth (Castel, 1965).

3.8.2 Diffraction Interference

The diffraction can cause a long-term interference in the VHF band. This is especially the case if a portion of the incident wave passes over a tall sharp obstacle, like the top of a mountain, or a building, and penetrates into the shadow area of that obstacle (Matthew, 1965). This phenomenon has been explained by Huygens–Fresnel principle in 1678, which states that a strong incident wave enables an obstacle to behave akin to a number of secondary point sources that produce a spherical radiation pattern at the near-field region. The signal density of the diffraction in the shadow area depends on the amplitude and phase of the secondary radiation sources. This phenomenon is also described in the Recommendation ITU-526-8, which provides diffraction equations, along with the Fresnel zones. The chart in Figure 29 demonstrates the diffraction's distance attenuation over the sea of a vertically polarized incident wave according to the ITU-526-8.

According to Figure 25, the diffraction is very efficient at low propagation frequencies relative to the VHF Band II. In other words, the lower the frequency, the more the wave is diffracted because the wavelength becomes longer relative to the Earth's radius. In Band II frequencies, the wavelength is approximately 3 m, which is negligible compared to the Earth's dimensions; thus, not much energy can be diffracted. The diffraction effects can be negligible where the propagation path is very long (> 200 km) at VHF bands (Son, 2002). Therefore, in this work, there is no need to consider the diffraction effect as a principal propagation mechanism that causes interference between Jerusalem and Lebanon and the coast of Limassol because the distances between these transmitted signals exceed 200 km.



Vertical polarization over sea
(The scales joined by arrows should be used together)

Figure 25: Diffraction by spherical earth –effect of Distance

3.8.3 Tropospheric Scattering

Tropospheric scattering is a long-range propagation mechanism used for microwave radio link communications between terrestrial stations beyond the horizon (Tropospheric-scatter observations, 1961). The system requires very high-gain antennas steered at very low angles compared to the horizon, whereby microwave signals are randomly scattered as they pass through the upper layers of the troposphere. Thus, such arrangement is used in high-frequency applications where the wavelength is short due to the high antenna gain requirements. As the troposphere is turbulent, and is characterized by a high proportion of moisture, the radio signals exhibit affected by tropospheric scatter exhibit great losses. Thus, troposcatter communications require amplifiers ranging from 1 kW to 50 kW and antennae with gain in the 40-60 dB range, in order to establish a successful link interface.

The methods for evaluating the path loss of the troposcatter communications are provided in the Recommendation ITU-R P.617-1, and are based on Eq.20 below:

$$L(dB) = M + 30 \log(f) + 10 \log(d) + 30 \log(\theta) + L_N + L_C - G_t - G_r \quad (20)$$

Where:

f denotes frequency in MHz, d is the distance in km, θ is the scatter angle (milliradians), L_N accounts for the height of the common volume, L_C is the aperture-medium coupling loss, and G_t and G_r are the antennae gains.

Based on Eq.20, the loss increases dramatically with the angle θ ; thus, the lowest losses are obtained when $\theta = 0$, i.e. when the transmitting and receiving antennae are steered at the horizon.

The angle θ can be calculated using Equation 21 as follows:

$$\theta = \theta_e + \theta_t + \theta_r \quad (21)$$

where θ_t and θ_r are the transmitter and receiver horizon angles, respectively, and

$$\theta_e = 1000 d/R_e \quad (22)$$

R_e = effective earth radius $\sim 4/3 \times 6370$ km.

L_N represents the transmission loss variation with the height of the common volume, as given by Equation 23 below.

$$L_N = 20 \log(5 + \gamma H) + 4.34\gamma H \quad (23)$$

Where:

$H = 10^{-3} \theta d/4$, $h = 10^{-6} \theta^2 R_e/8$, and γ is a climatological parameter $\sim 0.27 \text{ km}^{-1}$, based on the region, where L_c described by Equation 24.

$$L_C = 0.07 e^{0.055(G_t+G_r)} \quad (24)$$

Based on the calculations presented above, the troposcatter communication in Band II, between Limassol and Lebanon or Israel, will exhibit losses exceeding 160 dB. These losses correspond to a field intensity in Limassol of no more than 20 dBuV. According to the measurements presented in the previous section, the average intensity of the monitored signals is at least 45 dBuV and exceeds the free space value of the local channels on certain days. Therefore, the troposcatter propagation mechanism cannot cause the interference in the southern coastal regions of Cyprus and will not be explored further.

3.8.3 Refraction Interference

According to the fundamental properties of propagation, radio waves in the VHF band travel in a straight line, provided that the refractive index of the media through which the signal is passing is unity (Thayer, 1974). Essentially, the refractive index denotes the ratio of the speed of light in the free space to the incident wave velocity. Under normal atmospheric conditions, the actual value of the refractive index is about 1.0003, which causes a small refraction in the incident waves, as previously discussed. For this reason, the I.T.U. considers the radio horizon (under normal conditions) to be extended to the visual horizon by 4/3 times. However, under non-standard atmospheric conditions, when an incident wave is travelling through two atmospheric layers characterized by different dielectric constants, it will be refracted or bent at a certain angle, whose direction will be determined by the gradient of the refractive index. The Recommendation ITU-R P 453 provides the meteorological parameters that determine the radio refractive index n , in terms of the radio refractivity N , as shown in Eq.25 below:

$$n = (1 + N) \times 10^{-6} \quad (25)$$

However, the radio refractivity N can be also expressed by Eq.26, as follows:

$$N = N_{dry} + N_{wet} = \frac{77.6}{T} \left[P + 4810 \frac{e}{T} \right] N - Units \quad (26)$$

Where:

P is atmospheric pressure (hpa)

e represents water vapour pressure (hpa)

T denotes absolute temperature (K)

Radio refractivity can be otherwise expressed in terms of relative humidity in %, as given by ITU-R P 453 in Eq.27 below:

$$N = (n - 1) \times 10^{-6} = 77.6 \frac{P}{(T+273)} + 22.79 \times 10^{-3} \frac{RH}{(T+273)^2} \exp \frac{17.502 \times T}{(T+240.97)} \quad (27)$$

Where:

P is atmospheric pressure in hPa, T is temperature in C, and RH is relative humidity in %.

The refractivity N within the atmosphere varies with height and is defined as the vertical refractivity gradient (dN/dh). Thus, depending on the weather conditions, radio waves can be classified based on refraction as normal, sub-refraction, super-refraction or ducting, as

illustrated in Figure 26. The criteria for the occurrence of these refraction types, along with their properties, are discussed below.

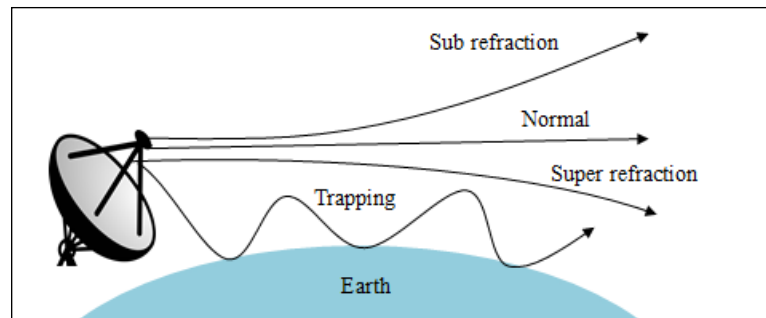


Figure26: The four Classifications of refraction

3.8.5 Normal Conditions

Under normal meteorological conditions, the refractive index value declines uniformly with height, as moisture, temperature, and pressure decrease with altitude. This exponential function, within 1 km of Earth's surface, is sufficiently regular to be approximated by a linear function, i.e. be defined as the standard gradient (Son, 2002). In this respect, the propagating wave will bend downwards and extend beyond the visual horizon by additional 4/3 times. The standard gradient is characterized by the decrease in refractivity N of 39 units per km of distance, i.e. -39 N/km. Similarly, the normal gradients will bend the radio waves downwards, whereby N will range from 0 to -79 N/km (or between 78 and 157 M-units per km, as will be explained later).

3.8.6 Sub-Refraction

Sub-refraction forces the propagated wave to be refracted less than normal. As a result, a wave travels upwards and away from the Earth's surface. The sub-refraction occurs when the temperature and humidity distribution increase the refractivity gradient. Therefore, when a non-line of sight overseas signal arrives in the coastal region of Cyprus, this phenomenon is not produced by sub-refraction.

3.8.7 Super Refraction

Super refraction occurs when refractivity decreases from the standard gradient due to temperature inversion within the troposphere, whereby the temperature increases (rather than decreases) with height. Water vapour content can also cause super refraction, when the moisture decreases with height. In this case, the N gradient lies between -157 N/km and approximately -79 N/km. As a result, the propagated wave will bend downwards more than it normally does, and its radius will eventually approach the radius of the Earth. Provided

that the propagated wave's and the Earth's radius are equal, the wave will continue to travel at a fixed height, maintaining the trajectory parallel to the Earth's surface.

3.8.8 Trapping

Trapping (Ducting) occurs when the N gradient exceeds -157 N/km. However, the same meteorological conditions cause trapping and super refraction interference. In this regard, the difference between trapping and super refraction pertains to the radius of the propagated wave, which becomes smaller than the Earth's radius as it decreases beyond the critical gradient. In such a case, the electromagnetic waves are trapped within a thin layer of the troposphere, denoted as duct. When the wave is trapped in this tropospheric channel, its energy can propagate over great ranges. Furthermore, according to the Rec. ITU-R P.453-8, ducts can be described in terms of modified refractivity $M(h)$ defined by Eq. 30:

$$M(h) = N(h) + 157h \quad (M - Units) \quad (30)$$

Where h (km) is the height.

Three types of ducts are encountered in nature, and can be classified as surface-based, elevated-surface, and elevated ducts, as illustrated in Figure 27.

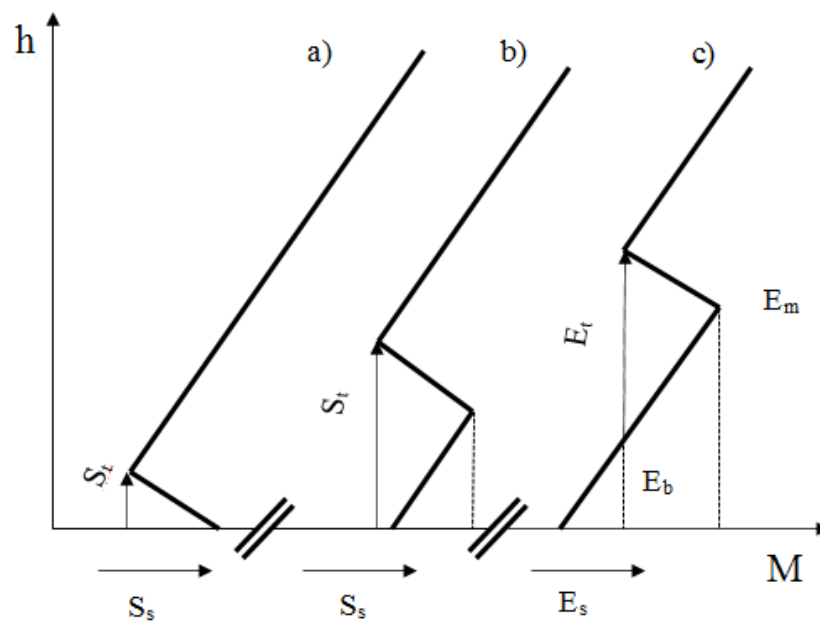


Figure 27: The three types of ducts: (a) Surface, (b) Surface-based, and (c) Elevated ducts.

When the air aloft is very warm compared to the temperature of the Earth or the sea, surface-based ducts occur. For example, they can arise due to the hot air masses that pass over the cool water surface of the Mediterranean Sea as presented in the next chapter. On

the other hand, elevated ducts occur when the meteorological conditions are favourable for such phenomena to occur aloft above the Earth's surface.

Since none of the propagation mechanisms discussed previously could cause the interference in Cyprus, refraction is likely the only contributor to the measurements obtained in this study. However, to fully elucidate the cause of the interference problem in Cyprus, meteorological analysis of the area was conducted, as discussed below.

3.9 The Climate of the Southern Coast of Cyprus

The analysis of the climatic conditions in Cyprus is based on the data sourced from the Meteorological Department of Cyprus, which provides information pertinent to the weather conditions on the island (Moa.gov.cy, 2016). Since the present study is limited to the southern coast of Cyprus, only the climatic conditions prevalent in Limassol will be considered.

Limassol is a coastal town with a Mediterranean climate. Its geographical coordinates are 34° 40' 30" North, 33° 2' 0" East. The area is affected by four distinct seasons, namely winter, spring, summer, and autumn. Winter is the rainiest season of the year, with the average temperature of 16 °C. On the other hand, Spring is characterized by very little rain and the average temperature of 20 °C. Summer in Limassol is very humid and the average temperature reaches 28 °C. During the summer months, the island is mainly under the influence of a shallow trough of low pressure extending from the great continental depression located over southwest Asia. High temperatures and almost cloudless skies make this season mostly dry and sunny. Although rainfall is almost negligible, isolated thunderstorms sometimes occur, which contribute to the average precipitation of less than 5%.

3.9.1 Air Temperature

While, in general, Limassol enjoys hot summers and mild winters, when the effects of altitude are taken into consideration, the findings reveal that air temperature declines by about 5 °C per 1,000 m of elevation. Marine influences are also noteworthy, as they result in cooler summers and warmer winters in the vicinity of most of the coastline, and especially on the west coast. The seasonal differences between mid-summer and mid-winter temperatures are significant, averaging at 18 °C inland and about 14 °C on the coasts. The mean monthly air temperature in Limassol is presented in Figure 28.

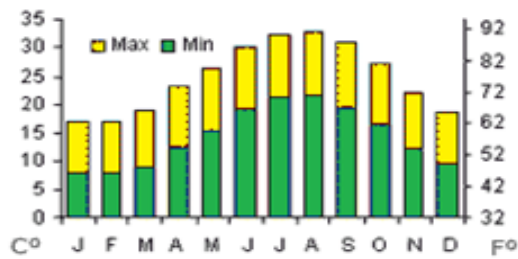


Figure 28: Mean monthly air temperature in Limassol

Differences between maximum day and minimum night temperatures are also significant, especially inland in summer. In winter, 8 to 10 °C difference is measured in the lowlands, with somewhat lower range of 5 to 6 °C observed in the mountains, increasing in summer to 16 °C on the central plain and 9 to 12 °C elsewhere. In July and August, the mean daily temperature ranges between 29 °C on the central plain, reducing to 22 °C on the Troodos mountains, with the average maximum temperature of 36 °C and 27 °C measured in these areas, respectively. The mean daily temperature in January ranges from 10 °C on the central plain, to 3 °C on the higher parts of Troodos mountains, with the average minimum temperature in these areas declining to 5 °C and 0 °C, respectively. While rarely severe, frosts are nonetheless frequent in winter and spring, especially inland, and can thus adversely affect the economically important production of early vegetable and main citrus crops’.

3.9.2 Sea Temperature

‘At the open sea, temperatures increase to 27 °C in August, declining to 22 °C between November and June. In addition, during each of the three coolest months (January, February and March), the average sea temperature declines further, to 16 or 17 °C. Throughout the year, near all coasts, at the water depth of 3-4 m, temperatures are very similar to those measured at the open sea, ranging from 15 to 17 °C in February, and 23 to 28 °C in August. With the exception of the very shallow waters (under 1 m depth) near coast, seawater temperature does not exhibit significant daily changes’.

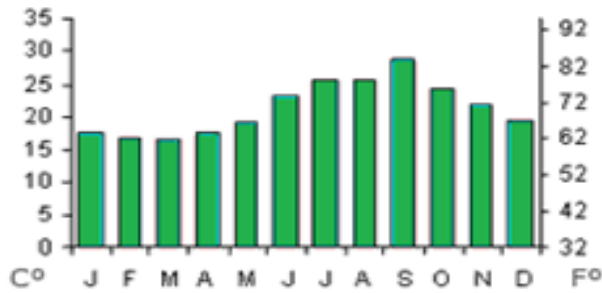


Figure 29: Mean monthly sea temperature near Limassol

3.9.3 Soil Temperature

‘Seasonal change in mean soil temperature measured at 10 cm depth ranges from about 10 °C in January to 33 °C in July, reducing to 14-28 °C variation at 1 m depth. On the mountains (at 1,000 m asl), these mean seasonal values are reduced by about 5 °C. Even at the highest elevations, penetration of frost into the ground is insufficient to cause problems for flora and fauna. On the other hand, a wide variation in the soil temperature is noted during summer, due to large amounts of solar energy being absorbed into the soil during the day, combined with high radiation losses in clear skies at night. The temperature at the soil surface measured in the lowlands on a typical July day varies between 15 °C near dawn to near 60 °C in the mid-afternoon. However, this variation is reduced to 24-42 °C at only 5 cm, with no perceptible daily temperature change at 50 cm depth’.

3.9.4 Relative Air Humidity

‘Elevation above the mean sea level and the distance from the coast also have considerable effects on the relative air humidity, which is to a large extent a reflection of temperature differences. In Limassol, at 65 to 95% during winter days, and at night throughout the year, humidity may be characterized as average or slightly low. It is even lower near midday in summer, with the values measured on the central plain usually not exceeding 30%, and occasionally declining to about 15%.

Fog is infrequent and usually confined to dawn; however, on maintains in winter season, when cloud envelopes the highest peaks, it can persist for longer periods. Visibility is generally very good or excellent. Still, on a few days each spring, the atmosphere is very hazy due to dust brought from the Arabian and African deserts’.

3.9.5 Wind

‘Over the eastern Mediterranean, surface winds are mostly westerly or south-westerly in winter and north-westerly or northerly in summer. They are usually of light or moderate strength, and rarely reach gale force. Over the island of Cyprus, however, wind direction varies considerably with orography that, along with local heating effects, is the main contributor in the determination of local wind direction and strength. Differences in temperature measured at sea and inland, which vary daily, cause considerable sea and land breezes in summer, when dry weather and clear skies predominate. Whilst these effects are mostly confined to the coastal areas, winds regularly penetrate far inland in summer, reaching the capital, Nicosia, bringing a welcome reduction of temperature, as well as increase in humidity. As noted above, gales are infrequent over Cyprus, but may occur occasionally on exposed coasts with winter depressions. Small whirlwinds are common in summer, appearing mostly near midday, in the form of so-called "dust devils" that can arise on the hot dry central plain. While vortices also occur very rarely, when they do, they take shape of waterspouts at sea and small tornadoes on land, with the diameter extending up to 100 m. They typically occur in thundery weather conditions. While localized damage caused by these winds has been reported on a few occasions, in general, Cyprus suffers relatively little wind damage’.

3.10 Results and Discussion

This section presents the upper air data obtained by the Meteorological Department of Cyprus during periods of very strong, medium and low field strength intensity of the overseas monitored signals transmitted at the frequencies of 95.5 MHz and 102.5 MHz, discussed in Section 3.11. In the Eastern Mediterranean, only two stations (Radiosonde) measure meteorological parameters relative to specific height—the Athalassa in Cyprus (WMO code 17607) and Bet Dagan in Israel (WMO code 40179). These stations obtain radiosonde data once a day at 1200 UTC. Because the aforementioned stations cannot obtain radiosonde data based on the coordinates in Figure 30, and the data are observed only once a day, for the present study the prognostic model WRF-ARW, Version 3.4 was used in the present study because it is a special weather forecasting software that enables upper air data simulation at any fixed coordinates and hour in the day.

The relevant data was obtained at the computing time $T + 10$ (i.e., 10 hours after the initial time $T + 0$ corresponding to 0000 UTC). Thus, the time $T + 10$ pertains to 13:00 PM and allows simultaneously obtaining meteorological data and field strength measurements at a fixed time point. The calculations pertained to 18 km distance grid, corresponding to the

boundary data from the Global Forecasting System (GFS) with a resolution of 0.5 degrees and time step boundary conditions set at 3 h. The step integration was adaptive / dynamic, rather than fixed, based on the CFL criterion. The number of vertical planes (eta levels / terrain following) was 60. The configurations used are given below:

1. Micro-physics: WRF Single-moment 3-class scheme
2. Radiation longwave: Rapid Radiative Transfer Model
3. Radiation shortwave: Dudhia Scheme
4. Surface layer: MM5 / Monin-Obukhov Scheme
5. Boundary layer: Yonsei University Non-local-K scheme
6. Cumulus / convection: Kain-Fritsch scheme

The main goal is to provide evidence-based explanation for the radio interference observed along the southern coast of Cyprus. As a result, the refractivity N can be obtained by applying Eq. 26 below:

$$N = N_{dry} + N_{wet} = \frac{77.6}{T} \left[P + 4810 \frac{e}{T} \right] N - Units \quad (31)$$

where P denotes atmospheric pressure (hpa), e represents water vapour pressure (hpa), T is absolute temperature (K), and RH is relative humidity expressed in %.

Given that the focus of this investigation is on the overseas signals from Jerusalem (95.5 MHz) and Lebanon (102.5 MHz), radiosonde data required for analyses have been obtained by examining three major points at the coordinates presented in Figure 30. The results are discussed in subsequent sections.



Figure 30: The coordinates under investigation for the radio signals emitted at frequencies of 95.5 and 102.5 MHz

3.11 Very Strong Signal Intensity

Table 7 presents the field strength measurements obtained on selected dates, when the strength of the 95.5 MHz signal was particularly strong. The tabulated information also includes the measurements of the 102.5 MHz signal for comparison. All measurements were obtained at 1:00 PM.

DATE	95.5MHz	102.5MHz
18/6/15	61dB	38dB
22/6/15	61dB	48dB
7/7/2015	64dB	25dB
11/7/2015	71dB	35dB
21/7/15	66dB	40dB
28/7/15	62dB	37dB

Table 7: Very strong field strength intensity

3.11.1 Results pertaining to measurements made on June 18th 2015

The simulation of the absolute temperature versus height as well as the N-units versus height at Point 3 (34°24'11.12"N, 33°18'8.87"E) are presented in Figure 31 and 32, respectively. As can be seen from the graph shown in Figure 31, temperature inversion occurs at the 250 m height.

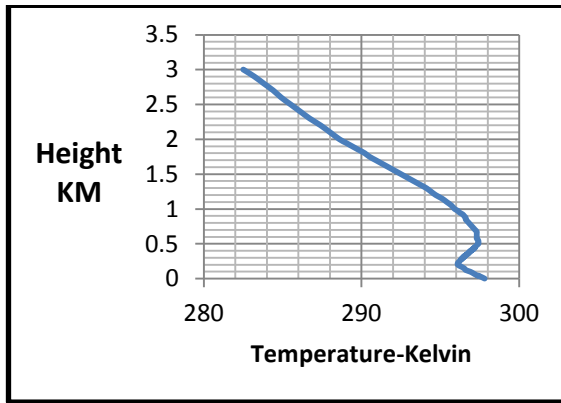


Figure 31: Temperature versus height measured on 18-06-2015 at Point 3

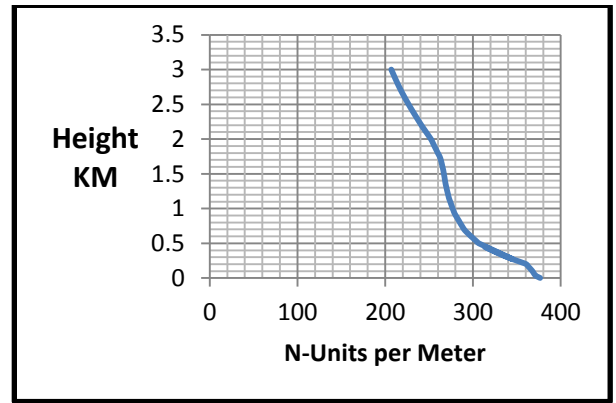


Figure 32: N-units per meter versus height measured on 18-06-2015 at Point 3

The results pertaining to the temperature inversion versus height and the N-units measurements versus height at Point 2 ($33^{\circ}47'17.48''N$, $33^{\circ}45'51.56''E$), are presented in figures 33 and 34 respectively. Once again, temperature inversion can be noted at the 250 m height, as illustrated in Figure 33.

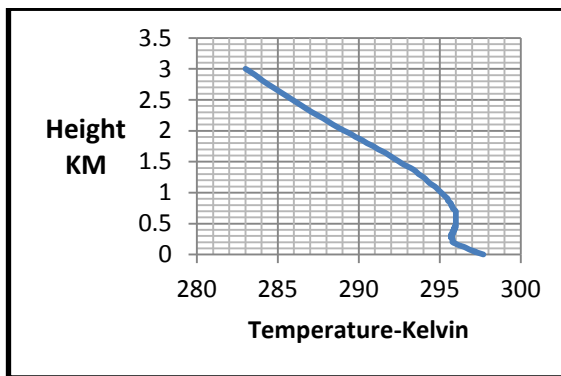


Figure 33: Temperature versus height measured on 18-06-2015 at Point 2.

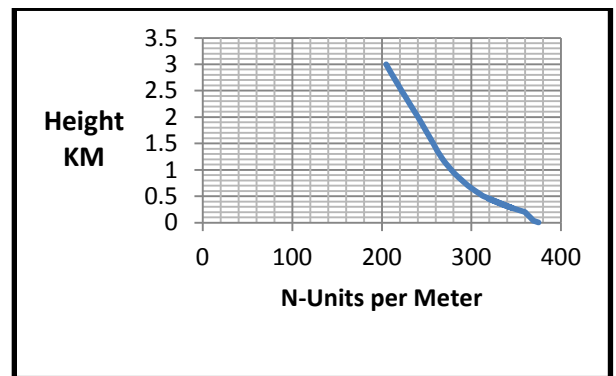


Figure 34: N-units per meter versus height measured on 18-06-2015 at Point 2.

The relationship between temperature and height at Point 1 ($32^{\circ}30'49.68''N$, $34^{\circ}37'42.44''E$), reveals a temperature inversion at 350 meters height presented in figure 35. The refractivity N in relation to the height of the measuring point is illustrated in Figure 36.

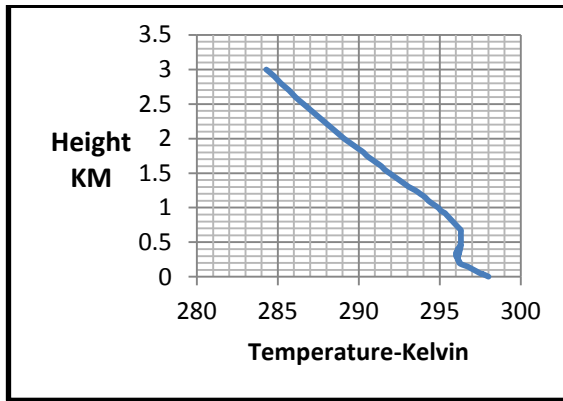


Figure 35: Temperature versus height measured on 18-06-2015 at Point 1

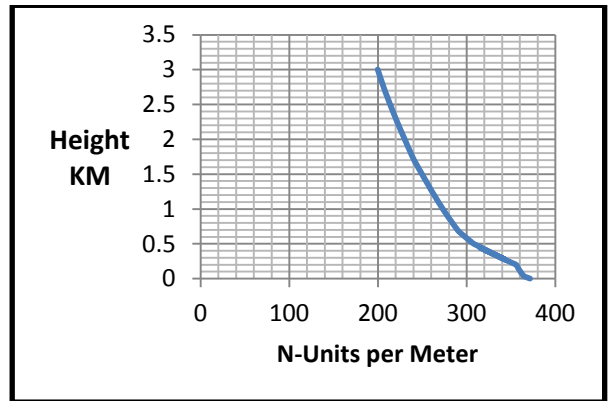


Figure 36: N-units per meter versus height measured on 18-06-2015 at Point 1.

3.11.2 Results pertaining to the measurements performed on July 7th 2015

The simulation of the absolute temperature in relation to height at Point 3 (34°24'11.12"N, 33°18'8.87"E), the location of which is shown in Figure 30, reveals a temperature inversion at the 400 m height, as illustrated in Figure 37. The refractivity N noted at different heights is illustrated in Figure 38.

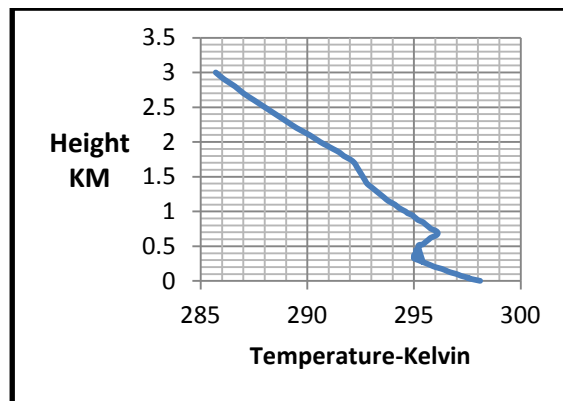


Figure 37: Temperature versus height measured on 7-7-2015 at Point 3.

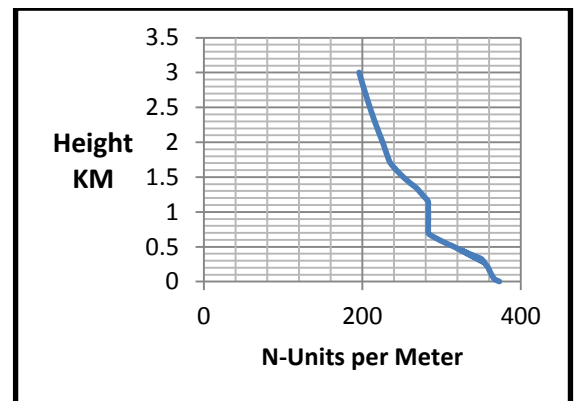


Figure 38: N-units per meter versus height measured on 7-7-2015 at Point 3.

The relationship between temperature and height at the measurement point is presented in figure 39 while the N-units measurements in relation to height are shown in Figure 40. At Point 2 (33°47'17.48"N, 33°45'51.56"E) shown in Figure 30, the temperature inversion occurs at the 600 m height, as shown in Figure 39.

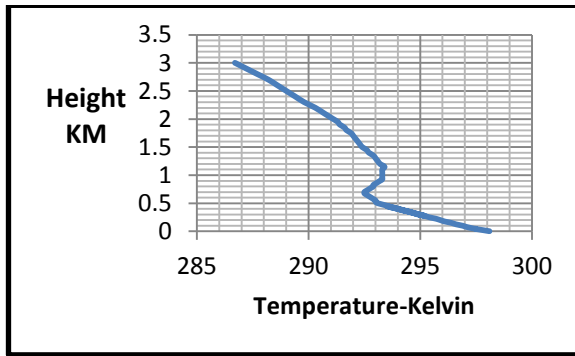


Figure 39: Temperature versus height measured on 07-07-2015 at Point 2.

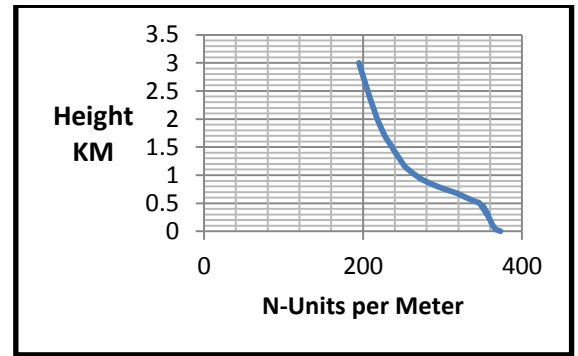


Figure 40: N-units per meter versus height measured on 07-07-2015 at Point 2.

The results pertaining to the link between temperature and measurement point height at Point 1 ($32^{\circ}30'49.68''\text{N}$, $34^{\circ}37'42.44''\text{E}$) are illustrated in Figure 41, revealing a temperature inversion at 650 m. The refractivity N relative to the height at which it is obtained at Point 1 is illustrated in Figure 42.

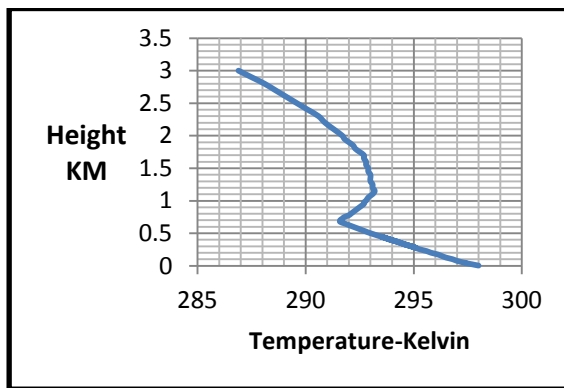


Figure 41: Temperature versus height measured on 07-07-2015 at Point 1.

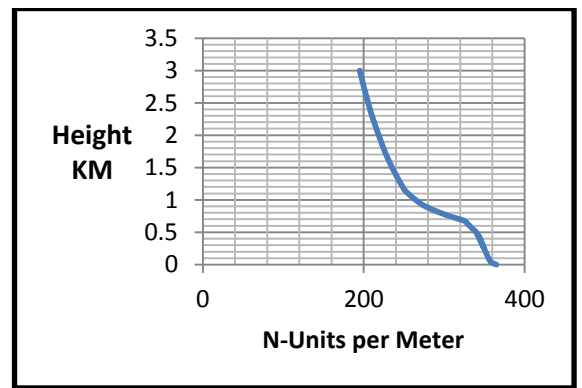


Figure 42: N-units per meter versus height measured on 07-07-2015 at Point 1.

3.11.3 Results pertaining to the measurements performed on July 11th 2015

Based on Figure 43 and 44, inversion occurs at 200 m.

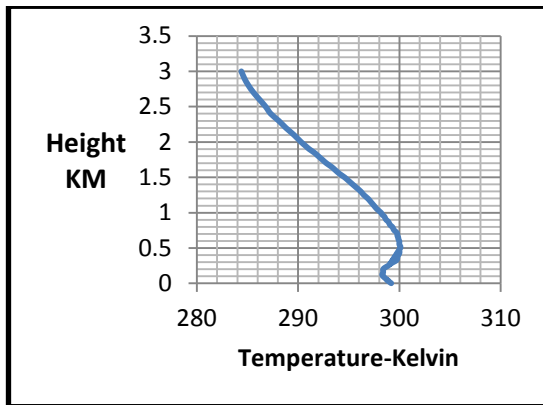


Figure 43: Temperature versus height measured on 11-07-2015 at Point 3.

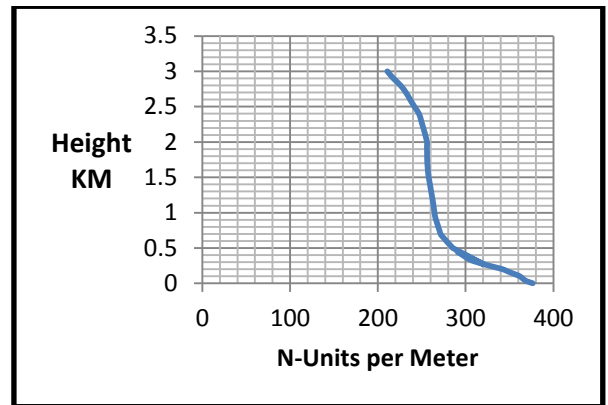


Figure 44: N-units per meter versus height measured on 11-07-2015 at Point 3.

The relationship between temperature and height is presented in figure 45 while the N-units measurements obtained at Point 2 (33°47'17.48"N, 33°45'51.56"E) are shown in Figure 46. As can be seen, temperature inversion occurs at 350 m.

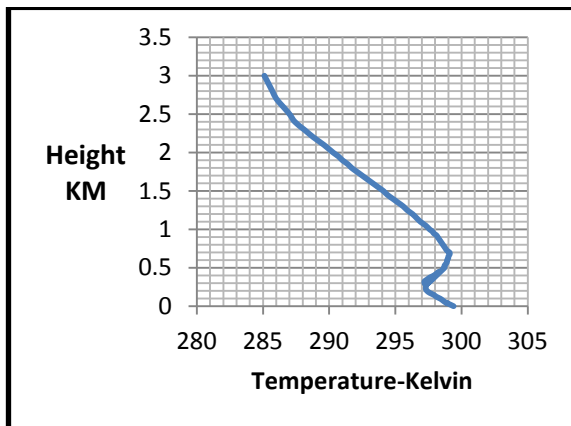


Figure 45: Temperature versus height measured on 11-07-2015 at Point 2.

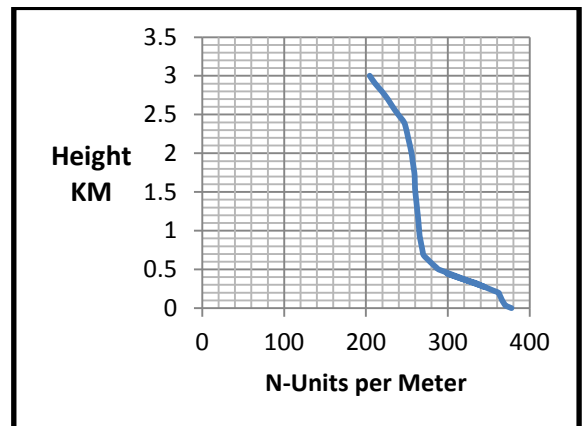


Figure 46: N-units per meter versus height measured on 11-07-2015 at Point 2.

The results pertaining to the temperature and refractivity N versus height at Point 1 (32°30'49.68"N, 34°37'42.44"E) are presented in figures 47&48 respectively. According to the data, in this case, temperature inversion takes place at 500 m height.

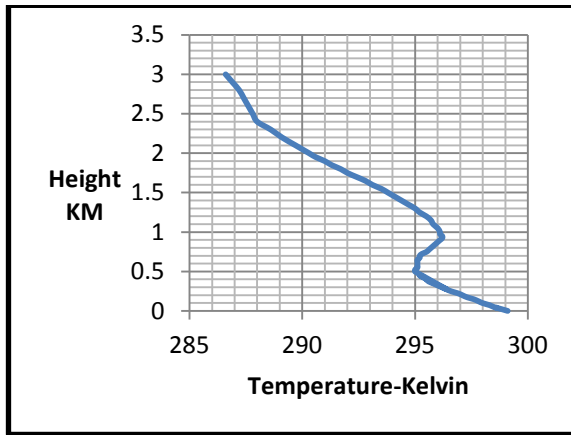


Figure 47: Temperature versus height measured on 11-07-2015 at Point 1.

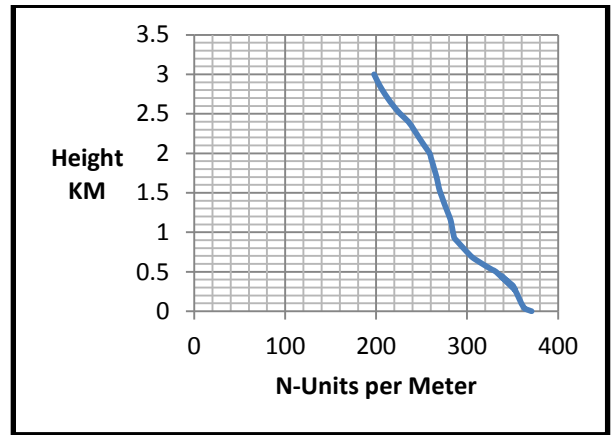


Figure 48: N-units per meter versus height measured on 11-07-2015 at Point 1.

3.11.4 Results pertaining to the measurements performed on July 21st 2015

The temperature inversion versus height at Point 3 is presented in figure 49, which occurs at 250 meters, while the refractivity curve is illustrated in Figure 50.

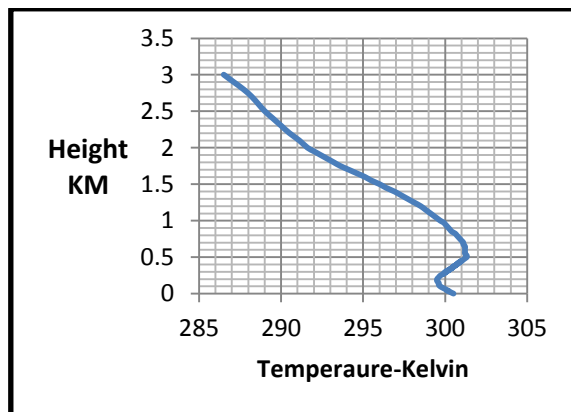


Figure 49: Temperature versus height measured on 21-07-2015 at Point 3.

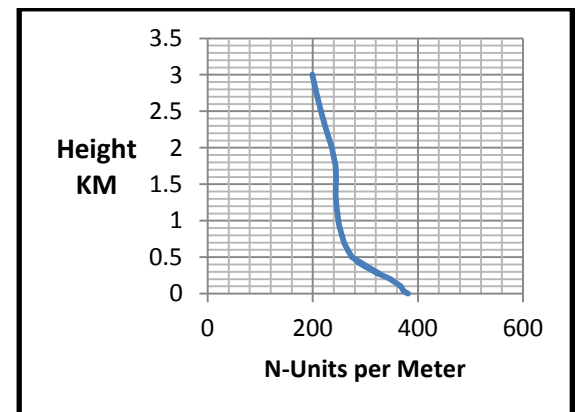


Figure 50: N-units per meter versus height measured on 21-07-2015 at Point 3.

The results pertaining to the changes in temperature with height are presented in figure 51, while figure 52 depicts those related to the N-units measurements at Point 2 (33°47'17.48"N, 33°45'51.56"E). As can be seen, the temperature inversion commences at 400 meters.

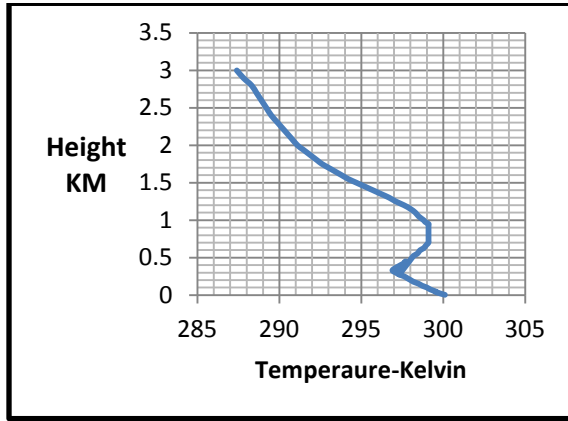


Figure 51: Temperature versus height measured on 21-07-2015 at Point 2.

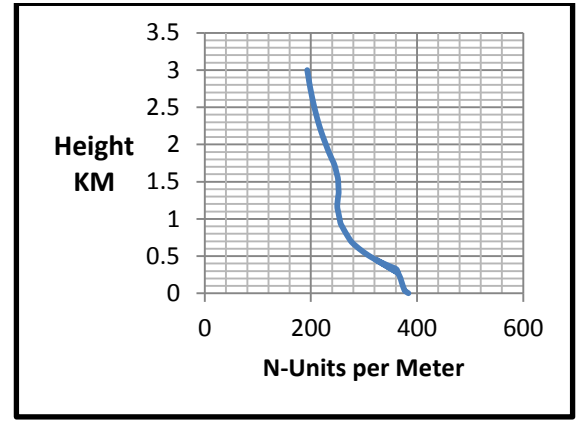


Figure 52: N-units per meter versus height measured on 21-07-2015 at Point 2.

The findings pertaining to the temperature changes at different heights at Point 1 (32°30'49.68"N, 34°37'42.44"E) are illustrated in Figure 53, which denotes a temperature inversion at 500 m. The refractivity N findings are shown in Figure 54.

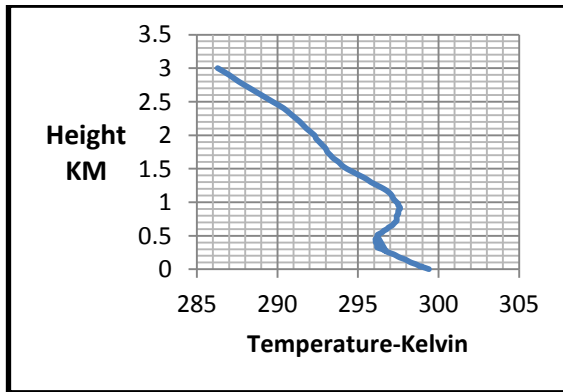


Figure 53: Temperature versus height measured on 21-07-2015 at Point 1.

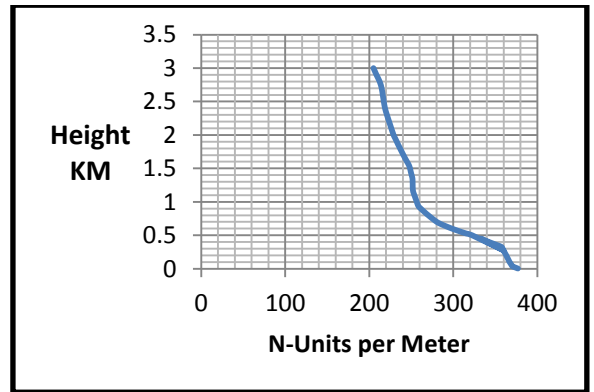


Figure 54: N-units per meter versus height measured on 21-07-2015 at Point 1.

3.12 Results pertaining to Medium Field Intensity

Field strength measurements obtained on selected dates presented on table 8, when the strength of the 95.5 MHz and 102.5 MHz signal was moderate (average). All measurements were obtained at 1:00 PM.

DATE	95.5MHz	102.5 MHz
12/7/2015	42dB	42dB
18/7/15	42dB	30dB
23/7/15	42dB	35dB
24/7/15	45dB	20dB
31/7/15	40dB	40dB
6/8/15	40dB	35dB
16/8/15	35dB	20dB

Table 8: Medium field strength intensity

3.12.1. Results pertaining to the measurements performed on July 12th 2015

Results obtained at Point 3 are depicted in Figures 55 and 56, revealing temperature inversion at 350 m.

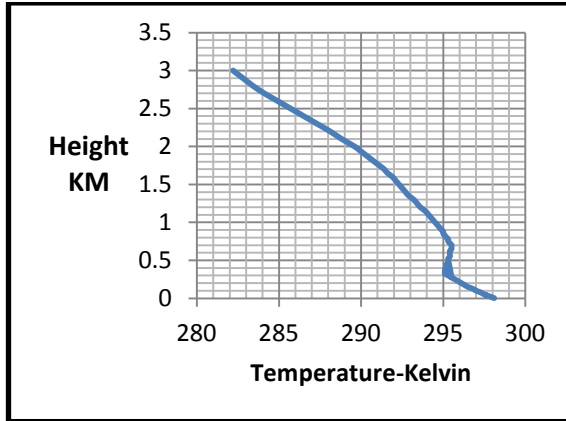


Figure 55: Temperature versus height measured on 12-07-2015 at Point 3.

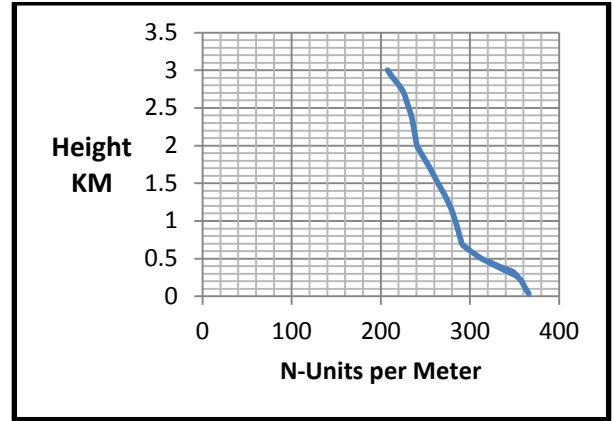


Figure 56: N-units per meter versus height measured on 12-07-2015 at Point 3.

Results obtained at Point 2 are presented in Figures 57 and 58 where inversion begins at 900 meters.

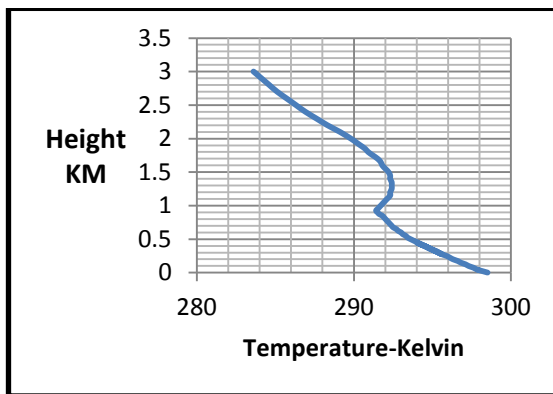


Figure 57: Temperature versus height measured on 12-07-2015 at Point 2.

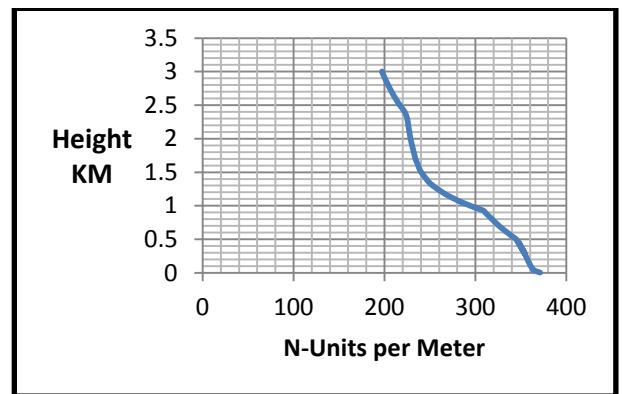


Figure 58: N-units per meter versus height measured on 12-07-2015 at Point 2.

Results obtained at Point 1 are presented in figures 59 and 60, where no inversion is noted.

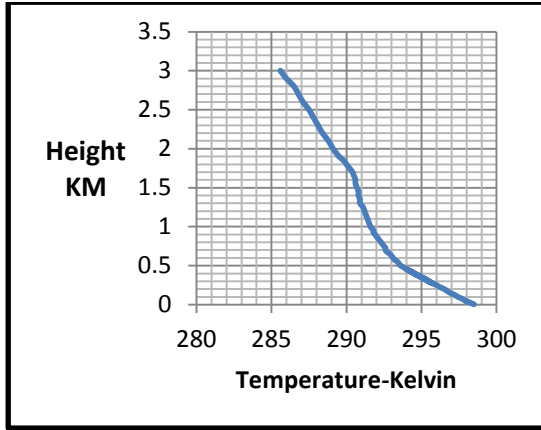


Figure 59: Temperature versus height measured on 12-07-2015 at Point 1.

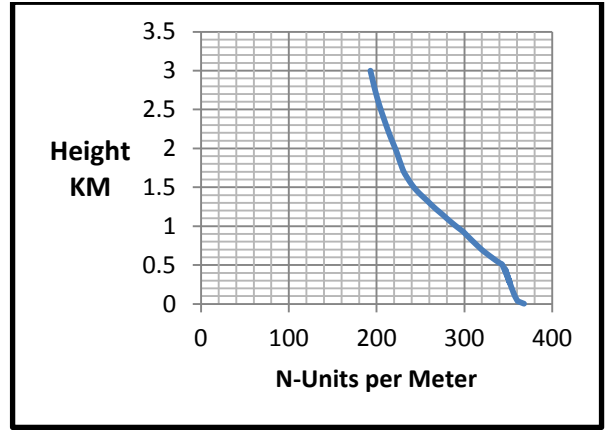


Figure 60: N-units per meter versus height measured on 12-07-2015 at Point 1.

3.12.2 Results pertaining to the measurements performed on July 31st 2015

Results obtained at Point 3 are presented in figures 61 and 62, where inversion begins at 350 meters.

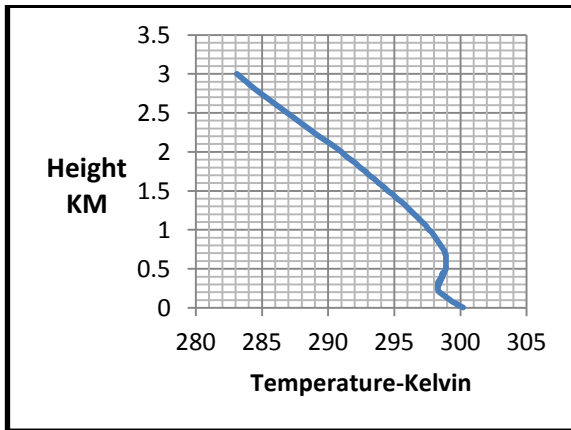


Figure 61: Temperature versus height measured on 31-07-2015 at Point 3.

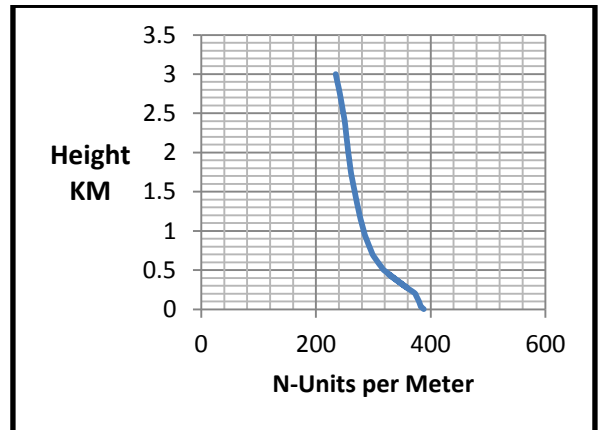


Figure 62: N-units per meter versus height measured on 31-07-2015 at Point 3.

Results obtained at Point 2 are presented in figures 63 and 64, where inversion begins at 500 meters.

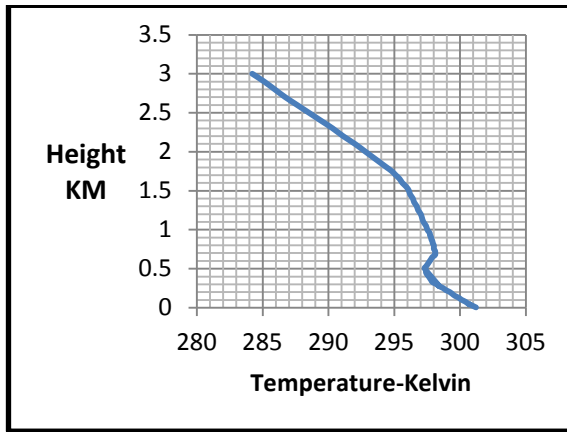


Figure 63: Temperature versus height measured on 31-07-2015 at Point 2.

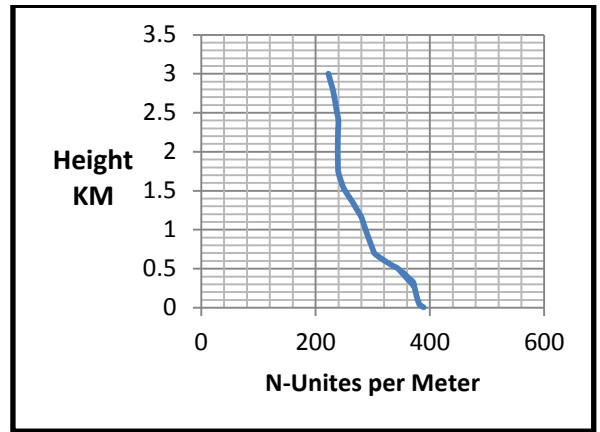


Figure 64: N-unites per meter versus height measured on 31-07-2015 at Point 2.

3.13 Results pertaining to Low Field Intensity

Field strength measurements obtained on the dates characterized by low field strength of the 95.5 MHz and 102.5 MHz signal are presented on Table 9. All measurements were obtained at 1:00 PM.

DATE	95.5MHz	102.5MHz
20/6/15	15dB	15dB
24/6/15	15dB	15dB
30/6/15	12dB	10dB
8/8/2015	10dB	10dB
10/8/2015	10dB	15dB
11/8/2015	12dB	12dB
30/8/15	10dB	20dB

Table 9: Low field strength intensity

3.13.1 Results pertaining to the measurements performed on June 20th 2015

Results obtained at Point 3 are presented in figure 65 and 66, where no temperature inversion was noted.

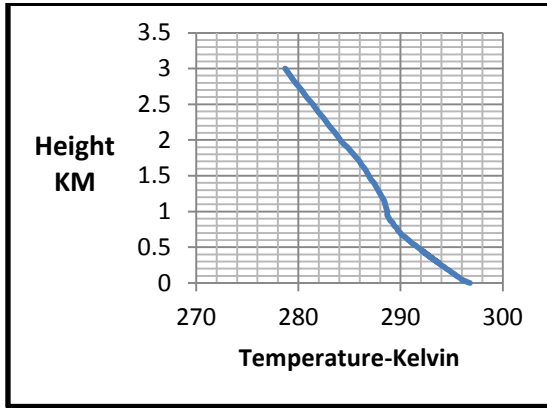


Figure 65: Temperature versus height measured on 20-06-2015 at Point 3.

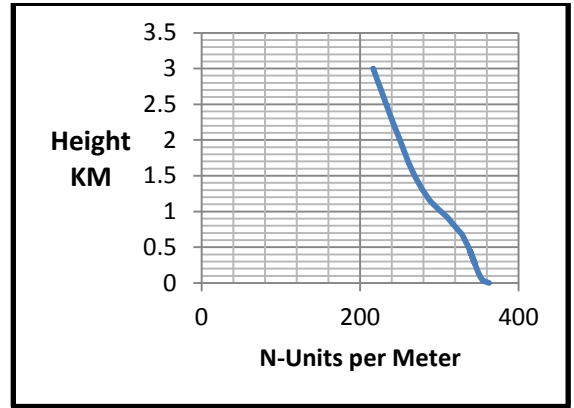


Figure 66: N-units per meter versus height measured on 20-06-2015 at Point 3.

Results obtained at Point 2 are presented in figures 67 and 68, where no temperature inversion was noted either.

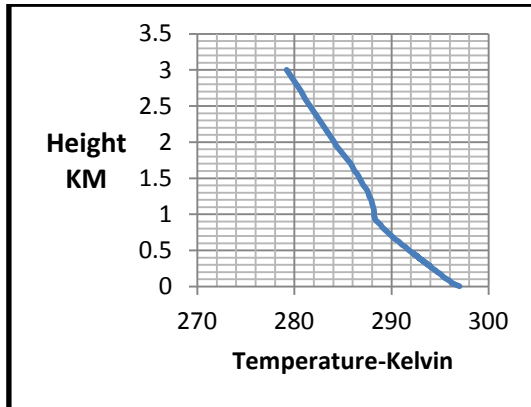


Figure 67: Temperature versus height measured on 20-06-2015 at Point 2.

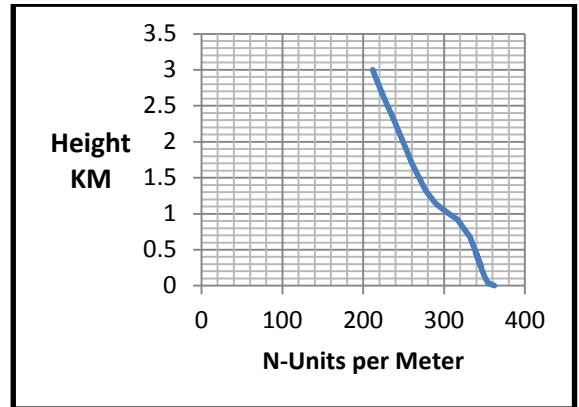


Figure 68: N-units per meter versus height measured on 20-06-2015 at Point 2.

Results obtained at Point 1 are presented in figures 69 and 70, revealing, once again, no temperature inversion.

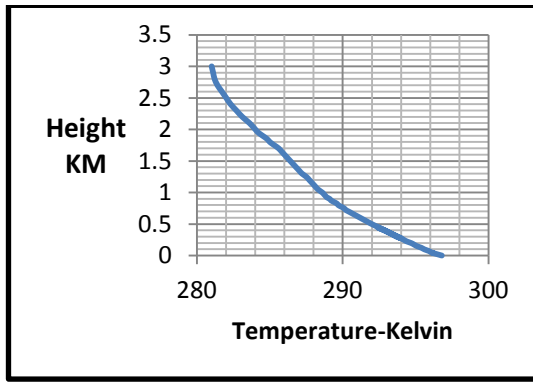


Figure 69: Temperature versus height measured on 20-06-2015 at Point 1.

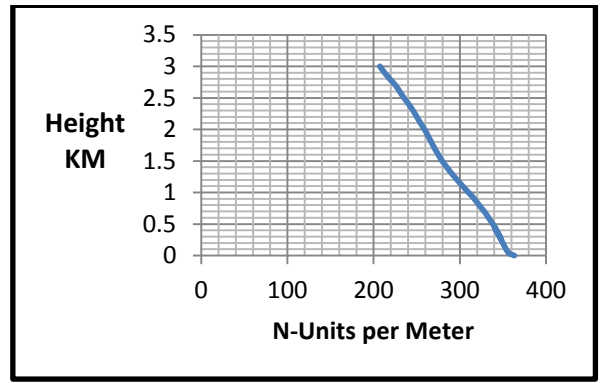


Figure 70: N-units per meter versus height measured on 20-06-2015 at Point 1.

3.13.2 Results pertaining to the measurements performed on June 30th 2015

Results obtained at Point 3 are presented in figures 71 and 72, revealing no temperature inversion.

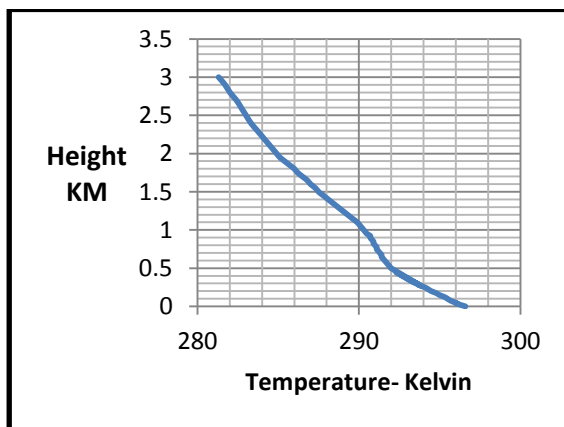


Figure 71: Temperature versus height measured on 30-06-2015 at Point 3.

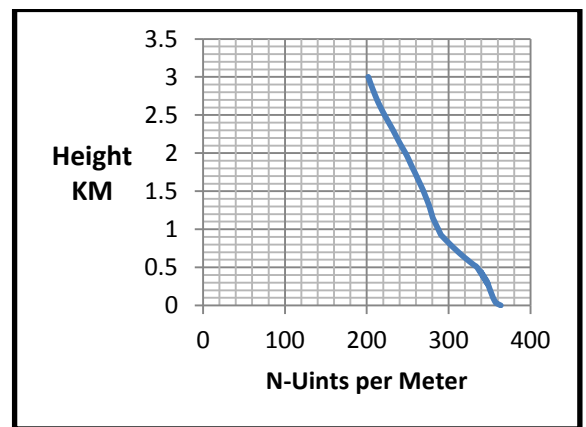


Figure 72: N-units per meter versus height measured on 30-06-2015 at Point 3.

Results obtained at Point 2 are presented in figures 73 and 74, where no temperature inversion was noted once again.

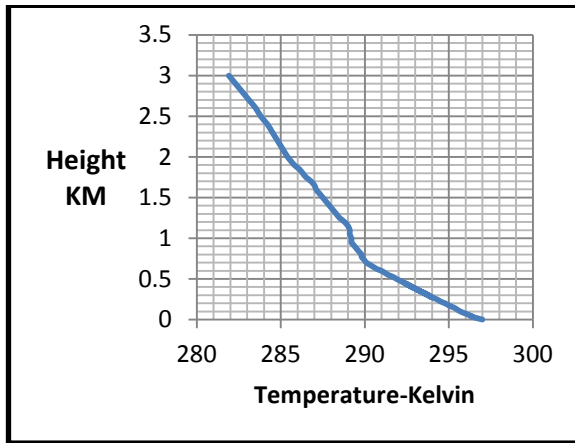


Figure 73: Temperature versus height measured on 30-06-2015 at Point 2.

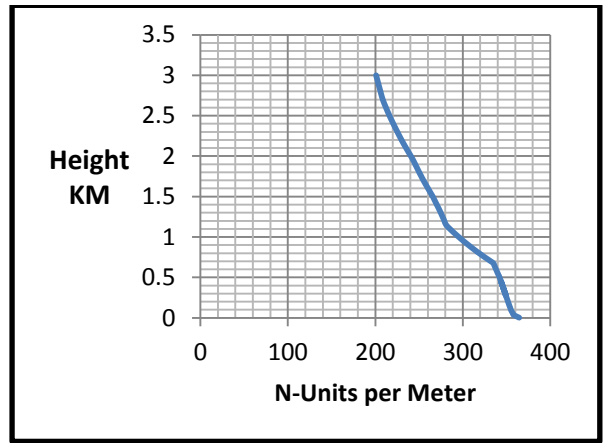


Figure 74: N-units per meter versus height measured on 30-06-2015 at Point 2.

Results presented in Figures 75 and 76 provide pertains to measurements made at Point 1, revealing no temperature inversion.

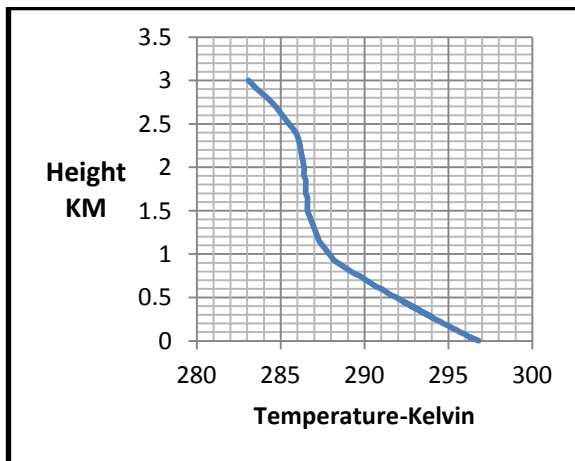


Figure 75: Temperature versus height measured on 30-06-2015 at Point 1.

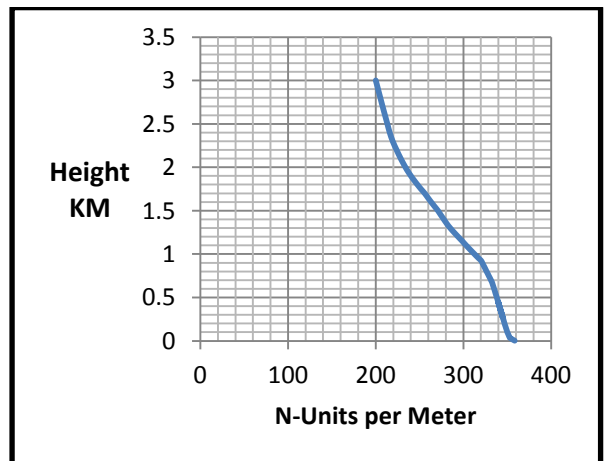


Figure 76: N-units per meter versus height measured on 30-06-2015 at Point 1.

3.13.3 Results pertaining to the measurements performed on August 30th 2015

Results presented in Figures 77 and 78 pertain to measurements made at Point 3, revealing that temperature inversion occurs at the height of 900 m.

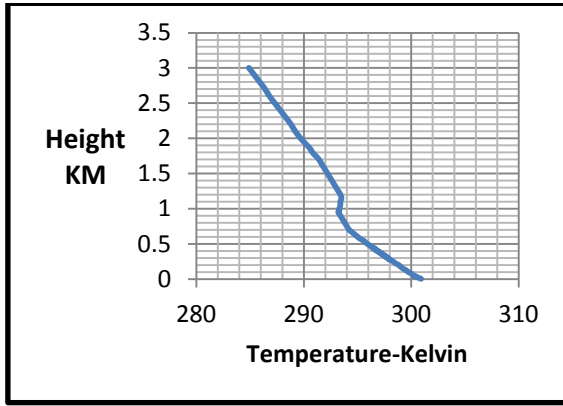


Figure 77: Temperature versus height measured on 30-08-2015 at Point 3.

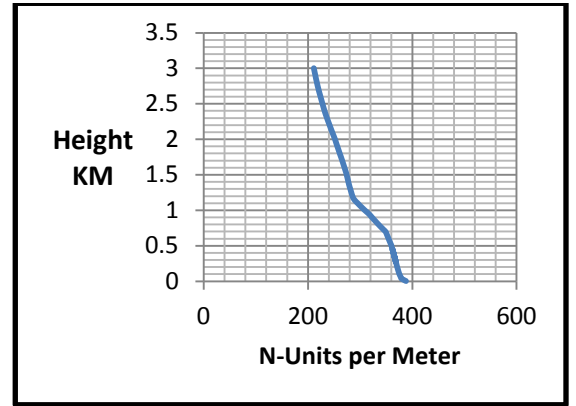


Figure 78: N-units per meter versus height measured on 30-08-2015 at Point 3.

Results obtained at Point 2 are presented in figures 79 and 80, where no temperature inversion was noted.

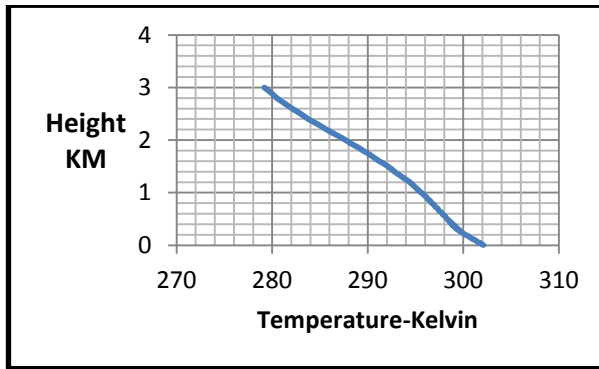


Figure 79: Temperature versus height measured on 30-08-2015 at Point 2.

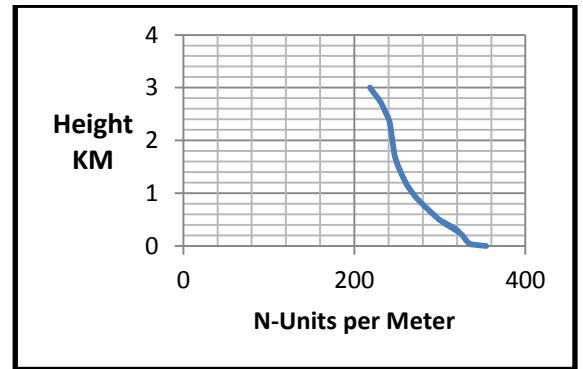


Figure 80: N-units per meter versus height measured on 30-08-2015 at Point 2.

Results obtained at Point 1 are presented in figures 81 and 82, where no temperature inversion was noted once again.

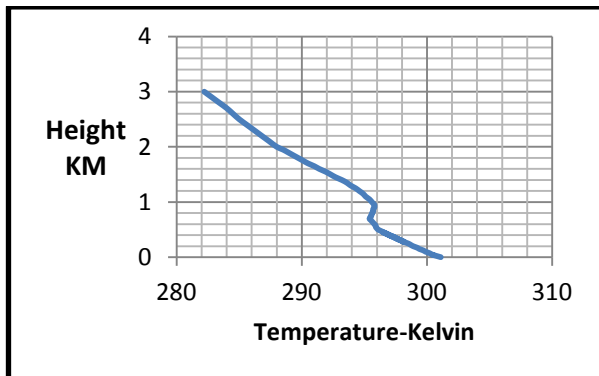


Figure 81: Temperature versus height measured on 30-08-2015 at Point 1.

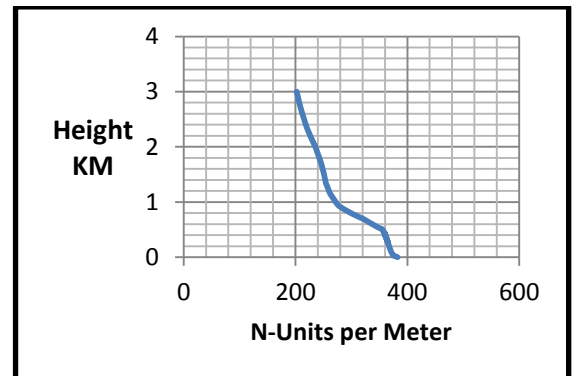


Figure 82: N-units per meter versus height measured on 30-08-2015 at Point 1.

3.14 The Type of Ducts along the Limassol Coast

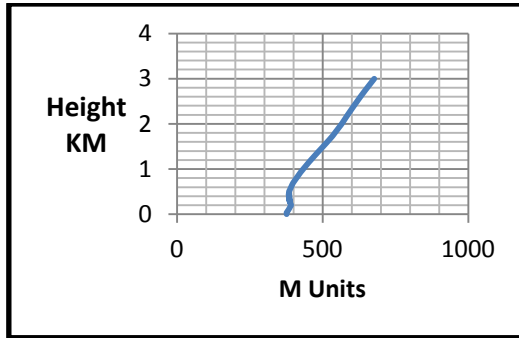


Figure 83: Surface Based Duct measurements made on 18-06-15 at Point 3.

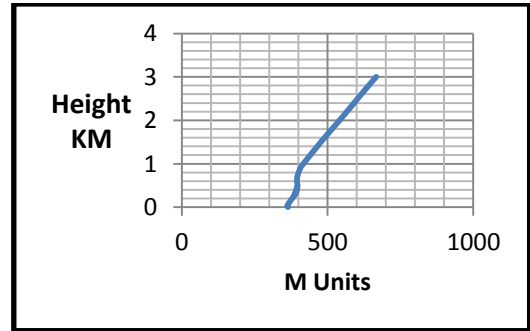


Figure 84: Surface Based Duct measurements made on 24-06-15 at Point 3

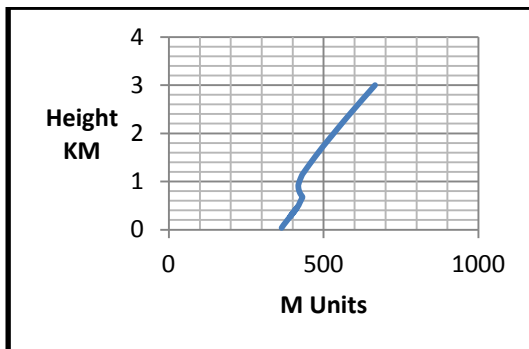


Figure 85: Surface Based Duct measurements made on 07-07-15 at Point 3.

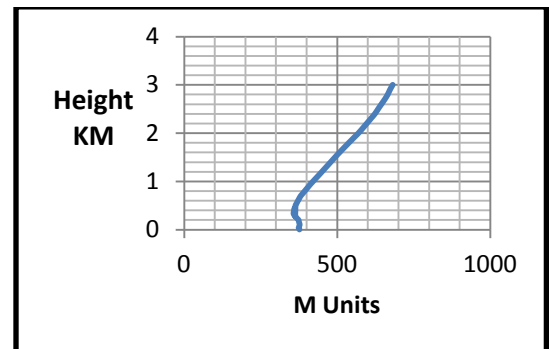


Figure 86: Surface Duct measurements made on 11-07-15 at Point 3.

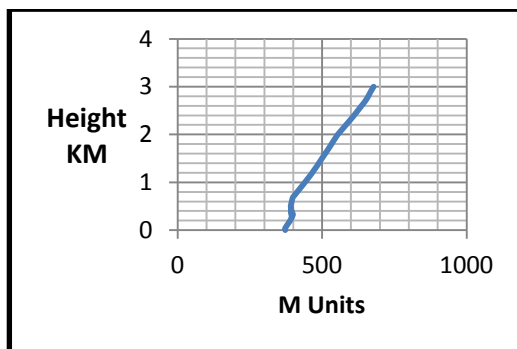


Figure 87: Surface Based Duct measurements made on 12-07-15 at Point 3.

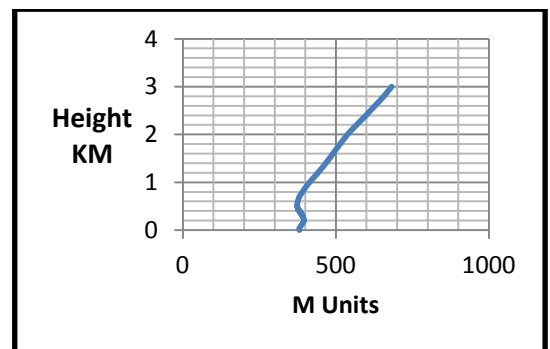


Figure 88: Surface Based Duct measurements made on 23-07-15 at Point 3

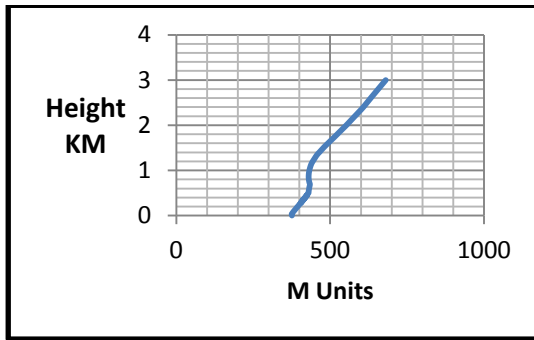


Figure 89: Elevated Duct measurements made on 24-07-15 at Point 3.

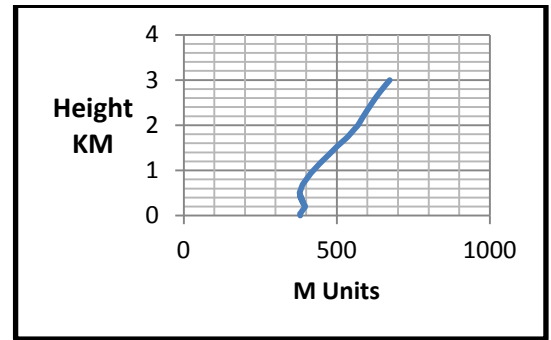


Figure 90: Surface Based Duct measurements made on 28-07-15 at Point 3.

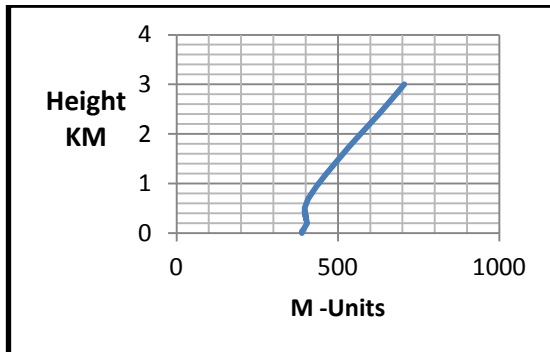


Figure 91: Surface Duct measurements made on 31-07-15 at Point 3.

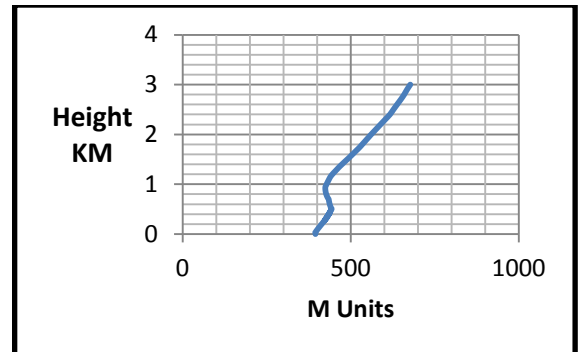


Figure 92: Surface Based Duct measurements made on 06-08-15 at Point 3.

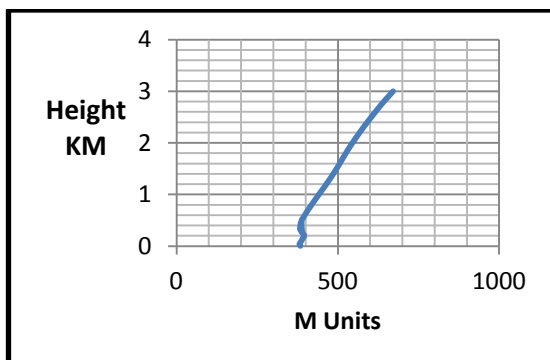


Figure 93: Surface Based Duct measurements made on 08-08-15 at Point 3.

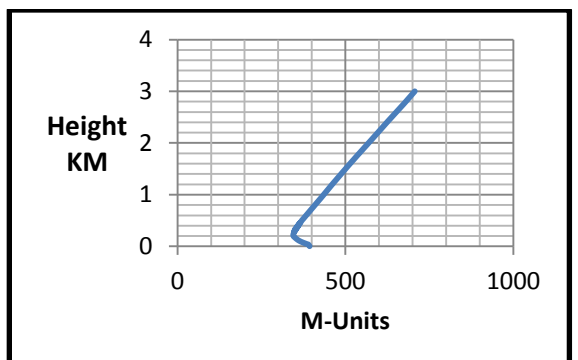


Figure 94: Surface Duct measurements made on 16-08-15 at Point 3.

The surface temperature inversion observed during the summer months in the Eastern Mediterranean region results from the movement of warm air masses from the mainland to the south or southeast of Cyprus, where the sea is colder. Thus, upon contact with the colder surface water, the hot air mass is cooled at the bottom, leading to surface temperature inversion. Consequently, the area is characterized by high humidity, low cloud and fog in some cases. When the air mass that affects the Cyprus region comes from west–

northwest, it is colder than the sea temperature and leads to surface inversion. In addition to the surface inversion, during summer, inversion arising from cathode currents (subsidence) is observed in the middle atmosphere. Its extent typically ranges from 3000 to 8000 m.

3.15 Chapter Conclusion

The problem of radio interference in Limassol was analysed in detail in this chapter by applying real field strength intensity measurements obtained by monitoring behaviours of two existing overseas radio signals transmitted at 95.5 MHz and 102.5 MHz, respectively, in various meteorological conditions, expressed through the parameters provided by the Meteorological Department of Cyprus during June, July and August of 2015. The findings presented here revealed that the radio interference experienced along the southern coast of Cyprus is caused by three major types of ducts, presented in Section 3.14.. Presence of these ducts has been verified close to the coast of Limassol, whereby they were classified as surface (i.e., Fig. 86), surface based (i.e., Fig. 84) and elevated ducts (i.e., Fig. 89). The analyses performed as a part of this study also demonstrated that the field strength of the monitored overseas signals (95.5 MHz from Jerusalem, and 102.5 MHz from Lebanon) is directly proportional i.e. related to the temperature inversion curves, which were discussed in detail in Sections 3.11-3.13.3, with the greatest effects noted close to the coast of Limassol. According to the interference assessment performed on specific dates, it can be posited that strong temperature inversion is directly proportional to strong radio interference in close proximity to the coast of Limassol. Moreover, the study results have shown the electromagnetic waves in Band II can travel through the ducts with stronger field strength intensity than the free space value when the elevation of the duct approaches the Earth's surface. Particularly, according to the findings presented in Section 3.7, the field strength intensity exceeds the free space value by approximately 15 dB. On the other hand, when there is no temperature inversion, a very low interference effect or its complete absence was noted.

Because the radio interference in Band II is caused by anomalous propagation conditions, which is governed by the climatic conditions of the Mediterranean Sea, it will never cease completely. In other words, it will continue to affect the local radio services during the hot and dry summer months.

The outcomes of this study are crucial not only for the assessment of the existing radio services, but also for utilization of the latest technology, state of the art digital radio

switchover, as the same problem of interference will affect any new Digital Radio Scheme. For example, interference will affect Band III signals, which is designated for Digital Audio Broadcasting (DAB+), as well as Band II utilized by Digital Radio Mondiale (DRM+) applications. In this regard, the overseas transmissions from the Middle East will arrive to the southern coast of Cyprus with the field strength intensity equivalent to that presented in Section 3.11, even after the switchover to digital radio.

In order to mitigate the aforementioned problem to a significant level, the radio interference must be blocked by the use of a new generation smart antennae, which is the topic of the following chapters.

Chapter 4: Phased Arrays-The solution to the Problem of Interference

The aim of this chapter is to present the implementation of a Band II smart receiving antenna, which was designed as a part of the present study based on the phased array topology. As noted in the previous chapter, tropospheric ducting radio interference arrives at the coast of Limassol from the direction of the Southern Mediterranean Sea, whereas the desired signals of the local terrestrial radio services arrive from the opposite direction, as the radio transmitting points are always installed on top of hills in order to ensure line of sight conditions within the service area.

The commercial traditional receivers employ vertically polarized telescopic whip antennas, which receive signals from all directions with equal density since a monopole antenna provides an omnidirectional radiation pattern (Khan, Azim and Islam, 2014). As a result, a telescopic whip antenna cannot distinguish the desired signal from the interference, as both penetrate into the receiver despite arriving from different directions. Moreover, once combined, these signals cause co-channel interference. In contrast, a phased array can minimize the reception strength of unwanted signals (Stuckman and Hill, 1990). Based on this concept, a phased array utilized for reception purposes can minimize the level of interference very efficiently as its main beam steers in the desired direction in order to disable penetration of other incoming (undesired) signals transmitted from the side and back positions. This effect can be achieved even if omnidirectional elements are used. The main beam's tilt direction of a phased array depends on the phase shift as well as the amplitude difference among the single elements that constitute the system (Rabinovich, 2011), as discussed in detail later in this thesis. The array's main beam steers in the desired direction by setting the phase among the radiators of the array through the use of electronic phase shifters, which are excited by a control system instructing the main beam to steer in the direction of the strongest signal.

As a result, the greatest advantage of this approach stems from dispensing with the need for mechanical movement, as the main beam of a phased array steers toward the desired direction (Lee and Kim, 2009). According to the pattern multiplication theorem, the single element radiation pattern (assuming that all array elements are identical) is multiplied by the array factor's pattern (Eq. 32), producing the final radiation pattern of the array, as shown below (Rabinovich and Alexandrov, 2013):

$$AF = [1 + e^{j(\Delta_2 + \beta d \cos \theta)} + e^{j(\Delta_3 + 2\beta d \cos \theta)} + \dots + e^{j(\Delta_N + (N-1)(\beta d \cos \theta))}] \quad (32)$$

Where $\beta = 2\pi/\lambda$

Δ = It is the phase variation of each individual element

Therefore, the geometry of the array and the single element properties are the two key factors determining the success of this implementation. Furthermore, the physical size of the radiators versus their performance, as well as the number of elements, is an important trade-off in the response of the entire system. Thus, they are determined in this research. As will be shown later in this work, applying phased array technology in the design of the future commercial receivers can be a powerful solution to the problem of interference, not only in Cyprus but in other regions of the world as well. As a result, the aim of the present study was to design a smart antenna that is small enough to allow incorporation in a deck receiver or installation on vehicles. Another important goal was to keep the smart antenna's design as simple as possible, without compromising on its performance, as this would ensure that the solution is cost-effective and widely applicable.

Furthermore, given several types of phased array topologies presently in use—such as linear, circular, planar and conformal arrays—it is essential to identify the one that is most suited for this application. In order to meet all the aforementioned goals, the present study comprised of (a) examining small antenna characteristics for optimizing the individual element of the array and (b) determining the array factors that would result in the most optimal radiation pattern.

The first step necessitated considering all crucial fundamental parameters of a stand-alone antenna in order to propose the design of an individual array element. The second step comprised of examining the phased array topology, as a means of identifying the most optimal specifications for suppressing the interference from a given direction most effectively. The concepts and parameters pertinent to these steps are discussed in subsequent sections.

4.1. Directivity, Gain & Effective Aperture

The polar diagram that presents the direction of the maximum power density of an individual array element within a given area in the far field is defined as “Directivity” and is provided without taking into account system efficiency, i.e. the radiated power versus the input power, which is discussed further below (Pojar, 1993). In this context, directivity is given in spherical coordinates as a function of electromagnetic energy radiated by a very short length isotropic radiator the directivity of which equals one (i.e. the energy is radiated to all directions at a uniform density). Directivity was expressed mathematically by Kraus as shown in Eq. 33 below:

$$D(\Theta, \Phi) = \frac{U(\theta, \Phi)_{max}}{\frac{1}{4\pi} \int_0^{2\pi} \int_0^\pi U(\theta, \Phi) \sin\theta d\theta d\Phi} \quad (33)$$

Where $U(\Theta, \Phi)$ is the radiation intensity

Θ =Azimuth Angle

Φ = Polar Angle

From the expression above, it is evident that the smaller the beam solid angle the greater the directivity. As high directivity antennae are characterized by approximately equal elevation and azimuth angles (Θ_{HP} , Φ_{HP}), directivity can be approximated by Eq. 34 as follows:

$$D \approx \frac{4\pi}{\theta_{HP}\Phi_{HP}} \approx \frac{41000}{\theta_{HP}\Phi_{HP}} \quad (34)$$

Another key parameter related to the array's performance, is "Gain", which determines the net radiated or received power (compared to the source) in the far field within a certain area. As a result, "Gain" is provided in terms of the radiation efficiency, denoting how much power is radiated or received in real conditions compared to a small isotropic radiator (Panchenko, 1984). Crucial factors that degrade radiator efficiency are related to insertion heat dissipation and reflection losses caused by the radiator construction materials. For instance, the antenna substrate properties and the need for matching between the source and the load can cause serious issues. Thus, antenna size is a very important design consideration, especially its impedance characteristics, as discussed later in this thesis. Furthermore, the aforementioned parameters should be considered very carefully, since low-efficiency antennae provide a very poor gain (Wheeler, 1975). More specifically, an antenna characterized by poor gain will degrade receiver sensitivity, preventing it from receiving the desired radio signals accurately. Thus, optimizing the individual array elements to ensure maximum gain is one of the most important objectives of the present study. This is achieved by a small-sized antenna, as discussed later in this work. In this context, it is also essential to define the "Effective Aperture" as a function of "Gain" (defined as the maximum energy absorption achieved by the antenna versus an incident wave), as given by Eq. 35 below (Whites, 1989):

$$\frac{A_{eff}}{\lambda^2/4\pi} = \text{Gain} \quad (35)$$

Where:

A_{eff} = Effective Aperture

From the expression above, it is evident that a large-aperture antenna exhibits high gain characteristics and thus a small angular beam width. The physical size of the individual array elements will be discussed in the next chapter.

4.2. Radiation Pattern

The polar diagram of the field strength intensity that an antenna receives or transmits per unit angle is presented in three dimensions in a diagram known as the radiation pattern (Martin, 1967). The aim of the radiation pattern diagram is to present the crucial angles in terms of the direction in which the main beam has the maximum intensity. This beam width is determined by the angles at which the power density decreases to 50% (3 dB), denoted as the half-power beam width. Additionally, the radiation pattern presents the level and the direction of the side lobes. Side lobes are particularly important in reception antennae, as they are weak beams that allow the unwanted signal to travel through them into the receiver, even though the main beam is steered in a different direction (Sharma and Calla, 1988). Thus, in the present study, the radiation pattern is considered as an essential specification parameter, as it will determine the overall antenna performance. Since the radiation pattern is given over an isotropic area (i.e. a sphere), it is always provided in three dimensions based on two principal components, such as the electric field (E) and the magnetic field (H) planes, respectively. These assertions can be substantiated by the fact that electromagnetic waves are treated as Poynting vectors (S) representing the directional energy flux density (in the direction of energy propagation), while oscillating in magnitude. They can be expressed mathematically in Abraham's form given below (Jackson, 2006):

$$S = E \times H$$

Where E is the electric field and H the magnetic field.

It is noteworthy that, in order to block the interference, the radiation pattern in this project must be directional with very high rejection in the back lobe.

4.3. The Effect of Physical Dimensions on the Antenna Performance

An antenna is a resonance circuit; therefore, its impedance is determined by the voltage to current ratio at the input of the antenna's terminal. As will be discussed below, the physical size of an antenna is directly related to its radiation resistance, which is one of the key parameters considered in this implementation, since the individual elements' physical size

constrain the practical utility of an antenna. For instance, the physical size of a half-wavelength dipole that operates at 100 MHz is approximately 1.5 m. Although these physical dimensions are impractical for incorporation into commercial receivers, its benefit stems from its ability to operate at resonance, i.e. it exhibits at its centre (feed point) a conjugate impedance of approximately 73Ω (Bailey, 1984). The same principle is also applied to a quarter-wavelength monopole, which exhibits a radiation resistance equivalent to the half of that measured for the dipole, i.e. 37Ω . The radiation resistance of a resonance antenna is crucial for most applications, because it can be easily matched to a $50\text{-}\Omega$ port without significant losses, making the antenna very efficient. In other words, the benefit of a high efficiency resonance antenna is that it matches directly to a commercial receiver's input impedance, which is usually 50Ω unbalanced. In this respect, the source energy (antenna) will provide maximum power transfer to the load (receiver), enhancing the signal to noise ratio. This assertion is justified by the maximum power transfer theorem, which states that absolute matching leads to maximum power transfer (Li, Chen and Xu, 2010).

In this respect, it is obvious that the radiation resistance versus the physical size of the individual element design is a crucial factor, as it determines its efficiency. In other words, owing to this factor, the physical size of most antennas in the market is chosen in order to allow them to operate in resonance mode. In this context, full wavelength (λ) dimensions (in m) are given by the quotient of the electromagnetic wave speed, travelling into the antenna constructive material (in m/s) over the operating frequency (MHz). Because most traditional antennas are constructed using aluminium or copper rods, they behave as air insulated lines, e.g. transmission lines with the air dielectric constant (ϵ_r) equal to unity. As a result, the physical size of the antenna in terms of free space wavelength becomes the reference physical size for shorter resonance or non-resonance antennae, which is discussed below.

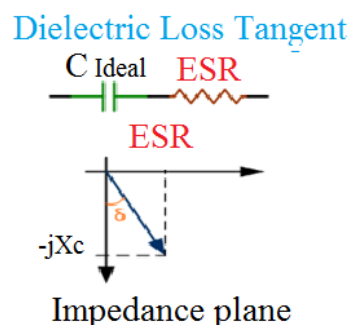


Figure 95: Dielectric loss tangent diagram

An antenna is usually considered small when its size is less than $\frac{\lambda}{10}$ (Shackelford, Kai-Fong Lee and Luk, 2003). A small-sized antenna can be constructed as a coaxial line, whereby the physical length of a radiator can be reduced in terms of free space wavelengths by the use of high ϵ_r (> 1) dielectric materials, while still achieving resonance. Dielectric materials are nonconductive or semi-conductive materials, such as water, Teflon, polyethylene, etc., which are commonly applied as insulators in PCBs or coaxial lines. In this design, it is essential to consider a very important drawback of a dielectric PCB small antenna, stemming from the substrate's propensity to absorb a significant proportion of energy from the incident electromagnetic waves. As a result, it behaves as an attenuator in series with the input impedance of the antenna. Furthermore, the dielectric loss tangent, $\tan(\delta)$, produces losses, as it is the angle between the capacitor's impedance vector and the negative reactive axis, as illustrated in fig. 95. When the speed of the plane wave declines due to a dielectric material, the wavelength becomes shorter, resulting in high losses the extent of which depends on the properties of the material used. Based on the transmission line theory, this can be justified as the velocity factor of the antenna's dielectric material that will eventually determine the antenna's physical size in terms of free space wavelengths but also a great amount of losses. This is best elucidated through an example based on a quarter-wavelength 100 MHz dielectric monopole antenna using highly dielectric material such as alumina with substrate characterized by $\epsilon_r = 10$. Despite the high losses incurred by the substrate, its physical size is relatively small, calculated as 25 cm. However, this is still excessive for most practical applications. In addition, it is essential to take into account the great losses due to the high " ϵ_r " arising from substrate's absorption. Owing to these factors, in the present study, individual array elements were not based on a dielectric material.

An alternative approach to constructing a small-sized antenna is based on the use of a non-dielectric material, such as a copper wire. In this case, the issue of absorption from the substrate's dielectric material is eliminated; however, the short antenna will exhibit a very low radiation resistance and very high reactive impedance. As a result, this type of small-sized antenna will be characterized by unacceptably low efficiency response due to its low radiation resistance and high reactance, i.e. it will exhibit very high losses due to VSWR. This design also introduces the issue of very narrow band response, which is expected in the performance of such small antennae. The bandwidth will also be limited due to the high impedance transformation ratio of the matching network, which must cancel the high reactive component. In order to confirm these assertions, as a part of the present study,

three small antenna topologies—the short dipole (Hertzian), short monopole, and the normal mode helical antenna—were investigated in real conditions. These antenna types were chosen because they exhibit omnidirectional radiation pattern and are capable of receiving vertically polarized waves.

4.4. The Short Dipole Antenna

The short dipole antenna consists of two rods of equal size, as illustrated in Figure 96. The advantage of the short dipole is that it does not require a perfect ground plane to operate properly, as does the short stub (monopole) discussed in the next chapter. However, since the feed point of the short dipole is symmetrical, it requires a special designed balun in order to be converted into asymmetrical configuration to match with the receiver's input that is unbalanced. Due to its low radiation resistance, a matching network must also be matched with the input of a commercial receiver, which is 50Ω .

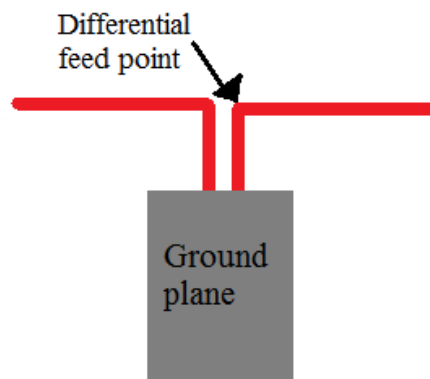


Figure 96: The short dipole

According to Breed (2007), using the Nec 2 numerical modeling, the input impedance of a short dipole with $\lambda/10$ length is calculated as $Z_{\text{feed}} = 1.96 - j1758 \Omega$, with the maximum gain of 1.77 dBi. Due to the above mentioned impedance response, the small dipole is very inefficient. This can be confirmed, according to Kulms (2015), based on equivalent circuit, which presents the input impedance of the small dipole, as illustrated in Figure 97.

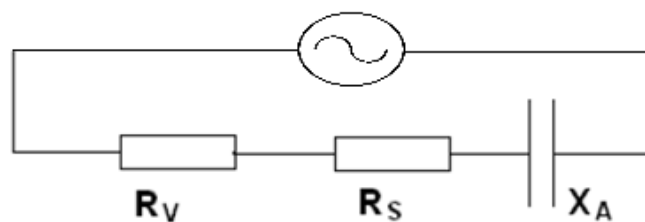


Figure 97: Equivalent circuit of the small dipole's impedance network

Where R_S is the radiation resistance, R_V is the loss resistance, and X_A is the capacitive component.

The radiation resistance of the short dipole is the real part of the impedance and is given by Breed (2007) in Eq. 36, 37 below:

$$R = 80\pi^2 \frac{h^2}{\lambda^2} \quad (36)$$

The dissipation resistance is given by Eq. 37:

$$R = \frac{1}{3\pi r \delta \sigma} \quad (37)$$

Where r is the conductor radius, δ is the skin depth, and σ is the metal conductivity.

Because of the low radiation resistance of the short dipole, the loss resistance and the reactive component become very important factors, as they degrade its efficiency. According to Kulms (2015), the feed point impedance of a short dipole with $\lambda/100$ length using a balun is given at a single frequency as $Z_{\text{feed}} = 7.5 - j994 \Omega$. Short dipole antennas have also been discussed by Evjen and Jonsrud (n.d.) in Texas Instruments application note AN003. In this respect, the report has revealed that the most crucial issue in the operation of the short dipole is the design of a low-loss matching network, which is characterized by a very narrow band as well. Particularly, given that the impedance of the short dipole is dominated by a high capacitive reactance, in order for it to be cancelled, a narrow band matching network with extremely high Q inductance is required. The aforementioned matching network will, however, introduce significant degradation in the antenna performance due to the insertion loss characterizing the high Q inductor. The Q of a short dipole described in the Texas Instruments application note AN003 is illustrated in Figure 98.

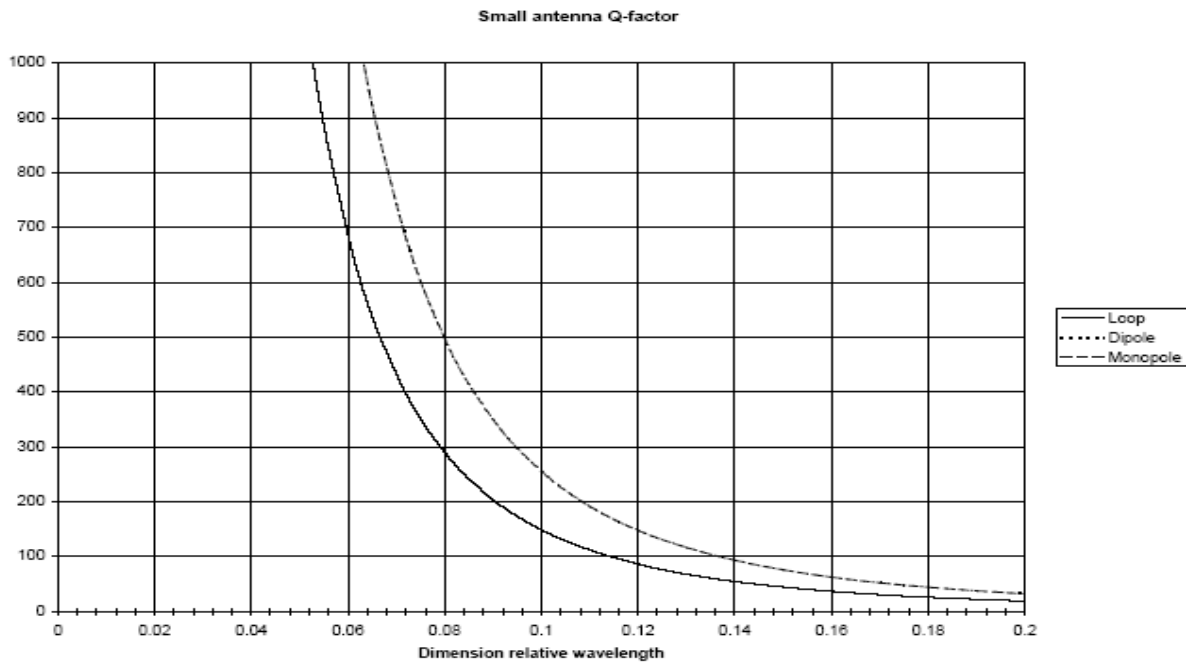


Figure 98: The Q factor of a small dipole

In this work, the impedance of a short dipole antenna with physical dimensions of $\lambda/30$ was simulated by EZNEC, as illustrated in Figure 99. The rod diameter is 1 mm and the dipole height is 10 cm. According to Figure 98, the impedance of the short dipole at 100 MHz is given as $Z_{\text{feed}} = 0.2561 - j4337$.

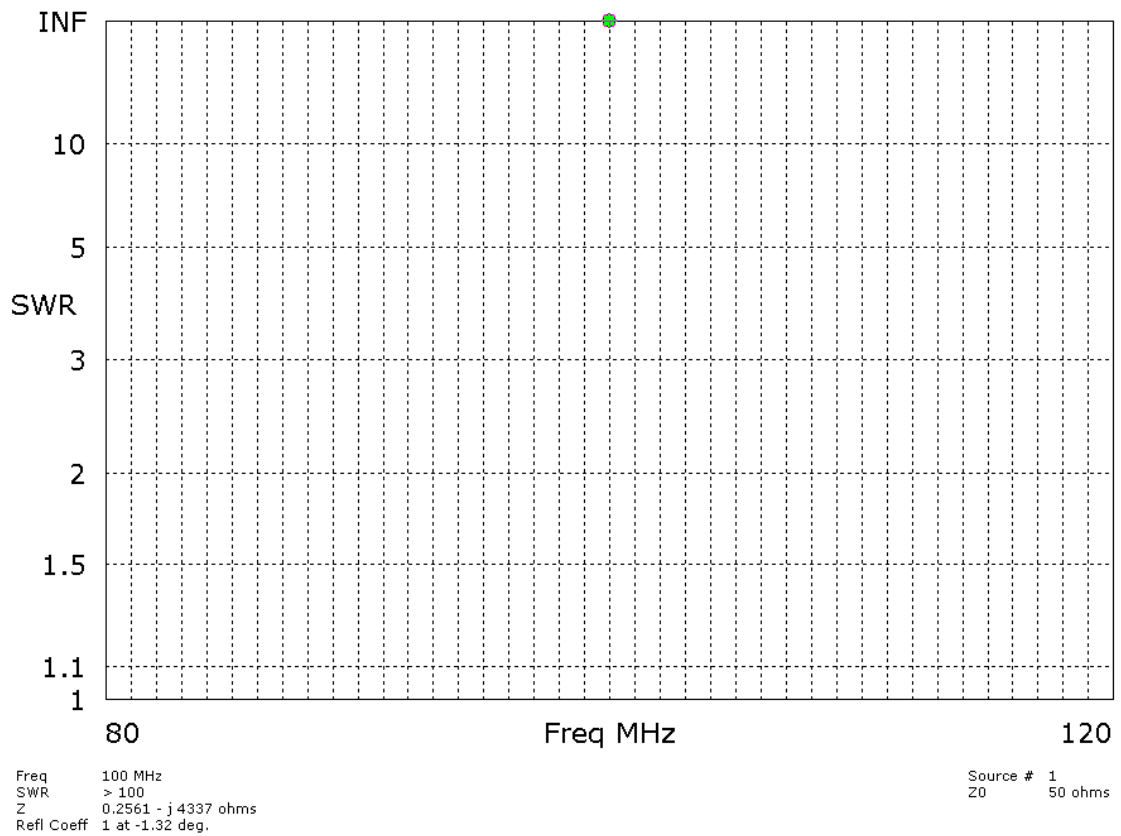


Figure 99: The impedance of the short dipole-the curve indicates infinite VSWR

As this ultra-low radiation resistance and the high reactive component make the short dipole antenna inappropriate for use in this application, it is investigated further.

4.5. The Short Monopole Antenna

The short monopole antenna, when mounted above a perfect ground plane, works similarly to the short dipole in terms of radiation pattern properties. In this respect, because the short monopole antenna provides an omnidirectional linearly polarized radiation pattern, as well as an unbalanced feed point that matches to a commercial's receiver input without the need of a balun, it was investigated in this project as a potential individual array element.

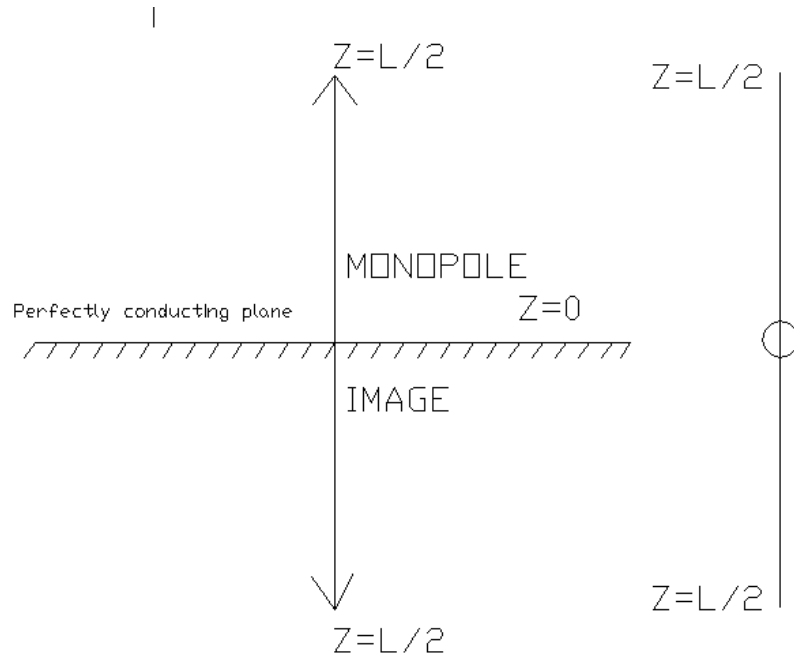


Figure 100: The monopole

The impedance response of the short monopole is analyzed in line with the evaluation of the short dipole. The low radiation resistance of the short monopole in number of wavelengths is given according to Texas Instruments application note AN003 in Figure 101, which indicates that low radiation resistance implies very poor efficiency. This relationship makes its application in this project inappropriate, as justified by Lee (1984) and discussed in the next section.

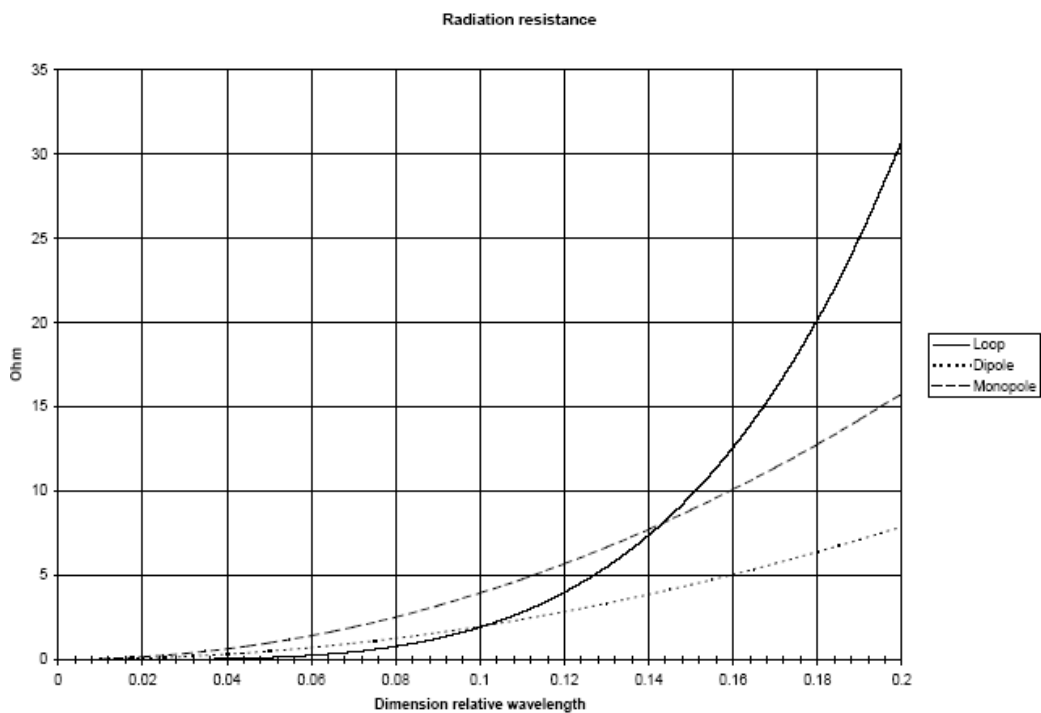


Figure 101: Radiation resistance as a function of wavelength

According to Lee (1984), a small monopole made of a copper conductor ($\sigma = 5.7 \times 10^7 \text{ ohm}^{-1}$ and $\mu = 4\pi \times 10^{-7} \text{ Hm}^{-1}$) with radius $4.06 \times 10^{-4} \text{ m}$ is considered as a Hertzian dipole since its length corresponds to 0.0066λ only. In this application, the use of small monopole is not justified, due to its very poor efficiency of 14.59%, according to Lee (1984) numerical analysis below:

$$\text{Efficiency} = \frac{R_r}{R_r + R_L}$$

$$R_s = \frac{\mu \times 2\pi \times F}{2\sigma} = \frac{4\pi \times 10^{-7}}{2 \times 5.7 \times 10^7} \cdot 2\pi \cdot 10^6 = 2.63 \times 10^{-4} \text{ ohm}$$

$$R_L = \frac{R_s}{2\pi\alpha} \Delta L = \frac{2 \times 2.63 \times 10^{-4}}{2\pi \times 4.06 \times 10^{-4}} = 0.206 \text{ ohm}$$

$$R_r = 789 \left(\frac{\Delta L}{\lambda}\right)^2 = 0.0352 \text{ ohm}$$

Hence:

$$\text{Efficiency} = \frac{R_r}{R_r + R_L} = \frac{0.0352}{0.0352 + 0.206} = 14.59\%$$

Due to this issue, the small stub will not be investigated further in this thesis.

4.6. The Normal Mode Helical Antenna (NMHA)

A helical antenna is an antenna consisting of a conducting wire wound in the form of a spring (Monich and Littmann, 1990). When the Helix antenna diameter is much smaller than λ (for example, $\leq 0.1\lambda$), it operates in a Normal Mode and is therefore defined as a Normal Mode Helical Antenna (NMHA). An NMHA can be mounted either vertically above a ground plane, or directly on a connector without grounding. The NMHA radiation pattern is identical to that of a monopole antenna (it is an omnidirectional side-fire radiation pattern, which is the desired radiation pattern in this application). In contrast to the NMHA, a Monofilar Axial Mode helix's pattern is directional and the antenna operates as a telescope, i.e. it must be pointed in the direction of the desired signal. As this is the issue the present study aimed to eliminate, this design is inappropriate and will not be investigated further.

The many advantages of the NMHA relative to the short stub or the Hertzian dipole (which have been examined previously) were discussed by Kraus (2000). According to Kraus, the NMHA resonates at a much shorter physical length than does the monopole. In theory, the NMHA resonates at 0.06λ of a $\frac{\lambda}{4}$ stub as a substitute of a quarter-wavelength stub. In this respect, the axial ratio of the NMHA is given by Kraus (2000) in Eq. 38 below:

$$AR = \frac{E_{\theta}}{E_{\phi}} = \frac{S\lambda}{2\pi A} = \frac{2S\lambda}{\pi^2 D^2} = \frac{2S\lambda}{C\lambda^2} \quad (38)$$

Where:

C: it is the circumference

S_{λ} : spacing between turns in wavelengths

The three special cases pertaining to the NMHA polarization sense are given as follows:

- 1) $E_{\phi} = 0$ Linear Vertical Polarization
- 2) $E_{\theta} = 0$ Linear Horizontal Polarization
- 3) $E_{\phi} = E_{\theta}$ Circular Polarization

Wheeler's relation for circular polarization is given by Eq. 39:

$$C_{\lambda} = \sqrt{2S_{\lambda}} \quad (39)$$

Thus, for vertically polarized reception, the normal mode helical antenna (figure 106) is investigated in order to determine whether it can be utilized as an individual element of the phased array. Since in this application a small-sized vertically polarized antenna is required, the most important benefit of the NMHA over the Hertzian dipole or the monopole is its much higher radiation resistance relative to that of a straight conductor of the same size, as discussed in the next chapter.

4.7. Real Conditions measurements of the NMHA

An NMHA depicted in Figure 102 was constructed as a part of this study in order to test its performance in real conditions and compare it with that of the quarter-wavelength monopole, the construction details of which are discussed in the next section.



Figure 102: The Normal Mode Helical Antenna (NMHA)

The three vital parameters of the NMHA under investigation are the radiation resistance, the VSWR response and the “Gain” at the operating frequency of the commercial band FM (88–108 MHz).

The construction details of the NMHA are given below:

Diameter = 3.3 cm (0.01λ)

N = 9 turns

S = 4 mm

Height = 4 cm (0.013λ)

Wire Diameter = 2 mm

In order to determine the Axial Ratio (AR) of the antenna, Equation 40 can be used:

$$AR = \frac{E\theta}{E\phi} = \frac{S\lambda}{2\pi A} \frac{2S\lambda}{\pi^2 D^2} = \frac{2S\lambda}{C\lambda^2} \quad (40)$$

$$\rightarrow \frac{2 \times 4 \times 3000}{33^2 \pi^2} = 2.23$$

The radiation resistance (the real part of the impedance) is illustrated in Figure 103. As can be seen from the graph, at 93 MHz, the radiation resistance is close to 50Ω . At other frequencies within the Band II, the radiation resistance becomes very low; thus, the antenna has a very narrow band response.

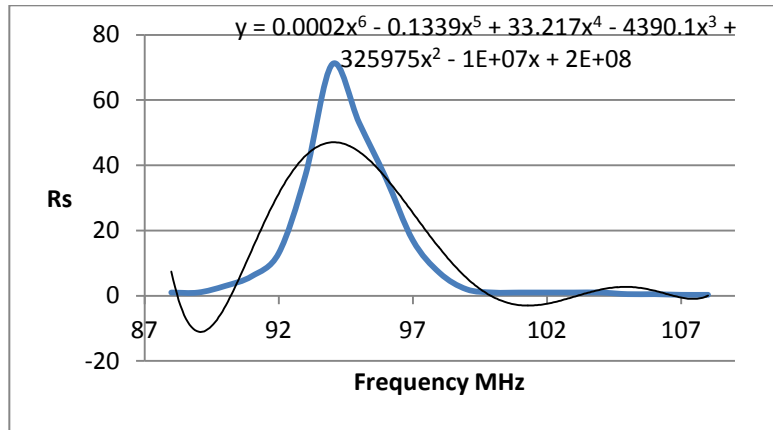


Figure 103: The radiation resistance of the NMHA

This is further illustrated by the VSWR response curve shown in Figure 104, which takes into account the imaginary part of the impedance.

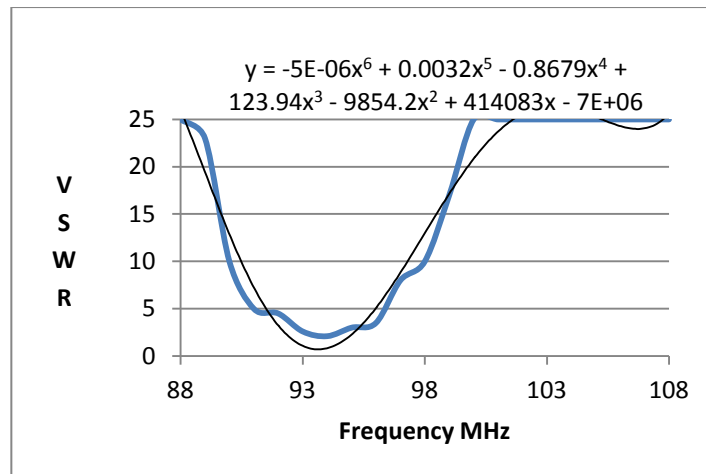


Figure 104: The VSWR response of the NMHA

According to the graph shown in Figure 104, the VSWR response of the NMHA makes it usable in the 90–96 MHz range, equivalent to 5:1 VSWR. Moreover, as the VSWR response exceeds 25:1 in the beginning and at the end of the Band II, the antenna cannot be used for broadband applications. The poor VSWR response of the NMHA also affects the gain response, examined below.

4.8. The Quarter-wavelength Monopole versus the NMHA

The “Gain” of the given NMHA relative to the quarter-wavelength monopole must be determined, as monopole whip antennae are presently used by almost all commercial receivers. In order to accomplish this, a monopole antenna was constructed using the same

wire diameter as that for the NMHA (2 mm width and 80 cm height). The response of the quarter-wavelength dipole versus the NMHA is discussed below.

The quarter-wavelength monopole's radiation resistance response, when mounted above the ground plane, is illustrated in Figure 105, while the VSWR curve is shown in Figure 106 below.

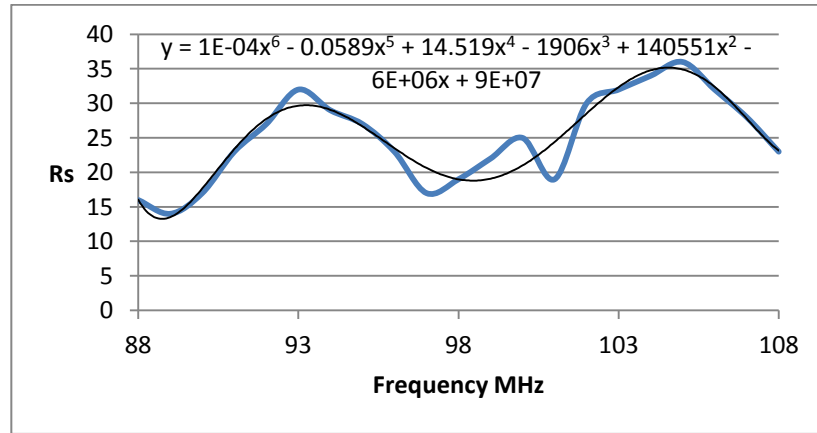


Figure 105: The radiation resistance of the quarter-wavelength monopole antenna

According to figure 105, the radiation resistance of the quarter-wavelength monopole antenna across the commercial FM band (87.5–108 MHz) is in the 13–36 Ω range. As shown in figure 105, the radiation resistance of the monopole is much flatter than that of the NMHA across the entire band. As a result, the maximum VSWR response does not exceed 3.5:1, compared to 25:1 for the NMHA, at the beginning and the end of the Band II, as discussed previously. The VSWR response of the monopole is illustrated in Figure 106.

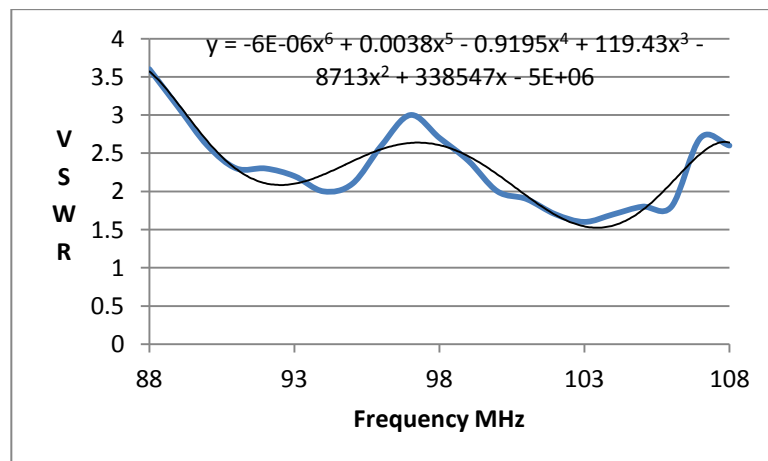


Figure 106: The VSWR response of the monopole antenna

Thus, the reception performance of the quarter-wavelength monopole versus the NMHA is investigated in the following chapter.

4.9. The Gain of the NMHA versus that of the Quarter-wavelength Monopole Antenna

The reception performance of the NMHA in real conditions versus a quarter-wavelength vertically polarized monopole antenna is presented in Table 10 and Figure 107. In order to perform the test, each antenna was mounted at the same point on a ground plane and the results were obtained via the Rover DL1 spectrum analyzer. According to the data reported in Table 10, the NMHA has an average gain of -4.7 dB relative to that of the quarter-wavelength monopole.

Frequency (MHz)	Helix (dBuV)	Monopole (dBuV)	ΔG (dBuV)
88.2	28	35	7
93.3	34	37	3
94.8	33	35	2
98.6	38	40	2
103.7	45	50	5
104.3	34	41	7
105.6	31	38	7
107.6	28	33	5
Min	28	33	2
Max	45	50	7
Average	34.4	39.2	4.7

Table 10: Field strength of the NMHA and the monopole

The gain difference ranged from -2 dB to -7 dB. The poor NMHA performance is attributed to the high VSWR response, as previously discussed.

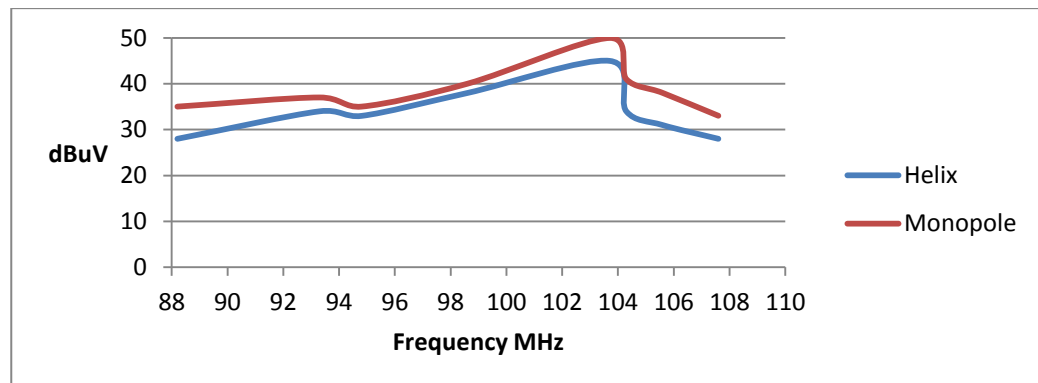


Figure 107: The field strength intensity of the NMHA versus the monopole

4.10. Optimization of the Normal Mode Helical Antenna

According to the previous measurements pertaining to the NMHA, it can be ascertained that its performance is limited due to the very high VSWR response across Band II. As a result, the antenna cannot be used as an individual array element unless this problem is eliminated by investigating a new method of optimizing the VSWR. Thus, a modified NMHA was designed, and its characteristics and implementation are presented in this section. The new antenna consists of two sections. It is a planar helix in series with a wire-wound helix, as illustrated in Figure 108. The modified NMHA's response relative to that of an unmodified helix in terms of bandwidth and gain was also investigated. For the purpose of this investigation, the planar helix was constructed on a PCB using FR-4 substrate. Its longest side was only 5 cm in length. It also comprised of a coil consisting of 5 turns, with line width of 1.5 mm and line spacing of 2 mm. The specifications of the NMHA are presented below:

- 1) $N = 26$ turns
- 2) Diameter = 10 mm (0.003λ)
- 3) Wire Diameter = 2mm
- 4) Height = 105 mm (0.035λ)

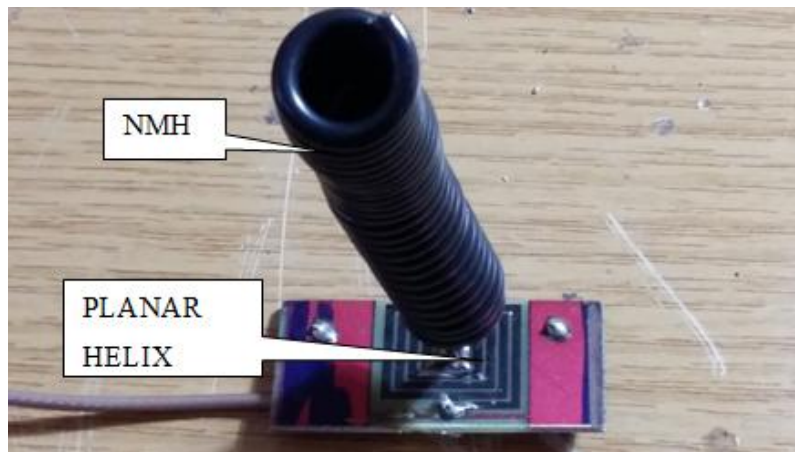


Figure 108: The NMHA mounted in series with the planar helix

The VSWR response of the modified helix is illustrated in Figure 109, which indicates its superior performance compared to that of the previously discussed unmodified helix. Particularly, the maximum VSWR of the modified helix was measured at 7:1, compared to 25:1 obtained for the unmodified helix. In order to confirm the improved performance of the modified helix, field strength measurements were carried out and the findings were

compared to those pertaining to the unmodified helix of the same specifications. The results are illustrated in Table 11.

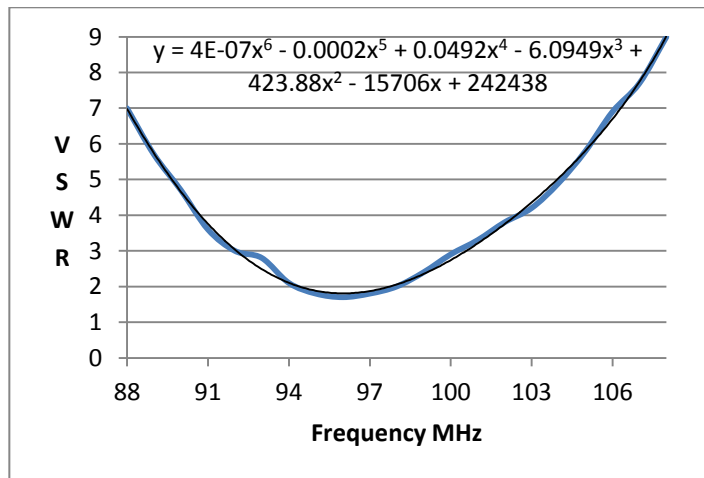


Figure 109: The VSWR response of the modified helix

Frequency (MHz)	Modified (dBuV)	Unmodified (dBuV)
88.2	32	22
93.3	38	28
94.8	33	22
98.6	40	38
103.7	48	43
104.3	38	34
105.6	37	34
107.6	33	33
Average	37.375	31.75
Max	48	43
Min	32	22

Table 11: The field strength intensity of the modified and unmodified helix

According to the data reported in Table 11, the modified helix has approximately 6 dB better performance across the 87.5–108 MHz band relative to the unmodified one.

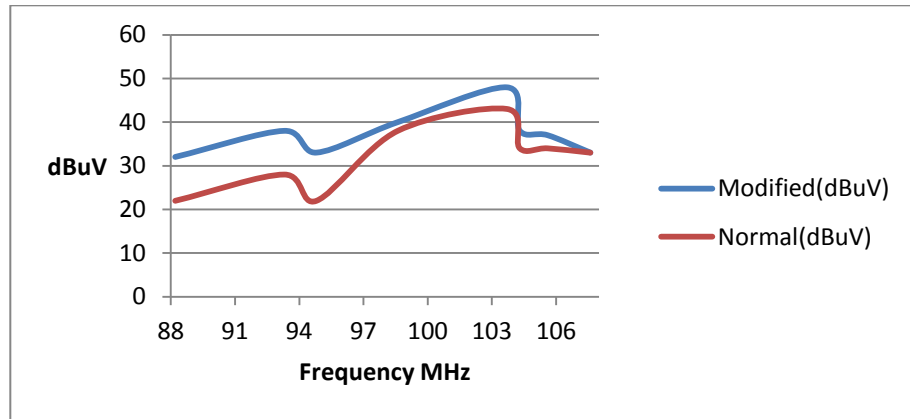


Figure 110: The field strength intensity of the modified and unmodified helix

Despite the improved performance of the modified helix, it is still affected by the issue of unacceptably large dimensions for this application. Hence, to mitigate this problem, a new modified helix with lower height was constructed. In order to compensate for the small height, 13 turns have been incorporated into the new design in the form of a printed helix. Its construction details and performance are discussed below.

4.11. The Final Design of the NMHA

This section is dedicated to the discussion of the performance of the new modified NMHA, which was constructed with smallest physical dimensions possible in order to be used as the individual element of the phase array, discussed in the next chapter. The modified NMHA is shown in Figure 111. As can be seen from the image, the antenna consists of two sections—a planar printed helix and a NMHA mounted in series with the printed planar helix, constructed on a PCB Fr-4 substrate material. The longest turn's side dimension of the planar helix is 80 mm and the total number of turns is 13, as noted above.



Figure 111: The modified NMHA

The NMHA's construction details are given below:

1. Diameter = 33 mm (0.011 λ)
2. N = 5 turns
3. Height: = 50 mm (0.01 λ)
4. Wire Diameter = 3 mm
5. Space = 4 mm

The modified NMHA incorporates 5 turns, allowing it to resonate at 101 MHz. Its height is 5 cm (0.01 λ) and its diameter is 3.3 cm. The the new modified NMHA's VSWR response in the 87.5–110 MHz range is presented in Figure 112. According to the experiments performed, the advantage of this topology stems from eliminating the need for a complex matching network, as only a simple 50 Ω quarter-wavelength transformer is required. According to the graph shown in Figure 112, performance of the new modified NMHA is superior to that of both the modified NMHA and the unmodified NMHA discussed in the previous sections. The maximum VSWR in the 87–110 MHz range does not exceed 5:1, whereas the average VSWR value is only 2.3:1.

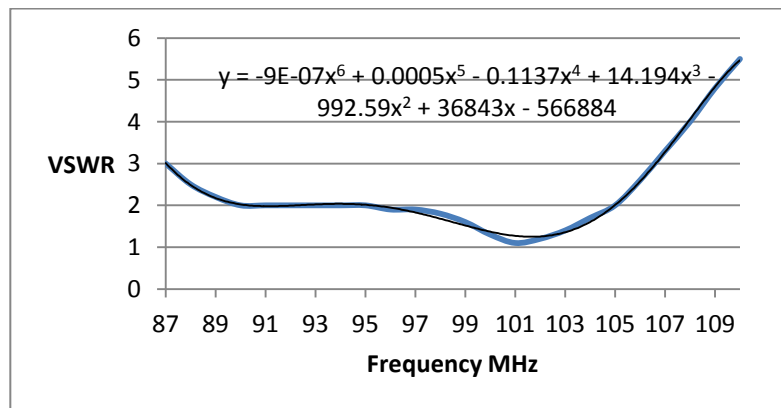


Figure 112: The VSWR response of the modified NMHA

In order to further confirm the superior performance of the new antenna, real conditions measurements were conducted with “on air” existing radio services and the results are reported in Table 12.

Frequency	Field Strength
88.2	34
93.3	39
94.8	39
98.6	45
103.7	60
104.3	46
105.6	45
107.6	39
Minimum	34
Maximum	60
Average	44.1

Table 12: Real conditions field strength measurements of the modified NMHA

According to the data presented in Table 12, the new modified NMHA enables an average field strength intensity of 44.1 dBuV across Band II, which exceeds the performance of all previously tested antennas.

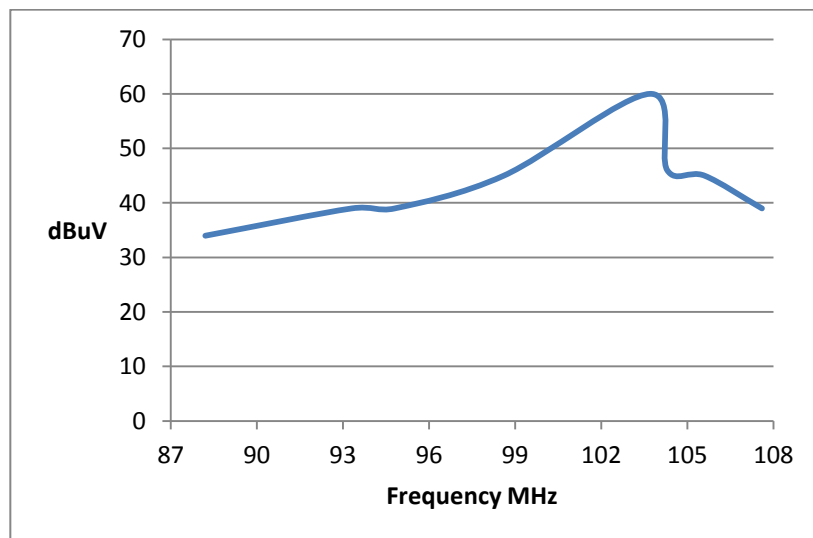


Figure 113: Real conditions field strength measurements of the modified NMHA

In this respect, the new modified NMHA antenna presented in this section, despite having the smallest permissible physical size, has been confirmed to exhibit the greatest efficiency

when compared to all other antennas examined in this work. As a result, its physical size, as well as its performance, fulfils the criteria for use as the individual element of the phased arrays, discussed in the next section.

4.12. Uniform Linear Arrays

One-dimensional linear phased arrays, also known as collinear arrays, are driven elements whose axes are located on a single straight line. The radiation pattern of a collinear array depends on the number of elements, the spacing, the phase and amplitude between the elements, and the radiation pattern of the individual elements under the condition that all elements are identical. When the array consists of equidistant identical elements aligned along the straight line, it is referred to as a uniform linear array. For example, a three-element uniform linear array with an element separation d and at the plane meeting the condition $\Theta = \pi/2$ is illustrated in Figure 114.

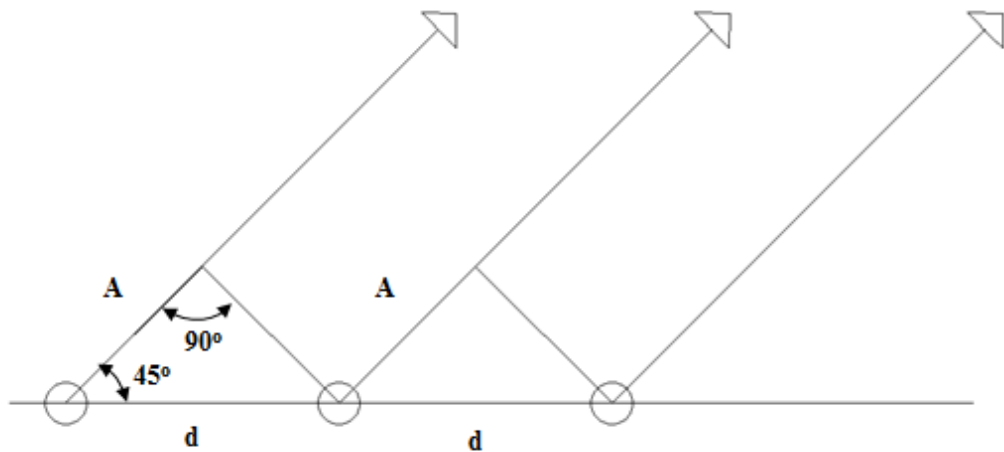


Figure 114: A three-element uniform antenna array with an element separation d and at the plane meeting the $\Theta = \pi/2$ criterion

According to Kraus, the maximum value of the electric field ‘E’ can be calculated using Equation 41 below:

$$E = \frac{1}{n} \frac{\sin\left(\frac{n\psi}{2}\right)}{\sin\left(\frac{\psi}{2}\right)} \quad (41)$$

where $\psi = \beta \cdot d \cdot \cos(\Phi) + \Delta$

In this respect, the maximum value of E in terms of the angle Φ is given as follows:

$$\Phi_{\max} = \cos^{-1} \left[\frac{\lambda}{2\pi d} (-\Delta \pm 2m\pi) \right]$$

where $\pm m\pi = 0.5 (\beta d \cos(\Phi) + \Delta) = 0.5\psi$

According to the above analysis, when the spacing between the adjacent arrays is $\leq \lambda$, no grating lobes can be formed for any value of the excitation phase Δ .

On the other hand, when the spacing between the arrays is $\geq \lambda$, grating lobes are formed for any value of the excitation phase Δ . Finally, when the spacing between the individual elements lies between $\lambda/2$ and λ , the formation of grating lobes depends strictly on the excitation phase β . The angles of null of the array factor occur based on Eq. 42 below:

$$\Phi_{\text{null}} = \cos^{-1} \left[\frac{\lambda}{2\pi d} \left(-\Delta \pm \frac{2n}{N} \pi \right) \right] \quad (42)$$

Although uniform arrays can be used for scanning for certain angles, equation 42 indicates that a closely spaced one-dimensional linear array will not provide the desired radiation pattern in all directions, as well as the desired null towards the interference, unless is rotated mechanically. In order to demonstrate this visually, the radiation pattern of a 0.2λ isotropic array is plotted for $\theta = \pi/2$. The two isotropic sources presented in circular form are illustrated in Figure 115.

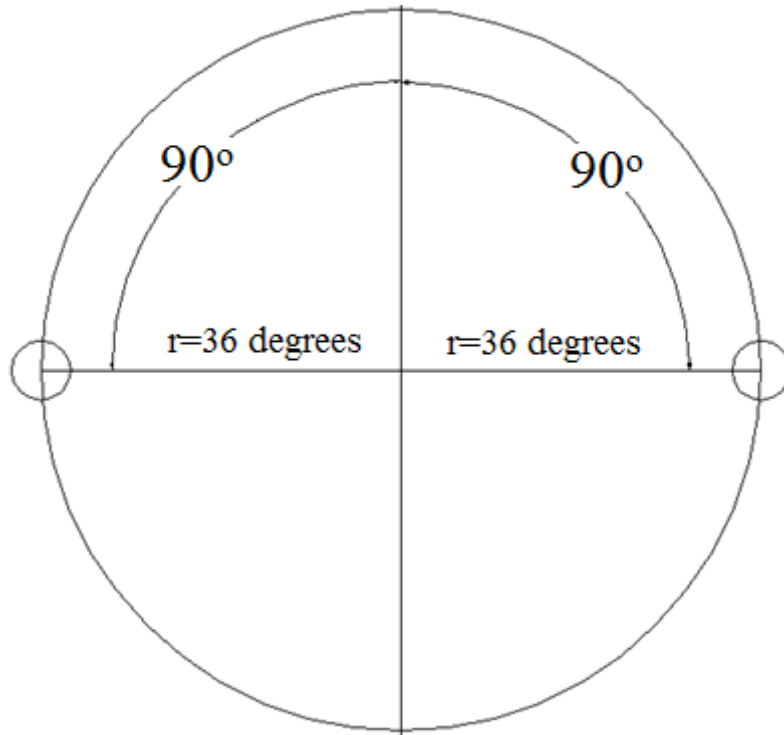


Figure 115: Two-element phased array

Using trigonometry, the path difference between the two elements can be obtained via

Eq. 43 below:

$$2 * \text{Radius} \cdot \sin(\theta/2) \cdot \sin(\Phi - \theta/2 - \alpha) \quad (43)$$

where θ is the angle between the individual element and the reference, α is the angle between the x axes and the reference and Φ is the angle of radiation. Applying Equation 43 results, Equation 44 is obtained:

$$\Delta\Phi = 72 \cdot \sin 90 \cdot \sin(\Phi - 90) - \Delta = 72 \cdot \sin(\Phi - 90) - \Delta \quad (44)$$

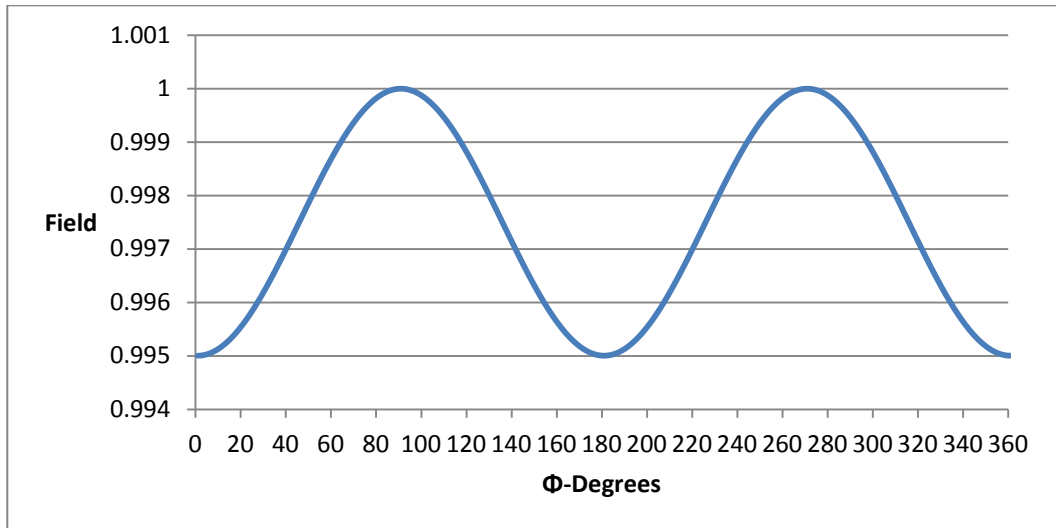


Figure 116: Radiation pattern of two-element phased array

The radiation pattern of the array with zero excitation phase is illustrated in Figure 116. As can be seen, the main lobe's maximum radiation is at 90 and 270 degrees. In order to create a null at the opposite direction of the main beam, the excitation phase must be equal to $2 \times 0.1\lambda$, i.e. 108° . In this case, the radiation pattern is illustrated in Figure 117.

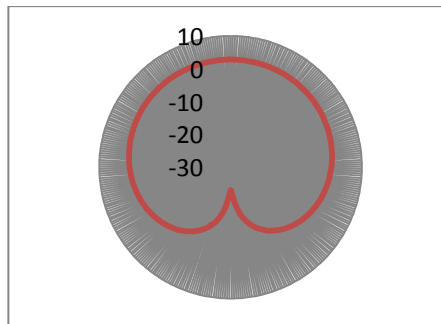


Figure 117: The radiation pattern of two-element phased array with the excitation phase of 108°

The radiation pattern in figure has a null at -90° . By switching the phase between the individual elements, the null will reverse at 0° . However, the two-element isotropic array, as a broad-side array, will not be able to create a null in any other direction without mechanical control.

4.13. Application of Circular Arrays

Circular arrays, as demonstrated in the previous analysis, are one-dimensional linear arrays in a circular form. The major advantage of circular arrays relative to linear arrays stems from their ability to scan horizontally across the entire 360° without distortion near the end-fire direction (Davies and Rizk, 1977). Therefore, circular arrays present the ideal topology for this application and will be investigated in detail in this section. Another great advantage of circular arrays is that the mutual coupling affects all individual elements of the array with equal density. Therefore, eliminating it is easier than in any other topology (Hon Tat Hui, 2007). The geometry of circular arrays is illustrated in Figure 118 below. The array factor of circular arrays is the sum of the far-field intensity of every individual element of the array and is given by Eq. 45 (Hon Tat Hui, 2007):

$$\sum_{n=1}^N I_n \cdot e^{j[\beta a \sin\theta \cos(\Phi - \Phi_n) + \Delta n]} \quad (45)$$

Where B_n is the excitation phase of every individual element (in this application, the modified helix antenna).

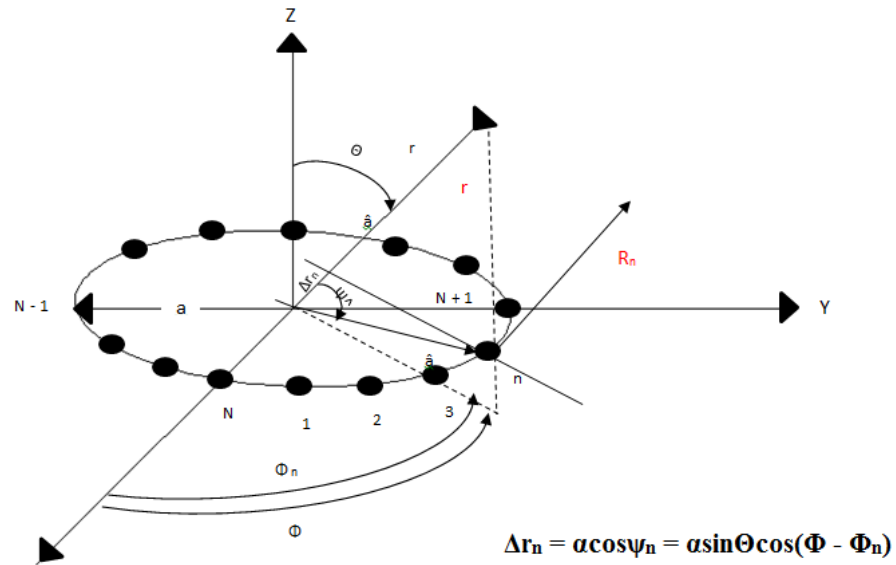


Figure 118: The circular array geometry

The maximum radiation angle ($\Theta_{\max}, \Phi_{\max}$) can be achieved based on Eq.46, 47, and 48:

$$\beta a \sin(\Theta_{\max}) \cos(\Phi_{\max} - \frac{2\pi}{N}) + B_1 = \pm 2q\pi \quad (46)$$

$$\beta a \sin(\Theta_{\max}) \cos(\Phi_{\max} - \frac{4\pi}{N}) + B_2 = \pm 2q\pi \quad (47)$$

$$\beta\alpha\sin(\Theta_{\max})\cos(\Phi_{\max}-2\pi) + B_N = \pm 2q\pi \quad (48)$$

Where $q = 1, 2, 3$

The maximum radiation direction in terms of the excitation phase is given by Eq. 49 below:

$$B_N = + 2q\pi - \beta\alpha\sin(\Theta_{\max}) \cos(\Phi_{\max} - \frac{2\pi n}{N}) \quad n = 1, 2, 3 \quad (49)$$

4.14. The Smart Antenna Design

Based on the preceding discussions, the performance of a four-element circular array, illustrated in Figure 119, is analyzed to ensure that it operates effectively in the 87.5–108 MHz range.

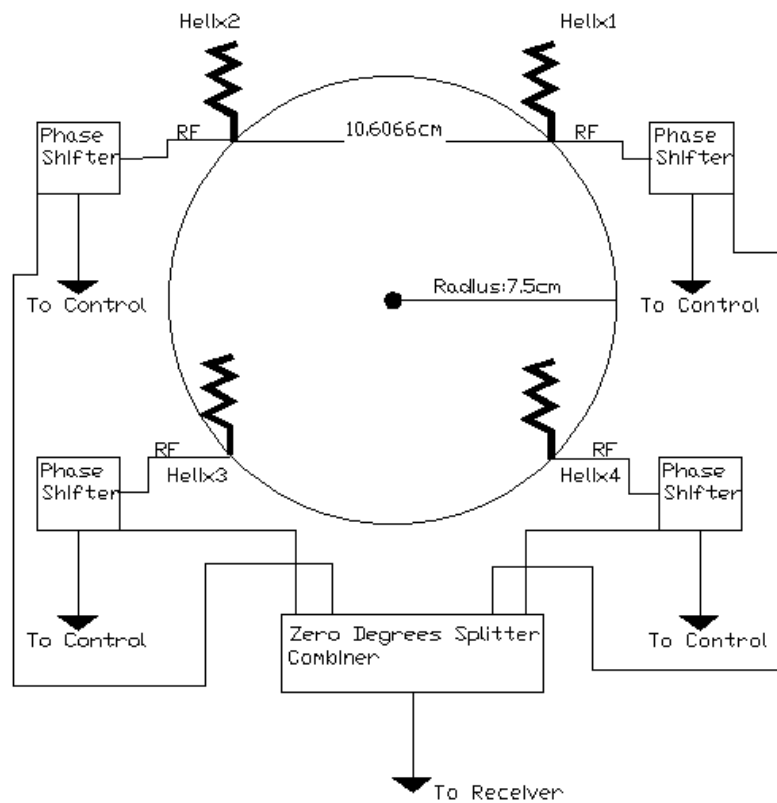


Figure 119: The circular array design

The circular array shown above comprises of four modified normal mode helical antennae discussed in the previous section. The antennae are mounted at a 90° distance. The phase of every individual helical antenna is controlled by an electronic phase shifter (Mini-Circuits JSPHS-150+) in order to create the desired radiation pattern in a given direction. The radius of the circle is 7.5 cm, which corresponds to 0.025λ . In this respect, the radiation pattern of the four-element circular array in the end-fire direction will be

analyzed below, according to the phase shift of every individual element. The weights are presented in Tables 13-16.

Antennas	Phase (degrees)
Helix1	0
Helix2	167
Helix3	167
Helix4	0

Table 13: The weights of the circular array at 270°

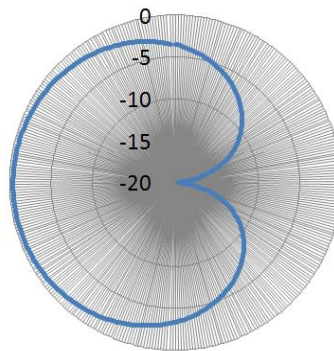


Figure 120: Cardioid radiation pattern of the four-element circular array at 270° HPBW = 90°

Antennas	Phase (degrees)
Helix1	167
Helix2	167
Helix3	0
Helix4	0

Table 14: The weights of the circular array at 90°

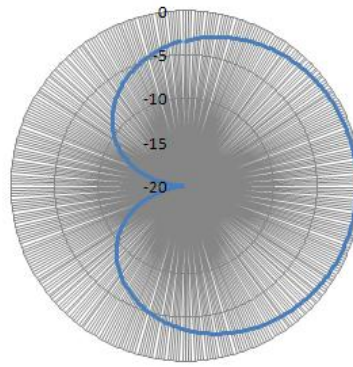


Figure 121: Cardioid radiation pattern of the four-element circular array at 90° , HPBW = 90°

Antennas	Phase (degrees)
Helix1	0
Helix2	0
Helix3	167
Helix4	167

Table 15: The weights of the circular array at 180°

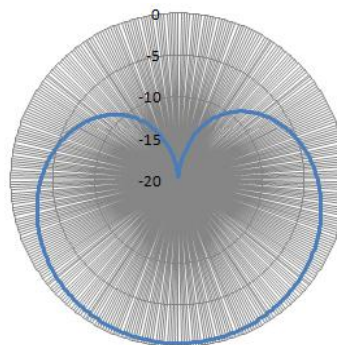


Figure 122: Cardioid radiation pattern of the four-element circular array at 180° , HPBW = 90°

Antennas	Phase (degrees)
Helix1	167
Helix2	0
Helix3	0
Helix4	167

Table 16: The weights of the circular array at 0°

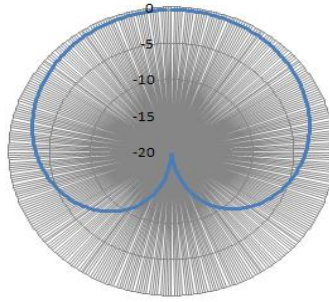


Figure 123: Cardioid radiation pattern of the four-element circular array at 0° , HPBW = 90°

4.15. Final Construction and Assessment of the Smart Antenna

The circular array has been constructed based on the NMHA discussed in section 3.11. The array consists of four NMHA, constructed on an FR-4 PCB, according to Figure 111, while the array is shown in Figure 124. In order to evaluate the array performance, the VSWR (caused by the mutual coupling between the elements and compensated for by rotating the helix) was first minimized for every individual helix.



Figure 124: Four-element circular array

In the next step, a simple zero-degree four-port Wilkinson splitter was constructed, as illustrated in Figure 125. The isolation between the ports of the splitter is important, as unequal splitting will affect the array radiation pattern, as the amplitude at every helix will

be different. To mitigate this issue, the splitter was terminated with 50-Ω load before verifying that it splits with equal amplitude to all ports before connecting it to the array. The VSWR of the splitter did not exceed the 1.5:1 across Band II, precluding the addition of the second section.

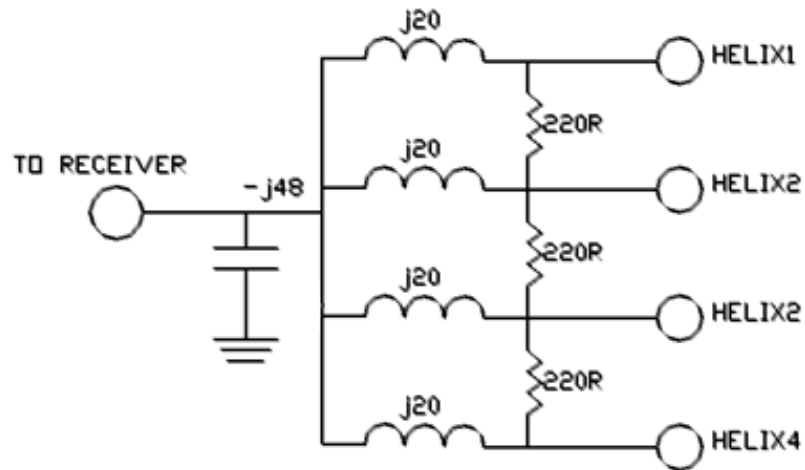


Figure 125: Four-port zero-degree splitter

Before testing the four-element circular array, the performance of a typical telescopic whip antenna of 53 cm length was tested in terms of the local radio services. This evaluation provided a reliable reference value of the field strength intensity for later comparison with the performance of the four-element circular array. The test was performed using the spectrum analyzer ROVER-DL1, as illustrated in Figure 126.



Figure 126: The quarter-wavelength monopole under test

In order to perform the test, a local radio service broadcasted at 93.3 MHz from the northern part of Limassol was selected. The telescopic whip antenna was calibrated to provide the maximum field strength at 93.3 MHz, which is 35.5 dBuV as illustrated in Figure 127.

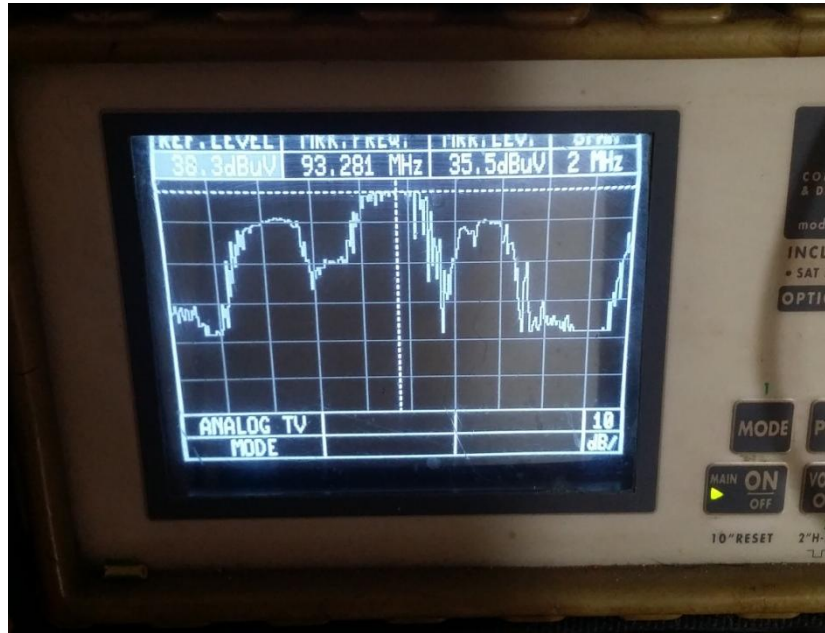


Figure 127: The reception of the quarter-wavelength monopole antenna

After measuring the field of the whip telescopic antenna, the circular array was tested in terms of gain and front to back ratio at a fixed phase, as illustrated in Table 17.

Antennae	Phase (degrees)
Helix1	0
Helix2	0
Helix3	167
Helix4	167

Table 17: The phase arrangement

The aim of this test was to ensure that the array is capable of satisfactory performance in terms of ‘Gain’ and can create null towards all desired directions. This test should be performed in order to verify the array’s response before connecting it to the voltage controlled phase shifters and the control circuit. The phase shift among the individual helixes is illustrated in Table 17. It has been arranged by settling the length of the coaxial cable RG-316 at every individual helix of the array. The array under investigation is illustrated in Figure 128.

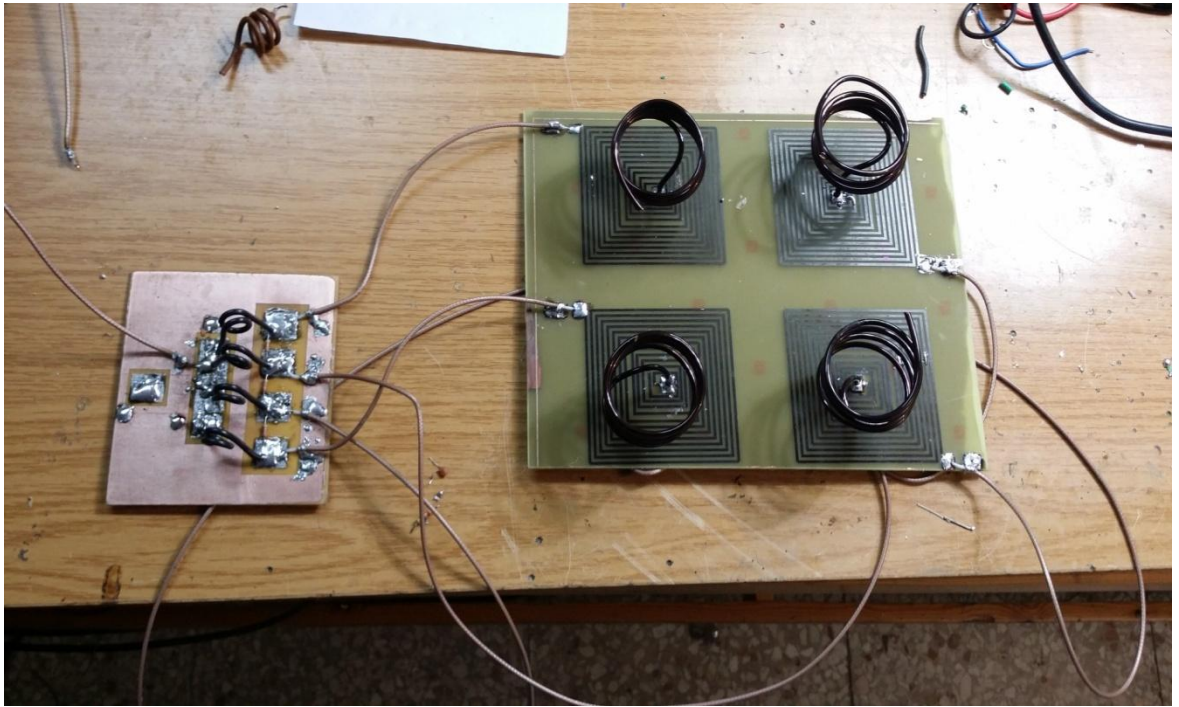


Figure 128: The circular Array under test

The gain of the four-element circular array relative to the performance of the whip telescopic antenna was evaluated by primarily steering manually the array towards the direction of the maximum radiation of the incident waves monitored via the spectrum analyzer shown in Figure 129. The monitored radio services are three local channels utilizing 91.6 MHz, 93.3 MHz, and 93.7 MHz frequencies. All monitored radio services are broadcasting from the same direction. The spectrum analyzer readings were obtained by connecting the input of the four-port Wilkinson splitter to the input of the spectrum analyzer ROVER-DL1. The maximum radiation is illustrated in Figure 129, which reveals the field strength of 93.3MHz is 33.7 dBuV versus 33.5 dBuV obtained for the whip telescopic antenna. As a result, the gain of the four-element array in Band II is very satisfactory. The next highly important test performed as a part of this work aimed to determine the null, created by the arranged phase shift by rotating the array by 180° in the opposite direction of the transmitting point. As a result of this adjustment, the field strength of the strongest radio service (which is 33.7 dBuV) declined to 9.9 dBuV, as illustrated in Figure 130. It is important to note that the field strength of the other two adjacent channels (91.6 MHz and 93.7 MHz, illustrated in the spectrum analyzer in Figure 129), broadcasting from the same transmitting point, was also reduced significantly. As a result, it can be asserted that the four-element circular array has enabled a reduction in gain of around 24 dB in the opposite direction of the transmitting point, which complies with the radiation patterns discussed in the previous section.

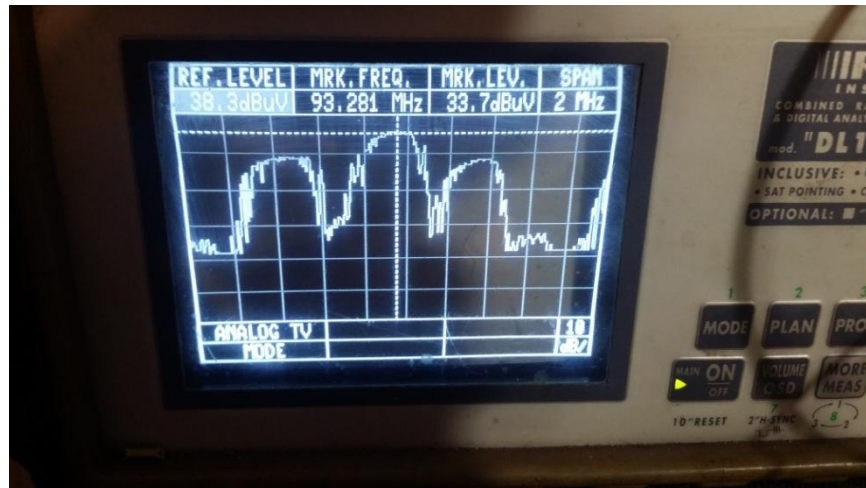


Figure 129: Monitoring “on air” radio services using the circular array

According to the graph shown in Figure 130, field strength of the remaining two radio services has been reduced by 20 dB.

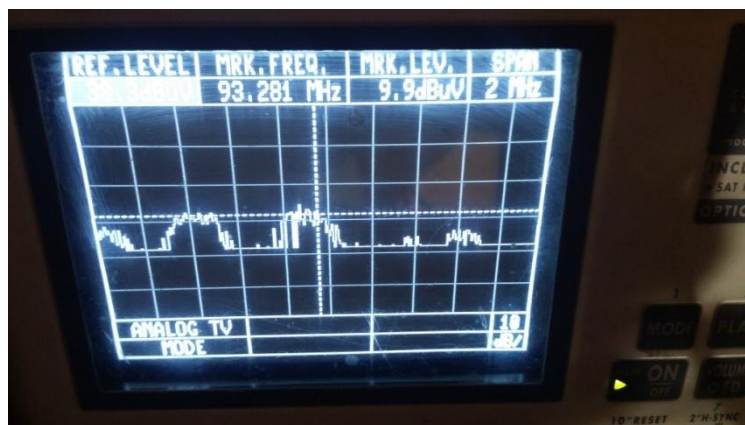


Figure 130: The spectrum analyzer readings of the null

Based on the findings noted above, it can be stated with certainty that the antenna is capable of rejecting signals arriving from undesired directions and operates as intended. The antenna was further tested at the upper frequencies of Band II and similar results were obtained. The next section discusses the interface of the smart antenna with a typical commercial receiver, which automatically steers the main beam towards the desired direction.

4.16. Interface between the Array and a Dedicated Commercial Receiver

In order to meet the study objectives, the circular array designed, implemented and tested as a part of this project must be interfaced with a commercial receiver. However, no commercial receiver that can be readily connected to the smart antenna is presently available. As a result, a dedicated commercial receiver must be constructed in order to provide the appropriate infrastructure. More specifically, the design must incorporate a

control system capable of steering the array electronically in the direction of maximum density.

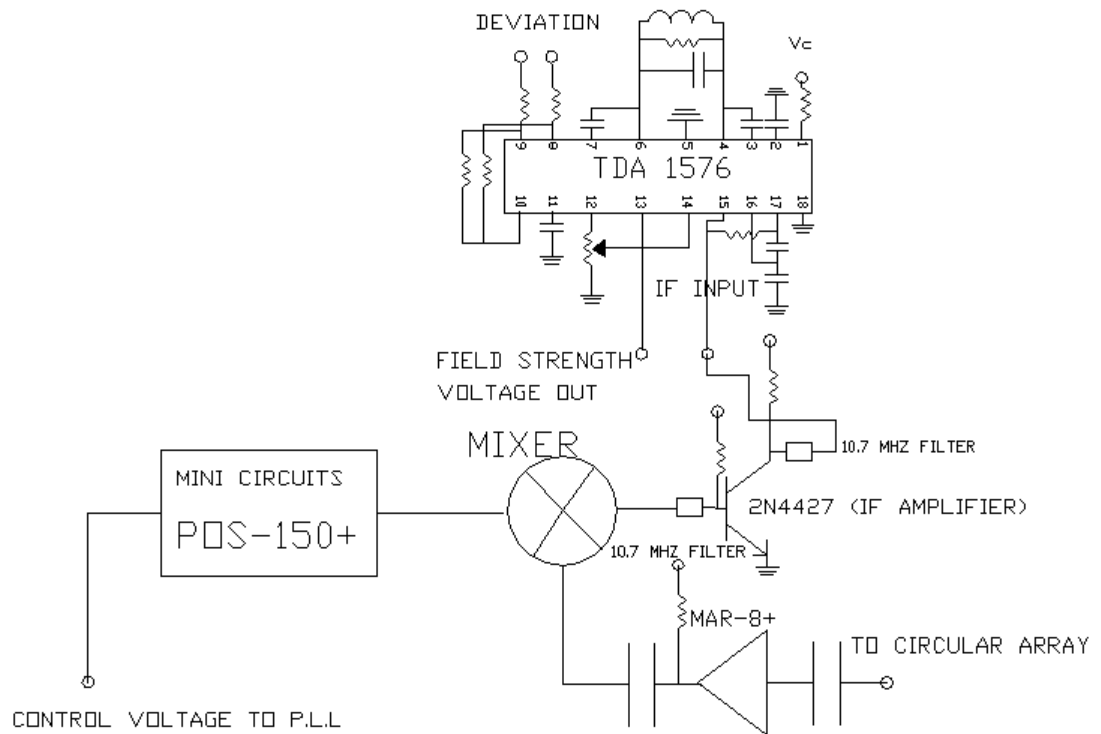


Figure 131: Receiver circuit diagram

This design goal can be achieved by utilizing the field strength voltage of the tuned signal detected by the receiver's demodulator circuitry illustrated in Figure 131. The output voltage can thus be interfaced with the control circuit, which is discussed later. In this case, the receiver was constructed around the TDA-1576, which is a typical FM demodulator that provides field strength voltage output at Pin 13. The schematic of the receiver-demodulator assembly is also illustrated in Figure 131, and the receiver circuit board is shown in Figure 132.



Figure 132: The receiver circuit board

The Mini Circuits MAR-8+ serves as a front-end amplifier that amplifies the signal of the circular array. It was selected because of its low cost, simplicity of its design, and a typical gain of 30 dB at 0.1 GHz. Thus, it improves the sensitivity of the receiver.

4.16.1. The Phase Locked Loop (PLL)

The tuned frequency of the receiver is determined by the Mini Curcuits POS-150+ that operates as a Voltage Controlled Oscillator (VCO) when mixed with the array's signal. The output of the mixer is filtered by two 10.7 MHz ceramic filters and is amplified via a common emitter transistor amplifier using the 2N 4427 in order to be connected at the demodulator's input. It provides a corner frequency of 150 KHz, in line with the FM broadcasting specifications. In order to avoid frequency drift caused by the free run oscillator, POS-150+, the frequency of the VCO was programmed by a typical single modulus pre-scaler phase-locked loop circuitry as illustrated in Figure 133.

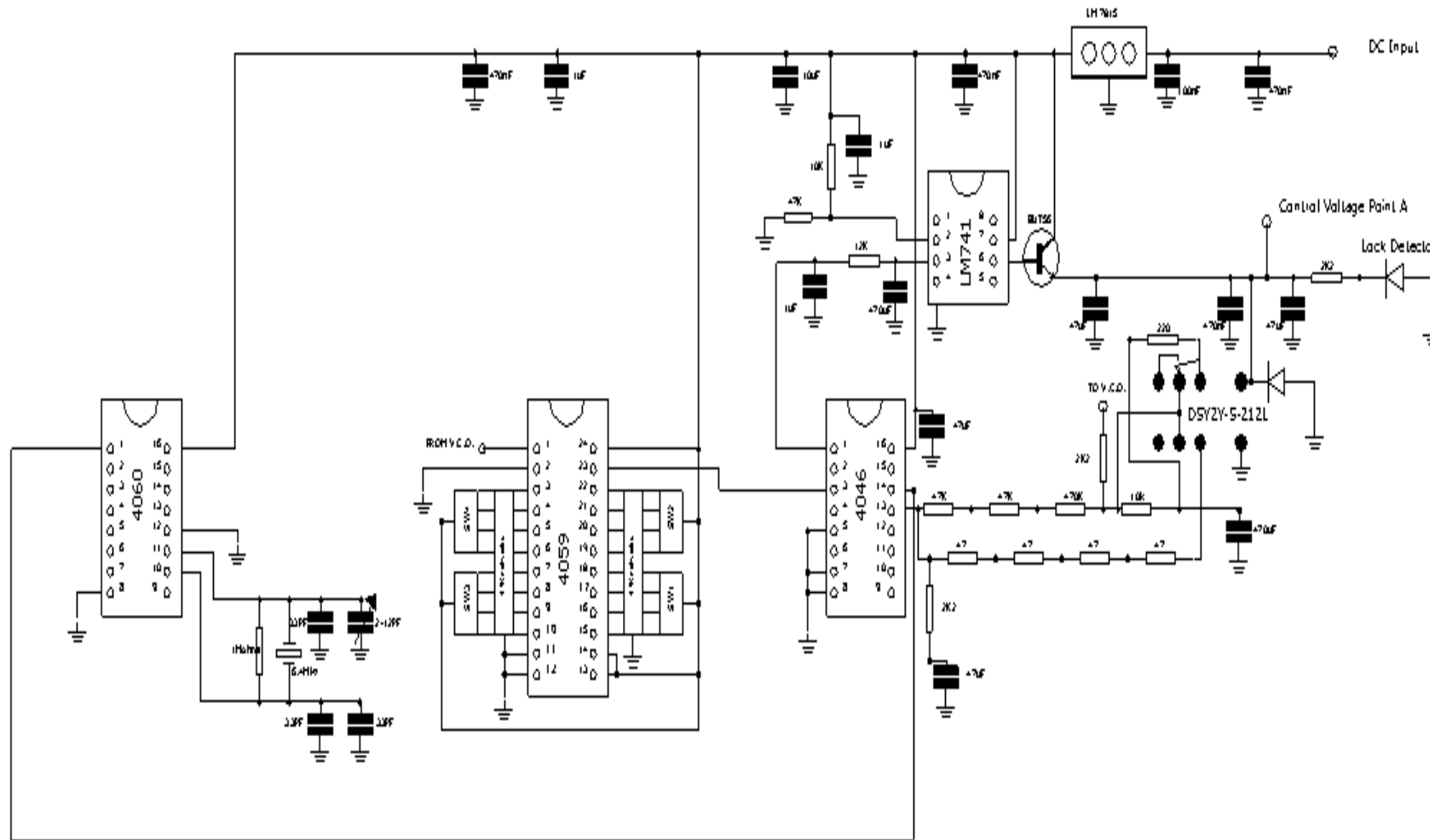


Figure 133: Circuit diagram of the phase-locked loop circuitry

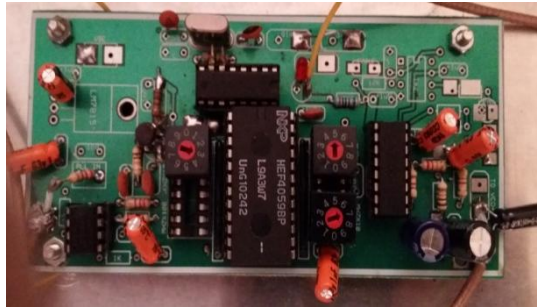


Figure 134: The PLL board

The PLL (Figure 134) was constructed by utilizing a few simple CMOS integrated circuits such as the CD 4046, which is a phase-locked loop circuit consisting of a linear VCO and two different phase comparators—the CD 4059 (a programmable divide by N counter) and the CD 4060 (an a14 stage ripple carry binary counter). In order to program the PLL with 100 KHz steps required in FM broadcasting, the reference frequency of the PLL was set at 390.625 Hz. This was achieved by dividing a 6.4 MHz crystal oscillator output by 2^{14} using the CD 4060 as a divider. The reference frequency was subsequently connected to the digital phase detector input of the CD 4046, at Pin 14. The second input of the phase detector is Pin 3 and was connected to the output of the CD 4059 in order to enable programming the receiver at the desired frequency by the use of rotary switches. In addition, the input of the CD 4059 was connected to a pre-scaler that divides the VCO frequency by 256. When the VCO frequency is equal to the reference frequency at the two inputs of the phase detector of the CD 4046 (i.e. both are 390.625 Hz), the system locks. When the system locks, Pin 1 becomes high and turns on a comparator, which has been constructed with the op-amp LM-741. The output of the comparator is important, as it is connected to the control circuitry described in the next page. The error voltage that tunes the varactors of the POS-150+ that operates as a VCO is the output of the phase detector at Pin 13. The error voltage is filtered by an RC low-pass filter with corner frequency of 0.03 Hz. The resulting graph is illustrated in Figure 135.

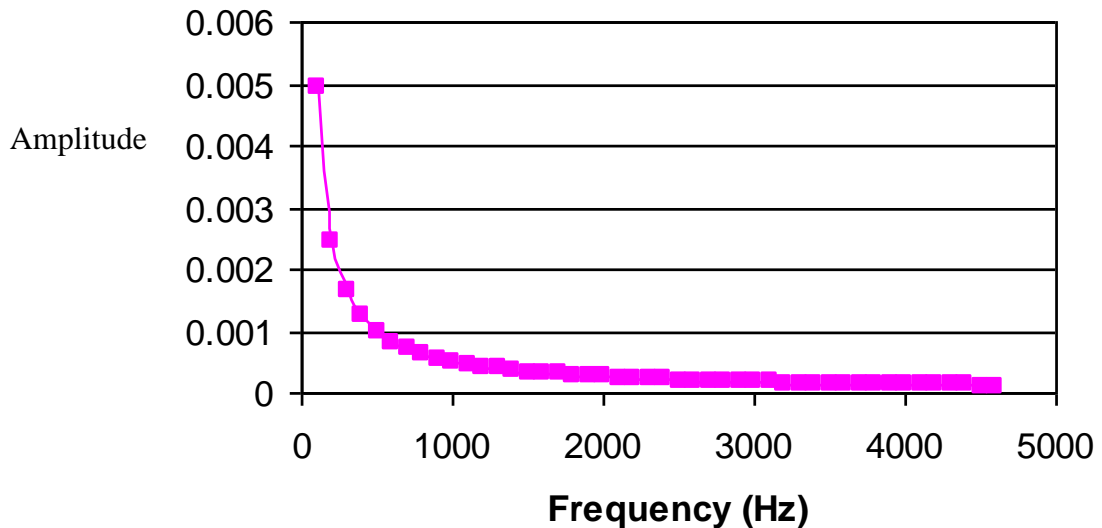


Figure 135: The PLL low-pass filter response

4.16.2. The Liquid Crystal Display (LCD) Monitor Circuit

In order to ensure that the smart antenna is steered in the desired direction, the receiver must display the tuned frequency, the field strength in dBuV, and the deviation in KHz using a four-character LCD. In this work, this was achieved by utilizing the monitor circuitry (illustrated in Figure 136) which drives a 16 × 4 character LCD. The circuit was designed around the Freescale 8-Bit HCS08 Central Processor Unit (CPU) M9SO8QG8. The circuit also employs a 16 MHz clock Colipitts oscillator and a CD 4060, which operates as a frequency divider. In order to display the tuned frequency, the signal from the PLL is amplified by a common emitter amplifier in order to be divided by 1024 by the CD 4060.

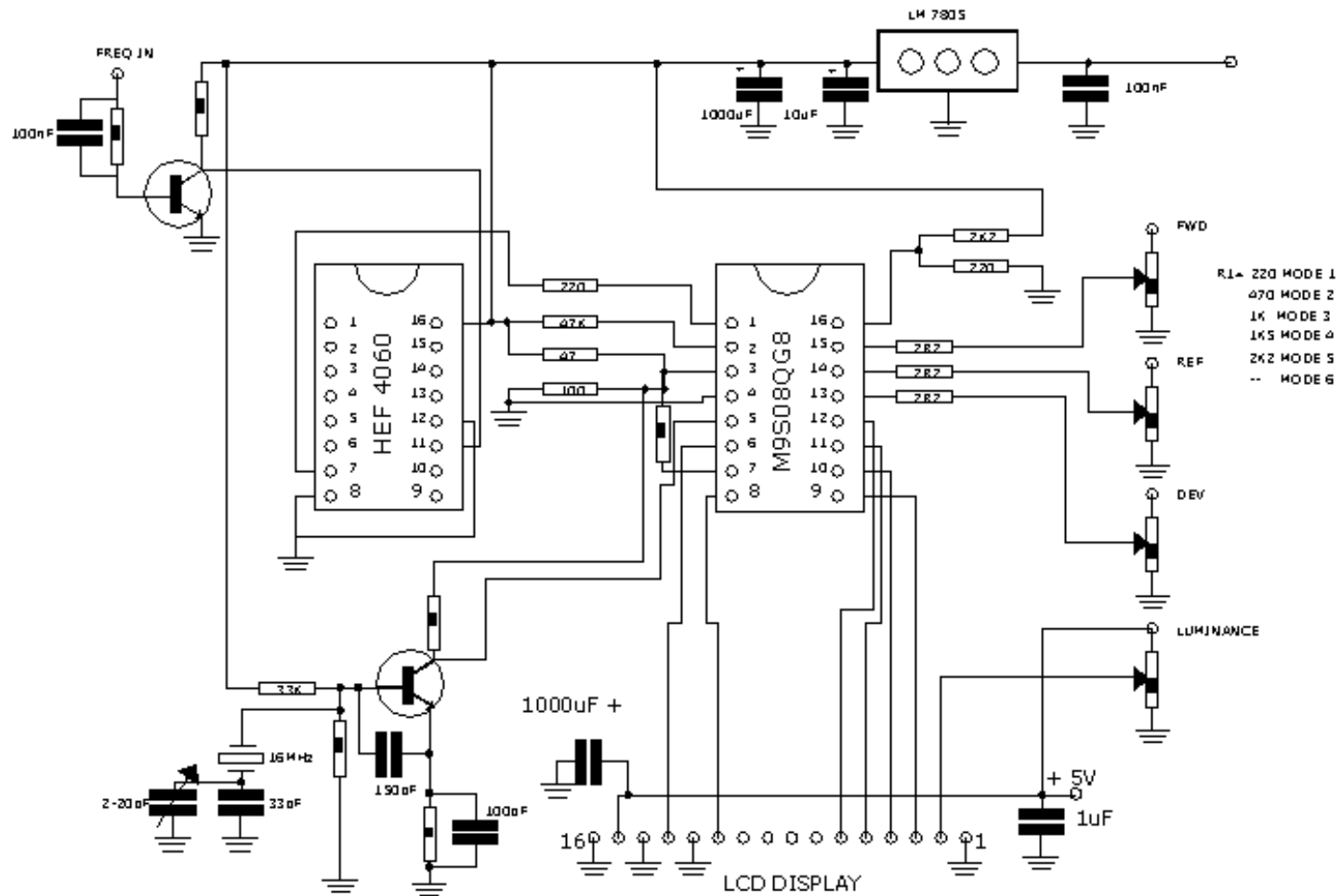


Figure 136: The monitor LCD circuit diagram


4.16.3. The Control Circuit

One of the most important parts in the receiver design is the control circuit because it is responsible for steering the array towards the direction of the maximum signal density based on the field strength of the tuned radio service, as illustrated in Figure 128. In order to ensure the proper phase shift in the array's individual helix, the Mini Circuits phase shifters JSPHS-150+ have been selected for this study, as they operate in Band II, as illustrated in Figure 137.

Narrow Band Phase Shifter

50Ω 180° Voltage Variable 100 to 150 MHz

JSPHS-150+



CASE STYLE: BK276

Maximum Ratings

Operating Temperature	-40°C to 85°C
Storage Temperature	-55°C to 100°C
RF Input Power	20 dBm max.
Control Voltage	20V

Permanent damage may occur if any of these limits are exceeded.

Pin Connections

IN	14
OUT	8
BIAS	1,7 [^]
GROUND	2,3,4,5,6,9,10,11,12,13

[^] proper operation is achieved with pins 1 or 7 or both connected to BIAS.

Features

- low insertion loss, 1.0 dB typ.
- good VSWR, 1.3 typ.
- solder-plated J-leads for excellent solderability and strain relief
- aqueous washable

Applications

- aircraft communication
- delay for feed-forward amplifier

+RoHS Compliant

The +Suffix identifies RoHS Compliance. See our web site for RoHS Compliance methodologies and qualifications

Phase Shifter Electrical Specifications

FREQUENCY (MHz)	PHASE RANGE (Degrees)	INSERTION LOSS (dB)		CONTROL VOLTAGE (V)	CONTROL BANDWIDTH (kHz)	VSWR (:1)	
		Min.	Typ. Max.			Typ.	Max.
100-150	180	1.2	2.5	0-12	DC-30	1.2	1.7

Maximum operating power, 0 dBm
DC input resistance at Control port: 5900 ohms typ.

Outline Drawing

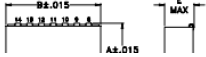


Figure 137: The JSPHS-150+ data sheet

Because the phase shifter JSPHS-150+ is a voltage controlled unit, the appropriate phase at every individual helix is arranged according to the voltages, as illustrated in Table 18 below.

Typical Performance Data

Control Voltage (V)	Phase Shift* (Degrees)			VSWR (:1)			Insertion Loss (dB)		
	100 MHz	125 MHz	150 MHz	100 MHz	125 MHz	150 MHz	100 MHz	125 MHz	150 MHz
0.00	0.00	0.00	0.00	1.47	1.23	1.19	1.00	0.84	0.83
2.00	17.45	9.44	5.29	1.43	1.22	1.19	1.06	0.89	0.86
3.00	30.77	16.64	9.21	1.39	1.21	1.19	1.09	0.92	0.88
5.00	79.43	44.98	24.15	1.29	1.19	1.19	1.17	1.07	0.97
7.00	164.59	129.35	76.74	1.27	1.25	1.20	0.92	1.26	1.31
9.00	210.43	209.45	181.98	1.28	1.08	1.31	0.72	0.81	1.22
11.00	223.27	232.18	225.01	1.31	1.03	1.25	0.69	0.70	0.93
12.00	226.44	237.51	234.67	1.32	1.02	1.22	0.69	0.69	0.87

* Normalized at control voltage = 0V

Table 18: The JSPHS-150+ performance data

The phase arrangement is classified into the four major modes illustrated in tables 13, 14, 15, 16. Every mode steers the beam towards a certain direction at one point of the horizon, such as east, west, north, or south. Since the HPBW of the array is 90° , it was not deemed important to steer the array's main beam at intermediate angles, as the field strength would exhibit very little change. In order to control the beam, PICAXE28A microprocessor with 28 pins was employed.

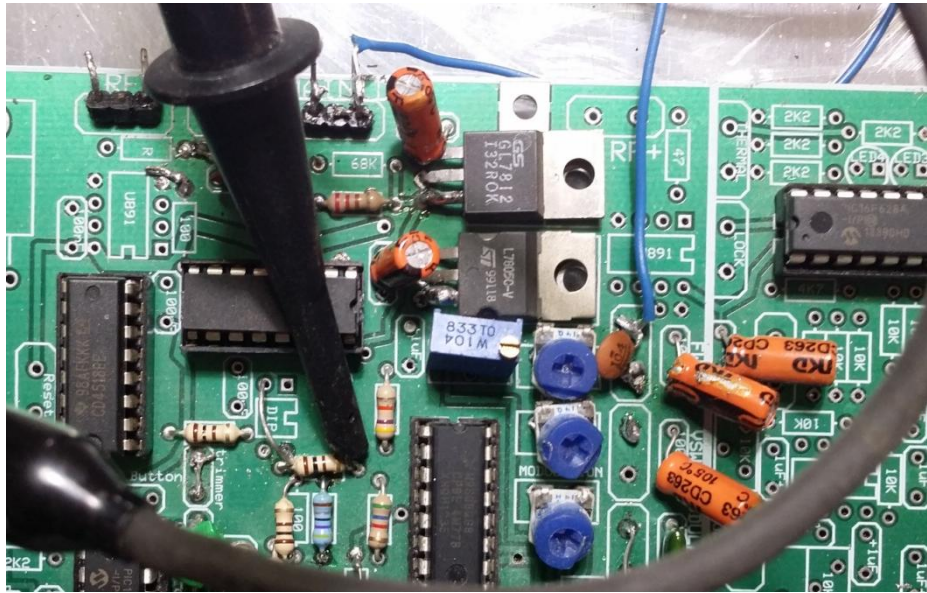


Figure 138: Control system under test

The PICAXE28A microprocessor was selected because it employs four analogue inputs at Pin 2, 3, 4, and 5. This enables a comparison among four inputs to determine the strongest signal, and arrange the proper phase shift in order to steer the array towards the direction of maximum intensity by repeating this procedure at 5 s intervals.

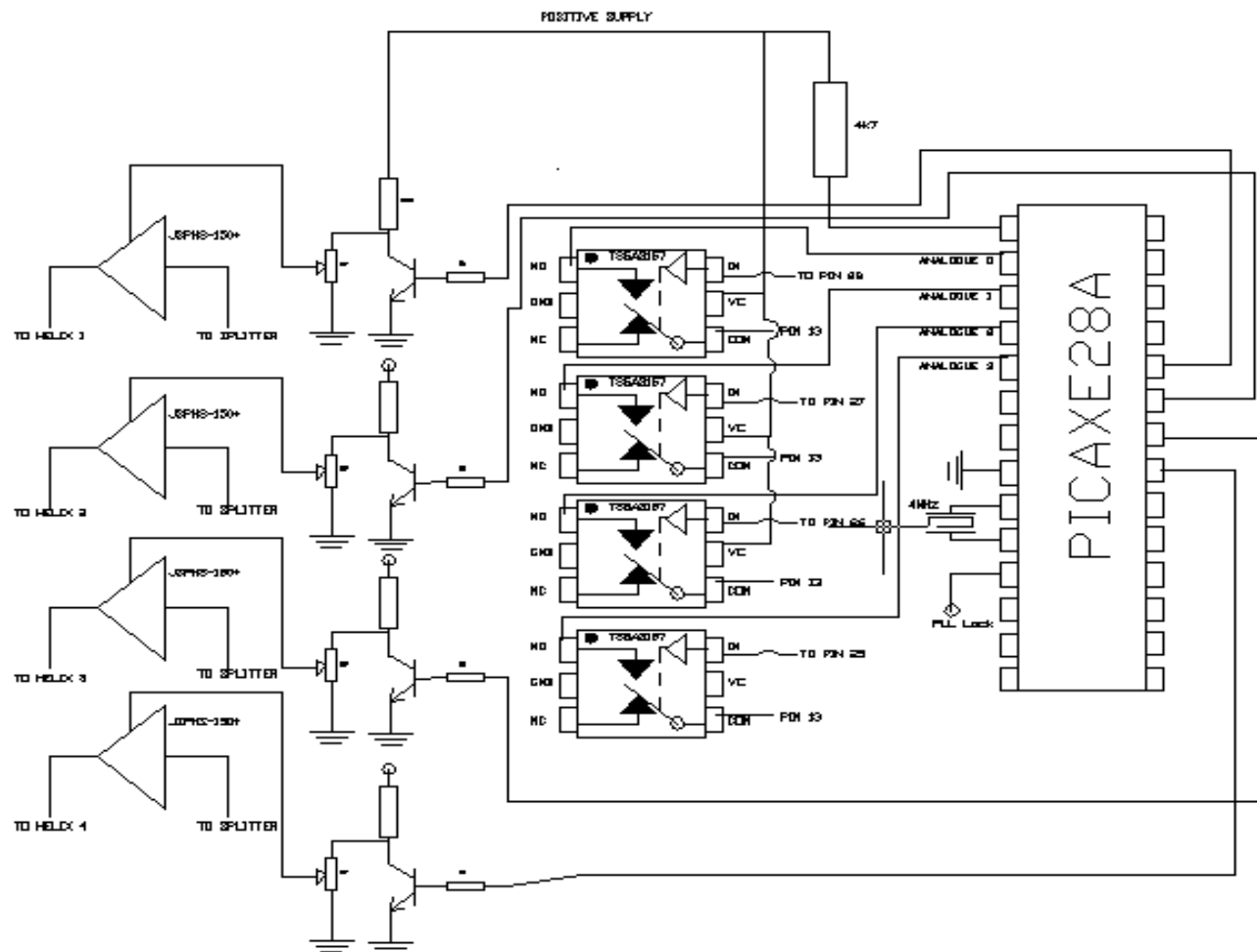


Figure 139: The control system circuit diagram



Figure 140: The four-character LCD

Particularly, the field strength voltage of the demodulator's TDA 1576 (Pin 13) is connected in parallel to the common port of the integrated circuit TS5A3157, comprising of solid-state switches that are connected to every individual helix. The control voltage that arranges the phase shift is controlled by the PICAXE28A outputs at Pin 21, 22, 23, and 24. The task of the PICAXE28A is to switch on every input

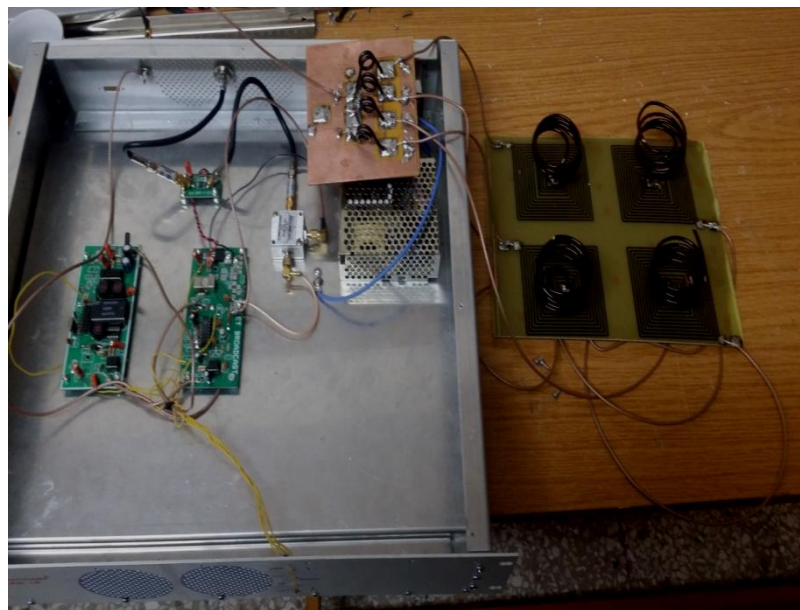


Figure 141: The complete receiver with the circular array

of the TS5A3157 by scanning across 360° every 5 seconds. By comparing the field strength at the four inputs, the output of the PICAXE28A remains “on” only at the ports of the maximum signal in order to supply the required phase shift voltage to the JSPHS-150+. This is achieved by activating a transistor switch, since the output of the PICAXE28A is 5 V and, according to table 13 the JSPHS-150+ requires up to 12 V.

The laboratory that served as the research facility is shown in Figure 142, with the main testing equipment shown in Figure 143. A complete list of the equipment used is given in the next page.



Figure 142: The laboratory in which the research was conducted

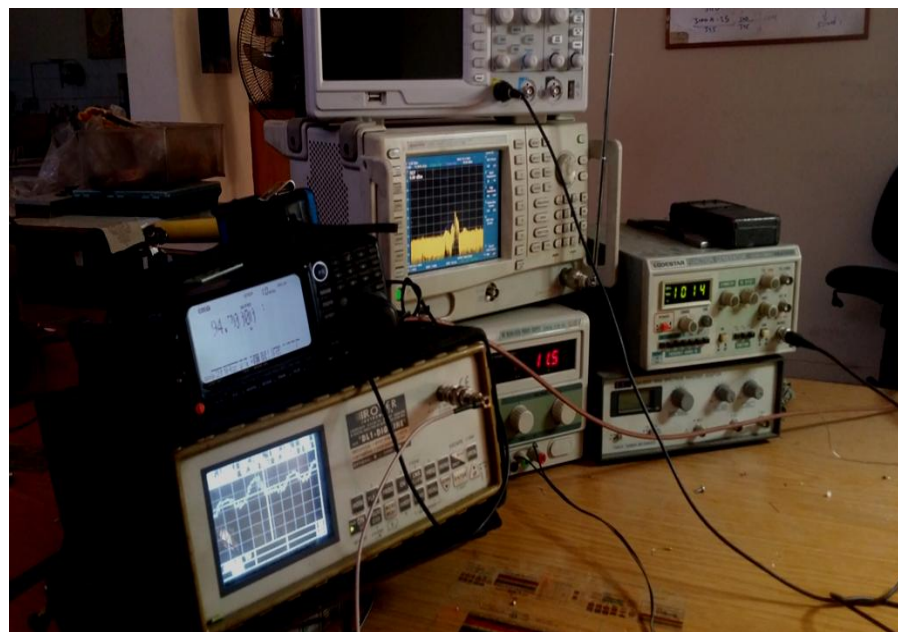


Figure 143: The key testing equipment employed in the present study

4.17. Key Equipment Used for the Research

Spectrum Analyzers:
Rover DL1-DIGILINE
ADVANTEST U 3751
TTi-TSA 1000
TTi-PSA 1301T
VSWR Analyzers
MFJ-259B HF/VHF Analyzer
Bird
Function Generators
Rover TS1-CNG
LODESTAR FG-2102 AD
Frequency Counters
Radioshack
TTi-PFM 1300
Multimeters
PHILIPS PM 2521
UNIGOR A4

Chapter 5: Conclusion and Future Work

The main goal of this work was to mitigate the radio interference along the southern coast of Cyprus caused by the Middle Eastern radio services during the hot dry summer months. According to the research findings, interference is caused by three major duct types—the surface, the surface-based, and the elevated duct. When the air aloft is very warm compared to the temperature at the Earth’s surface or the sea, the surface-based ducts occur. For example, they can arise due to the hot air masses that pass over the cool water surface of the Mediterranean Sea. On the other hand, elevated ducts occur when the meteorological conditions are favourable for such phenomena to manifest aloft above the Earth’s surface. In order to be able to analyze the overseas signals based on the ITU Recommendations, the upper air data required for the present study (Figure 30) was obtained using WRF-ARW Version 3.4 at a fixed time simultaneously with the measurement of the field strength intensity of the radio signals under consideration. The prediction error of this arrangement is small. Moreover, it is outweighed by the fact that radiosonde is inherently inaccurate as a data collection instrument, as it does not remain at a fixed point, but rather moves depending on the wind speed. In this regard, the results reported here confirm that the aforementioned program can be employed to accurately predict intensity of any interference signal in VHF-UHF Bands for the period of up to five days in advance. Thus, the findings reported in this study can be utilized for future planning of new radio services and schemes beyond FM radio technology, such as DAB+, Digital Radio Mondiale (DRM+) and Digital Video Broadcasting Terrestrial (DVB-T). As this matter is very important for future research, it has been discussed with the Department of Meteorology and was ascertained that summer weather conditions have been observed during autumn, winter and spring. However, as historical data is not retained for periods exceeding three months (except upon request), analyses pertaining to other seasons were not possible in this work. In this respect, the current research can be expanded by performing measurements throughout the year for a period of five years in order to obtain a comprehensive longitudinal data set that can be subjected to statistical analysis, with the aim of determining the probability of enhanced VHF signals arriving to Cyprus as a function of season, month, and time of day. The aforementioned project can be executed in collaboration with the “Department of Electronic Communications” and the “Department of Meteorology” of the Cyprus Government, whereby the author of this thesis would act as a research coordinator. In addition, the implementation of the smart antenna based on

circular array topology was confirmed as successful project, even though its performance was tested in FM Band II, characterized by a large wavelength. One of the major problems that had to be overcome as a part of the present study arose due to the need to construct a very compact and efficient antenna with a broadband response. As this has been successfully achieved, the study has provided a valuable contribution to the field, stemming primarily from the optimization of the NMHA that, despite its small dimensions, exhibits a very satisfactory performance in Band II. This methodology for optimizing the NMHA performance was beneficial, as it enables the application of this research in High Frequency HF band (3–30 MHz), where short antennas are a vital aspect of research design, as well as in Ultra High Frequency UHF band (300–3000 MHz), where short antennas are requisite for commercial applications. Particularly, applying the circular array as it has been implemented in this study in Band III (174 to 240 MHz) for Digital Audio Broadcasting (DAB+) will enhance the SNR of digital receivers during motion. More specifically, the DAB+ receiver requires field strength of 55 dBuV in order to provide a good reception without interruptions during motion. Thus, the DAB+ terrestrial radio technology requires many gap fillers within the service area in order to achieve robust reception. Because the circular array steers in the direction of the maximum signal, a fruitful goal for future research in this field would be to determine a new DAB+ radio plan with minimum gap filler requirements due to the enhancement of the receiver's SNR (provided that it employs a circular array smart antenna).

Circular arrays can also be a valuable addition to the future digital video broadcasting terrestrial (DVB-T) technology that broadcasts television in UHF Band between the channels 21 and 69 (i.e., in the 512–800 MHz frequency range). One of the drawbacks of the terrestrial television relative to the radio is that it cannot be viewed in motion, thus limiting its usage to stationary reception only. In order to ensure good visual signal reception, the TV sets are usually utilizing an external Yagi directional antenna that steers mechanically at the transmitting point. Because the UHF band has a small wavelength, for future research, the aim will be to design and construct a circular array smart antenna of very small dimensions that will employ a greater number of individual elements than presently incorporated into the commercial band FM, due to the physical constraints associated with the VHF band. A greater number of elements ensures higher "Gain" and fine scanning across the entire 360° range. This design would ensure robust TV reception, as the circular array smart antenna will be steering at multiple TV transmitting points automatically during motion. As an alternative, the circular array can be incorporated into the future TV sets, thus eliminating the need for an external TV antenna.

In closing, it should be noted that one of the limitations of the present study was lack of testing equipment, particularly a UHF vector/network analyzer, which would have allowed expanding the research by experimenting with the NMHA performance and the circular array at higher frequencies. Another important issue that should be addressed pertains to the design of the control circuit that steers the array automatically in the direction of the maximum signal density. This task involves two distinct engineering sectors, radio and Digital Signal Processing (DSP). Although the control system was tested in this work and was shown to exhibit satisfactory performance, in future applications, it can be optimized by using digital signal processing in order to enhance its performance. As a result, for future expansion of the work presented in this thesis, the antenna array algorithms developed as a part of this study can be provided to a team of DSP (Digital Signal Processing) engineers who can enhance the control system utilizing DSP Technology.

REFERENCES

- Adediji, and Ajewole, (2008). Progress In Electromagnetics Research. *VERTICAL PROFILE OF RADIO REFRACTIVITY GRADIENT IN AKURE SOUTH-WEST NIGERIA*, 4, pp.157-168.
- Antenna. *IETE Journal of Research*, 34(6), pp.463-465.
- Bailey, M. (1984). Broad-band half-wave dipole. *IEEE Trans. Antennas Propagat.*, 32(4). pp.410-412.
- Balanis, C. (2012). Antenna Technology: Past, Present and Future. *IEEE*, pp.5-7.
- Breed, G. (2007). *Basic Principles of Electrically Small Antennas*. [Online] Available at: <http://citeseerx.ist.psu.edu/viewdoc/download?doi=10.1.1.399.4843&rep=rep1&type=pdf> [Accessed 19 Feb. 2016].
- Burberry, R. (1992). *VHF and UHF Antennas*. Peter Peregrinus LTD, pp.193-196.
- Castel, FD. (Editor): ‘‘Progress in Radio Science’’, Elsevier Publishing Company, 1960-1963 Volume 2-Radio and Troposphere, pg.127-135, (1965).
- Davies, D. and Rizk, M. (1977). Electronic steering of multiple nulls for circular arrays. *Electron. Lett.*, 13(22), p.669.
- Delfino, F., Procopio, R. and Rossi, M. (2004). Current and Near Field Calculations for Cellular Base-Station Collinear Array Antennas. *IEEE Trans. Magn.*, 40(2), pp.1480-1483.
- Debus, W. (2006). *RF Path Loss & Transmission Distance Calculations*.
- Fanning, C. (2009). Improving monopole radiated emission measurement accuracy; RF chamber influences, antenna height and counterpoise grounding. In: *Electromagnetic Compatibility, 2009. EMC 2009. IEEE International Symposium*.
- Evjen, and Jonsrud, (n.d.). *SRD Antennas*. [Online] Application Note AN 003. Available at: <http://www.ti.com/lit/an/swra088/swra088.pdf> [Accessed 19 Feb. 2016].
- Gil, J. (2005). *Smart Antennas for Mobile Communications The Importance of the Propagation Channel and Scenarios*.
- Gorbachev, A. and Egorov, V. (2009). A Modified Planar Quasi-Yagi Antenna for Wireless Communication Applications. *Antennas Wirel. Propag. Lett.*, 8, pp.1091-1093.
- Greb, U. (2003). *Pflegewissenschaft*, 12(5), p.3200.
- Green, H. (1983). Book Review: The Handbook of Antenna Design, Volume I. *International Journal of Electrical Engineering Education*, 20(3), pp.246-246.
- HEWLETT PACKARD, APPLICATION NOTE 95-1. (1995). Hon Tat Hui, B. (2007). Decoupling Methods for the Mutual Coupling Effect in Antenna Arrays: A Review. *Recent Patents on Engineering*, 1(2), pp.187-193.
- Howard, J. and Fung, C. Clever Dumb Antenna: Passive Multibeam Antenna for

Broadband Wireless Communication.

ITU-R Recommendation P.452-11(2003), *Prediction procedure for the evaluation of microwave interference between stations on the surface of the Earth at frequencies above about 0.7 GHz*

ITU-R Recommendation P.453-8: The radio refractive index: its formula and refractivity data

ITU-R Recommendation P.834-4(2003), *Effects of tropospheric refraction on radiowave propagation*

ITU-R Recommendation P.526-8(2003), *Propagation by diffraction.*

ITU-R Recommendation BS.412-9(1998) *Planning standards for terrestrial FM sound broadcasting at VHF.*

ITU-R Recommendation P.617-1(1992) *Propagation Prediction Techniques and Data Required For the Design of Trans-Horizon Radio-Relay Systems.*

ITU-R Recommendation ITU-R P.844-1* (1994) *Ionospheric Factors Affecting Frequency Sharing in the VHF and UHF BANDS (30 MHz-3 GHz)*

Jackson, G. (1987). The early history of radio interference. *Journal of the Institution of Electronic and Radio Engineers*, 57(6), p.244.

Jackson, J. (2006). How an antenna launches its input power into radiation: The pattern of the Poynting vector at and near an antenna. *Am. J. Phys.*, 74(4), p.280.

K. Chy, D. (2015). Evaluation of SNR for AWGN, Rayleigh and Rician Fading Channels Under DPSK Modulation Scheme with Constant BER. *International Journal of Wireless Communications and Mobile Computing*, 3(1), p.7.

Khan, N., Azim, A. and Islam, S. (2014). Radiation Characteristics of a Quarter-Wave Monopole Antenna above Virtual Ground. *Journal of Clean Energy Technologies*, 2(4), pp.339-342.

Kraus, J. (1988). *Antennas*. New York: McGraw-Hill.

Kulms, U. (2015). *Calculation of short dipole antennas*. [Online] Available at: http://www.darc.de/uploads/media/Short_Dipole_Antenna.pdf [Accessed 19 Feb. 2016].

Laverghetta, T. (1996). *Practical microwaves*. Englewood Cliffs, N.J.: Prentice Hall.

Lee, K. (1984). *Principles of Antenna Theory*. Lee, M. and Kim, Y. (2009). Development of a K-band FMCW phased array radar sensor with low complexity receiver based on antenna switching. *Microwave and Optical Technology Letters*, 51(12), pp.2848-2850.

* Radiocommunication Study Group 3 made editorial amendments to this Recommendation in 2000 in accordance with Resolution ITU-R 44.

- Li, W., Chen, T. and Xu, W. (2010). On impedance matching and maximum power transfer. *Electric Power Systems Research*, 80(9), pp.1082-1088.
- Mappatao, G. (2010). Radiation Pattern Shaping for FM Broadcast- Optimizing Coverage. *IEEE Symposium on Industrial Electronics and Applications*, pp.222-225.
- Marriott, R. (1923). Interference. *Proceedings of the IRE*, 11(4), pp.375-388.
- Martin, W. (1967). Computation of antenna radiation pattern from near-field measurements. *IEEE Trans. Antennas Propagat.*, 15(2), pp.316-318.
- Moa.gov.cy. (2016). *Department of Meteorology - Climate of Cyprus*. [Online] Available at: http://www.moa.gov.cy/moa/ms/ms.nsf/DMLcyclimate_en/DMLcyclimate_en?OpenDocument [Accessed 10 Jun. 2016].
- Mounich, G. and Littmann, B. (1990). Helical antenna and spiral antenna with fast switch selection of the polarisation sense. *Electron. Lett.*, 26(22), p.1918.
- Mouhamadou, M., Armand, P., Vaudon, P. and Rammal, M. (2006). Interference Supression Of The Linear Antenna Arrays Controlled By Phase With Use Of SQP Algorithm. *Progress In Electromagnetics Research*, 59, pp.251-265.
- Ndt.net. (2017). *Phased Array technology: concepts, probes and applications*. [Online] Available at: <http://www.ndt.net/article/v07n05/poguet/poguet.htm> [Accessed 5 Feb. 2017]
- Nishi, M., Shinbara, H., Shin, K. and Yoshida, T. (2011). Observation results of non-line-of sight 77.1 MHz FM radio waves on three different paths for three years. *Journal of Atmospheric Electricity*, 31(1), pp.11-22.
- Olsson, M., Broström, A., Craig, S. and Arslan, H. (n.d.). Single Antenna Interference Rejection in GSM/EDGE Networks.
- Panchenko, V. (1984). Precision measurement of antenna gain. *Measurement Techniques*, 27(6), pp.543-545.
- Pozar, D. (1993). Directivity of omnidirectional antennas. *IEEE Antennas and Propagation Magazine*, 35(5), pp.50-51.
- Rudd, R. (n.d.). *Statistics of Anomalous Tropospheric Propagation at UHF Frequencies*.
- Rabinovich, V. (2011). Direction finding system for automotive applications using small phased antenna array. *Microwave and Optical Technology Letters*, 53(10), pp.2441-2446.
- Rabinovich, V. and Alexandrov, N. (2013). *Antenna arrays and automotive applications*. New York, NY: Springer.
- Shackelford, A., Kai-Fong Lee, and Luk, K. (2003). Design of small-size wide-bandwidth microstrip-patch antennas. *IEEE Antennas and Propagation Magazine*, 45(1), pp.75-83.
- Sharma, S. and Calla, O. (1988). Gain Optimisation with Suppressed Side Lobes and Grating Lobes in SBF.

- Sim, C. and Warrington, E. Signal strength measurements at frequencies of around 300 MHz over two sea paths in the British Channel Islands. *Radio Sci.*, 41(3), p.n/a-n/a.
- Slingsby, P. (1991). Modelling tropospheric ducting effects on VHF/UHF propagation. *IEEE Trans. on Broadcast.*, 37(2), pp.25-34.
- Son, and Lee, (2002). IEEE. *The Prediction of Radio Interference through Ducting and Proposal measures for Protecting Interference.*
- Stuckman, B. and Hill, J. (1990). Method of null steering in phased array antenna systems. *Electron. Lett.*, 26(15), p.1216.
- Straw, R. (2000). *The ARRL antenna book*. Newington, Conn.: American Radio Relay League.
- Straw, R. (2002). *The ARRL antenna compendium*. Newington, CT: American Radio Relay League.
- Thayer, G. (1974). An improved equation for the radio refractive index of air. *Radio Sci.*, 9(10), pp.803-807.
- Tropospheric-scatter observations. (1961). *Journal of the Institution of Electrical Engineers*, 7(79), pp.452-452.
- Vedula, V., Paladuga, S. and Prithvi, M. (2015). Synthesis of Circular Array Antenna for Sidelobe Level and Aperture Size Control Using Flower Pollination Algorithm. *International Journal of Antennas and Propagation*, 2015, pp.1-9.
- Wang, J., Lv, Z. and Li, X. (2014). Analysis of MIMO Diversity Improvement Using Circular Polarized Antenna. *International Journal of Antennas and Propagation*, 2014, pp.1-9.
- Wheeler, H. (1975). Small antennas. *IEEE Trans. Antennas Propagat.*, 23(4), pp.462-469
- Winters, J. (1998). Smart antennas for wireless systems. *IEEE Pers. Commun.*, 5(1), pp.23-27
- Whites, K. (1989). *Electromagnetic wave propagation through circular waveguides containing radially inhomogeneous lossy media*. Champaign, Ill.: US Army Corps of Engineers, Construction Engineering Research Laboratory.
- Yeo, J. and Lee, J. (2016). BROADBAND FLAT GAIN ENHANCEMENT OF PLANAR DOUBLE-DIPOLE QUASI-YAGI ANTENNA USING MULTIPLE DIRECTORS. *Progress In Electromagnetics Research C*, 65, pp.1-9.
- Γιαννοπουλος, (1963). *Οι κεραιές στην Τηλεόραση*. 1st ed. Αθήνα.
- Μαλαχιας, Ν. and Σαγος, Γ. (1998). *Αρχές Ραντάρ και Ηλεκτρονικού Πολέμου*. Αθήνα: Παπασωτηρίου, pp.161-164.

APPENDICES

APPENDIX 1: Government Measurements of Lebanon 92.1 MHz from 1/9/14 to 14/9/14

ΣΤΑΘΜΟΣ ΜΕΤΡΗΣΗΣ ΑΡΑΔΙΠΠΟΥ (ΕΝΔΕΑΛΟΣ)

ASL= 330m και ύψος πύργου 35 m - Κεραία στην κορυφή του πύργου.

ΣΥΧΝΟΤΗΤΑ 92.1 ΜΗz ΑΠΟ ΛΙΒΑΝΟ

Μετρήσεις 7:00 - 8:00 πρωί, 13:00 - 14:00 μεσημέρι, 22:00 - 23:00 βράδυ.

Περίοδος Μετρήσεων 1/9/2014 - 14/9/2014

DATE - TIME	FREQUENCY (Hz)	LEVEL (dBμV/m)
1409011500	92099945	94.1
1409011501	92100128	94.2
1409011502	92100750	94.3
1409011502	92100555	96.1
1409011504	92100120	93.8
1409011504	92100405	93.6
1409011504	92100171	93.5
1409011504	92100020	93.4
1409011505	92099998	93.5
1409011506	92100033	92.8
1409011506	92100107	92.8
1409011506	92099942	92.8
1409011506	92099893	93.7
1409011507	92100094	92.6
1409011507	92100181	93.5
1409011508	92100046	91.4
1409011508	92099989	92.5
1409011509	92099840	92.1
1409011511	92100022	92.2
1409011511	92100078	92
1409011511	92099928	92.1
1409011511	92099760	92.1
1409011512	92099918	92.3
1409011512	92099977	93.4
1409011513	92100194	93.5
1409011514	92100193	92.7
1409011515	92099332	93.2
1409011516	92100000	92.6
1409011517	92100225	94.5
1409011518	92099913	93.8
1409011518	92100009	93.8
1409011518	92099999	93.9
1409011519	92099919	93.9
1409011520	92100050	94
1409011520	92099198	93.7

1409011520	92100090	94
1409011521	92099804	94.3
1409011523	92099965	94.7
1409011524	92100470	94.7
1409011525	92099959	95.2
1409011526	92100547	93.6
1409011527	92100251	93
1409011527	92100393	92.7
1409011529	92099983	92.7
1409011530	92100101	92.2
1409011530	92100039	92.7
1409011530	92100208	92.4
1409011531	92100125	92.3
1409011531	92100942	93.4
1409011532	92100589	93.3
1409011532	92099946	93
1409011533	92099959	92.9
1409011535	92100227	91
1409011535	92099921	92.5
1409011536	92100052	93.1
1409011536	92101064	93.2
1409011537	92100419	93
1409011538	92099707	93.1
1409011538	92099446	94.1
1409011538	92098908	93.3
1409011539	92099961	94.1
1409011540	92100296	92.7
1409011542	92099964	95.3
1409011542	92100400	95.5
1409011542	92099958	94.6
1409011543	92100070	94.2
1409011543	92099988	94.9
1409011544	92099981	95
1409011544	92100095	94.1
1409011544	92098690	95.1
1409011544	92099887	96.1
1409011545	92099989	95.3
1409011546	92099820	96
1409011546	92099979	95.1
1409011546	92099768	94.8
1409011546	92100033	95.2
1409011547	92100424	95
1409011547	92100001	93.9
1409011548	92098937	95.2
1409011548	92099951	96.1
1409011549	92100020	94
1409011550	92100161	94.8
1409011551	92100167	94.7

1409011551	92100275	95.5
1409011551	92100163	94.7
1409011552	92100192	94.5
1409011553	92100130	95.5
1409011554	92100073	94.5
1409011555	92100334	96.6
1409011556	92100073	93.4
1409011557	92099318	95.4
1409011558	92097778	95.4
1409011558	92099003	94.6
1409011559	92098346	95.3
1409011600	92099695	94.3
1409011601	92100057	94.3
1409011602	92099952	94.7
1409011602	92099834	93.6
1409011603	92100015	96.9
1409011605	92100097	95.5
1409011606	92100020	95.5
1409011606	92100200	93.5
1409011606	92100364	94.4
1409011608	92100195	95.5
1409011608	92100282	95.5
1409011608	92100045	95.9
1409011608	92099990	94.9
1409011608	92100154	94.9
1409011609	92099396	95.8
1409011609	92099582	95.6
1409011609	92099601	95.7
1409011609	92099796	95.6
1409011610	92099968	95.7
1409011611	92099842	93.7
1409011611	92099969	95.6
1409011611	92099593	94.6
1409011612	92099902	94.5
1409011613	92100094	94.4
1409011613	92099999	94.4
1409011614	92100105	94.4
1409011614	92100133	94.2
1409011615	92100267	94.4
1409011615	92100082	95.4
1409011615	92100020	94.4
1409011615	92099987	93.7
1409011616	92100411	95.6
1409011617	92099829	93.5
1409011617	92100414	94.6
1409011617	92099938	94.5
1409011617	92099945	95.5
1409011618	92099304	95.5

1409011618	92100775	94.6
1409011618	92100057	93.5
1409011618	92100681	95.6
1409011619	92100000	95.6
1409011619	92099886	94.4
1409011619	92099974	93.5
1409011619	92099801	95.5
1409011619	92100088	93.5
1409011620	92100144	94.7
1409011620	92100425	94.6
1409011620	92099497	93.4
1409011620	92100344	95.4
1409011621	92100268	94.4
1409011621	92099697	94.4
1409011621	92100018	94.3
1409011622	92099871	95.2
1409011622	92099953	93.9
1409011623	92099956	95.2
1409011623	92100066	96.5
1409011623	92099856	93
1409011624	92099952	93.3
1409011625	92099495	93.1
1409011627	92100009	94.1
1409011627	92100349	95.2
1409011627	92100645	94.1
1409011628	92100169	95.3
1409011629	92100525	95.2
1409011631	92099822	93.1
1409011632	92099889	95.2
1409011632	92099966	95.5
1409011632	92101383	94.5
1409011632	92099167	94.4
1409011634	92099927	95.3
1409011634	92099952	94.5
1409011634	92099618	95.4
1409011634	92099105	95.4
1409011635	92100136	95.4
1409011635	92099973	95.6
1409011635	92100087	95.6
1409011635	92100255	93.4
1409011636	92099994	94.6
1409011637	92100087	93.4
1409011637	92100253	94.4
1409011637	92100086	95.5
1409011638	92099868	95.6
1409011639	92100005	95.7
1409011640	92099918	95.7
1409011640	92100086	94.4

1409011640	92099970	94.3
1409011640	92100046	94.4
1409011641	92099974	94.4
1409011641	92100149	94.4
1409011641	92100020	93.4
1409011641	92099429	94.7
1409011642	92099702	94.6
1409011642	92099649	94.5
1409011643	92100225	94.5
1409011643	92100067	95.5
1409011644	92100085	94.4
1409011645	92100147	94.2
1409011646	92099905	95.4
1409011646	92100085	94.7
1409011647	92099983	94.5
1409011648	92099906	94.5
1409011649	92099918	94.5
1409011651	92099596	93.2
1409011652	92100087	95.4
1409011653	92100474	95.4
1409011653	92100036	95.5
1409011653	92100097	95.5
1409011654	92099920	95.5
1409011655	92099975	94.9
1409011655	92099978	93.8
1409011655	92100019	93.8
1409011656	92100069	95.8
1409011656	92099982	94.9
1409011656	92099996	95.8
1409011656	92100020	94.9
1409011656	92099452	95.5
1409011657	92099824	95.5
1409011657	92100283	94.8
1409011657	92099797	95.7
1409011658	92100184	94.5
1409011700	92099909	95.6
1409011700	92099843	94.5
1409011700	92100120	95.7
1409011700	92099789	95.6
1409011701	92100508	94.7
1409011702	92100046	94.5
1409011703	92099975	94.5
1409011704	92100106	94.7
1409011704	92100385	93.5
1409011704	92100737	94.4
1409011705	92101174	95.4
1409011705	92099989	94.6
1409011706	92100772	94.6

1409011706	92100638	94.3
1409011707	92100081	94.7
1409011707	92100003	95.4
1409011707	92099926	95.5
1409011707	92099461	94.7
1409011707	92100582	94.6
1409011709	92099625	95.5
1409011710	92100328	95.4
1409011710	92100115	94.5
1409011710	92099742	94.6
1409011711	92099766	95.4
1409011712	92100437	93.4
1409011712	92099954	94.7
1409011712	92099801	95.4
1409011712	92100184	95.4
1409011713	92099878	94.6
1409011714	92100008	94.4
1409011714	92100129	94.5
1409011714	92099793	95.4
1409011714	92099991	96.5
1409011715	92100039	95.4
1409011715	92100069	94.5
1409011715	92100148	95.4
1409011715	92100085	94.5
1409011717	92100142	94.9
1409011717	92099842	94.4
1409011717	92100486	93.3
1409011718	92099558	95.4
1409011719	92100161	95.4
1409011720	92100019	94.6
1409011720	92100191	95.3
1409011720	92099828	95.3
1409011720	92100092	94.8
1409011721	92100910	94.6
1409011721	92100015	94.5
1409011721	92100399	95.4
1409011721	92100895	94.4
1409011721	92100858	94.4
1409011723	92100186	95.5
1409011723	92100374	95.3
1409011723	92100434	94.4
1409011723	92100169	94.5
1409011725	92099946	95.6
1409011725	92100173	94.6
1409011725	92099846	95.7
1409011726	92099737	95.5
1409011726	92099967	94.6
1409011727	92099992	95.8

1409011727	92100008	95.5
1409011727	92100070	94.5
1409011727	92100312	95.4
1409011728	92099826	94.7
1409011729	92100122	94.3
1409011729	92100134	95.3
1409011729	92100099	94.3
1409011729	92100278	95.4
1409011730	92100159	95.3
1409011730	92100284	94.3
1409011730	92100245	94.3
1409011730	92100434	94.4
1409011731	92100208	95.3
1409011732	92099477	94.6
1409011732	92099157	94.7
1409011732	92099242	94.6
1409011732	92100042	95.7
1409011734	92099911	94.6
1409011734	92100254	94.5
1409011734	92099911	96.6
1409011734	92100062	95.5
1409011735	92099609	94.2
1409011735	92099791	95.3
1409011736	92099782	95.4
1409011737	92099962	94.9
1409011737	92100001	94.6
1409011738	92099731	94.5
1409011738	92100046	95.5
1409011739	92099897	95.5
1409011740	92099829	93.4
1409011741	92099527	95.5
1409011743	92099959	94.9
1409011743	92100014	94.8
1409011743	92099242	95.6
1409011744	92099972	95.8
1409011745	92099964	94.7
1409011746	92100007	94.9
1409011746	92099971	94.9
1409011746	92100001	94.9
1409011747	92100002	94.9
1409011748	92100009	94.7
1409011749	92100071	95.6
1409011749	92100178	94.6
1409011750	92099966	95.6
1409011751	92099959	94.8
1409011752	92099992	94.9
1409011753	92099995	94.8
1409011755	92100030	94.9

1409011755	92099977	94.9
1409011755	92099975	94.7
1409011755	92100003	94.9
1409011757	92100500	94.6
1409011757	92100021	95.6
1409011757	92099538	95.6
1409011758	92099565	94.5
1409011759	92099625	95.6

1409012100	92100036	95.2
1409012101	92100316	96
1409012101	92099991	96.1
1409012102	92099997	94.9
1409012103	92099895	94.8
1409012103	92100124	94.8
1409012104	92100277	95.9
1409012104	92099846	96
1409012105	92100116	95.9
1409012107	92100010	95.9
1409012108	92099861	94.9
1409012109	92099843	96.3
1409012110	92100205	96.3
1409012110	92100205	96.1
1409012111	92099996	96.2
1409012111	92099901	97.1
1409012111	92099996	95.1
1409012111	92100064	94.9
1409012112	92099926	96.3
1409012113	92100098	95.3
1409012114	92099952	96.4
1409012114	92100094	95.2
1409012115	92099647	96.4
1409012116	92099878	96.2
1409012117	92099841	96.3
1409012117	92099985	96.3
1409012117	92100084	96.3
1409012117	92100080	95.4
1409012118	92100107	96.4
1409012118	92100049	95.2
1409012118	92100023	95.2
1409012118	92099763	96.5
1409012119	92099818	95.4
1409012119	92099766	95.3
1409012119	92099705	95.4
1409012119	92099983	96.5
1409012120	92099991	95.7
1409012120	92100043	95.2
1409012120	92100166	95.5

1409012120	92100213	95.5
1409012121	92100091	96.5
1409012122	92100277	96.3
1409012123	92100568	95.2
1409012124	92101147	95.3
1409012124	92100089	96.6
1409012124	92100100	96.7
1409012125	92101424	97.5
1409012125	92100931	96.5
1409012126	92099932	96.8
1409012127	92099927	95.7
1409012128	92101113	96.7
1409012129	92101238	96.7
1409012129	92101127	96.7
1409012129	92100615	95.6
1409012130	92100536	96.6
1409012131	92100711	95.4
1409012131	92100610	95.3
1409012131	92100141	97.7
1409012132	92099970	96.4
1409012132	92099861	95.3
1409012134	92100397	96.5
1409012134	92100396	95.6
1409012134	92100052	97.7
1409012135	92099333	95.5
1409012136	92100262	95.7
1409012138	92099634	96.7
1409012138	92099765	96.7
1409012138	92099814	97
1409012138	92100306	95.8

1409020300	92100202	95.1
1409020301	92100079	95
1409020303	92099997	94.2
1409020304	92099987	95.3
1409020305	92100086	94.2
1409020306	92099893	95.5
1409020307	92100032	93.4
1409020308	92100031	96.5
1409020310	92100027	94.5
1409020311	92100201	94.5
1409020312	92100298	94.4
1409020313	92100005	94.2
1409020315	92100076	94.3
1409020316	92100187	94
1409020317	92100125	95.3
1409020318	92100417	95
1409020320	92100039	93.8

1409020321	92099995	95.3
1409020322	92100333	93.2
1409020323	92100517	94
1409020324	92100101	95.2
1409020326	92100080	95.1
1409020327	92099700	95.3
1409020328	92100133	95.1
1409020329	92099968	93.2
1409020331	92100195	95.3
1409020332	92099681	95.3
1409020333	92100045	95.2
1409020335	92099902	94.1
1409020336	92100070	94.1
1409020337	92100041	94.9
1409020338	92099930	94.8
1409020340	92100291	94.5
1409020341	92100062	94.6
1409020342	92100069	93.8
1409020343	92099982	93.8
1409020344	92099380	93.8
1409020345	92099813	95
1409020347	92099339	94.9
1409020348	92100005	94
1409020349	92101061	95
1409020351	92099996	95
1409020352	92100173	95.3
1409020353	92100289	95
1409020354	92100122	94
1409020355	92100979	93.1
1409020356	92100635	93.2
1409020357	92099907	95.1
1409020359	92099961	95.3
1409020400	92100048	94.3
1409020401	92099945	95.2
1409020402	92100552	93.9
1409020404	92100151	94.9
1409020405	92100092	94
1409020406	92099922	94.9
1409020407	92100117	94.7
1409020408	92100072	93.8
1409020409	92099725	93.6
1409020410	92099637	94.4
1409020411	92099997	93.6
1409020412	92099926	94.6
1409020413	92099786	93.6
1409020415	92100150	94.5
1409020416	92100233	94.1
1409020417	92100170	93

1409020419	92100042	93.8
1409020420	92099982	93.5
1409020421	92100008	93.5
1409020422	92099988	94.6
1409020423	92099997	93.7
1409020424	92099984	93.5
1409020425	92099998	92.4
1409020426	92099982	94.4
1409020427	92099996	93.5
1409020428	92099656	92.8
1409020429	92100220	94
1409020430	92100358	94.1
1409020432	92099951	94.6
1409020433	92099972	94.7
1409020434	92099874	94.7
1409020435	92099934	94.8
1409020436	92099956	94.7
1409020437	92099727	94.7
1409020438	92099951	94.5
1409020439	92099760	93.6
1409020440	92099963	94.5
1409020441	92100677	94.6
1409020442	92100443	94.6
1409020443	92100525	93.5
1409020444	92100080	93.7
1409020445	92100241	93.4
1409020447	92099903	93.7
1409020448	92099719	93.6
1409020448	92099947	93.6
1409020449	92100007	93.8
1409020450	92100063	94.6
1409020451	92100139	93.4
1409020453	92099951	94.8
1409020453	92100155	94.5
1409020455	92099910	94.6
1409020455	92099955	94.8
1409020456	92100147	93.7
1409020457	92099985	94.5
1409020458	92099801	93.5
1409020459	92100065	94.4
1409020500	92100007	93.5
1409020501	92099909	94.6
1409020502	92100128	93.7
1409020503	92100393	94.6
1409020504	92100007	95
1409020505	92099836	93.8
1409020505	92099874	94.5
1409020506	92100032	93.8

1409020507	92100163	94.8
1409020508	92099728	93.7
1409020509	92099994	94.7
1409020510	92100138	93.4
1409020511	92100040	94.4
1409020512	92099872	93.7
1409020513	92099976	93.7
1409020514	92100414	94.4
1409020515	92100507	93.5
1409020516	92100222	94.7
1409020517	92100001	96.1
1409020518	92100025	94.8
1409020519	92099919	93.5
1409020519	92100057	93.5
1409020520	92100026	93.7
1409020521	92100076	94.3
1409020522	92100122	92.6
1409020523	92100165	94.5
1409020524	92100029	93.7
1409020524	92100001	94.5
1409020525	92100086	93.7
1409020526	92100014	94
1409020527	92100003	96.2
1409020528	92099992	94
1409020529	92100189	95
1409020531	92099997	95
1409020532	92100385	95.1
1409020533	92100096	95.2
1409020534	92100173	94.2
1409020535	92099981	95.4
1409020536	92099618	94.2
1409020537	92100225	94.2
1409020538	92100018	94
1409020539	92100155	95.3
1409020540	92099762	95.2
1409020541	92099984	95.4
1409020543	92100194	95.4
1409020544	92100115	95.5
1409020545	92100029	94.6
1409020546	92099825	94.3
1409020547	92099942	94.5
1409020548	92100152	94.4
1409020550	92099756	95.3
1409020551	92099986	95.6
1409020552	92100082	95.4
1409020553	92099997	95.4
1409020554	92099604	95.3
1409020556	92100080	95.5

1409020557	92100071	96.6
1409020558	92100159	94.1
1409020559	92100101	93.9

1409021200	92100063	94.3
1409021201	92099856	94.2
1409021202	92100321	95.1
1409021203	92100000	94.1
1409021204	92100000	95
1409021206	92099781	95
1409021207	92100073	95.1
1409021208	92099919	94.1
1409021209	92100080	94.2
1409021210	92099956	94
1409021212	92099963	94.3
1409021213	92099954	94.3
1409021214	92099849	95.2
1409021215	92100041	94.3
1409021216	92100261	94.1
1409021217	92099966	94.3
1409021219	92099774	93.9
1409021220	92099801	93.8
1409021221	92099371	92.9
1409021222	92100094	94
1409021223	92099982	94
1409021224	92100139	94
1409021226	92099939	95.3
1409021227	92099892	95.2
1409021228	92099974	94.3
1409021229	92099998	93.2
1409021230	92099910	94
1409021231	92100752	93.9
1409021232	92099769	94.2
1409021233	92100148	94.9
1409021234	92100295	94.1
1409021235	92099982	94
1409021236	92099939	95.9
1409021238	92099836	94.2
1409021239	92100280	94.2
1409021240	92099234	94.2
1409021241	92099730	95
1409021242	92099735	94.2
1409021243	92099443	94.2
1409021243	92100107	94.4
1409021245	92100198	94.1
1409021246	92100497	95.1
1409021247	92100043	93.8
1409021248	92099844	93.8

1409021249	92100710	94.2
1409021250	92099533	95.3
1409021251	92097878	95.2
1409021252	92099953	95.1
1409021253	92099780	94.2
1409021254	92099838	95.1
1409021254	92100566	94.2
1409021256	92099933	94
1409021257	92100065	94.1
1409021257	92100111	94.2
1409021258	92099996	93.9
1409021259	92099702	95
1409021300	92100294	94.2
1409021301	92100179	94.2
1409021302	92099932	94
1409021304	92100211	94.1
1409021305	92100463	94.2
1409021305	92100136	94.1
1409021307	92100377	94.1
1409021308	92100687	94.2
1409021309	92100603	94.3
1409021310	92099883	94.1
1409021311	92100242	94.2
1409021312	92100328	95
1409021313	92099557	94.2
1409021314	92100063	95.2
1409021315	92099743	94.2
1409021317	92100079	93.8
1409021318	92100222	94.1
1409021319	92100082	95.1
1409021320	92100156	94.2
1409021321	92100179	94.2
1409021322	92100106	94.2
1409021323	92100121	94.2
1409021324	92099913	94.2
1409021325	92102175	94.4
1409021326	92099894	94.5
1409021328	92099933	94.1
1409021329	92100033	94.3
1409021330	92100132	94.1
1409021331	92099895	95.1
1409021332	92100371	95
1409021333	92100990	94.2
1409021335	92099993	94.2
1409021336	92101187	94.3
1409021337	92100258	94.3
1409021338	92100005	94.3
1409021339	92100286	94.3

1409021340	92099985	94
1409021342	92100029	94
1409021343	92099909	95
1409021344	92099994	94.2
1409021345	92099986	94.2
1409021346	92099921	95.2
1409021347	92099970	94.3
1409021349	92100005	94.1
1409021350	92099929	94.2
1409021351	92099919	93
1409021352	92099889	94.2
1409021353	92100095	95
1409021355	92100235	94.3
1409021356	92099996	94
1409021357	92099267	94.4
1409021358	92099958	94.3
1409021359	92099930	92.8
1409021400	92099886	94.3
1409021402	92100382	95
1409021403	92100085	94.2
1409021404	92099895	94.9
1409021405	92098813	94.1
1409021406	92100595	95.1
1409021407	92099859	95

1409030820	92099984	97.1
1409030821	92100190	96.3
1409030822	92100476	96.1
1409030823	92100002	97.6
1409030825	92100039	96.4
1409030826	92100326	97.5
1409030827	92099968	96.5
1409030828	92099404	97.2
1409030830	92099961	96.4
1409030831	92099914	96
1409030832	92100113	95.8
1409030833	92100118	95.7
1409030835	92099891	96.7
1409030836	92099803	95.5
1409030837	92100066	96.7
1409030838	92100211	96.4
1409030839	92100061	96.6
1409030840	92099921	95.3
1409030842	92100257	96.4
1409030843	92100767	96.6
1409030844	92099914	96.5
1409030845	92100272	96.3
1409030847	92100552	96.1

1409030848	92099968	95
1409030849	92100184	96
1409030850	92100408	96.1
1409030851	92100190	95.1
1409030853	92100190	94.7
1409030854	92099991	95.1
1409030855	92100018	96.2
1409030856	92099960	96.2

1409031300	92100071	94.2
1409031301	92100155	94
1409031302	92099988	94
1409031303	92100411	94
1409031304	92100093	94.1
1409031305	92099850	94.1
1409031306	92100063	94.9
1409031307	92099939	93.9
1409031308	92099692	93.9
1409031309	92099793	94.8
1409031310	92099661	92.8
1409031311	92100060	94.9
1409031312	92099986	94
1409031313	92100155	94.9
1409031314	92100288	94.1
1409031315	92100022	94.2
1409031316	92100070	95.1
1409031317	92100083	95.2
1409031318	92100168	94.2
1409031319	92100117	95.2
1409031320	92100097	94.3
1409031321	92100194	94.2
1409031322	92099945	95.1
1409031323	92100091	95
1409031325	92100138	94.2
1409031325	92099767	95.2
1409031326	92099849	95.2
1409031327	92100035	94.3
1409031328	92100072	95.2
1409031329	92099506	94.3
1409031329	92100087	94.3
1409031330	92099688	94.5
1409031331	92100004	94.3
1409031332	92100469	94.4
1409031333	92100047	94.5
1409031334	92099869	94.4
1409031335	92100899	95.2
1409031336	92101019	94.3
1409031337	92100144	94.2

1409031338	92100002	95.3
1409031339	92099996	94.4
1409031340	92100015	94.4
1409031341	92100002	94.2
1409031342	92099985	95.2
1409031343	92100119	94.3
1409031344	92100067	95.1
1409031345	92100084	93
1409031346	92099851	94.1
1409031346	92099976	93.9
1409031347	92100070	95.1
1409031348	92100061	95
1409031349	92100278	93.9
1409031350	92100158	94.9
1409031351	92100201	94.1
1409031352	92100319	94
1409031353	92099809	94.3
1409031355	92100014	95.3
1409031355	92099827	95.1
1409031356	92099874	94.2
1409031358	92100328	94.3
1409031359	92100167	94.1

1409032200	92099762	97.7
1409032201	92100334	99.1
1409032202	92100122	97.9
1409032203	92099635	97.8
1409032204	92099845	97.9
1409032206	92099980	99
1409032207	92099764	98.8
1409032208	92100426	99
1409032209	92100105	99
1409032210	92099787	98.9
1409032211	92099351	98.9
1409032213	92099620	98.8
1409032214	92100052	97.9
1409032215	92100454	98.6
1409032216	92099949	99.1
1409032217	92100483	98.9
1409032218	92100555	97.7
1409032220	92100001	99.1
1409032221	92099313	98.9
1409032222	92100116	100.1
1409032223	92100449	98.8
1409032224	92100523	98.8
1409032226	92099618	97.2
1409032227	92099951	97.7
1409032228	92100297	98.5

1409032229	92100032	97.3
1409032230	92100047	97.3
1409032231	92099746	97.4
1409032233	92099983	99.8
1409032234	92099823	97.5
1409032235	92099972	98.6
1409032236	92099968	97.5
1409032237	92100059	97.3
1409032238	92099995	98.5
1409032240	92099962	98.6
1409032241	92099992	97.5
1409032242	92099682	97.5
1409032243	92099957	97.5
1409032244	92099803	97.5
1409032245	92099563	97.3
1409032247	92099107	97.4
1409032248	92099996	98.8
1409032249	92099968	98.5
1409032250	92099666	97.4
1409032251	92099998	98.7
1409032252	92100138	99.5
1409032254	92099929	98.5
1409032255	92100036	98.5
1409032256	92099914	97.5
1409032257	92100122	98.6
1409032258	92100117	97.3
1409032259	92099983	98.7

1409040700	92100099	100.2
1409040701	92100080	99.5
1409040702	92099956	100.4
1409040703	92100107	100.4
1409040704	92100019	100.2
1409040706	92099818	101.1
1409040707	92099986	99.3
1409040708	92100051	99.3
1409040709	92099948	99.4
1409040710	92099721	100.9
1409040711	92099791	100
1409040713	92100163	100.1
1409040714	92099676	99.7
1409040715	92099911	99.7
1409040716	92099366	99.6
1409040717	92099932	99
1409040719	92099920	100.8
1409040720	92100093	100.8
1409040721	92100043	99
1409040722	92099948	100

1409040723	92099886	100
1409040724	92099852	100
1409040726	92100248	100.1
1409040727	92100228	99.9
1409040728	92099919	99.9
1409040729	92100389	98.9
1409040730	92100158	100
1409040731	92099815	100
1409040733	92099852	100.2
1409040734	92100038	99.9
1409040735	92100042	99.8
1409040736	92100160	99.8
1409040737	92099962	100.1
1409040738	92099997	100.1
1409040740	92099963	100.1
1409040741	92099948	99.1
1409040742	92099949	100.1
1409040743	92099885	100.1
1409040744	92100668	100
1409040745	92099961	98.1
1409040747	92099991	100.1
1409040748	92099834	98.8
1409040749	92099931	99.9
1409040750	92100010	98.8
1409040751	92100091	98.5
1409040752	92100054	98.7
1409040754	92099971	98.5
1409040755	92099858	98.2
1409040756	92099911	99.3
1409040757	92099595	99.4
1409040758	92100483	98.3
1409040759	92100023	99.6

1409041300	92100381	95.2
1409041301	92100027	95
1409041302	92099951	94.1
1409041303	92100007	94.1
1409041304	92100309	93.9
1409041306	92100567	94
1409041307	92100392	94.9
1409041308	92100078	93.9
1409041309	92100154	94
1409041310	92100176	94
1409041311	92099983	95
1409041313	92099908	94.1
1409041314	92099983	94.1
1409041315	92100037	93.9
1409041316	92099821	94.1

1409041317	92100072	94.9
1409041318	92100394	93.8
1409041320	92100147	93.9
1409041321	92100521	94.8
1409041322	92100392	93.8
1409041323	92099915	93.9
1409041324	92099999	94
1409041325	92100159	93.9
1409041327	92100093	93.9
1409041328	92099793	94
1409041329	92099997	94
1409041330	92099411	94
1409041331	92099722	94.2
1409041333	92099922	94.1
1409041334	92100268	94.1
1409041335	92100161	94
1409041336	92100324	94
1409041337	92099968	94.9
1409041338	92099833	95
1409041340	92100196	94.1
1409041341	92100034	94.2
1409041342	92100026	94.1
1409041343	92100179	94.1
1409041344	92099859	94.2
1409041345	92100185	94
1409041347	92100074	94
1409041348	92099987	94.1
1409041349	92100107	94
1409041350	92100367	94.1
1409041351	92100220	94.9
1409041352	92100123	94.9
1409041354	92100415	95.1
1409041355	92100312	94.2
1409041356	92100000	94.2
1409041357	92100117	94.2
1409041358	92100153	94.1
1409041359	92100013	94.3

1409042200	92100179	96.7
1409042201	92100014	97.6
1409042202	92100000	97.7
1409042203	92099931	97.1
1409042204	92100087	96.9
1409042206	92100022	95.4
1409042207	92100046	96.6
1409042208	92099851	96.3
1409042209	92100109	96.1
1409042210	92099958	95

1409042211	92099949	95.6
1409042213	92100011	96.6
1409042214	92100067	95.4
1409042215	92100214	95.4
1409042216	92100039	95.4
1409042217	92100345	95.4
1409042218	92099986	95.5
1409042220	92099926	94.7
1409042221	92099910	95.7
1409042222	92099900	95.8
1409042223	92100112	94.9
1409042224	92099997	96.1
1409042225	92100007	96
1409042227	92100002	96.1
1409042228	92100062	96.2
1409042229	92099989	96.4
1409042230	92099751	95.2
1409042231	92099626	95.3
1409042232	92099527	97.2
1409042234	92100178	96.2
1409042235	92100154	95.7
1409042236	92099959	95.8
1409042237	92099851	95.8
1409042238	92099933	97.1
1409042240	92099831	96.2
1409042241	92100004	97.2
1409042242	92100324	95.8
1409042243	92099831	96
1409042244	92100113	95.9
1409042245	92100110	96.2
1409042247	92100315	97.4
1409042248	92100186	96.2
1409042249	92099974	97.6
1409042250	92099971	96.7
1409042251	92100025	96.9
1409042252	92100240	96.7
1409042254	92100170	96.8
1409042255	92099931	97
1409042256	92099936	97.2
1409042257	92100070	97.4
1409042258	92099848	98.3
1409042259	92100086	97.5

1409050700	92100075	96.8
1409050701	92099875	95.5
1409050702	92100312	95.7
1409050703	92100050	95.8
1409050705	92100819	96.9

1409050706	92100023	97.2
1409050707	92099910	96.1
1409050708	92100100	96.1
1409050709	92100647	96.1
1409050711	92100873	97.3
1409050712	92099981	96.3
1409050713	92100065	95.2
1409050714	92099951	96
1409050715	92100041	97.1
1409050717	92099914	95.7
1409050718	92099959	96.8
1409050719	92099945	95.8
1409050720	92100156	95.8
1409050721	92099832	97.7
1409050723	92099979	96.4
1409050724	92099944	96.6
1409050725	92100269	96.4
1409050726	92099888	96.3
1409050727	92099789	96.2
1409050728	92100001	96.1
1409050730	92099846	96.4
1409050731	92099758	95.1
1409050732	92099986	96.1
1409050733	92099784	95.3
1409050734	92099833	95.3
1409050736	92100215	94.1
1409050737	92100254	96.2
1409050738	92100631	95.3
1409050739	92099816	95.2
1409050740	92099620	95.5
1409050741	92100109	95.3
1409050743	92100052	95.3
1409050744	92100430	95.6
1409050745	92100253	96.5
1409050746	92099941	95.5
1409050747	92100102	96.4
1409050748	92100031	96.4
1409050750	92099563	95.3
1409050751	92100006	96
1409050752	92099890	96
1409050753	92100053	95
1409050754	92100399	96.2
1409050756	92099644	95.2
1409050757	92100074	96.1
1409050758	92100344	96
1409050759	92100433	95.3
1409051300	92100074	94.1

1409051301	92099964	95
1409051302	92099942	94
1409051303	92100351	94.1
1409051305	92100428	94.9
1409051306	92100260	94
1409051307	92099992	93.9
1409051308	92099941	94
1409051309	92099948	94.1
1409051310	92100014	94.1
1409051312	92100244	92.9
1409051313	92100313	94.2
1409051314	92100156	95.2
1409051315	92100340	95.2
1409051316	92100113	93.1
1409051317	92100152	93.9
1409051319	92100322	95
1409051320	92099886	94.1
1409051321	92100013	95.1
1409051322	92099958	94.1
1409051323	92099794	94.1
1409051325	92099931	94.2
1409051326	92099994	94.1
1409051327	92100026	94.1
1409051328	92100293	95.1
1409051329	92100256	94.1
1409051330	92100079	94.1
1409051332	92099995	95.3
1409051333	92100182	95.1
1409051334	92099815	93
1409051335	92100066	94.1
1409051336	92100059	94.2
1409051338	92099865	93.7
1409051339	92099363	94
1409051340	92100340	94.9

1409052200	92099969	95.4
1409052201	92100044	96.6
1409052202	92099885	95.8
1409052204	92100038	95.6
1409052205	92100005	93.7
1409052206	92099989	95.6
1409052207	92099963	95.7
1409052208	92099972	95.8
1409052210	92100040	95.6
1409052211	92099965	94.4
1409052212	92100125	94.4
1409052213	92100092	94.3
1409052214	92099978	94.4

1409052216	92099974	96.9
1409052217	92100177	95.8
1409052218	92099984	95.7
1409052219	92099865	94.5
1409052220	92100184	96.8
1409052222	92100002	95.6
1409052223	92099996	95.8
1409052224	92099990	94.7
1409052225	92100001	95.8
1409052226	92099912	94.6
1409052228	92100189	94.7
1409052229	92100224	95.7
1409052230	92099966	94.6
1409052231	92099920	95.8
1409052232	92100013	95.9
1409052234	92100124	94.6
1409052235	92100139	95.8
1409052236	92100038	95.7
1409052237	92100064	93.8
1409052238	92099972	95.7
1409052239	92100221	96.7
1409052241	92099991	94.8
1409052242	92099934	94.7
1409052243	92099970	95.4
1409052244	92099881	95.6
1409052245	92099962	95.7
1409052247	92100150	94.4
1409052248	92100009	93.5
1409052249	92100688	94.3
1409052250	92099984	94.8
1409052251	92100166	95.5
1409052253	92100042	95.5
1409052254	92100256	94.5
1409052255	92100195	95.6
1409052256	92100013	94.5
1409052257	92099914	95.7
1409052259	92100058	93.7

1409060700	92099941	95.9
1409060701	92100759	95.9
1409060702	92100024	95.9
1409060703	92100103	95.2
1409060704	92099904	96.5
1409060705	92100160	95.4
1409060706	92100156	96.4
1409060707	92099639	96.3
1409060707	92100212	96.4
1409060708	92100302	96.3

1409060709	92099666	97.2
1409060711	92099623	95
1409060712	92100183	95.1
1409060713	92099502	94.9
1409060714	92100329	95.7
1409060715	92100131	95.7
1409060716	92102415	96.1
1409060717	92099824	95.3
1409060717	92100019	94.1
1409060719	92099675	95.4
1409060720	92100402	96.5
1409060721	92100864	95.3
1409060722	92100059	96.6
1409060723	92100330	96.7
1409060724	92099973	97.1
1409060725	92100373	96.1
1409060726	92099883	96.9
1409060727	92100217	94.9
1409060727	92100077	96.9
1409060728	92100558	95.8
1409060729	92100046	96
1409060730	92100443	95.9
1409060731	92100186	96.1
1409060732	92100299	97.1
1409060733	92100093	96.1
1409060734	92100122	96.1
1409060735	92100003	97.2
1409060736	92099685	97.2
1409060737	92099824	95.9
1409060738	92100032	96.2
1409060739	92098556	96.3
1409060741	92099967	97.6
1409060742	92100178	98.5
1409060743	92100082	97.6
1409060744	92099833	97.5
1409060745	92099988	97.5
1409060746	92100015	96.8
1409060747	92099911	96.7
1409060748	92099267	97.7
1409060749	92099154	97.7
1409060750	92100283	96.7
1409060751	92100135	96.6
1409060752	92100096	97.8
1409060753	92100136	97.6
1409060755	92099106	96.8
1409060755	92100256	97
1409060756	92099697	96.9
1409060758	92098580	98.1

1409060758	92099978	98.3
1409060759	92099964	98.2

1409061300	92100263	94.1
1409061301	92100099	95.1
1409061302	92100130	94.1
1409061303	92099617	94.2
1409061305	92099941	94.3
1409061306	92100033	94.3
1409061307	92099983	94.3
1409061308	92099919	94.2
1409061309	92100024	94.1
1409061310	92099982	94.1
1409061312	92100079	93.2
1409061313	92100236	95.1
1409061314	92100122	94.2
1409061315	92100308	94.2
1409061316	92099877	94.1
1409061318	92100353	94.2
1409061318	92099880	94.9
1409061320	92099998	95
1409061321	92099954	94.3
1409061322	92099942	95.2
1409061323	92100022	94.4
1409061324	92099995	94.3
1409061325	92100015	92.8
1409061326	92100018	94.3
1409061327	92100186	93.2
1409061329	92099972	94.4
1409061330	92099919	94.1
1409061331	92099853	94.2
1409061332	92100555	94.2
1409061333	92099644	94.3
1409061334	92099751	94.2
1409061335	92099788	94.3
1409061336	92100035	95.6
1409061337	92099926	94.3
1409061338	92099764	95.2
1409061339	92100108	94.3
1409061340	92100048	95.3
1409061342	92099794	94.3
1409061342	92100090	95.2
1409061344	92099942	95.1
1409061345	92099600	94.1
1409061346	92099732	94.4
1409061347	92099992	94.2
1409061348	92099950	94.4
1409061349	92099966	94.6

1409061351	92100491	94.7
1409061352	92100463	94.7
1409061353	92100264	95.6
1409061354	92100358	94.6
1409061355	92099998	94.7
1409061356	92100151	95.7
1409061357	92100648	94.5
1409061358	92100000	94.5
1409061359	92100029	94.8

1409062200	92100079	95.9
1409062201	92100096	96.8
1409062202	92100030	96.7
1409062203	92100070	96.7
1409062205	92100053	95.9
1409062206	92099939	94.9
1409062207	92100061	97
1409062208	92099957	97.1
1409062209	92099940	96.1
1409062210	92099828	96.1
1409062212	92099967	97.2
1409062213	92099811	96.4
1409062214	92100024	96.3
1409062215	92099980	97.2
1409062216	92099893	97.2
1409062217	92099925	96.3
1409062219	92100228	95.1
1409062220	92099996	97.3
1409062221	92100074	97.3
1409062222	92100035	96.4
1409062223	92099834	97.3
1409062225	92099974	96.5
1409062226	92100268	97.4
1409062227	92100101	97.5
1409062228	92099861	96.3
1409062229	92100119	96.6
1409062230	92100074	96.2
1409062232	92100003	96.3
1409062233	92099936	97.4
1409062234	92099992	96.5
1409062235	92099928	96.5
1409062236	92099949	97.3
1409062237	92100026	97.3
1409062239	92099964	96.8
1409062240	92099761	96.9
1409062241	92099968	98.1
1409062242	92100012	96.9

1409070700	92099811	98.7
1409070701	92099918	96.7
1409070702	92099969	98
1409070703	92099964	98.1
1409070705	92100025	98.9
1409070706	92100034	97.8
1409070707	92100012	98.8
1409070708	92099971	97.6
1409070709	92100003	97.6
1409070711	92100049	97.4
1409070712	92100051	98.1
1409070713	92100113	98
1409070714	92099940	97.1
1409070715	92100033	98.3
1409070716	92099964	97.2
1409070718	92099450	99.3
1409070719	92100043	98.2
1409070720	92100333	96.8
1409070721	92100485	97.5
1409070722	92100049	98.4
1409070724	92099968	95.2
1409070725	92100158	96.8
1409070726	92099904	98
1409070727	92100483	96.9
1409070728	92100180	95.3
1409070729	92100406	94.6
1409070731	92100801	96.7
1409070732	92099925	95.6
1409070733	92099154	96.6
1409070734	92099949	96.5
1409070735	92100048	95.4
1409070737	92100349	94.5
1409070738	92100004	95.4
1409070739	92099830	95.3
1409070740	92099907	95.4
1409070741	92099886	96.3
1409070742	92099757	96.3
1409070744	92099977	96.3
1409070745	92099971	96.6
1409070746	92099871	95.4
1409070747	92100330	96.2
1409070748	92099820	95.3
1409070750	92099014	95.4
1409070751	92099866	95.3
1409070752	92099641	96.1
1409070753	92099775	95.2
1409070754	92100539	95.1
1409070755	92100003	95.3

1409070757	92099683	94.1
1409070758	92100255	96
1409070759	92099921	95.1

1409071300	92099966	94.1
1409071301	92098734	95.1
1409071302	92099980	94.9
1409071303	92100650	94.1
1409071305	92099625	94.2
1409071306	92099892	94
1409071307	92100258	94
1409071308	92100181	95
1409071309	92098611	95
1409071310	92099968	95
1409071312	92099687	94.1
1409071313	92099614	94.1
1409071314	92099962	93.8
1409071315	92100027	95.1
1409071316	92100101	94.9
1409071317	92100058	94.3
1409071319	92100095	95
1409071320	92100403	94.2
1409071321	92100658	95.2
1409071322	92099966	93.1
1409071323	92099981	94.2
1409071324	92100689	94.4
1409071326	92099067	94.5
1409071327	92100137	94.3
1409071328	92099868	93
1409071329	92100229	93
1409071330	92099716	94.1
1409071331	92099905	92.8
1409071333	92100108	94
1409071334	92100653	94.2
1409071335	92100657	94.3
1409071336	92100284	94.9
1409071337	92100397	94.3
1409071339	92099769	94.4
1409071340	92099847	94.3
1409071341	92099963	94.2
1409071342	92101306	94.2
1409071343	92100232	94
1409071344	92100239	94.1
1409071346	92100256	93.9
1409071347	92099957	94.3
1409071348	92100148	94
1409071349	92099904	94.1
1409071350	92100038	93

1409071351	92100130	94.3
1409071353	92099080	94.4
1409071354	92100081	94.3
1409071355	92100193	94
1409071356	92099918	94.2
1409071357	92099836	94.5
1409071358	92099309	94.4

1409072200	92099840	99.1
1409072201	92100256	99.2
1409072202	92100042	99.1
1409072203	92099781	98.9
1409072205	92099651	97.8
1409072206	92099255	98
1409072207	92099703	97.9
1409072208	92100497	99
1409072209	92099725	99
1409072210	92100018	98.6
1409072212	92099605	97.9
1409072213	92099992	97.8
1409072214	92099860	97.6
1409072215	92099949	97.5
1409072216	92099598	98.7
1409072218	92100146	97.3
1409072219	92099921	97.6
1409072220	92099901	97.6
1409072221	92099933	97.6
1409072222	92099916	97.7
1409072223	92100201	97.7
1409072225	92100069	97.7
1409072226	92100129	97.4
1409072227	92099985	97.3
1409072228	92100534	99.5
1409072229	92100125	98.4
1409072231	92099757	97.1
1409072232	92100148	96.8
1409072233	92100048	98.2
1409072234	92100180	98.5
1409072235	92098685	97.5
1409072236	92100139	97.6
1409072238	92099846	98.9
1409072239	92099948	97.6
1409072240	92100773	97.7
1409072241	92100180	98.5
1409072242	92099411	97.7
1409072243	92100022	98.8
1409072245	92100148	98.6
1409072246	92099818	97.4

1409072247	92099221	100.1
1409072248	92100847	98.9
1409072249	92099976	100.3
1409072251	92100108	100
1409072252	92100022	97.8
1409072253	92100079	98
1409072254	92099850	98
1409072255	92100076	99
1409072256	92099587	97.8
1409072258	92100353	97.7
1409072259	92100210	97.4

1409080700	92100133	96.2
1409080701	92100093	96.4
1409080702	92100117	97.3
1409080703	92100248	97.5
1409080705	92100089	97.3
1409080706	92099773	97.3
1409080707	92100167	97.2
1409080708	92100088	96.6
1409080709	92099636	97.7
1409080710	92100062	97.4
1409080712	92099969	96.4
1409080713	92100115	96.4
1409080714	92100116	96.5
1409080715	92099550	97.5
1409080716	92100314	97.5
1409080718	92100241	97.5
1409080719	92100047	96.2
1409080720	92100031	96.9
1409080721	92100054	95
1409080722	92099983	97.1
1409080723	92099946	96.3
1409080725	92099737	96.6
1409080726	92100034	96.8
1409080727	92100239	97.3
1409080728	92099840	97.4
1409080729	92100403	97.3
1409080731	92100173	98.1
1409080732	92100032	96.1
1409080733	92100083	97.1
1409080734	92099929	97.3
1409080735	92100352	97.5
1409080736	92100249	97.6
1409080738	92100095	97.2
1409080739	92099869	95
1409080740	92099232	96.7
1409080741	92099795	95.8

1409081300	92099902	94.7
1409081301	92099872	93.5
1409081302	92100135	93.4
1409081303	92100180	93.5
1409081305	92100124	92.5
1409081306	92100197	93.4
1409081307	92098798	93.4
1409081308	92099910	94.4
1409081309	92099920	92.4
1409081310	92100136	94.6
1409081312	92100200	93.5
1409081313	92100018	93.6
1409081314	92100357	93.4
1409081315	92100000	93.6
1409081316	92099957	93.6
1409081318	92100145	93.6
1409081319	92099949	93.5
1409081320	92100073	93.7
1409081321	92099540	93.6
1409081322	92099862	93.6
1409081324	92100057	94.6
1409081325	92099944	94.7
1409081326	92099806	94.5
1409081327	92099853	93.5
1409081328	92099944	93.7
1409081329	92099833	93.5
1409081331	92099838	93.3
1409081332	92099952	93.3
1409081333	92100027	93.6
1409081334	92099938	93.5
1409081335	92100073	94.6
1409081337	92100016	93.3
1409081338	92100703	94.5
1409081339	92100215	94.6
1409081340	92100043	94.7
1409081341	92099993	94.6
1409081342	92100035	93.5
1409081344	92099949	93.5
1409081345	92100073	93.5
1409081346	92100109	93.4
1409081347	92100023	93.6
1409081348	92098799	92.5
1409081350	92099893	93.6
1409081351	92100304	93.7
1409081352	92100012	93.8
1409081353	92099824	94.8
1409081354	92099596	95.8

1409081356	92100039	93.7
1409081357	92099998	94.8
1409081358	92099869	93.6
1409081359	92100040	94.8

1409082200	92099853	96.6
1409082201	92099890	97
1409082202	92097859	96.8
1409082203	92100151	96.9
1409082205	92099796	97
1409082206	92099882	96.9
1409082207	92100000	97.3
1409082208	92099996	97.4
1409082209	92100006	98.3
1409082210	92099857	96.1
1409082212	92099644	97.3
1409082213	92100585	97.1
1409082214	92100047	97.2
1409082215	92099591	97.5
1409082216	92099885	98.5
1409082217	92099831	98.4
1409082219	92100412	97.4
1409082220	92101071	98
1409082221	92100259	97.2
1409082222	92100196	97.3
1409082223	92100035	98.3
1409082225	92099886	97.2
1409082226	92100430	96.9
1409082227	92099889	94.8
1409082228	92100314	97
1409082229	92100439	97.8
1409082230	92100145	96.7
1409082232	92100291	97.3
1409082233	92100076	97.7
1409082234	92100239	98
1409082235	92099965	97.8
1409082236	92101126	96.9
1409082237	92100094	97.6
1409082239	92100453	97.5
1409082240	92100226	98
1409082241	92101326	96.4
1409082242	92100021	98.9
1409082243	92100889	96.9
1409082245	92100311	97.1
1409082246	92100543	98.2
1409082247	92099875	97.6
1409082248	92100712	96.4
1409082249	92100770	97.8

1409082250	92101134	97.7
1409082252	92100530	97.6
1409082253	92100025	97.9
1409082254	92100276	97.8
1409082255	92099817	97.6
1409082256	92100128	97.5
1409082257	92100139	97.6
1409082259	92100362	97.6

1409090700	92099978	95.9
1409090701	92100119	95.5
1409090702	92100111	96.9
1409090703	92100327	96.7
1409090705	92100819	96
1409090706	92100126	95.9
1409090707	92100133	96.9
1409090708	92099937	96.8
1409090709	92100188	95.6
1409090710	92100103	96.7
1409090712	92100000	95.8
1409090713	92099783	95.8
1409090714	92099802	96.9
1409090715	92099829	95.7
1409090716	92099966	96.9
1409090718	92100165	96.7
1409090719	92100078	96.8
1409090720	92099938	96.7
1409090721	92100138	96.5
1409090722	92099877	96.4
1409090723	92099996	95.4
1409090725	92100118	95.2
1409090726	92100027	95.5
1409090727	92099791	96.4
1409090728	92100185	96.4
1409090729	92100048	95.4
1409090730	92100024	95.7
1409090732	92099995	95.8
1409090733	92100646	95.3
1409090734	92100094	96.5
1409090735	92100043	96.7
1409090736	92099541	96.8
1409090738	92099787	96.8
1409090739	92099956	97
1409090740	92099622	97.1
1409090741	92099955	96.1
1409090742	92099953	97.1
1409090743	92100468	97.2
1409090745	92100225	97.2

1409090746	92100192	97.2
1409090747	92099987	97.3
1409090748	92100137	96.3
1409090749	92099866	96.1
1409090751	92100002	95.9
1409090752	92099876	96.7
1409090753	92101062	94.6
1409090754	92100101	96.8
1409090755	92099892	96.9
1409090756	92099997	95.9
1409090758	92100059	96.9
1409090759	92099756	97

1409091300	92100001	94.6
1409091301	92100003	92.5
1409091302	92100039	93.5
1409091303	92100008	94.6
1409091305	92100115	94.4
1409091306	92099990	93.3
1409091307	92100059	93.3
1409091308	92099940	93.3
1409091309	92099880	93.2
1409091310	92099394	93.3
1409091312	92100078	93.3
1409091313	92100135	93.4
1409091314	92100126	94.4
1409091315	92099842	93.1
1409091316	92099753	94.3
1409091317	92100127	93.1
1409091319	92100329	94.1
1409091320	92099904	94.4
1409091321	92099889	94.5
1409091322	92099060	93
1409091323	92099972	94.1
1409091325	92099791	93
1409091326	92100003	94.5
1409091327	92099969	94.5
1409091328	92100308	94.3
1409091329	92099991	93.3
1409091330	92100404	94
1409091332	92100141	93.1
1409091333	92100068	93
1409091334	92099762	94.5
1409091335	92100145	94.4
1409091336	92100207	92.5
1409091338	92099937	93.4
1409091339	92100712	95.4
1409091340	92100160	95.3

1409091341	92100013	94.2
1409092200	92100026	96
1409092201	92099936	96
1409092202	92099843	94.8
1409092203	92096027	94.6
1409092205	92099816	94.9
1409092206	92099807	94
1409092207	92099919	96
1409092208	92099996	95.9
1409092209	92099430	94.7
1409092211	92099993	95.9
1409092212	92099731	96
1409092213	92099813	96.2
1409092214	92099544	94.8
1409092215	92099211	95.1
1409092216	92099601	95
1409092218	92100012	96.3
1409092219	92099919	94.1
1409092220	92099928	96.2
1409092221	92099857	96.1
1409092222	92100039	95
1409092224	92100067	94.9
1409092225	92099704	94.9
1409092226	92099768	94
1409092227	92100075	93.8
1409092228	92099849	95.9
1409092230	92098581	94.8
1409092231	92099995	95.8
1409092232	92100052	94.6
1409092233	92100000	94.7
1409092234	92099992	94.8
1409092235	92099589	95.4
1409092237	92099075	94.3
1409092238	92099614	94.2
1409092239	92100251	94.3
1409092240	92100368	95.4
1409092241	92100054	94.6
1409092243	92099536	94.4
1409092244	92099982	94.2
1409092245	92099781	94.5
1409092246	92100211	94.4
1409092247	92100180	95.3
1409092249	92100200	94.3
1409092250	92100124	94.2
1409092251	92099773	94.3
1409092252	92099871	94.3
1409092253	92099995	95.2

1409092254	92099836	94.2
1409092256	92099989	94.2
1409092257	92100003	94.1
1409092258	92099817	94.1
1409092259	92100208	94.1

1409100700	92100027	93.2
1409100701	92100078	93.9
1409100702	92100000	95.1
1409100703	92100138	92.2
1409100705	92100740	94.7
1409100706	92100131	93.6
1409100707	92100616	93.5
1409100708	92100006	94
1409100709	92100006	93.9
1409100711	92100084	94.8
1409100712	92100060	92.6
1409100713	92100261	94.8
1409100714	92100726	95
1409100715	92100109	95
1409100717	92100431	93.8
1409100718	92100052	95
1409100719	92099929	93.7
1409100720	92100244	94
1409100721	92099975	95.1
1409100722	92099630	94
1409100724	92099816	93.9
1409100725	92100287	94.9
1409100726	92099693	94.8
1409100727	92099805	94.9
1409100728	92099885	93.7
1409100730	92100219	92.8
1409100731	92100173	93.5
1409100732	92100171	94.7
1409100733	92100225	93.4
1409100734	92100055	94.6
1409100736	92100331	93.5
1409100737	92099994	93.4
1409100738	92099761	93.6
1409100739	92100345	94.8
1409100740	92099864	95
1409100741	92099381	95
1409100743	92099822	94.8
1409100744	92099541	96
1409100745	92100299	94.7
1409100746	92100329	93.5
1409100747	92100207	93.5
1409100749	92100002	93.3

1409100750	92099732	94.5
1409100751	92100260	93.4
1409100752	92100326	93.3
1409100753	92100002	93.5
1409100755	92100066	93.4
1409100756	92100092	92.3
1409100757	92099742	93.4
1409100758	92100275	93.3
1409100759	92100581	93.3

1409101300	92099834	94.3
1409101301	92100279	94.5
1409101302	92100230	93.1
1409101303	92100260	94.3
1409101305	92100096	93.3
1409101306	92100332	93.5
1409101307	92098892	93.4
1409101308	92100230	94.5
1409101309	92100257	94.4
1409101310	92100546	94.5
1409101312	92100289	93.4
1409101313	92100155	94.5
1409101314	92099999	93.4
1409101315	92099816	94.7
1409101316	92099956	93.2
1409101317	92100035	93.1
1409101319	92099832	93.4
1409101320	92100341	95.7
1409101321	92101090	93.5
1409101322	92100163	93.2
1409101323	92099865	93.2
1409101325	92100192	93.2
1409101326	92100304	93.5
1409101327	92100080	93.6
1409101328	92100083	93.6
1409101329	92100006	94.7
1409101330	92100598	93.4
1409101332	92099773	94.7
1409101333	92100461	94.6
1409101334	92099871	94.8
1409101335	92100169	93.5
1409101336	92099798	94.7
1409101338	92099525	93.5
1409101339	92100159	92.6
1409101340	92099893	94.6
1409101341	92099967	93.5
1409101342	92100100	93.6
1409101343	92099995	93.6

1409101345	92100478	95.9
1409101346	92099996	93.6
1409101347	92101286	92.5
1409101348	92100079	94.6
1409101349	92099272	93.6
1409101350	92100223	93.7
1409101352	92099856	93.8
1409101353	92099825	93.7
1409101354	92100004	93.7
1409101355	92100666	93.7
1409101356	92100014	93.7
1409101358	92100018	93.5
1409101359	92099358	93.6

1409102200	92099743	95.4
1409102201	92099998	92.2
1409102202	92100109	94.2
1409102203	92099846	94.5
1409102205	92099948	94.5
1409102206	92100026	92
1409102207	92099964	94.5
1409102208	92099907	95.3
1409102209	92099985	95.6
1409102211	92100053	94.5
1409102212	92099972	93.5
1409102213	92100062	94.7
1409102214	92099952	95.5
1409102215	92099621	94.4
1409102216	92099564	94.5
1409102218	92098855	95
1409102219	92099867	94.6
1409102220	92099870	93.3
1409102221	92099111	94.2
1409102223	92099743	95.2
1409102224	92100064	95
1409102225	92099654	94.4
1409102226	92099761	95.6
1409102227	92099799	93.6
1409102229	92100051	94.9
1409102230	92100181	94.6
1409102231	92100002	94.9
1409102232	92100038	94.7
1409102233	92099891	94.8
1409102235	92099834	95.9
1409102236	92099860	93.7
1409102237	92100047	95.5
1409102238	92100002	95.4
1409102239	92099931	94.3

1409102240	92099995	95.3
1409102242	92099951	94.1

1409110700	92099999	96.3
1409110701	92099868	94.8
1409110702	92099882	96
1409110703	92100327	96
1409110705	92100423	95.9
1409110706	92100026	97.2
1409110707	92099933	95
1409110708	92100241	96.2
1409110709	92099825	96.1
1409110710	92100055	96.2
1409110712	92099737	95.1
1409110713	92100077	96.3
1409110714	92100241	95.2
1409110715	92099987	95.3
1409110716	92100426	96.2
1409110718	92099960	96.2
1409110719	92099937	95
1409110720	92100022	95
1409110721	92099929	95.1
1409110722	92099918	95.3
1409110724	92099881	96.1
1409110725	92099890	96.1
1409110726	92100200	95.1
1409110727	92100015	95
1409110728	92100373	97.1
1409110729	92099999	94.9
1409110731	92100174	95.8
1409110732	92099888	94.8
1409110733	92099845	95.7
1409110734	92100319	94.6
1409110735	92100127	94.7
1409110737	92100307	94.6
1409110738	92099973	95.9
1409110739	92100301	95.8
1409110740	92099982	95
1409110741	92100033	96
1409110743	92099766	94.8
1409110744	92099670	94.8
1409110745	92099651	94.6
1409110746	92100037	94.7
1409110747	92100218	95.9
1409110748	92099963	94.7
1409110750	92099935	95.7
1409110751	92100508	95.6
1409110752	92099598	94.4

1409110753	92099724	94.2
1409110754	92099598	95.4
1409110756	92099764	94.4
1409110757	92099565	94.3
1409110758	92099831	96.5
1409110759	92099895	95.1

1409111416	92100184	94.2
1409111417	92100275	94
1409111418	92099898	93.9
1409111419	92100175	95
1409111420	92100092	93.9
1409111422	92099998	93.8
1409111423	92099987	93.9
1409111424	92099401	94
1409111425	92099996	96
1409111426	92099879	94.7
1409111427	92100205	94
1409111429	92100885	94.1
1409111430	92100619	94
1409111431	92100271	94.2
1409111432	92100511	95
1409111433	92099913	94.1
1409111435	92099942	94.1
1409111436	92100096	94.2
1409111437	92100000	94.2
1409111438	92099713	93.2
1409111439	92100058	94.2
1409111440	92099786	95.1
1409111442	92099981	95
1409111443	92099857	95.1
1409111444	92099928	94.4
1409111445	92100178	94.4
1409111446	92100178	94.4
1409111447	92100136	94.2
1409111449	92099741	94.2
1409111450	92099294	93.2
1409111451	92099930	95.3
1409111452	92100156	94.3
1409111453	92099848	94.4
1409111455	92100422	93.1
1409111456	92100012	94.3
1409111457	92101090	94.4
1409111458	92101502	94.3
1409111459	92099369	94.3

1409112200	92100396	97.9
1409112201	92100022	98

1409112202	92100071	99
1409112203	92099972	98.8
1409112204	92100457	98.6
1409112206	92100122	99.7
1409112207	92100634	97.8
1409112208	92100711	97.5
1409112209	92100273	98.3
1409112210	92100230	99.2
1409112212	92100046	98.1
1409112213	92100200	98.2
1409112214	92100130	97.3
1409112215	92099978	97.1
1409112216	92099928	98.5
1409112217	92100118	98.6
1409112219	92100366	98.7
1409112220	92100283	98.7
1409112221	92100332	98
1409112222	92099955	99
1409112223	92100057	98.9
1409112224	92100164	96.9
1409112226	92100053	98.3
1409112227	92100126	98.4
1409112228	92100483	99
1409112229	92100160	98.3
1409112230	92100014	98.2
1409112231	92099961	98.1
1409112233	92099802	98.3
1409112234	92099882	99.3
1409112235	92100392	99
1409112236	92100181	98.5
1409112237	92099726	98.5
1409112239	92100215	98.5
1409112240	92100018	99.6
1409112241	92100132	99.3
1409112242	92100997	98.3
1409112243	92100463	100.1
1409112244	92100167	98.5
1409112246	92100718	98.7
1409112247	92100039	98.3
1409112248	92099914	98.4
1409112249	92099971	99.4
1409112250	92100070	98.8
1409112251	92099960	98.7
1409112253	92100186	99.4
1409112254	92100233	98.1
1409112255	92099987	98.7
1409112256	92099912	98.5
1409112257	92099793	98.4

1409112259	92100120	99.2
1409120700	92099873	94.8
1409120701	92100034	95.9
1409120702	92100274	96.1
1409120704	92100202	96.5
1409120705	92099638	96.4
1409120706	92099948	95.5
1409120707	92100079	96.4
1409120708	92100081	96.6
1409120709	92099872	94.7
1409120711	92100025	96
1409120712	92099995	95.6
1409120713	92099885	95.9
1409120714	92100536	95.8
1409120715	92100090	97
1409120716	92100018	95.9
1409120718	92100058	96.2
1409120719	92100003	96.2
1409120720	92100020	96.2
1409120721	92100545	98.5
1409120722	92100420	96.4
1409120724	92100297	97.6
1409120725	92099874	96.6
1409120726	92100131	96
1409120727	92100186	97.2
1409120728	92100230	97.2
1409120729	92100510	96.2
1409120731	92099871	96.3
1409120732	92100634	97.5
1409120733	92099872	96.4
1409120734	92100071	96.1
1409120735	92100270	96.9
1409120736	92100042	97.3
1409120738	92099956	96.1
1409120739	92099426	97.4
1409120740	92100055	96.4
1409120741	92100369	96.4
1409120742	92099970	97.6
1409120744	92099979	97.7
1409120745	92099891	97.7
1409120746	92099706	97.7
1409120747	92100106	97.8
1409120748	92101111	97.9
1409120749	92100583	98.9
1409120751	92100169	97.7
1409120752	92099892	96.7
1409120753	92100234	96.7

1409120754	92100167	96.5
1409120755	92100071	96.6

1409121300	92100025	94.1
1409121301	92100211	94.9
1409121302	92100074	94
1409121303	92100063	94
1409121304	92100022	94.9
1409121306	92100099	94
1409121307	92099942	95.1
1409121308	92099989	95.1
1409121309	92100011	94
1409121310	92099954	95
1409121312	92100070	94.9
1409121313	92100160	93.8
1409121314	92100169	94
1409121315	92100236	93.6
1409121316	92100052	93.9
1409121317	92100148	94.9
1409121319	92099986	94.2
1409121320	92099702	94.1
1409121321	92099970	94.1
1409121322	92099872	94.9
1409121323	92100244	93.8
1409121324	92100247	94.1
1409121326	92100061	94.4
1409121327	92100329	95.1
1409121328	92100274	94.1
1409121329	92099962	93.9
1409121330	92100178	95
1409121331	92100142	94
1409121333	92100068	93.9
1409121334	92100295	94.1
1409121335	92100043	94
1409121336	92100087	94.2
1409121337	92099901	94.2
1409121338	92099674	94.3
1409121340	92099544	94.5
1409121341	92100746	95.3
1409121342	92100959	94.5
1409121343	92101281	95.5
1409121344	92099986	95.4
1409121345	92100666	94.5
1409121347	92099707	94.3
1409121348	92100003	94.5
1409121349	92099980	94.5
1409121350	92099876	94.5
1409121351	92099916	94.2

1409121352	92099692	94.4
1409121354	92099647	95.3
1409121355	92099742	94.3
1409121356	92100485	95.2
1409121357	92099937	94.3
1409121358	92099519	94.3
1409121359	92100068	94.3

1409122200	92099977	97
1409122201	92099790	96.9
1409122202	92100156	96.9
1409122203	92100024	97.9
1409122204	92100099	97.8
1409122206	92099899	96.7
1409122207	92100008	96.5
1409122208	92100236	96.4
1409122209	92100227	96.1
1409122210	92100475	96.7
1409122211	92100121	96.4
1409122213	92099645	96.3
1409122214	92099788	96.5
1409122215	92100333	96.1
1409122216	92100117	97
1409122217	92100224	96
1409122218	92100056	96.7
1409122220	92100113	97.1
1409122221	92099836	96.5
1409122222	92100025	95
1409122223	92100024	94.7
1409122224	92100178	96.5
1409122225	92099956	95.3
1409122227	92100322	96.5
1409122228	92099915	96.6
1409122229	92099783	95.4
1409122230	92100038	95.2
1409122231	92100169	95.5
1409122233	92100259	95.7
1409122234	92100058	95.8
1409122235	92099983	95.8
1409122236	92099971	96.3
1409122237	92099860	96.4
1409122238	92098827	96
1409122240	92099722	96.7
1409122241	92100026	96
1409122242	92100103	95.7
1409122243	92099957	95.9
1409122244	92099898	96
1409122245	92100071	96.1

1409122247	92100097	96
1409122248	92099937	95
1409122249	92100101	96.3
1409122250	92100003	96.5
1409122251	92100111	96.2
1409122252	92100335	96.6
1409122254	92099913	97.6
1409122255	92099928	96.7
1409122256	92100613	97.7
1409122257	92100044	96.7
1409122258	92099907	96.8
1409122259	92100500	97.4

1409130700	92099834	97.6
1409130701	92100027	97.5
1409130702	92100010	97.8
1409130703	92099916	95.5
1409130705	92101014	97.7
1409130706	92100177	97.4
1409130707	92100403	97.5
1409130708	92099973	96.6
1409130709	92100058	96.4
1409130710	92100338	98.3
1409130712	92099942	97.4
1409130713	92100171	97.1
1409130714	92100185	97
1409130715	92100115	96.1
1409130716	92100024	97.5
1409130718	92100488	97.3
1409130719	92099629	98.3
1409130720	92100135	97.3
1409130721	92100214	97.2
1409130722	92099880	96.1
1409130723	92099970	95.1
1409130725	92099987	96.1
1409130726	92100347	95.6
1409130727	92100127	95.7
1409130728	92099930	95.6
1409130729	92100216	95.6
1409130730	92100157	95.7
1409130732	92099998	95.3
1409130733	92100354	96.2
1409130734	92100401	97
1409130735	92099976	96.4
1409130736	92100051	96.4
1409130738	92099874	95.3
1409130739	92099643	95.9
1409130740	92100066	96.8

1409130741	92099247	96
1409130742	92099671	94.9
1409130743	92100429	95
1409130745	92100526	96.7
1409130746	92100663	94.8
1409130747	92100145	94.7
1409130748	92100067	95.7
1409130749	92100222	94.7
1409130750	92100097	95.5
1409130752	92099833	96
1409130753	92100156	96
1409130754	92100352	95.8
1409130755	92100094	95.7
1409130756	92101113	94.9
1409130757	92100026	96.2
1409130759	92100995	95.1

1409131300	92100084	94
1409131301	92100011	94.1
1409131302	92100031	94.7
1409131303	92099032	93.8
1409131305	92099365	93.8
1409131306	92100037	94.8
1409131307	92100097	94
1409131308	92100047	94.9
1409131309	92099641	93.9
1409131310	92099873	95
1409131312	92099684	93.8
1409131313	92099898	94.8
1409131314	92099986	93.7
1409131315	92100027	94
1409131316	92099979	95
1409131317	92100033	94
1409131319	92100035	95
1409131320	92100081	93.9
1409131321	92101147	93.7
1409131322	92100504	93.9
1409131323	92100440	93.8
1409131324	92100306	94
1409131326	92100122	93.8
1409131327	92099994	94
1409131328	92099927	94.2
1409131329	92099832	93.8
1409131330	92100131	95
1409131332	92101127	93.9
1409131333	92099985	94.8
1409131334	92099738	94
1409131335	92098982	94.8

1409131336	92100010	94.2
1409131337	92100093	94.2
1409131339	92100110	95.1
1409131340	92099977	95.2

1409132200	92100215	98.7
1409132201	92100463	97.6
1409132202	92099975	98.9
1409132203	92099918	98.7
1409132204	92100113	98.8
1409132206	92099941	100.6
1409132207	92100047	98.7
1409132208	92099988	99.8
1409132209	92099833	99
1409132210	92100007	99.8
1409132212	92099966	100.2
1409132213	92100023	100
1409132214	92100335	99.8
1409132215	92099797	99.4
1409132216	92099889	99
1409132217	92100294	98.6
1409132219	92100031	99
1409132220	92099934	99.7
1409132221	92099959	98.6
1409132222	92099725	99.8
1409132223	92100010	99.7
1409132224	92099960	99.5
1409132226	92099951	98.9
1409132227	92100010	97.9
1409132228	92100026	99.7
1409132229	92100349	99.7
1409132230	92100362	99.4
1409132232	92100923	99.3
1409132233	92100078	99.3
1409132234	92100227	98.1
1409132235	92100067	99
1409132236	92100143	97.9
1409132237	92100065	98.7
1409132239	92100164	99.9
1409132240	92100109	100.1
1409132241	92100106	98
1409132242	92100014	99.4
1409132243	92100020	99
1409132244	92099600	98.9
1409132246	92100003	98.9
1409132247	92100061	98.9
1409132248	92100069	99
1409132249	92100050	99.2

1409132250	92099974	99.5
1409132252	92099971	98.4
1409132253	92100056	99.2
1409132254	92100032	98.3
1409132255	92100215	98.1
1409132256	92099933	100.4
1409132257	92099837	98.2
1409132259	92100188	99.2

1409140700	92099981	97.3
1409140701	92100004	97.3
1409140702	92100237	97
1409140703	92100217	95.7
1409140705	92099904	97.5
1409140706	92100263	96
1409140707	92100038	97.5
1409140708	92100630	96.3
1409140709	92099785	97.4
1409140710	92100142	97.3
1409140712	92099636	97.2
1409140713	92100258	96.1
1409140714	92099735	97.2
1409140715	92100060	97.6
1409140716	92099963	97.7
1409140718	92099985	97.9
1409140719	92099921	96.7
1409140720	92100084	96.5
1409140721	92100604	96.4
1409140722	92099367	96.6
1409140723	92099959	97.7
1409140725	92099988	96.6
1409140726	92099999	97.6
1409140727	92099296	97.4
1409140728	92100082	97.3
1409140729	92099884	96.2
1409140731	92099572	96.1
1409140732	92099835	97.1
1409140733	92100046	96.8
1409140734	92100172	96.9
1409140735	92100036	96.8
1409140737	92099983	96.3
1409140738	92100165	96.9
1409140739	92100006	97.1
1409140740	92099991	96.3
1409140741	92099935	97
1409140743	92100232	98
1409140744	92099078	97.2
1409140745	92099817	96

1409140746	92099909	97.3
1409140747	92100000	96
1409140749	92099811	97
1409140750	92100054	97.1
1409140751	92100039	96.9
1409140752	92100808	96.7
1409140753	92099975	96.6
1409140755	92100448	94.3
1409140756	92101127	96.5
1409140757	92100136	95
1409140758	92099332	94.3
1409140759	92099946	96.5

1409141300	92099982	94.7
1409141301	92100098	93.9
1409141302	92099866	93.8
1409141303	92099897	93.9
1409141304	92099636	94.8
1409141306	92100246	93.7
1409141307	92099835	93.6
1409141308	92100112	93.8
1409141309	92100072	94
1409141310	92099957	94.1
1409141312	92100176	94.8
1409141313	92099986	94
1409141314	92099930	94
1409141315	92099975	94.6
1409141316	92099976	93.7
1409141317	92099738	93.7
1409141319	92099928	94.8
1409141320	92099900	93.6
1409141321	92100130	94.7
1409141322	92099730	92.5
1409141323	92099758	93.8
1409141324	92100005	94.1
1409141326	92099825	94.1
1409141327	92100334	94.1
1409141328	92100003	93.7
1409141329	92100311	94.1
1409141330	92100342	93.9
1409141332	92099696	92.9
1409141333	92100289	93.9
1409141334	92100456	94
1409141335	92099884	94.7
1409141336	92100073	94
1409141337	92100572	93.8
1409141339	92100470	93.8
1409141340	92100510	93.8

1409141341	92100304	93.8
1409141342	92099952	94.8
1409141343	92099862	93.8
1409141344	92100033	92.7
1409141346	92100148	94.7
1409141347	92099841	94
1409141348	92099950	93.9
1409141349	92099823	94.8
1409141350	92099651	94.8
1409141351	92100097	93.9
1409141353	92099880	93.7
1409141354	92100316	93.8
1409141355	92100025	93.8
1409141356	92099834	94.8
1409141357	92099515	95
1409141359	92100004	93.8

1409142200	92100041	98.5
1409142201	92100115	100.4
1409142202	92099779	100.4
1409142203	92099680	100.5
1409142205	92099985	100.5
1409142206	92100483	99.6
1409142207	92099732	100.6
1409142208	92099131	98.6
1409142209	92100215	99.4
1409142210	92100032	99.4
1409142212	92099617	99.4
1409142213	92100120	99.3
1409142214	92100134	100.6
1409142215	92100019	101
1409142216	92099970	99.6
1409142217	92101501	101.6
1409142219	92099467	101
1409142220	92101740	99.6
1409142221	92099527	100.9
1409142222	92098598	101
1409142223	92099647	100.8
1409142225	92100082	100.9
1409142226	92100358	100.6
1409142227	92100900	100.7
1409142228	92099767	98.3
1409142229	92100295	99.5
1409142230	92099824	101.3
1409142232	92100066	99.2
1409142233	92100316	99.3
1409142234	92099904	99.8
1409142235	92100334	100.5

1409142236	92100983	99.7
1409142237	92100223	100.7
1409142239	92099982	101
1409142240	92100019	100.1
1409142241	92099978	100

APPENDIX 2: UPPER AIR DATA OBTAINED BY WRF-ARW VERSION

3.4

POINT ONE

Date/Time	: 2015-06-18 9 :00UTC	(T+9)					
Location:	34d 24m	11 12s	N, 33d	18m 8.87sE			
Height	Pressure	V	apP	ressur	e Temperature	RH	N
m	hPa	h	Pa		K	%	
2	1006.7			27.1	297.8	88.9	376.5
35	1002.6			26	297.5	86.7	371.1
40	1002			25.9	297.4	86.8	370.8
45	1001.5			25.9	297.4	86.9	370.6
50	1000.9			25.9	297.3	87	370.3
75	998.1			25.6	297.1	87.4	369
100	995.2			25.4	296.9	87.9	367.7
125	992.4			25.1	296.6	87.9	366
150	989.5			24.8	296.5	87.8	364.2
175	986.7			24.5	296.3	87.7	362.4
200	983.9			24.2	296.1	87.6	360.7
225	981.1			23.2	296.1	84.1	355.6
250	978.3			22.1	296.2	79.7	350
275	975.5			21	296.3	75.4	344.6
300	972.7			20	296.4	71.1	339.4
325	969.9			19	296.5	66.8	334.4
350	967.1			18.1	296.7	63.4	329.9
375	964.4			17.3	296.8	60.4	325.6
400	961.6			16.6	296.9	57.3	321.4
425	958.9			15.8	297.1	54.2	317.3
450	956.1			15.1	297.2	51.2	313.4
275	975.5			21	296.3	75.4	344.6
500	950.7			13.9	297.4	45.9	306.5
525	948			13.5	297.4	44.8	304.3
550	945.3			13.1	297.4	43.7	302.1
575	942.6			12.8	297.3	42.5	299.9
600	940			12.4	297.3	41.4	297.7
625	937.3			12.1	297.3	40.3	295.6
650	934.6			11.7	297.3	39.1	293.5
675	931.9			11.4	297.3	38	291.5
700	929.2			11.2	297.2	37.2	289.8
725	926.6			11	297.1	36.9	288.5
750	924			10.9	297	36.6	287.3
775	921.4			10.7	296.9	36.4	286.1
800	918.7			10.6	296.8	36.1	284.9
825	916.1			10.4	296.7	35.8	283.8

850	913.5			10.3	296.6	35.5	282.6
875	910.9			10.1	296.6	35.2	281.4
900	908.2			10	296.5	34.9	280.2
925	905.6			9.9	296.4	34.7	279.1
950	903			9.8	296.2	34.6	278.2
975	900.4			9.7	296.1	34.8	277.5
1000	897.9			9.7	295.9	34.9	276.7
1050	892.7			9.6	295.7	35.2	275.3
1100	887.6			9.5	295.4	35.6	273.9
1150	882.4			9.4	295.1	35.9	272.5
1200	877.3			9.4	294.7	36.6	271.5
1250	872.3			9.4	294.4	37.4	270.5
1300	867.3			9.4	294.1	38.2	269.6
1350	862.2			9.5	293.7	39	268.7
1400	857.3			9.5	293.3	40.3	268
1450	852.3			9.6	292.9	41.6	267.4
1500	847.4			9.6	292.5	42.9	266.7
1550	842.5			9.7	292.1	44.1	266
1600	837.6			9.6	291.7	45.2	265.1
1650	832.7			9.6	291.3	46.3	264.2
1700	827.9			9.6	290.9	47.5	263.2
1750	823			9.5	290.5	47.9	261.8
1800	818.3			9.2	290.2	47.8	259.7
1850	813.5			9	289.8	47.6	257.8
1900	808.8			8.7	289.4	47.4	255.8
1950	804			8.5	289	47.3	253.9
2000	799.3			8.3	288.6	47.1	251.9
2100	790			7.5	288	44.4	246.4
2200	780.7			6.7	287.4	41.6	241
2300	771.5			6	286.7	38.8	236
2400	762.3			5.4	286.1	35.9	231.1
2500	753.3			4.7	285.5	33.2	226.4
2600	744.4			4.2	284.9	30.5	221.9
2700	735.5			3.7	284.4	27.8	217.7
2800	726.7			3.2	283.8	25.5	213.8
2900	718.1			2.9	283.2	23.6	210.2
3000	709.4			2.5	282.5	21.8	206.7

POINT TWO

Date/Time	: 2015-08	- 30	9	:00UTC	(T+9)		
Location:	33d 47m	17	48s	N, 33d	45m 51.56sE		
Height	Pressure	V	apP	ressur	e Temperature	RH	N
m	hPa	h	Pa		K	%	
2	1010.5			23.2	302.1	58.6	354.3
35	1006.4			18.7	301.8	47.9	335.4
40	1005.8			18.6	301.7	47.8	335.1
45	1005.3			18.6	301.7	47.8	334.8
50	1004.7			18.5	301.6	47.8	334.4
75	1001.9			18.2	301.4	47.7	332.8
100	999.1			17.9	301.2	47.6	331.2
125	996.3			17.8	300.9	47.7	330.1
150	993.5			17.6	300.7	47.9	328.9
175	990.7			17.4	300.5	48.1	327.8
200	987.8			17.2	300.2	48.3	326.7
225	985.1			17	300	48	325
250	982.3			16.7	299.8	47.8	323.3
275	979.5			16.4	299.6	47.5	321.7
300	976.7			16.1	299.4	47.2	320
325	973.9			15.8	299.2	46.9	318.4
350	971.1			15.2	299.1	45.7	315.6
375	968.4			14.7	298.9	44.4	312.6
400	965.6			14.1	298.8	43	309.7
425	962.9			13.6	298.7	41.7	306.9
450	960.1			13.1	298.6	40.3	304.2
275	979.5			16.4	299.6	47.5	321.7
500	954.7			12.2	298.3	38	299.3
525	952			11.9	298.2	37.4	297.6
550	949.3			11.6	298.1	36.8	295.8
575	946.6			11.3	297.9	36.2	294.1
600	943.9			11	297.8	35.6	292.4
625	941.2			10.8	297.7	35	290.7
650	938.5			10.5	297.5	34.4	289
675	935.8			10.2	297.4	33.8	287.4
700	933.2			10	297.3	33.2	285.8
725	930.5			9.7	297.1	32.6	284.1
750	927.9			9.5	297	32.1	282.5
775	925.3			9.2	296.9	31.5	280.9
800	922.6			9	296.7	30.9	279.4
825	920			8.8	296.6	30.4	277.8
850	917.4			8.5	296.5	29.8	276.3

875	914.7			8.3	296.3	29.2	274.8
900	912.1			8.1	296.2	28.7	273.3
925	909.4			7.9	296.1	28.1	271.9
950	906.8			7.7	295.9	27.7	270.6
975	904.2			7.6	295.8	27.4	269.5
1000	901.7			7.4	295.6	27.2	268.3
1050	896.5			7.1	295.3	26.7	266.1
1100	891.3			6.9	295	26.1	263.9
1150	886.1			6.6	294.7	25.6	261.7
1200	881			6.5	294.4	25.6	260.1
1250	875.9			6.3	294	25.7	258.6
1300	870.9			6.2	293.6	25.8	257
1350	865.8			6.1	293.2	25.9	255.6
1400	860.8			6	292.8	26.1	254.2
1450	855.8			5.9	292.5	26.4	252.9
1500	850.8			5.8	292.1	26.6	251.5
1550	845.8			5.8	291.7	27	250.3
1600	840.9			5.7	291.2	27.7	249.3
1650	836			5.7	290.8	28.3	248.3
1700	831.1			5.7	290.4	29	247.3
1750	826.3			5.8	290	30.2	246.7
1800	821.5			5.9	289.5	31.7	246.2
1850	816.7			5.9	289.1	33.2	245.8
1900	811.9			6	288.6	34.7	245.4
1950	807.1			6.1	288.1	36.2	244.9
2000	802.3			6.2	287.7	37.7	244.5
2100	793			6.4	286.7	41.6	243.6
2200	783.6			6.5	285.7	45.6	242.7
2300	774.3			6.7	284.8	49.5	241.8
2400	765			6.7	283.8	52.6	240.3
2500	755.9			6.5	283	53.4	237.4
2600	746.9			6.2	282.1	54.3	234.5
2700	737.8			5.9	281.3	55.2	231.6
2800	728.9			5.4	280.5	53.4	227.5
2900	720.2			4.8	279.9	49.8	222.7
3000	711.4			4.3	279.2	46.2	218.3

POINT THREE

Date/Time	: 2015-07-12 9 :00UTC	(T+9)					
Location:	32d 30m	49 68s	N, 34d	37m 42.44sE			
Height	Pressure	V	apP	ressur	e Temperature	RH	N
m	hPa	h	Pa		K	%	
2	1006.8			25.4	298.5	79.5	368
35	1002.8			23.7	298.1	76.2	360.7
40	1002.2			23.7	298	76.2	360.4
45	1001.6			23.6	298	76.3	360.2
50	1001			23.6	297.9	76.4	359.9
75	998.2			23.4	297.7	76.9	358.7
100	995.4			23.2	297.4	77.4	357.5
125	992.5			23.1	297.2	78.1	356.6
150	989.7			23	296.9	78.8	355.7
175	986.9			22.8	296.7	79.6	354.9
200	984.1			22.7	296.5	80.3	354
225	981.3			22.6	296.2	81.2	353.2
250	978.5			22.5	296	82	352.4
275	975.7			22.4	295.7	82.9	351.6
300	972.9			22.3	295.5	83.7	350.9
325	970.1			22.2	295.3	84.6	350.1
350	967.3			22.1	295	85.6	349.3
375	964.5			22.1	294.8	86.5	348.6
400	961.7			22	294.5	87.5	347.9
425	959			21.9	294.3	88.5	347.2
450	956.2			21.8	294	89.5	346.4
475	953.4			21.7	293.7	90.5	345.6
500	950.7			21.3	293.6	89.7	343.4
525	948			20.7	293.5	87.8	340.2
550	945.2			20.1	293.4	85.9	337
575	942.5			19.5	293.2	84	333.9
600	939.8			18.9	293.1	82.1	330.9
625	937.1			18.3	293	80.2	327.9
650	934.4			17.8	292.9	78.3	325
675	931.7			17.3	292.7	76.4	322.1
700	929			16.8	292.6	74.9	319.5
725	926.4			16.4	292.6	73.4	317.1
750	923.7			16	292.5	72	314.7
775	921.1			15.6	292.4	70.6	312.4
800	918.4			15.2	292.3	69.2	310.1
825	915.8			14.8	292.2	67.8	307.8
850	913.2			14.4	292.1	66.4	305.6
875	910.5			14	292	65	303.3
900	907.9			13.7	291.9	63.6	301.2

925	905.2			13.3	291.8	62.2	299
950	902.6			12.8	291.8	60.3	296.2
975	900			12.3	291.7	58.2	293.3
1000	897.4			11.8	291.6	56.2	290.4
1050	892.1			10.8	291.5	52.1	285
1100	886.9			9.9	291.4	48	279.8
1150	881.6			9.1	291.3	43.9	274.9
1200	876.5			8.2	291.2	40.1	269.6
1250	871.4			7.3	291.1	36.3	264.6
1300	866.3			6.6	290.9	32.5	260
1350	861.2			5.8	290.9	28.9	255.4
1400	856.2			5	290.8	25.5	250.6
1450	851.2			4.3	290.8	22.1	246.2
1500	846.2			3.7	290.7	18.7	242.3
1550	841.3			3.3	290.6	16.4	239
1600	836.3			2.9	290.6	14.7	236.1
1650	831.4			2.5	290.5	13.1	233.3
1700	826.5			2.2	290.4	11.4	230.8
1750	821.8			2.1	290.2	10.8	229
1800	817			2	290	10.4	227.4
1850	812.2			1.9	289.8	10	225.8
1900	807.5			1.8	289.5	9.6	224.3
1950	802.7			1.7	289.3	9.1	222.8
2000	798			1.6	289.1	8.7	221.1
2100	788.7			1.2	288.8	7.3	217.4
2200	779.5			0.9	288.4	5.9	213.9
2300	770.2			0.7	288.1	4.5	210.7
2400	761.1			0.5	287.8	3.4	207.6
2500	752.2			0.3	287.5	2.6	204.6
2600	743.3			0.2	287.1	1.8	201.8
2700	734.4			0.1	286.8	1	199.3
2800	725.7			0.1	286.5	0.7	197
2900	717.2			0.1	286	0.6	194.9
3000	708.6			0.1	285.6	0.5	192.8

APPENDIX 3: L.C.D MONITOR PROGRAMMING CODE

S104FFBDE05F

S104FFBFC07D

S11FFDD0E200E21FE232E269E28BE2BDE2C8E2D8E2EAE33CE35DE372E387E399F
B

S123E2004F4C87F6AF019EE10686270D4D2708410D05410A0220EA99814A9EE70598
819E28

S123E220E605270C4A270987F6E70186AF014BF798819EE605271AF6898B9EFE0BF1
8A88CE

S123E24026104A270CAF019E6C0A26EB9E6C0920E6988587A487879EE606A4789EE
706860C

S123E2609EEA059EE705868481F6898B9EFE0BFA8A8827DDF6898B9EFE0BF18A88
26D3AFDB

S123E280019E6C0A26E39E6C0920DEF6898B9EFE0BFA8A8827BBF6CDED8F898B9
EFE0B872B

S123E2A0F6CDED8F879EE6029EE10186868A8826A1AF019E6C0A26D39E6C0920C
EF62716B8S104FFBDE05F

S104FFBFC07D

S11FFDD0E200E21FE232E269E28BE2BDE2C8E2D8E2EAE33CE35DE372E387E399F
B

S123E2004F4C87F6AF019EE10686270D4D2708410D05410A0220EA99814A9EE70598
819E28

S123E220E605270C4A270987F6E70186AF014BF798819EE605271AF6898B9EFE0BF1
8A88CE

S123E24026104A270CAF019E6C0A26EB9E6C0920E6988587A487879EE606A4789EE
706860C

S123E2609EEA059EE705868481F6898B9EFE0BFA8A8827DDF6898B9EFE0BF18A88
26D3AFDB

S123E280019E6C0A26E39E6C0920DEF6898B9EFE0BFA8A8827BBF6CDED8F898B9
EFE0B872B

S123E2A0F6CDED8F879EE6029EE10186868A8826A1AF019E6C0A26D39E6C0920C
EF62716B8

S123E2C0CDED8FF7AF0120F5F6270BAF0187F6CDED8FF7864BF598814F7D27094C
2704AF9F

S123E2E00120F699819EE70598819EE6059E6D0927489EE6094A87899EEB018897240
58BF6

S123E3009E6C018A86F6271187E601879EE602E70186A701AF014D26EFE7019EEE03
898A83

S123E3209EEE069EE6094A87899EEB01889724058B9E6C018A869EE605F798819EE6
05279F

S123E3401A4A87899EEB01889724058B9E6C018A867D2707E601F7AF0120F698819E
E605DC

S123E360F12706A601830920F44D27EFA601830998819EE6057D270D879EE60AF186
260198

S123E380F7AF0120F098819EE605270B87F69EE806F786AF014BF59881830725424D2
73FBB

S123E3A087898B87899EEB01889724058B9E6C018A86AFF898B449EE7059EFE03F
6879EEC

S123E3C0FE02F69EFE04F7869EFE01F7AFF9EFF019EFE03AF019EFF039E6B05DD
A7059828

S104E3E081B7

S107FDECE3E1E43F28

S123E3E10E11FDA7FC6EF916A6409EE7039E6F019E6F026E1A100F10FDBE12B613
9EEB0279

S123E4019EE7029F9EE9019EE7019E6B03E54500409EE601529EE7019EE602529EE7
029EF3

S123E421E602A0EF9EE7029EE601A2009EE7019E6802A6199EE002A7049EE7059881
9E6F8A

S123E441069EE6052A0140AE0942879F4500055286529E6D052A01409E6D052A039E
63066B

S116E461AB209EE7059EE606A9009EE706859EE70498816A

S123FDF0E499E53AE474E4C9E523E527E628E62DE55DE602E484E490E66BE65EE6
62E65AF6

S119FE10E653E645E64CE632E635E63DE641E56EE571E575E57964

S123E474A601AD044500607FAD4D4500028345814500607C9EE605CDE57D2063450
0607C01

S123E4949EE605205AAD7945002D8345A628AD5CAD2F4500058345AD1ECDE62DA
DC2AD1560

S123E4B445E687831F45E698832045E6A9832145E6B9832281A60CCDE677AD30AD0
3CCE6ED

S123E4D477AD3DAD05180287200418028762A40F87B602A4F09EEA01B7028686190
281CD0C

S123E4F4E677AD05ADDBCCE6771C02811D028187C61842AA0FC71842B603A4F0B
703868176

S123E51487B603AA50B703B603AA0FB7038681A60D20A4A60E20A0A43FAA40209
AA1402544

S123E53404A040AA80819EE605A107221A484848ADE5A60887F6CDE677A41FADA
2AF019EA8

S123E5546B01F2864F200599819EE6054D2A02AB40A47FB760AA80CCE4CB4F20EF
A68020C1

S123E574EBA61020E7A69020E3898B45E592710AAF0165E60225F78A8881F68A8881
804161

S123E594814282D483008445855A864887D68849894B8AD78B4D8C4E8DD88E4F8FD
99050B2

S123E5B491DA9254935994DC955896DD97DE98DF99E09AF29BE29CE39DE49EE59
FE6A0E739

S123E5D4A1E8A2E9A3EAA4EBA5ECA66FA7EDA8EEA9EFAA01ABF0ACF1AD02
AE03AFF3E0F4D2

S123E5F4E1DFE2E3E5A1E6A2E7A3E48BE89AAD73B66087A43FA1102302A01040A
B10270DA0

S123E6142B0B87A620CDE4F39E6B01F98686CDE531CCE560A604CCE4CBA606CC
E4CB4F20FD

S123E63402A640CDE560831981A61020F6A69020F2A610CDE5602012A690CDE5602
00BA684

S123E65440CDE56020044FCDE560AD0220D8F62710831AAF0120F79EFE07ADF2AF
019EFF04

S123E674079881898B450032AFF65000026F98A88998141535069535953204669726D
7708

S123E694617265004F532D38204C434420447269766572200020417468656E732020477
208

S118E6B465656365002863292032303038207620322E303400A3

S10BFE26E6C9E6E8E6FAE6EDA0

S123E6C99EFE07832D831D832E4C87899EEB01889724058B9E6C018A869EFF078319
818371

S123E6E92D831D819E6F057D27169E6C05AF0120F6832E40AB1044270797A620831
A5BFCAF

S123E7099881A60587A60145E71E83114CAF089E6B01F78681101010101010101010
145D

S123E72914141410101414141414141414141414141414151515151414151515151515151515898B87
E9

S123E7499EE602AE06429EEE014287898C9EEE058652865245000652270A87A605831
B9E48

S112E7696B01FA868B86410002831B868A8881A6

S123FE2EE77AE786E79AE7C8E803E81DE827E8BBEC7AEC86E974ECD9ECF5ED02
ED33EB54E7

S10BFE4EEBDEEC5AEC45EC601C

S123E77899819EE60527F97FAF014BFB98819EE60527ED874FFAAF019E6B01F94D8
626E033

S123E79898819EE60527D987898B9EAE898B9EFE039ECE02898B9EFE03F6AF019EF
F039E1C

S123E7B8FE01F7AF019EFF019E6B07EAA7079881A800859EE7049EE60527A587898
B9EAE46

S123E7D8898B9EFE039ECE02898B9EFE03F6AF019EFF039EFE01F185AF019EFF018
42604F4

S123E7F89E6B07E6A7079EE70484819EE60573AF014BFB9EE6058799AFFFF6A900F
79E6BE3

S123E81801F68698819EE604A4FE9EE704200C9EE604AA019EE704200299819EE605
27F9C6

S123E838A7EE9EFF099EAE87899EEB01889724058B9E6C018A86AFF9EFF079EFE
099ECE4A

S123E8580287899EEB01889724058B9E6C018A86AFF9EFF059EFE099ECE0487899E
EB0113

S123E878889724058B9E6C018A86AFF9EFF039EE701989EFE07F6AFF9EFF079EF
E05870F

S123E8989EE617A501862603F92001F2AFF9EFF059EFE03F7AFF9EFF039E6B01D
5A71294

S123E8B88199819EE60527F9A7EE9EE70B9EFF099EAE87899EEB01889724058B9E6
C018ADF

S123E8D8869EFF079EFE099ECE049EFF037F6F01AF024BF9C718009EFE07AFFF9E
FF079EE7

S123E8F8FE099ECE029EE6179EE70C87899EEB01889724058B9E6C018A869EFF059
EFE0590

S123E918AFFF9EFF05F69EFE07FE429EEF0D9EE70E9EFE039EE60B9EEB0C9EE701
87899E8E

S123E938EB01889724058B9E6C018A86AFFE9EE60EEB01E7019EE60DF9F79E6A01
9E6A013B

S123E958270AAFFFF6A900F79E6B01F69E6B0CAD9E6B0B80A7129881A7129981A7
EE9EE612

S123E9781727F59EFF099ECE06832F9EFE099ECE04832F9EFE099EAE83302503CCE
B4E9E48

S123E998FE099ECE02833024CF898B9EFE0B9EAE898B958332A704271924329EFE0
99ECE89

S123E9B806898B9EFE0B9EAE898B958331A704CCEB4E9EFE099ECE04AFFF87899
EEB01883C

S123E9D89724058B9E6C018A867CCCEB4EAE08429EEF019EE702C718009EE6179E
FE099E6A

S123E9F8CE02898B9EFE0B9ECE06898B958332A704245C9EFE099ECE06833A9EFE
099EAEBO

S123EA18F6A4804849879EFE0A9ECE069EE6184A87899EEB01889724058B9E6C018
A86F62C

S123EA38A4FE9EEA01F7869EE6179EFE099ECE08898B9EFE0B9EAE898B958331A7
049EFEB3

S123EA58099EAE833A9EFE01AFFF9EFF0120879EE6179EFE099EAE898B9EFE0B9E
CE0889B4

S123EA788B958331A7049EFE099ECE06833B9EFE01AF019EFF01C718009EFE01260
3CCEBDF

S123EA984EAFF9EFF019EE6179EFE099ECE06833A9EFE099EAEF6A4804849879E
FE0A9EEA

S123EAB8CE069EE6184A87899EEB01889724058B9E6C018A86F6A4FE9EEA01F786
9EE617BF

S123EAD89EFE099ECE08898B9EFE0B9ECE02898B9EFE0D9ECE06898B958335A70
69EE61700

S123EAF89EFE099EAE833A9EFE099ECE08F6A880A4804849879EE6189EFE0A9EC
E04833A6A

S123EB184A87899EEB01889724058B9E6C018A86F6A4FE9EEA01F7864100189EE61
79EFED9

S123EB38099ECE06898B9EFE0B9ECE08898B958331A704CCEA8EA712988199819E
E6052727

S123EB58F9A7EE9EFF099EAE9EFF079EFF119EFE099ECE02898BAE0C42898AAE0
5528A887A

S123EB784C9EE70287899EEB01889724058B9E6C018A867FAFF9EFF0D9EE6179EE
7019E88

S123EB98FE079EFF1145000AC718009EFF0B9EFE11F69EFE0B529EFF0B9EFE11F7
AF019E9A

S123EBB8FF119EFE0B9E6B01DF8B869EFF0B9EFE0DAB30F7AFF9EFF0D9EFE0B
9E6B02B9A2

S123EBD8A712988199819EE60527F9A7EE9EFF099EAE9EFF077FAF014BFB9EFE09
9ECE02D1

S123EBF89EFF03C718009EFE079EE61783379EE6179EE7019EFE03F6AF019EFF0341
002912

S123EC18879EFE089EE6184A87899EEB01889724058B9E6C018A8686A030F9F74FA
FFF9E5E

S123EC386B01F79EFE037D26BAA7129881C71800A630F1260B6D012707A620F7AF0
120ED9A

S123EC589881898BADE78A88A620F12613898BC718007D2707E601F7AF0120F38A8
820E87C

S123EC789881A60A879EE6068338868199819EE60527F987899EEB01889724058B9E6
C01A1

S123EC988A86874F878787C71800AFFF89F69EEE0E429EEB039EEF03974FA900879
F889EFE

S123ECB8EB049EEF0488F74F9EE9039EE7039E6B04D59EE6029EEB03A7049EE705
988199FD

S123ECD8819EE60527F987899EEB01889724058B9E6C018A8698AFFF794BFB98819
EE605BF

S123ECF827DD9876AF014BFB98819EE60527D07D2B1287899EEB01889724058B9E6
C018A9B

S123ED188698201087899EEB01889724058B9E6C018A8699AFFF794BFB98819EE605
279F93

S119ED389876AF014BFB85879EEE04898A9EEE077886847698816A

S115FE56ED88ED9AEDA7EDCCEDC1EDFFEE10EE2DEE228A

S123ED4E9EE601A50826019A8B9EFE05F6AF019EFF05974F5849878A9EBEFDD089
8B898B51

S123ED6E45ED7E9EFF039EEE05898A9EEE089881859E6402849E69028A809EE605A
D022068

S123ED8E13A1612506A17A2202A02081A6019E64054924FA9EE7059881C718006500
00277E

S123EDAE72898B4503E4AFFF65000026F98A88AFFF20E69EE605ADC9AD2124D89
9819EE630

S123EDCE06ADBEAD1625F562A40F979EE605ADB1AD0925E8899EEA018820B9A1
3025DDA196

S123EDEE4622D9A1392306A14125D1A007A03098819EE605A13025C4A13922C0A0
309EE701

S123EE0E05819EE60562AD0D9EE7069EE605AD059EE7059881A40FAB9072A94072
98819EDA

S123EE2E6F069E6F05F627EB834825E8F79E68059E69069EE606879EE606879E68079
E6914

S123EE4E089E68079E6908869EEB069EE706869EE9069EE7069EE605FB9EE7059EE6
06A9FD

S10BEE6E009EE706AF0120BD80

S105FFFCED4EC4

S123EE76A601C71809A650C71802A680C71803C6FFAF41FF07B73AC6FFAEB73B6E
3A396EAA

S123EE96B8383F003F023F013F034FC71840C718444500617FAF0165009325F86E057
F6E8B

S123EEB605806E0581814500618351B602A420B773B67441070FCDF570CDF57BCDF
594CD0B

S123EED6F5CECCF5D9CDF586CCF58DC7180045026094AD8C8310835045F6A6A60
783114505

S123EEF6F6AE4A8311CDE70B8312C718008FADB6B674410705CDF616241BB674A1
012605CB

S123EF16CDF4522010AD3C8319AD448319AD4D8319AD568319834F25D1317424B7
7432FF60

S123EF3605357732FF0735796E787BA10626036E0A7BA103260A32FF09357732FF0B
357958

S123EF5620A8818327B67441075D410340206D8328B6744107314104E9CCF1118329B
674A4

S123EF76410736410418CCF13C832AB67441071A41040841030B4105022009CCF1DF
CCF203

S123EF964FCCF31ACCF19BCCF154CCF178832B3D3D3D3D3D3D3D3D0081831C20
202B2D2B18

S123EFB62D2B2D2B2D00810A0208832B4D4F4E4F0081832B53544552454F0081831C
465225

S123EFD6513A20000A020C831C554E4C4F434B45440081B661BA62BA63BA64BA65
260D839C

S123EFF61C4E6F207369676E616C0081B674A1042631C6FF10BB65B765C6FF0FB964
B764BC

S123F016C6FF0EB963B763C6FF0DB962B7628785879E6F02C6FF0D2A039E6302868
486B9DA

S123F03661B761A7DC95AF0A9EFF01AF059EFF03AF059EFF05AF059EFF07AF059E
FF0995DD

S123F056B6619EE70BB6629EE70CB6639EE70DB6649EE70EB6659EE70F9E6F24B66
5A01043

S123F076B664A227B663A200B662A200B661A200254A9E6F109E6F119E6F129E6F13
A60ACC

S123F0969EE7149E6C24B665A080B664A296B663A298B662A200B661A200250D9E6
C24A636

S123F0B6279EE713A6109EE714A60583399EFE1535619EFE1735639EE619B76545006
19E32

S123F0D6FF0195AF059EFF0395A605833E9EFE0383409EE6242709CDF41FA7244B1
5200BBC

S123F0F6831DA724831C20487A0081831C204B487A0081831C204D487A0081831C46
57446D

S123F1163A2000BE67B66898CDF4A798CDF370557765000A2408831C206D57200081
831C46

S123F136205720200081831C5245463A2000BE69B66A99CDF4AF98CDF370557920D3
831C2F

S123F1564C2D00B671CDF20FB671B17D2302B77D3B80084E7D6D6E05803F7DB671
BE6DCCB1

S123F176F215831C522D00B672CDF20FB672B17E2302B77E3B81084E7E6E6E05813F
7EB644

S123F19672BE6E207A831C4465763A2000B674410607B66BCDF6322005B66BCDF64
EB17CF3

S123F1B62302B77C3B7F084E7C6C6E057F3F7CB66CCDF342B674410605CDF101200
3CDF1FE

S123F1D609B66B4503FFCCE746831C4D6F643A2000B66BCDF632B17C2302B77C3B
7F084EE7

S123F1F67C6C6E057F3F7CB66CCDF342831C252000B66B4506FFCCE7464508FFCC
E7468926

S123F21687AE304287894500FF86528652450006525F898B885D27039E6C019EEB018
840AD

S123F236AB082706831C20004BFA86889FCDF63FCDF330831C64620081831C525353
3A205A

S123F25600B66FBA70260E831C4E6F207369676E616C002074BE6FB670A7E79EEF01
9EE78F

S123F27602C6FF03C0FF02979EE6029EEF02429EEF0C9EE70D9EEE029EE601429EE
B0C9E48

S123F296E70C9FA9009EE70B9E6F0E4503FF9EFF0F95AF0A9EFF01AF039EFF03AF
039EFFEE

S123F2B605AF039EFF07AF039EFF09A6039583399EE613CBFF029EE7139EE612A90
0979E18

S123F2D6E613A71998AD53AD188328831C5253533A2000450BFF346FB67046346F46
CCE768

S123F2F646831C2064420656200081831C2D00815D2A0EADF65343AB01879F88A900
879F08

S123F31688992056831C546D703A20005FB6662A0153ADDC831C07430081874D2A09
831C80

S123F3362D009E60012004831C200086898B87450064522602A6F0AB30831A8B86450
00AF2

S123F3565226099EEE01A3642402A6F0AB30831A8B86AB30831A868A8881898B87A
7F79ED1

S123F376EF019EE702859EE70945000A9EE601529EE7019EE602529EE7028B86AB30
9EE76D

S123F396078C9EE601529EE7019EE602529EE7028B86AB309EE7068C9EE601529EE7
019E06

S123F3B6E602529EE7028B86AB309EE7058C9EE601529EE7019EE602529EE7028B86
AB30C8

S123F3D69EE7048C9EE601529EE7019EE602529EE7028B86AB309EE703A702956F0
5A63046

S123F3F6F1261D6D012719A62EE10127139EE607842406A601830920E5A620F7AF01
20DE45

S123F41695831EA707868A8881898B874F7D27054CAF0120F84A2605831C2E3000879
EFE99

S123F436039E6D0127089E6B0104A62E831AF62706831AAF0120EA86868A88818312
83279D

S123F456832B2863292041535069535953204C7464008328832B312E3037204C6963656
E56

S123F47673656420746F008329832B412E432E20456C656374726F6E696300832A832B
5422

S123F496656C65636F6D73204C696D6974656400814E77834E788420064E79834E7A84
872C

S123F4B6898B558365000A240F450083A6028337A6028337A60283378A8886A7D39E
EF0B0C

S123F4D69EE70C9EEF0D9EE70E95AF0A9EFF01AF029EFF03AF069EFF0595A60283
369E6FBD

S123F4F6179E6F18B6839EE719B6849EE71A95AF129EFF01AF049EFF03AFF49EFF0
595A63F

S123F5160483369EE60E9EE70B9EE60F9EE70C9EE6109EE70D9EE6119EE70E9EE61
29EE765

S123F5360F9E6F109E6F11A60F9EE71245F8019EFF1395AF0A9EFF01AF059EFF03A
F059E9B

S123F556FF05AF059EFF07AF059EFF0995A60583399EEE189EE619A72D81AE20A60
1834D04

S123F576BF67B76881AE20A602834DBF69B76A81A601AD11B77181A602AD0AB77
281A603DB

S123F596AD03B76B8187A7FD9E6F039E6F019E63019E6F02AE019EE604834C9EE10
12403F7

S123F5B69EE7019EE10225039EE7029E6B03E79EE6029EE001A70481AE20A602834
DBF6FE3

S123F5D6B77081830ECBFF04AE03895F4D2A015387899EE602BB669EE702863D662
A04A968

S123F5F6FF2002A900879E6B03E8A6029EE7039E67019E66029E6B03F68686A701B7
66811C

S123F616898B874500614FFBAF0165007425F8317605B77699200198868A8881898BA
E7821

S123F63642898AAEFF528A8881898BAE1842898AAEFF52A0158A8881898BAE0A42
898AAE84

S123F656FF528A8881C6FF10B786C6FF0FB785C6FF0EB784C6FF0DB7832A0B45008
3A604C9

S123F6768333A62D2002A620831A45F691A604833E4500876F078341831D810083008
78971

S123F6968B4500FA2005898B4505DC83458A8881060909060000000000000001212121D
104B

S10BFE68F6B6F6FAF787F75C21

S123F6B60E11FD6E71169EE605A41F87895F89899EE604AD249EEB029EE70286A90
0879E93

S123F6D66B03ED6E1F108A86A7029EEE0627035220028B869EE7059881B710C71800
0F10B6

S123F6F6FAB613810E11FD6E79169EE605A41F5D2602AE40A3402505AE409EEF068
7895FD7

S123F71689899EE604AD329EEB029EE7029F9EE9019EE7019E6B03EA6E1F109EEEE0
A8C9E44

S123F736E601529EE7019EE602529EE7028886A7029EE7059EEF069881B710C718000
F10DF

S123F756FABE12B61381834E251397AD12834E250C899EE1018826059EE7059881998
18918

S123F7768B4502FEC71800AFF65000026F68A8881A600AE20834C450007D1F79E24
045B86

S113F796F999819F9EE705988100032D5781ABD582

S107FE70F7A6F7DB1B

S123F7A66E5840453D0835434500937FAF0165009E25F86E073D6E7C3F6E01936EF49
4C677

S123F7C6FF012706349336944BFA4E93954E94966E403C9881859B4E989B4E999C4E
9A9D82

S123F7E684B69BAE09428789B69BAE3D429EEB019EE7019FA900874F8787B69D9E
EB059EE8

S123F806E705B69C9EE9049EE7049EE603A9009EE7039EE602A9009EE70286A90087
C6FFA3

S123F82600CBFF01AB009E68059E69049E69039E69029E69014BEF9EEE08898A9EE
E0B8619

S123F846F786E70186E70286E70386E70498818B1F3C5595AFF359526154E41994E42
9AFB

S119F8664E97981A3C3F413F974E93954E94968A801F403C9780B5

S105FFE6F855C8

S105FFF0F8779C

S119FFD0ED87EEE1EEE1ED87ED87ED87ED87ED87ED87ED87ED87ED8765

S10BFFE8EEE1EEE1EEE1EEE1D1

S10DFFF2ED87ED87EEE1ED87ED8762

S105FFFEEEE12E

S108FF000A001973F66C

S105FF0504B042

S105FF07006490

S105FF092710BB

S105FF0B01F4FB

S107FF0D00A344E025

S903EEE12D

S123E2C0CDED8FF7AF0120F5F6270BAF0187F6CDED8FF7864BF598814F7D27094C
2704AF9F

S123E2E00120F699819EE70598819EE6059E6D0927489EE6094A87899EEB018897240
58BF6

S123E3009E6C018A86F6271187E601879EE602E70186A701AF014D26EFE7019EEE03
898A83

S123E3209EEE069EE6094A87899EEB01889724058B9E6C018A869EE605F798819EE6
05279F

S123E3401A4A87899EEB01889724058B9E6C018A867D2707E601F7AF0120F698819E
E605DC

S123E360F12706A601830920F44D27EFA601830998819EE6057D270D879EE60AF186
260198

S123E380F7AF0120F098819EE605270B87F69EE806F786AF014BF59881830725424D2
73FBB

S123E3A087898B87899EEB01889724058B9E6C018A86AFF898B449EE7059EFE03F
6879EEC

S123E3C0FE02F69EFE04F7869EFE01F7AFF9EFF019EFE03AF019EFF039E6B05DD
A7059828

S104E3E081B7

S107FDECE3E1E43F28

S123E3E10E11FDA7FC6EF916A6409EE7039E6F019E6F026E1A100F10FDBE12B613
9EEB0279

S123E4019EE7029F9EE9019EE7019E6B03E54500409EE601529EE7019EE602529EE7
029EF3

S123E421E602A0EF9EE7029EE601A2009EE7019E6802A6199EE002A7049EE7059881
9E6F8A

S123E441069EE6052A0140AE0942879F4500055286529E6D052A01409E6D052A039E
63066B

S116E461AB209EE7059EE606A9009EE706859EE70498816A

S123FDF0E499E53AE474E4C9E523E527E628E62DE55DE602E484E490E66BE65EE6
62E65AF6

S119FE10E653E645E64CE632E635E63DE641E56EE571E575E57964

S123E474A601AD044500607FAD4D4500028345814500607C9EE605CDE57D2063450
0607C01

S123E4949EE605205AAD7945002D8345A628AD5CAD2F4500058345AD1ECDE62DA
DC2AD1560

S123E4B445E687831F45E698832045E6A9832145E6B9832281A60CCDE677AD30AD0
3CCE6ED

S123E4D477AD3DAD05180287200418028762A40F87B602A4F09EEA01B7028686190
281CD0C

S123E4F4E677AD05ADDBCCE6771C02811D028187C61842AA0FC71842B603A4F0B
703868176

S123E51487B603AA50B703B603AA0FB7038681A60D20A4A60E20A0A43FAA40209
AA1402544

S123E53404A040AA80819EE605A107221A484848ADE5A60887F6CDE677A41FADA
2AF019EA8

S123E5546B01F2864F200599819EE6054D2A02AB40A47FB760AA80CCE4CB4F20EF
A68020C1

S123E574EBA61020E7A69020E3898B45E592710AAF0165E60225F78A8881F68A8881
804161

S123E594814282D483008445855A864887D68849894B8AD78B4D8C4E8DD88E4F8FD
99050B2

S123E5B491DA9254935994DC955896DD97DE98DF99E09AF29BE29CE39DE49EE59
FE6A0E739

S123E5D4A1E8A2E9A3EAA4EBA5ECA66FA7EDA8EEA9EFAA01ABF0ACF1AD02
AE03AFF3E0F4D2

S123E5F4E1DFE2E3E5A1E6A2E7A3E48BE89AAD73B66087A43FA1102302A01040A
B10270DA0

S123E6142B0B87A620CDE4F39E6B01F98686CDE531CCE560A604CCE4CBA606CC
E4CB4F20FD

S123E63402A640CDE560831981A61020F6A69020F2A610CDE5602012A690CDE5602
00BA684

S123E65440CDE56020044FCDE560AD0220D8F62710831AAF0120F79EFE07ADF2AF
019EFF04

S123E674079881898B450032AFF65000026F98A88998141535069535953204669726D
7708

S123E694617265004F532D38204C434420447269766572200020417468656E732020477
208

S118E6B465656365002863292032303038207620322E303400A3

S10BFE26E6C9E6E8E6FAE6EDA0

S123E6C99EFE07832D831D832E4C87899EEB01889724058B9E6C018A869EFF078319
818371

S123E6E92D831D819E6F057D27169E6C05AF0120F6832E40AB1044270797A620831
A5BFCAF

S123E7099881A60587A60145E71E83114CAF089E6B01F78681101010101010101010
145D

S123E729141414101014141414141414141414141415151515141415151515151515898B87
E9

S123E7499EE602AE06429EEE014287898C9EEE058652865245000652270A87A605831
B9E48

S112E7696B01FA868B86410002831B868A8881A6

S123FE2EE77AE786E79AE7C8E803E81DE827E8BBEC7AEC86E974ECD9ECF5ED02
ED33EB54E7

S10BFE4EEBDEEC5AEC45EC601C

S123E77899819EE60527F97FAF014BFB98819EE60527ED874FFAAF019E6B01F94D8
626E033

S123E79898819EE60527D987898B9EAE898B9EFE039ECE02898B9EFE03F6AF019EF
F039E1C

S123E7B8FE01F7AF019EFF019E6B07EAA7079881A800859EE7049EE60527A587898
B9EAE46

S123E7D8898B9EFE039ECE02898B9EFE03F6AF019EFF039EFE01F185AF019EFF018
42604F4

S123E7F89E6B07E6A7079EE70484819EE60573AF014BFB9EE6058799AFFFF6A900F
79E6BE3

S123E81801F68698819EE604A4FE9EE704200C9EE604AA019EE704200299819EE605
27F9C6

S123E838A7EE9EFF099EAE87899EEB01889724058B9E6C018A86AFF9EFF079EFE
099ECE4A

S123E8580287899EEB01889724058B9E6C018A86AFF9EFF059EFE099ECE0487899E
EB0113

S123E878889724058B9E6C018A86AFF9EFF039EE701989EFE07F6AFF9EFF079EF
E05870F

S123E8989EE617A501862603F92001F2AFF9EFF059EFE03F7AFF9EFF039E6B01D
5A71294

S123E8B88199819EE60527F9A7EE9EE70B9EFF099EAE87899EEB01889724058B9E6
C018ADF

S123E8D8869EFF079EFE099ECE049EFF037F6F01AF024BF9C718009EFE07AFF9E
FF079EE7

S123E8F8FE099ECE029EE6179EE70C87899EEB01889724058B9E6C018A869EFF059
EFE0590

S123E918AFF9EFF05F69EFE07FE429EEF0D9EE70E9EFE039EE60B9EEB0C9EE701
87899E8E

S123E938EB01889724058B9E6C018A86AFFE9EE60EEB01E7019EE60DF9F79E6A01
9E6A013B

S123E958270AAFFFF6A900F79E6B01F69E6B0CAD9E6B0B80A7129881A7129981A7
EE9EE612

S123E9781727F59EFF099ECE06832F9EFE099ECE04832F9EFE099EAE83302503CCE
B4E9E48

S123E998FE099ECE02833024CF898B9EFE0B9EAE898B958332A704271924329EFE0
99ECE89

S123E9B806898B9EFE0B9EAE898B958331A704CCEB4E9EFE099ECE04AFF987899
EEB01883C

S123E9D89724058B9E6C018A867CCCEB4EAE08429EEF019EE702C718009EE6179E
FE099E6A

S123E9F8CE02898B9EFE0B9ECE06898B958332A704245C9EFE099ECE06833A9EFE
099EAEBO

S123EA18F6A4804849879EFE0A9ECE069EE6184A87899EEB01889724058B9E6C018
A86F62C

S123EA38A4FE9EEA01F7869EE6179EFE099ECE08898B9EFE0B9EAE898B958331A7
049EFEB3

S123EA58099EAE833A9EFE01AFF9EFF0120879EE6179EFE099EAE898B9EFE0B9E
CE0889B4

S123EA788B958331A7049EFE099ECE06833B9EFE01AF019EFF01C718009EFE01260
3CCEBDF

S123EA984EAEFF9EFF019EE6179EFE099ECE06833A9EFE099EAEF6A4804849879E
FE0A9EEA

S123EAB8CE069EE6184A87899EEB01889724058B9E6C018A86F6A4FE9EEA01F786
9EE617BF

S123EAD89EFE099ECE08898B9EFE0B9ECE02898B9EFE0D9ECE06898B958335A70
69EE61700

S123EAF89EFE099EAE833A9EFE099ECE08F6A880A4804849879EE6189EFE0A9EC
E04833A6A

S123EB184A87899EEB01889724058B9E6C018A86F6A4FE9EEA01F7864100189EE61
79EFED9

S123EB38099ECE06898B9EFE0B9ECE08898B958331A704CCEA8EA712988199819E
E6052727

S123EB58F9A7EE9EFF099EAE9EFF079EFF119EFE099ECE02898BAE0C42898AAE0
5528A887A

S123EB784C9EE70287899EEB01889724058B9E6C018A867FAFF9EFF0D9EE6179EE
7019E88

S123EB98FE079EFF1145000AC718009EFF0B9EFE11F69EFE0B529EFF0B9EFE11F7
AF019E9A

S123EBB8FF119EFE0B9E6B01DF8B869EFF0B9EFE0DAB30F7AFF9EFF0D9EFE0B
9E6B02B9A2

S123EBD8A712988199819EE60527F9A7EE9EFF099EAE9EFF077FAF014BFB9EFE09
9ECE02D1

S123EBF89EFF03C718009EFE079EE61783379EE6179EE7019EFE03F6AF019EFF0341
002912

S123EC18879EFE089EE6184A87899EEB01889724058B9E6C018A8686A030F9F74FA
FFF9E5E

S123EC386B01F79EFE037D26BAA7129881C71800A630F1260B6D012707A620F7AF0
120ED9A

S123EC589881898BADE78A88A620F12613898BC718007D2707E601F7AF0120F38A8
820E87C

S123EC789881A60A879EE6068338868199819EE60527F987899EEB01889724058B9E6
C01A1

S123EC988A86874F878787C71800AFFF89F69EEE0E429EEB039EEF03974FA900879
F889EFE

S123ECB8EB049EEF0488F74F9EE9039EE7039E6B04D59EE6029EEB03A7049EE705
988199FD

S123ECD8819EE60527F987899EEB01889724058B9E6C018A8698AFFF794BFB98819
EE605BF

S123ECF827DD9876AF014BFB98819EE60527D07D2B1287899EEB01889724058B9E6
C018A9B

S123ED188698201087899EEB01889724058B9E6C018A8699AFFF794BFB98819EE605
279F93

S119ED389876AF014BFB85879EEE04898A9EEE077886847698816A

S115FE56ED88ED9AEDA7EDCCEDC1EDFFEE10EE2DEE228A

S123ED4E9EE601A50826019A8B9EFE05F6AF019EFF05974F5849878A9EBEFDD089
8B898B51

S123ED6E45ED7E9EFF039EEE05898A9EEE089881859E6402849E69028A809EE605A
D022068

S123ED8E13A1612506A17A2202A02081A6019E64054924FA9EE7059881C718006500
00277E

S123EDAE72898B4503E4AFF65000026F98A88AFF20E69EE605ADC9AD2124D89
9819EE630

S123EDCE06ADBEAD1625F562A40F979EE605ADB1AD0925E8899EEA018820B9A1
3025DDA196

S123EDEE4622D9A1392306A14125D1A007A03098819EE605A13025C4A13922C0A0
309EE701

S123EE0E05819EE60562AD0D9EE7069EE605AD059EE7059881A40FAB9072A94072
98819EDA

S123EE2E6F069E6F05F627EB834825E8F79E68059E69069EE606879EE606879E68079
E6914

S123EE4E089E68079E6908869EEB069EE706869EE9069EE7069EE605FB9EE7059EE6
06A9FD

S10BEE6E009EE706AF0120BD80

S105FFFCED4EC4

S123EE76A601C71809A650C71802A680C71803C6FFAF41FF07B73AC6FFAEB73B6E
3A396EAA

S123EE96B8383F003F023F013F034FC71840C718444500617FAF0165009325F86E057
F6E8B

S123EEB605806E0581814500618351B602A420B773B67441070FCDF570CDF57BCDF
594CD0B

S123EED6F5CECCF5D9CDF586CCF58DC7180045026094AD8C8310835045F6A6A60
783114505

S123EEF6F6AE4A8311CDE70B8312C718008FADB6B674410705CDF616241BB674A1
012605CB

S123EF16CDF4522010AD3C8319AD448319AD4D8319AD568319834F25D1317424B7
7432FF60

S123EF3605357732FF0735796E787BA10626036E0A7BA103260A32FF09357732FF0B
357958

S123EF5620A8818327B67441075D410340206D8328B6744107314104E9CCF1118329B
674A4

S123EF76410736410418CCF13C832AB67441071A41040841030B4105022009CCF1DF
CCF203

S123EF964FCCCF31ACCF19BCCF154CCF178832B3D3D3D3D3D3D3D0081831C20
202B2D2B18

S123EFB62D2B2D2B2D00810A0208832B4D4F4E4F0081832B53544552454F0081831C
465225

S123EFD6513A20000A020C831C554E4C4F434B45440081B661BA62BA63BA64BA65
260D839C

S123EFF61C4E6F207369676E616C0081B674A1042631C6FF10BB65B765C6FF0FB964
B764BC

S123F016C6FF0EB963B763C6FF0DB962B7628785879E6F02C6FF0D2A039E6302868
486B9DA

S123F03661B761A7DC95AF0A9EFF01AF059EFF03AF059EFF05AF059EFF07AF059E
FF0995DD

S123F056B6619EE70BB6629EE70CB6639EE70DB6649EE70EB6659EE70F9E6F24B66
5A01043

S123F076B664A227B663A200B662A200B661A200254A9E6F109E6F119E6F129E6F13
A60ACC

S123F0969EE7149E6C24B665A080B664A296B663A298B662A200B661A200250D9E6
C24A636

S123F0B6279EE713A6109EE714A60583399EFE1535619EFE1735639EE619B76545006
19E32

S123F0D6FF0195AF059EFF0395A605833E9EFE0383409EE6242709CDF41FA7244B1
5200BBC

S123F0F6831DA724831C20487A0081831C204B487A0081831C204D487A0081831C46
57446D

S123F1163A2000BE67B66898CDF4A798CDF370557765000A2408831C206D57200081
831C46

S123F136205720200081831C5245463A2000BE69B66A99CDF4AF98CDF370557920D3
831C2F

S123F1564C2D00B671CDF20FB671B17D2302B77D3B80084E7D6D6E05803F7DB671
BE6DCCB1

S123F176F215831C522D00B672CDF20FB672B17E2302B77E3B81084E7E6E6E05813F
7EB644

S123F19672BE6E207A831C4465763A2000B674410607B66BCDF6322005B66BCDF64
EB17CF3

S123F1B62302B77C3B7F084E7C6C6E057F3F7CB66CCDF342B674410605CDF101200
3CDF1FE

S123F1D609B66B4503FFCCE746831C4D6F643A2000B66BCDF632B17C2302B77C3B
7F084EE7

S123F1F67C6C6E057F3F7CB66CCDF342831C252000B66B4506FFCCE7464508FFCC
E7468926

S123F21687AE304287894500FF86528652450006525F898B885D27039E6C019EEB018
840AD

S123F236AB082706831C20004BFA86889FCDF63FCDF330831C64620081831C525353
3A205A

S123F25600B66FBA70260E831C4E6F207369676E616C002074BE6FB670A7E79EEF01
9EE78F

S123F27602C6FF03C0FF02979EE6029EEF02429EEF0C9EE70D9EEE029EE601429EE
B0C9E48

S123F296E70C9FA9009EE70B9E6F0E4503FF9EFF0F95AF0A9EFF01AF039EFF03AF
039EFFEE

S123F2B605AF039EFF07AF039EFF09A6039583399EE613CBFF029EE7139EE612A90
0979E18

S123F2D6E613A71998AD53AD188328831C5253533A2000450BFF346FB67046346F46
CCE768

S123F2F646831C2064420656200081831C2D00815D2A0EADF65343AB01879F88A900
879F08

S123F31688992056831C546D703A20005FB6662A0153ADDC831C07430081874D2A09
831C80

S123F3362D009E60012004831C200086898B87450064522602A6F0AB30831A8B86450
00AF2

S123F3565226099EEE01A3642402A6F0AB30831A8B86AB30831A868A8881898B87A
7F79ED1

S123F376EF019EE702859EE70945000A9EE601529EE7019EE602529EE7028B86AB30
9EE76D

S123F396078C9EE601529EE7019EE602529EE7028B86AB309EE7068C9EE601529EE7
019E06

S123F3B6E602529EE7028B86AB309EE7058C9EE601529EE7019EE602529EE7028B86
AB30C8

S123F3D69EE7048C9EE601529EE7019EE602529EE7028B86AB309EE703A702956F0
5A63046

S123F3F6F1261D6D012719A62EE10127139EE607842406A601830920E5A620F7AF01
20DE45

S123F41695831EA707868A8881898B874F7D27054CAF0120F84A2605831C2E3000879
EFE99

S123F436039E6D0127089E6B0104A62E831AF62706831AAF0120EA86868A88818312
83279D

S123F456832B2863292041535069535953204C7464008328832B312E3037204C6963656
E56

S123F47673656420746F008329832B412E432E20456C656374726F6E696300832A832B
5422

S123F496656C65636F6D73204C696D6974656400814E77834E788420064E79834E7A84
872C

S123F4B6898B558365000A240F450083A6028337A6028337A60283378A8886A7D39E
EF0B0C

S123F4D69EE70C9EEF0D9EE70E95AF0A9EFF01AF029EFF03AF069EFF0595A60283
369E6FBD

S123F4F6179E6F18B6839EE719B6849EE71A95AF129EFF01AF049EFF03AFF49EFF0
595A63F

S123F5160483369EE60E9EE70B9EE60F9EE70C9EE6109EE70D9EE6119EE70E9EE61
29EE765

S123F5360F9E6F109E6F11A60F9EE71245F8019EFF1395AF0A9EFF01AF059EFF03A
F059E9B

S123F556FF05AF059EFF07AF059EFF0995A60583399EEE189EE619A72D81AE20A60
1834D04

S123F576BF67B76881AE20A602834DBF69B76A81A601AD11B77181A602AD0AB77
281A603DB

S123F596AD03B76B8187A7FD9E6F039E6F019E63019E6F02AE019EE604834C9EE10
12403F7

S123F5B69EE7019EE10225039EE7029E6B03E79EE6029EE001A70481AE20A602834
DBF6FE3

S123F5D6B77081830ECBFF04AE03895F4D2A015387899EE602BB669EE702863D662
A04A968

S123F5F6FF2002A900879E6B03E8A6029EE7039E67019E66029E6B03F68686A701B7
66811C

S123F616898B874500614FFBAF0165007425F8317605B77699200198868A8881898BA
E7821

S123F63642898AAEFF528A8881898BAE1842898AAEFF52A0158A8881898BAE0A42
898AAE84

S123F656FF528A8881C6FF10B786C6FF0FB785C6FF0EB784C6FF0DB7832A0B45008
3A604C9

S123F6768333A62D2002A620831A45F691A604833E4500876F078341831D810083008
78971

S123F6968B4500FA2005898B4505DC83458A888106090906000000000000001212121D
104B

S10BFE68F6B6F6FAF787F75C21

S123F6B60E11FD6E71169EE605A41F87895F89899EE604AD249EEB029EE70286A90
0879E93

S123F6D66B03ED6E1F108A86A7029EEE0627035220028B869EE7059881B710C71800
0F10B6

S123F6F6FAB613810E11FD6E79169EE605A41F5D2602AE40A3402505AE409EEF068
7895FD7

S123F71689899EE604AD329EEB029EE7029F9EE9019EE7019E6B03EA6E1F109EEE0
A8C9E44

S123F736E601529EE7019EE602529EE7028886A7029EE7059EEF069881B710C718000
F10DF

S123F756FABE12B61381834E251397AD12834E250C899EE1018826059EE7059881998
18918

S123F7768B4502FEC71800AFF65000026F68A8881A600AE20834C450007D1F79E24
045B86

S113F796F999819F9EE705988100032D5781ABD582

S107FE70F7A6F7DB1B

S123F7A66E5840453D0835434500937FAF0165009E25F86E073D6E7C3F6E01936EF49
4C677

S123F7C6FF012706349336944BFA4E93954E94966E403C9881859B4E989B4E999C4E
9A9D82

S123F7E684B69BAE09428789B69BAE3D429EEB019EE7019FA900874F8787B69D9E
EB059EE8

S123F806E705B69C9EE9049EE7049EE603A9009EE7039EE602A9009EE70286A90087
C6FFA3

S123F82600CBFF01AB009E68059E69049E69039E69029E69014BEF9EEE08898A9EE
E0B8619

S123F846F786E70186E70286E70386E70498818B1F3C5595AFFF359526154E41994E42
9AFB

S119F8664E97981A3C3F413F974E93954E94968A801F403C9780B5

S105FFE6F855C8

S105FFF0F8779C

S119FFD0ED87EEE1EEE1ED87ED87ED87ED87ED87ED87ED87ED87ED87ED87ED87ED8765

S10BFFE8EEE1EEE1EEE1EEE1D1

S10DFFF2ED87ED87ED87EEE1ED87ED8762

S105FFFEEEE12E

S108FF000A001973F66C

S105FF0504B042

S105FF07006490

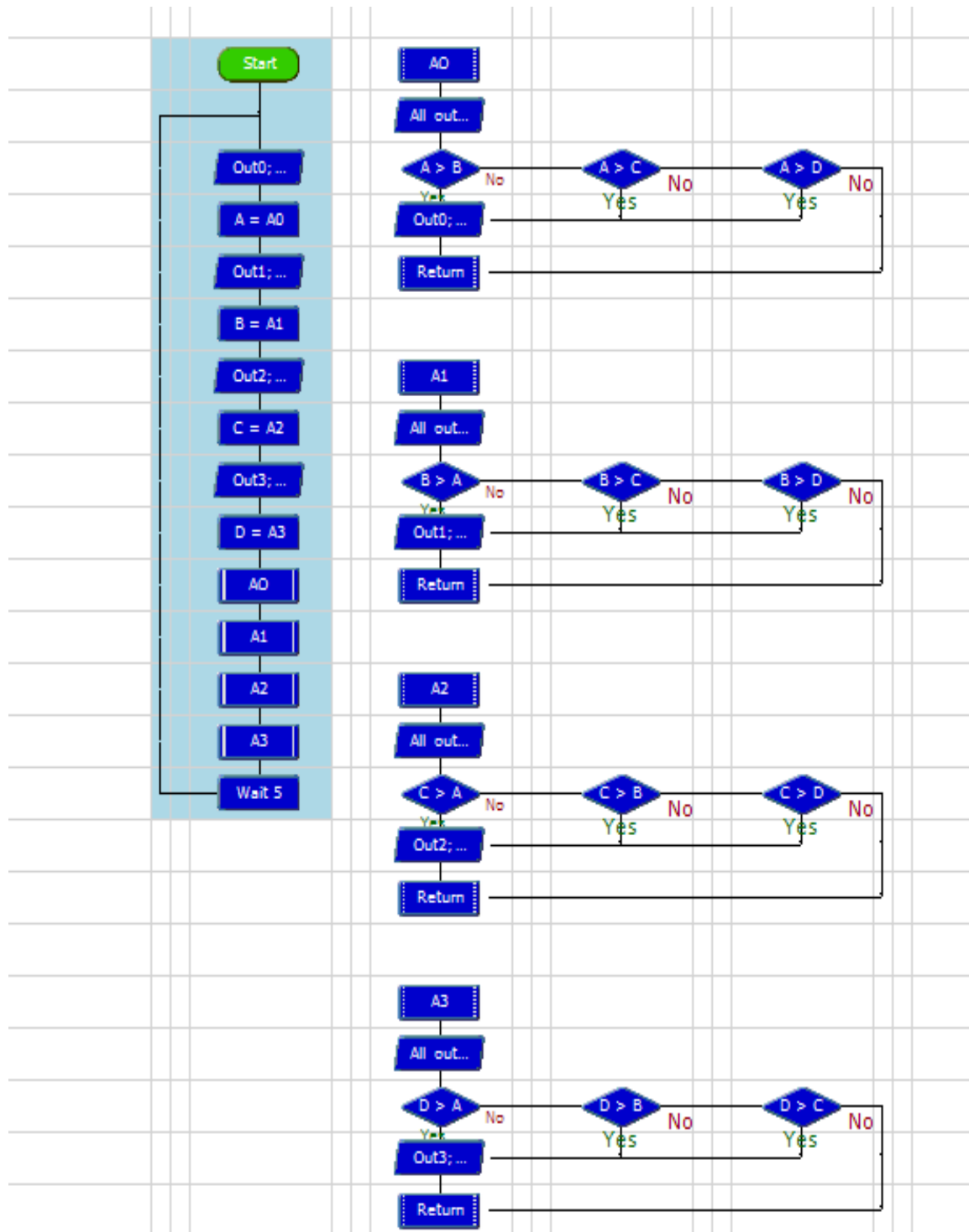
S105FF092710BB

S105FF0B01F4FB

S107FF0D00A344E025

S903EEE12D

APPENDIX 4: CONTROL SYSTEM PROGRAMMING CODE



APPENDIX 5: BASIC CONVERTED FROM LOGICATOR FOR PICAXE FLOWCHART

;Symbols

{

Symbol varA = b0

Symbol varB = b1

Symbol varC = b2

Symbol varD = b3

Symbol varE = b4

Symbol varF = b5

Symbol varG = b6

Symbol varH = b7

}

Main:

```
label_9:    let pins = 3    '%00000011
            readadc 0,b8    'read A0 into b8
            let varA = b8  'Expression command
            let pins = 6    '%00000110
            readadc 1,b9    'read A1 into b9
            let varB = b9  'Expression command
            let pins = 12   '%00001100
            readadc 2,b10   'read A2 into b10
            let varC = b10  'Expression command
            let pins = 24   '%00011000
```

```
readadc 3,b11      'read A3 into b11

let varD = b11     'Expression command

gosub prc_AO 'Do Procedure

gosub prc_A1 'Do Procedure

gosub prc_A2 'Do Procedure

gosub prc_A3 'Do Procedure

pause 5000      'Wait command

goto label_9
```

prc_A3:

```
let pins = 0      '%00000000

if varD > varA then label_66 'Compare command

if varD > varB then label_66 'Compare command

if varD > varC then label_66 'Compare command
```

label_67: return 'Return

label_66: let pins = 24 '%00011000

goto label_67

prc_A2:

```
let pins = 0      '%00000000

if varC > varA then label_59 'Compare command

if varC > varB then label_59 'Compare command

if varC > varD then label_59 'Compare command
```

```

label_60:    return      'Return

label_59:    let pins = 12    '%00001100

             goto label_60

prc_A1:

             let pins = 0    '%00000000

             if varB > varA then label_51 'Compare command

             if varB > varC then label_51 'Compare command

             if varB > varD then label_51 'Compare command

label_52:    return      'Return

label_51:    let pins = 6    '%00000110

             goto label_52

prc_AO:

             let pins = 0    '%00000000

             if varA > varB then label_39 'Compare command

             if varA > varC then label_39 'Compare command

             if varA > varD then label_39 'Compare command

label_44:    return      'Return

label_39:    let pins = 3    '%00000011

             goto label_44

```

#no_data 'reduce download time

APPENDIX 6: PRESENTATIONS CONFERENCES RELATED TO THE RESEARCH PROJECT

International Conference: ICECECE 2014: International Conference on Electrical, Computer, Electronics and Communication Engineering.

Web: <http://waset.org/conference/2014/07/london/ICECECE>

Location: Hotel Holiday Inn, Wembley, Empire Way, London, UK

Date: July, 27-28, 2014

Duration: 2 Days

International Conference: ICECECE 2015: International Conference on Electrical, Computer, Electronics and Communication Engineering.

Web: <http://waset.org/conference/2015/05/berlin/ICECECE>

Location: Hollywood Media Hotel GmbH, Kurfürstendamm 202, 10719 Berlin, Germany

Date: May, 21 – 22, 2015

Duration: 2 Days

APPENDIX 7: PUBLICATIONS RELATED TO THE RESEARCH PROJECT

Analysis of VHF Propagation Mechanisms that Cause Interference from the Middle East within the Southern Coastal Regions of Cyprus

Antonis Constantinides, Panayiotis Michael

Abstract—Interference is a very important factor in the planning of digital and analog VHF terrestrial radio services. The most common cause of interference in band II & III occurs under line of sight conditions and thus many times can be skipped. Nevertheless, a more complicated case of interference occurs when an unwanted signal travels beyond the horizon due to atmospheric refraction based on specific weather conditions. A case of such abnormal propagation mechanism has been examined in the Mediterranean Sea during the months June, July and August 2015 due to the radio interference which plaguing the southern coast of Cyprus for years. The model based on which calculations were made is the Weather Research Forecasting (WRF-ARW version 3.4). Furthermore, this study utilizes real world measurements in Band II based on current overseas radio transmissions monitored beyond the horizon in clear spectrum during the hot dry months of the summer. The focus was specifically on the field strength variations versus the type of duct favouring the radio waves in Band II, allowing them to travel between the Middle East to beyond the horizon in Cyprus, since line of sight conditions do not exist between the two regions.

Keywords: Abnormal Interference, Propagation Mechanism, Tropospheric Ducting, Refraction.

1. INTRODUCTION

THIS PAPER presents the types of *tropospheric ducting* that favours the overseas transmissions from the Middle East, allowing them to cause a strong destructive interference in the local radio services along the southern coast of Cyprus during the hot dry months of the summer. The research has been executed as the co-channel and adjacent-channel radio interference degrades the reception quality in major service areas within the cities of Limassol, Paphos, Larnaca and their suburbs, as illustrated on the map presented in Figure 1.



Figure 1: The Area Affected by Interference from the Middle East

For example, the interference adversely affects the "in car listening" quality across the main highway that connects the aforementioned cities. Under severe interference conditions, at random locations within the affected area, an automobile receiver demodulates unwanted signals, rather than the desired program to which it has been tuned. Empirical evidence indicates that this phenomenon is more pronounced in motion due to multipath-induced fading. [1] According to the study, the monthly average field strength intensity of the unwanted overseas transmissions fluctuates. However, the graphs

demonstrated in this report, indicate that sometimes these effects, exceeds the free space level of the local radio transmissions even in the order of 10dB with duration of few hours when a surface duct causing trapping conditions. Furthermore, the field strength intensity of these unwanted transmissions depends on the weather conditions, and thus varies with the season and the time of reception. For instance,

the phenomenon appears weak during the spring and peaks during the hot, dry summer months. During the autumn, the effect weakens again and vanishes completely in the winter. In contrast with other extant propagation mechanism case studies conducted in other regions of the world such as Korea, Nigeria, Japan[2][3][4][8], the model based on which calculations were made in this study is the Weather Research Forecasting (WRF-ARW version 3.4). Furthermore, real world measurements in Band II (87.5 to 108.0 MHz) have been carried out based on existing overseas radio transmissions monitored beyond the horizon in clear spectrum which are given below. The aim was to investigate their characteristics in terms of propagation mechanisms provided by the following ITU Recommendations (ITU-RP.452, 453, and 834) [5][6][7]. These recommendations provide the testing procedures and mathematical expressions incorporating the meteorological parameters that affect the radio refractivity of the Troposphere that permits the overseas radio waves to travel beyond the horizon and cause interference (more details on this phenomenon are provided below).

2. LOCATION AND INSTRUMENTATION SETUP

It was not practically possible to conduct field strength measurements at every single reception point within the southern coast of Cyprus. Consequently, it was important to identify a reference point that can serve as a permanent and reliable source of measurements of field strength intensity of the unwanted overseas transmissions on a daily basis. This was achieved in the northern part of Limassol (34°42'37.14"N, 33°1'15.26"E). The location is at 393 ft above sea level (asl) and has an absolute line of sight with the coast of Limassol. For reception purposes, a broadband response, -1.5dB gain circular polarized dipole antenna has been installed outdoors, on a mast, one meter above the ground in order to represent the height of a typical commercial receiver's antenna. The testing equipment arrangement is illustrated in Figure 2.

30 dBuV, and ranged from 10 dBuV to 48 dBuV, with the fluctuations essentially comprising of noise.

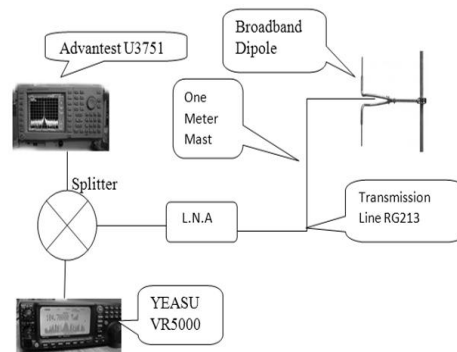


Figure 2: Testing Equipment Arrangement

3. MONITORING THE UNWANTED OVERSEAS TRANSMISSIONS

During the study many unwanted overseas transmissions have been monitored in Band II, to overlap with the local radio services, thus, their behaviour could not be studied.

The field strength variation of the aforementioned signal was in the order of 38 dBuV. Similarly, the field strength intensity of the 95.5 MHz signal arriving from Israel was measured between June 17th and September 2nd, 2015, at 1:00 PM, with the data

Frequency	Location	Path Length	Height	ERP
102.5 MHz	Lebanon	271 km	2995 m	50 kW
95.5 MHz	Israel	376 km	860 m	40 kW
94.8 MHz	Cyprus	29 km	1549 m	30 kW

Table 1: The Technical Specifications of the Transmitting Signals under study

Nonetheless, two overseas signals could be detected in a very clear spectrum in Limassol, namely the Lebanon "Radio Libran Libre" 102.5 FM, broadcast from Beirut Lebanon, and the 95.5 MHz, broadcast from Jerusalem, Israel. The technical specifications of the aforementioned overseas signals, versus the national radio Cyprus Broadcasting Corporation "CYBC" are illustrated in table 1.

illustrated in Figure 6. The measurements pertaining to the local national radio CYBC signal were performed within the same period as well. The field strength variations of the three signals under study are merged on the graph depicted in Figure 7. The green colour represents the field strength intensity of the local 94.8 MHz radio signal, whereas the red and blue lines correspond to the overseas signals at 102.5 MHz and 95.5 MHz, respectively. According to Figure 7, the field strength of the 95.5 MHz prevails over the local radio 94.8 MHz on the specific dates depicted on the graph. Thus, the Carrier-to-interference ratio will determine the interference's density. The worse case occurs when the level of these unwanted signals exceeds that of the local services [8]. Therefore, the worst case scenario of co-channel interference has been established, and is evident from Figure 7, which reveals that the peaks of the overseas 95.5 MHz signal can exceed by approximately 10dBuV the field strength of the CYBC national radio.

4. THE PATH LENGTH CALCULATIONS OF THE DETECTED SIGNALS

The path length from the aforementioned regions to the coast of Limassol has been determined, by the use of Google Earth professional software tools. The path length between Israel and Limassol, as well as Lebanon and Limassol, has been calculated based on the coordinates given in Figures 3&4. The transmitting point's altitude of the 95.5 MHz signal from Jerusalem is 860 m, and the path length to Limassol is 376 km. Similarly, the path length of the Lebanese 102.5 MHz signal from Beirut measured at 271 km, whereby the transmitting point is located at 2295 m asl.

5. MEASUREMENTS OF 102.5 MHz, 95.5 MHz, AND 94.8 MHz, PERFORMED AT 1:00 PM BETWEEN JUNE 17th AND SEPTEMBER 2nd, 2015

The field strength variations in the 102.5 MHz signal from Beirut (Lebanon) are demonstrated in Figure 5. The measurements have been conducted from June 17th until September 2nd, 2015, at 1:00 PM. During this period, the average field strength intensity of 102.5 MHz was measured at

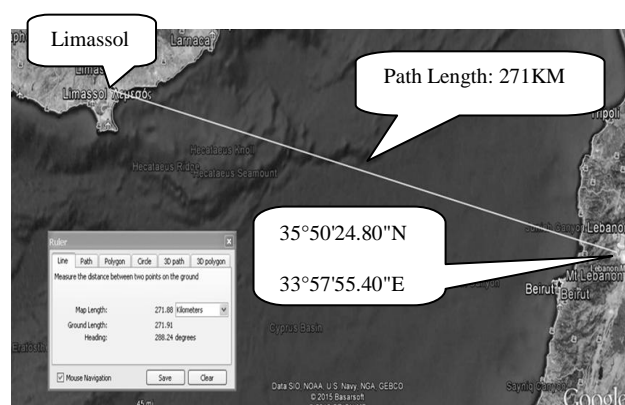


Figure 3: Path Length between Limassol and Israel, 376 km, Height 860 m

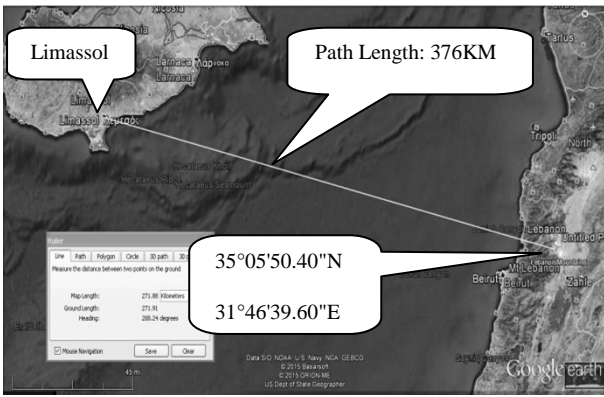


Figure 4: Path Length between Limassol and Lebanon, 271 km, Height 2995 m

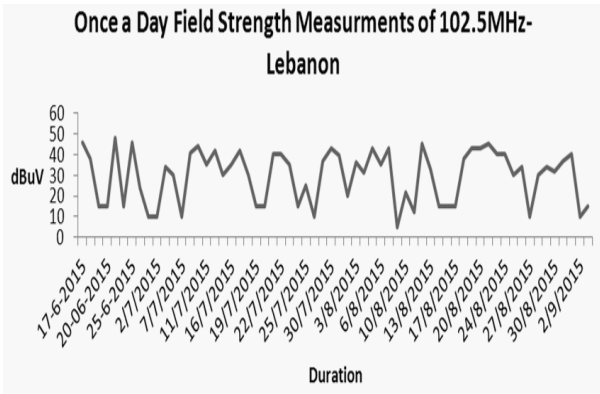


Figure 5: The Field Strength Intensity of 102,5 MH

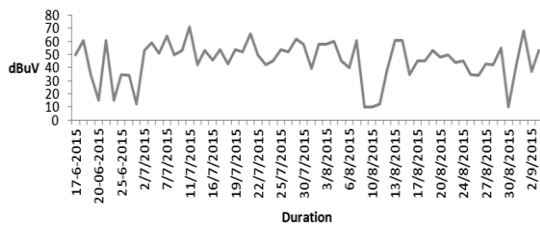


Figure 6: The Field Strength Intensity of 95.5 MHz

Figure 8 illustrates the variations in this phenomenon and elucidates the cause of a severe interference, which would occur in the evening on the given dates, provided that the local radio services would share the same spectrum as that adopted by the overseas signals.

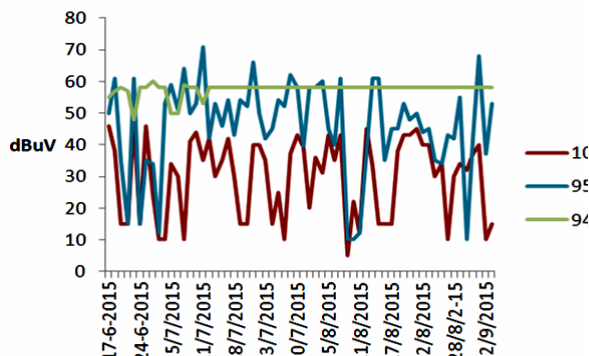


Figure 7: The Field Strength Intensity of the Three Signals under Study

6. SHORT-TERM MEASUREMENTS OF THE 95.5 MHz AND 94.8 MHz SIGNALS CONDUCTED BETWEEN JUNE 17th TO SEPTEMBER 2nd, 2015, FROM 11:00 AM TO 7:00 PM

Figure 9 illustrates the field strength variations of 95.5 MHz signal between 11:00 AM to 7:00 PM, based on the measurements conducted on August 24th and 25th, 2015.

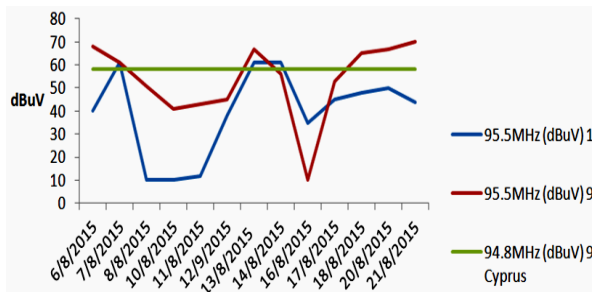


Figure 8: The Field Strength Variations in the 95.5 MHz and 94.8 MHz Signal, as Measured at 1:00 and 9:00 PM

These measurements revealed that the field strength intensity of the overseas signal was sporadic, i.e. comprised of various values. An

important observation is that its intensity measured on August 24th at 4:00 PM exceeded the free space value of the local national radio services CYBC, whereas the values were below the reference value at all other times.

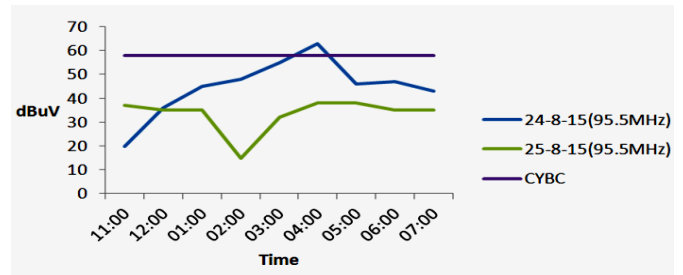


Figure 9: The Field Strength Variations of the 95.5 MHz and 94.8 MHz Signals, as measured between 11:00 and 7:00 PM

The average field intensity measurements of the monitored 95.5 MHz signal from Israel during the summer months (June, July and August) are illustrated in Figure 10 below.

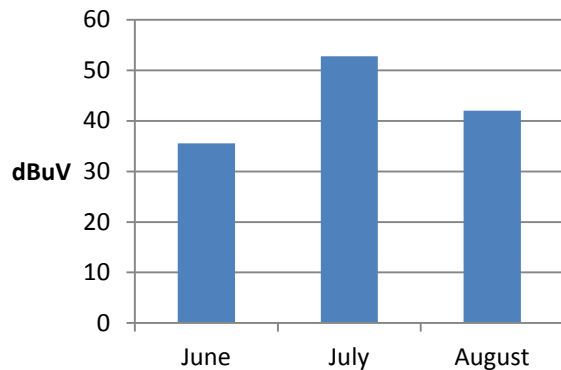


Figure 10: Average Field Intensity of 95.5MHz during summer 2015

However, it is noteworthy that the average field intensity of the 102.5 MHz signal arriving from Lebanon (illustrated in Figure 11) is different from the 95.5 MHz signal. The field has an average intensity of 13 dBuV in June, after which it increases to 31 dBuV in July, before declining to 30 dBuV in August

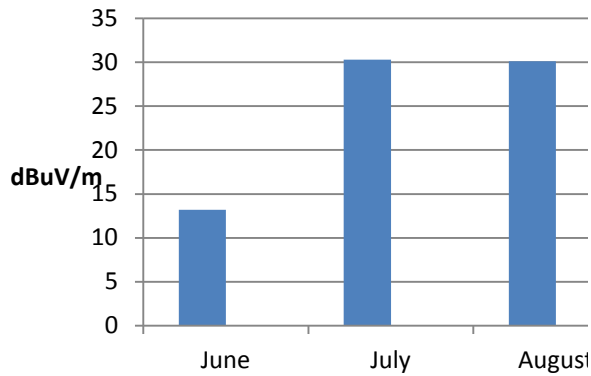


Figure 11: Average Field Intensity of 102.5 MHz during summer 2015

7. THE TYPE OF DUCTS ALONG THE LIMASSOL COAST

This chapter presents the results obtained by the Meteorological Department of Cyprus during the periods of very strong, medium and low field strength intensity of the overseas monitored signals discussed before. The coordinates under investigation for the radio signals transmitted at frequencies of 95.5 and 102.5 MHz are illustrated in fig.10

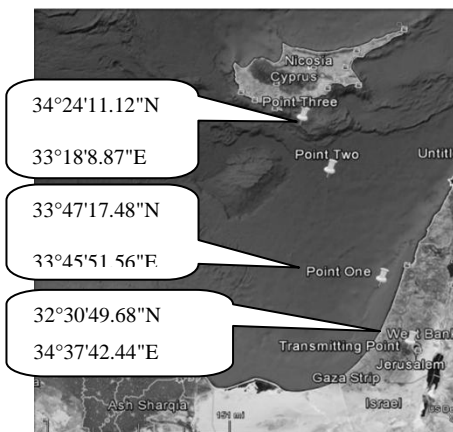


Figure 10: The coordinates under investigation for the radio signals transmitted at frequencies of 95.5 and 102.5 MHz

The model based on which calculations were made is the WRF-ARW, version 3.4. The calculations were made to 18 km distance grid initially / boundary data from the Global Forecasting System (GFS) with a resolution of 0.5 degrees and time step boundary conditions three hours. The step integration was not fixed but adaptive / dynamic, based on the criterion CFL. The number of vertical planes (eta levels / terrain following) was 60. The configurations used are given below:

1. Micro-physics: WRF Single-moment 3-class scheme
2. Radiation longwave: Rapid Radiative Transfer Model
3. Radiation shortwave: Dudhia Scheme

4. Surface layer: MM5 / Monin-Obukhov Scheme
5. Boundary layer: Yonsei University Non-local-K scheme
6. Cumulus / convection: Kain-Fritsch scheme.

For the aforementioned, the main goal is to provide evidence-based explanation for the radio interference observed along the southern coast of Cyprus. As a result, the refractivity N can be obtained based on the Recommendation ITU-R P.453-8 by applying Equation 1 below:

$$N = N_{\text{dry}} + N_{\text{wet}} = \frac{77.6}{T} [P + 4810 \frac{e}{T}] \quad \text{N-Units} \quad \text{Eq. (1)}$$

Where P denotes atmospheric pressure (hpa), e represents water vapour pressure (hpa), T is absolute temperature (K), and RH is relative humidity expressed in %.

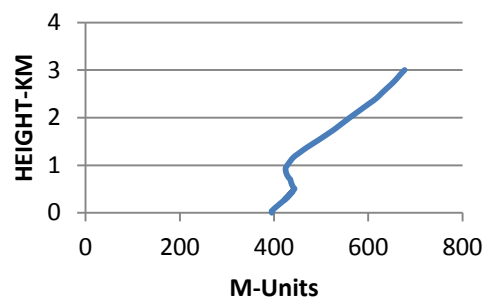


Figure 12: Temperature inversion on 06-Aug-15 at Point 3

Based on equation 1, trapping occurs when the N gradient exceeds -157 N/km . However, the same meteorological conditions cause trapping and super refraction interference. In this regard, the difference between trapping and super refraction pertains to the radius of the propagated wave, which becomes smaller than the Earth's radius as it decreases beyond the critical gradient. In such case, the electromagnetic waves are trapped within a thin layer of the troposphere, denoted as duct. When the wave is trapped in this tropospheric channel, its energy can propagate over great ranges. Furthermore, according to the Rec. ITU-R P.453-8, ducts can be described in terms of modified refractivity which is expressed by the equation below:

$M(h)$ defined by Equation 2 :

$$M(h) = N(h) + 157h \quad \text{(M-units)} \quad \text{Eq. (2)}$$

where h (km) is the height.

Applying equation 2 denotes an elevated duct in fig.12 a surface based duct in fig.13 and a surface duct in figure 14. This phenomenon can be

explained as the air aloft is very warm compared to the temperature of the sea. Thus, the surface-based ducts occur. For example, they can arise due to the hot air masses that pass over the cool water surface of the Mediterranean Sea. On the other hand, elevated ducts occur when the meteorological conditions are favourable for such phenomena to occur aloft above the Earth's surface.

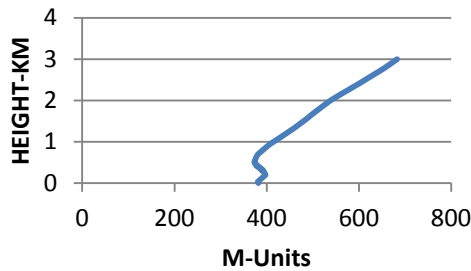


Figure 13: Surface Based Duct measurements made on 11-Aug-15 at Point 3.

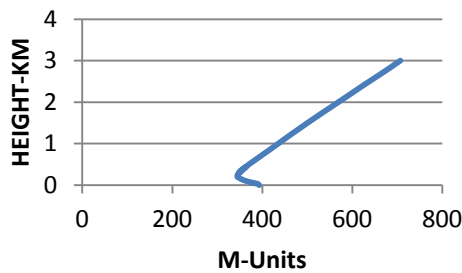


Figure 14: Surface Duct measurements made on 08-Jul-15 at Point 3.

I. CHAPTER CONCLUSION

From this study, it has emerged that with the aid of the WRF-ARW, version 3.4 may predict the level of interference of at least 10 hours foregoing without needing other meteorological complicated procedures. This is verified by the intersection of the results of signal intensity with the meteo conditions that create the ducts. Within this context, it has also emerged that the type and amount of Duct plays a very important role in signal intensity.

The findings presented in this paper revealed that the radio interference experienced along the southern coast of Cyprus is caused by three major types of ducts. Presence of these ducts has been verified close to the coast of Limassol, whereby they were classified as surface, surface based and elevated ducts. According to the interference assessment performed on specific dates, it can be posited that strong temperature inversion is

directly proportional to strong radio interference in close proximity to the coast of Limassol. Moreover, the study results have shown the electromagnetic waves in Band II can travel through the ducts with stronger field strength intensity of the free space value when the elevation of the duct approaches the Earth's surface. Particularly, according to the findings presented in this paper, the field strength intensity exceeds the free space value by approximately 10 dB. On the other hand, when there is no temperature inversion, a very low interference effect or its complete absence was noted.

REFERENCES

- [1] D. K. Chy, 'Evaluation of SNR for AWGN, Rayleigh and Rician Fading Channels Under DPSK Modulation Scheme with Constant BER', *International Journal of Wireless Communications and Mobile Computing*, vol. 3, no. 1, p. 7, 2015.
- [2] H. Son, J. Kim and C. Kim, *Journal of the Korean institute of electromagnetic engineering and science*, vol. 12, no. 1, pp. 94-100, 2012.
- [3] M. Nishi, H. Shinbara, K. Shin and T. Yoshida, 'Observation results of non-line-of sight 77.1 MHz FM radio waves on three different paths for three years', *Journal of Atmospheric Electricity*, vol. 31, no. 1, pp. 11-22, 2011.
- [4] 'Terrestrial microwave radio relay system development at frequencies above 10 Ghz', *Radio Electron. Eng. UK*, vol. 42, no. 4, p. 195, 1972.
- [5] RECOMMENDATION ITU-R P.452-11(2003), *Prediction procedure for the evaluation of microwave interference between stations on the surface of the Earth at frequencies above about 0.7 GHz*
- [6] RECOMMENDATION ITU-R P.453-8(2001), *the radio refractive index: its formula and refractivity data*.
- [7] RECOMMENDATION ITU-R P.834-4(2003), *Effects of tropospheric refraction on radiowave propagation*.
- [8] P. Petrov, 'Prediction of interference by modelling a radio interference meter', *Measurement Techniques*, vol. 37, no. 6, pp. 676-683, 1994.
- [9] C. Sim and E. Warrington, 'Signal strength measurements at frequencies of around 300 MHz over two sea paths in the British Channel Islands', *Radio Sci.*, vol. 41, no. 3, p. n/a-n/a, 2006.
- [10] 'D. Siddle and E. Warrington, 'Diurnal changes in UHF propagation over the English Channel', *Electron. Lett.*, vol. 41, no. 21, p. 1152, 2005.

A Very Compact Normal Mode Multiloop Helical Antenna with Enhanced Bandwidth

Antonis A. Constantinides

Institute of Work Based Learning, Middlesex University, London, UK

Email: AC1379@live.mdx.ac.uk

How to cite this paper: Constantinides, A.A. (2016) A Very Compact Normal Mode Multiloop Helical Antenna with Enhanced Bandwidth. *Open Journal of Antennas and Propagation*, 4, 159-165.
<http://dx.doi.org/10.4236/ojapr.2016.44012>

Received: November 3, 2016

Accepted: November 21, 2016

Published: November 24, 2016

Copyright © 2016 by author and Scientific Research Publishing Inc.

This work is licensed under the Creative Commons Attribution International License (CC BY 4.0).

<http://creativecommons.org/licenses/by/4.0/>



Open Access

Abstract

The physical size of an antenna becomes an important characteristic when receiving signals in bands with long wavelengths. Size determines two important aspects of antenna performance; impedance and efficiency. For example, the VHF antennas installed on radio sets that intended to receive FM or the latest technology Digital Audio Broadcasting (DAB) radio signals in Bands II, III respectively. Antennas that are installed on mobile platforms (*i.e.* portable receivers) require a receiver that utilizes a whip telescopic antenna with adjustable length which can operate as a $\lambda/4$ monopole antenna. Whereas, non-portable applications like a deck commercial receiver has no built in antenna due to the large size of the radiator needed and so must be connected with an external antenna. This paper presents a new design of a very small size Normal Mode Multiloop Helical Antenna (NMMHA) with superior performance developed for commercial receivers operate in band II, III. The major drawback which has been overcome with this design is the very narrow bandwidth of the Normal Mode Helical Antenna, which originally was optimized to provide the minimum Voltage Standing Wave Ratio VSWR response across Band II (87.5 - 108 MHz). The NMMHA's size allows it to be a build in block of a deck commercial receiver.

Keywords

Normal Mode Multiloop Helical Antenna, Radio services, Impedance, Bandwidth, Gain

1. Introduction

A helical antenna is an antenna consisting of a conducting wire wound in the form of a spring [1] [2] [3]. When the Helix antenna diameter is much smaller than λ (for example, $\leq 0.1\lambda$), it operates in a Normal Mode and is therefore defined as a Normal Mode

Helical Antenna (NMHA). An NMHA can be mounted either vertically above a ground plane, or directly on a connector without grounding. The NMHA radiation pattern is identical to that of a monopole antenna (it is an omnidirectional side-fire radiation pattern, which is the desired radiation pattern in this application) [3]. The many advantages of the NMHA relative to the short stub or the Hertzian dipole were discussed by Kraus [3]. According to Kraus, the NMHA resonates at a much shorter physical length than does the monopole but in a very narrow bandwidth. In this respect, the axial ratio of the NMHA is given by Kraus (1988) in Equation (1) below:

$$AR = \frac{E\theta}{E\Phi} = \frac{S\lambda}{2\pi A} = \frac{2S\lambda}{\pi^2 D^2} = \frac{2S\lambda}{C\lambda^2} \quad (1)$$

where:

C: it is the circumference

Sλ: spacing between turns in wavelengths

The three special cases pertaining to the NMHA polarization sense are given as follows:

$E\Phi = 0$ Linear Vertical Polarization

$E\Theta = 0$ Linear Horizontal Polarization

$E\Phi = E\Theta$ Circular Polarization

Wheeler's relation for circular polarization is given by Equation (2):

$$C\lambda = \sqrt{2S\lambda} \quad (2)$$

Because a NMHA has very small dimensions, and therefore, it is an important antenna in all wireless communication engineering sectors where the physical size of the radiator plays a very significant role [4]. As a result, over the years, many researchers have attempted to increase the bandwidth of the NMHA by consisting of two strips [5], applying the properties of a Log-Periodic arrays [6], or constructing the antenna of two flat wire strips [7]. This paper presents a new design of a very compact Normal Mode Multiloop Helical Antenna (NMMHA) with superior performance developed to operate in the VHF band II. The antenna consists of two sections—a multiloop antenna constructed on a PCB Fr-4 substrate material and a NMHA mounted in series as will be discussed in the following sections.

2. Measured and Simulated Results of the NMHA

An NMHA depicted in **Figure 1** was constructed as a part of this study in order to test its performance in real conditions and compare it with that of the quarter-wavelength monopole, the construction details of which are discussed in the next section.

The three vital parameters of the NMHA under investigation are the radiation resistance, the Voltage Standing Wave Ratio (VSWR) response and the "Gain" at the operational frequency of the commercial band FM (87.5 - 108 MHz).

The construction details of the NMHA are given below:

Diameter = 33 mm (0.01λ)

N = 9 turns

$S = 4 \text{ mm}$
 Height = 40 mm (0.013λ)
 Wire Diameter = 2 mm
 Pitch Angle: 7 Degrees

In order to determine the Axial Ratio (AR) of the antenna, Equation (3) can be used:

$$AR = \frac{E_\theta}{E_\Phi} = \frac{S\lambda}{2\pi A} = \frac{2S\lambda}{\pi^2 D^2} = \frac{2S\lambda}{C\lambda^2} \rightarrow \frac{2 \times 4 \times 3000}{33^2 \pi^2} = 2.23 \quad (3)$$

The radiation resistance (R_s , the real part of the impedance) has been measured by the use of the VSWR analyzer MFJ 269C and the results are illustrated in **Figure 2**. As can be seen from the graph, at 93 MHz, the radiation resistance is close to 50Ω . At other frequencies within the Band II, the radiation resistance becomes very low; thus, the antenna has a very narrow band response [8] [9] [10] [11].

This is further illustrated by the VSWR response curve shown in **Figure 3** which has been measured experimentally by the MFJ 269C as well, that takes into account the imaginary part of the impedance.

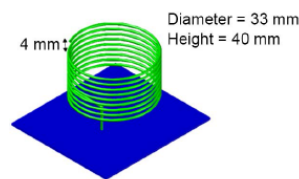


Figure 1. The normal mode helical antenna.

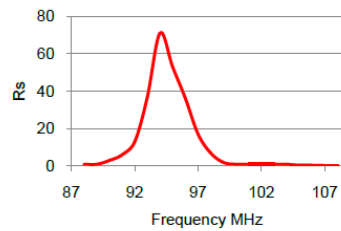


Figure 2. The radiation resistance of the NMHA.

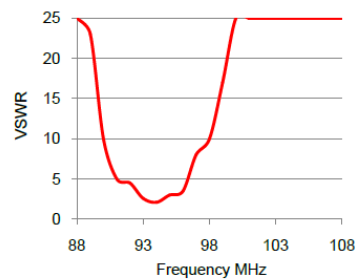


Figure 3. The VSWR response of the NMHA.

According to the graph shown in **Figure 3**, the VSWR response of the NMHA makes it usable in the 90 - 96 MHz range, equivalent to 5:1 VSWR. Moreover, as the VSWR response exceeds 25:1 in the beginning and at the end of the Band II, the antenna cannot be used for broadband applications. The poor VSWR response of the NMHA also affects the gain response, examined below.

3. Measured and Simulated Results of the NMHA over the Quarter Wavelength Monopole Antenna

The reception performance of the NMHA in real conditions (with “on air” existing radio services) versus a quarter-wavelength vertically polarized monopole antenna has been measured experimentally and simulated with the Excel program as presented in **Table 1**. In order to perform the test, each antenna was mounted at the same point on a ground plane and the results were obtained via the Advantest U3751 spectrum analyzer. According to the data reported in **Table 1**, the NMHA has an average gain of -4.7 dB relative to that of the quarter-wavelength monopole.

The gain ranged from -2 dB to -7 dB. The poor NMHA performance is attributed to the high VSWR response, as previously discussed.

4. Discussion—The Performance of the NMMHA

This section is dedicated to the discussion of the performance of the Normal Mode Multiloop Helical antenna (NMMHA), which was constructed with smallest physical dimensions possible. The NMMHA is shown in **Figure 4**. As can be seen from the image, the antenna consists of two sections—a multiloop antenna constructed on a PCB Fr-4 substrate material and a NMHA mounted in series. The longest turn’s side dimension of the planar helix is 80 mm and the total number of turns is 13.

Table 1. The gain of the NMHA versus that of the quarter-wavelength monopole antenna.

Frequency (MHz)	Helix (dBuV)	Monopole (dBuV)	ΔG (dBuV)
88.2	28	35	7
93.3	34	37	3
94.8	33	35	2
98.6	38	40	2
103.7	45	50	5
104.3	34	41	7
105.6	31	38	7
107.6	28	33	5
Min	28	33	2
Max	45	50	7
Average	34.4	39.2	4.7

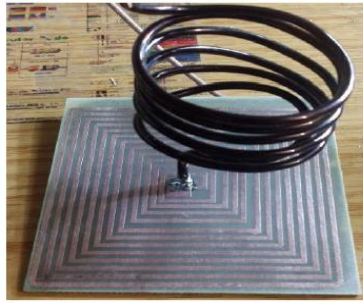


Figure 4. The normal mode multiloop helical antenna.

The NMMHA's construction details are given below:

Diameter = 33 mm (0.011λ)

$N = 5$ turns

Height = 50 mm (0.01λ)

Wire Diameter = 3 mm

Space = 4 mm

Pitch Angle: 7 Degrees

Standing alone, the NMHA incorporates 5 turns, allowing it to resonate at 101 MHz. Its height is 5 cm (0.01λ) and its diameter is 3.3 cm.

The NMMHA's VSWR response has been measured by the MFJ 269C in the 87.5 - 110 MHz range and is presented in Figure 5. According to the experiments performed, the advantage of this topology stems from eliminating the need for a complex matching network, as only a simple 50Ω quarter-wavelength transformer is required. According to the graph shown in Figure 5, performance of the new NMMHA is superior to that of a NMHA discussed in the previous sections. The maximum VSWR in the 87 - 110 MHz range does not exceed 5:1, whereas the average VSWR value is only 2.3:1.

In order to further confirm the superior performance of the new NMMHA, real conditions measurements by the use of the Advantest U3751 spectrum analyzer were conducted with "on air" existing radio services and the results are reported in Table 2.

According to the data presented in Table 2, the NMMHA enables an average field strength intensity of 44.1 dBuV across Band II over 34.4 dBuV of a NMHA and 39.2 dBuV of the monopole (Table 1). In this respect, the NMMHA antenna presented in this section, despite having the smallest possible physical size, has been confirmed to exhibit the greatest efficiency when compared to all other antennae examined in this work.

5. Conclusion

The Normal Mode Multiloop Helical Antenna has been demonstrated in this research is capable of providing excellent specifications as a stand-alone antenna in VHF Band. The novelty of the modified NMHA stems from its small dimensions relative to other

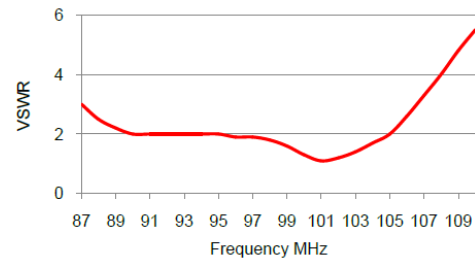


Figure 5. The VSWR response of the NMMHA.

Table 2. Real conditions field strength measurements of the modified NMHA.

Frequency MHz	Field Strength dBuV
88.2	34
93.3	39
94.8	39
98.6	45
103.7	60
104.3	46
105.6	45
107.6	39
Minimum	34
Maximum	60
Average	44.1

small antennas, such as the Herzian dipole or the short stub, without requiring complicate matching networks with higher efficiency. As a result, it would be highly important for future research pertaining to the NMHA to apply this topology across Band I or in lower frequency applications, *i.e.* the HF band where antennas must be constructed with large physical dimensions.

References

- [1] Kraus, J. (1949) The Helical Antenna. *Proceedings of the IRE*, 37, 263-272. <https://doi.org/10.1109/jrproc.1949.231279>
- [2] Abd-Alhameed, R. and Excell, P. (1999) Analysis of a Normal-Mode Helical Antenna Including Non-Uniform Wire Surface Current Effects. *IEE Proceedings of Microwaves, Antennas and Propagation*, 146, 1.
- [3] Kraus, J. (1988) *Antennas*. McGraw-Hill, New York.
- [4] Huang, J.X. and Yu, Y. (2014) An Electrically Small Normal-Mode Helical Antenna with Capacitive Coupling Feed. *The 8th European Conference on Antennas and Propagation (EuCAP 2014)*, The Hague, 2915-2917.

A Very Compact Circular Adaptive Array for New Generation Mobile Commercial Receivers

Antonis A. Constantinides

Institute of Work Based Learning Middlesex University, London, UK

Email: AC1379@live.mdx.ac.uk

How to cite this paper: Constantinides, A.A. (2017) A Very Compact Circular Adaptive Array for New Generation Mobile Commercial Receivers. *Open Journal of Antennas and Propagation*, 5, 1-6.
<https://doi.org/10.4236/ojapr.2017.51001>

Received: December 1, 2016

Accepted: January 20, 2017

Published: January 23, 2017

Copyright © 2017 by author and Scientific Research Publishing Inc. This work is licensed under the Creative Commons Attribution International License (CC BY 4.0).
<http://creativecommons.org/licenses/by/4.0/>



Open Access

Abstract

The antenna is a receiver's component that collects electromagnetic waves from various directions. The rationale behind focusing on the circular array is that its tuning ensures that the receiver processes the desired signal only, while rejecting the unwanted interference. This can only be achieved by a directional external antenna that is large in size and must be steered mechanically in the desired direction. As this arrangement is not practical, smart antennae have been proposed as an alternative. A circular phased array can produce a predicted radiation pattern, whereby it receives maximum energy from the desired direction without the need for mechanical control. Owing to these characteristics, phased arrays exhibit high gain as well as immunity to interference, making them ideal for use in high interference environments. This combination would ensure that it could be incorporated into a commercial deck receiver or installed on vehicles.

Keywords

Normal Mode Helical Antenna, Radio Services, Impedance, Bandwidth, Gain

1. Introduction

Today, the commercial car's receivers employ vertically polarized antennae, which receive signals from all directions with equal density. As a result, a traditional vertically polarized antenna cannot distinguish the desired signal from the interference, as both penetrate into the receiver, despite arriving from different directions. Based on this concept, a phased array utilized for reception purposed in mobile communications can minimize the level of interference very efficiently as its main beam steers in the desired direction in order to disable penetration of all other incoming (undesired) signals transmitted from the side and back positions. The main beam's tilt direction of a phased array depends on the phase

shift as well as the amplitude difference among the single elements that constitute the system [1]. As a result, the greatest advantage of this approach stems from dispensing with the need for mechanical movement, as the main beam of a phased array steers toward the desired direction [2]. For instance, Howard and Fung [3] conducted their study, focusing on an antenna, which they labelled “Clever Dumb Antenna” in reference to its ability to derive the great benefits of the multi-beam antennas interfaced by a beamformer. According to the authors, “the great benefit of such antennas enables dividing up to 360 degree cell site into several high gain sectors”. It is important to note that a beamformer the authors refer to is a signal processing technique based on a network comprised by phase shifters that enable programming of the adequate phase shift of the radiators in order to produce an optimum radiation pattern as well as beam tilt. In a different study, Panduro [4] presented a non-uniform circular phased array, referring to it as a smart antenna, due to its ability to provide a low side lobe response for scanning purposes. As the side lobes are minor beams, scanning antennas enable reception from different angles of the main beam. Owing to these properties, low side-lobe response arrays are primarily aimed for use in a high interference environment. Furthermore, Winters and Gil [5] extended the aforementioned research by examining the parameters of the two major categories of smart antennas, namely the phased and adaptive arrays. The adaptive arrays’ radiation pattern, as the authors’ state, “It is auto adjusted according to the move of interference, the phased arrays” radiation pattern are not. They further explained that “it is steered or different beams are selected as the desired user moves”. According to this view, the smart antennas are highly recommended for new generation wireless communications. Presently, they are being applied experimentally in 4G/5G wireless radio communication systems and it is likely that their range of applications will expand in the future, given that this promising area of research will be explored for many years to come.

2. The Adaptive Array Topology

Circular arrays are one-dimensional linear arrays in a circular form. The major advantage of circular arrays relative to linear arrays stems from their ability to scan horizontally across the entire 360° without distortion near the end-fire direction [6]. Therefore, circular arrays present the ideal topology for this application and will be investigated in detail in this section. Another great advantage of circular arrays is that the mutual coupling affects all individual elements of the array with equal density. Therefore, eliminating it is easier than in any other topology [7]. The array factor of circular arrays is the sum of the far-field intensity of every individual element of the array and is given by Equation (1):

$$\sum_{n=1}^N e^{j[\beta\alpha \sin\theta \cos(\Phi - \Phi_n) + \Delta n]} \quad (1)$$

where Δn is the excitation phase of every individual element (in this application, the normal mode helix antenna). The maximum radiation angle (Θ_{\max} , Φ_{\max}) can be achieved based on Equations (2), (3), and (4):

$$\beta a \sin(\Theta_{\max}) \cos\left(\Phi_{\max} - \frac{2\pi}{N}\right) + B_1 =_{-}^{+} 2q\pi \tag{2}$$

$$\beta a \sin(\Theta_{\max}) \cos\left(\Phi_{\max} - \frac{4\pi}{N}\right) + B_2 =_{-}^{+} 2q\pi \tag{3}$$

$$\beta a \sin(\Theta_{\max}) \cos(\Phi_{\max} - 2\pi) + B_N =_{-}^{+} 2q\pi \tag{4}$$

The maximum radiation direction in terms of the excitation phase is given by Equation (5) below:

$$B_N = +2q\pi - \beta a \sin(\Theta_{\max}) \cos\left(\Phi_{\max} - \frac{2\pi n}{N}\right) \tag{5}$$

$N = 1, 2, 3.$

Based on the preceding discussions, the performance of a four-element circular array, illustrated in **Figure 1**, is analyzed to ensure that it operates effectively in the 87.5 - 108 MHz range. The circular array shown above comprises of four modified normal mode helical antennae. The antennae are mounted at a 900 distance. The phase of every individual helical antenna is controlled by an electronic phase shifter (Mini-Circuits JSPHS-150+) in order to create the desired radiation pattern in a given direction. The radius of the circle is 7.5 cm, which corresponds to 0.025λ . In this respect, the radiation pattern of the four-element circular array in the end-fire direction will be analyzed below, according to the phase shift of every individual element. The weights and radiation patters are presented in **Figure 2**.

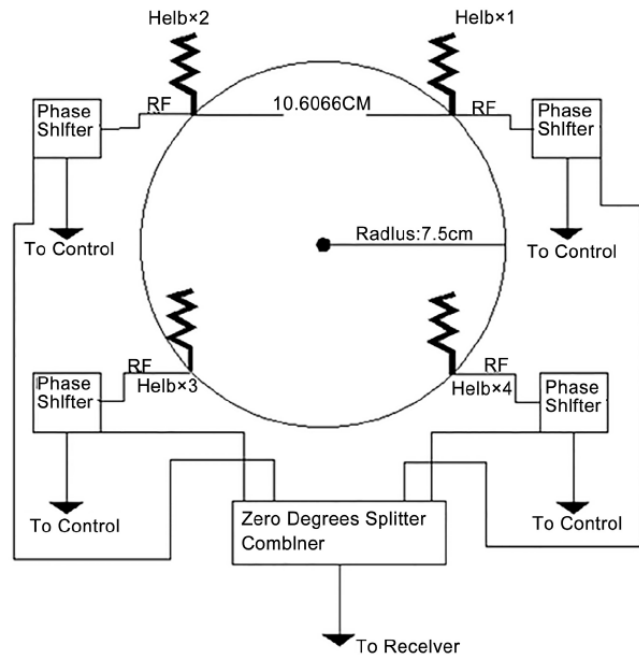


Figure 1. The smart Antenna’s architecture.

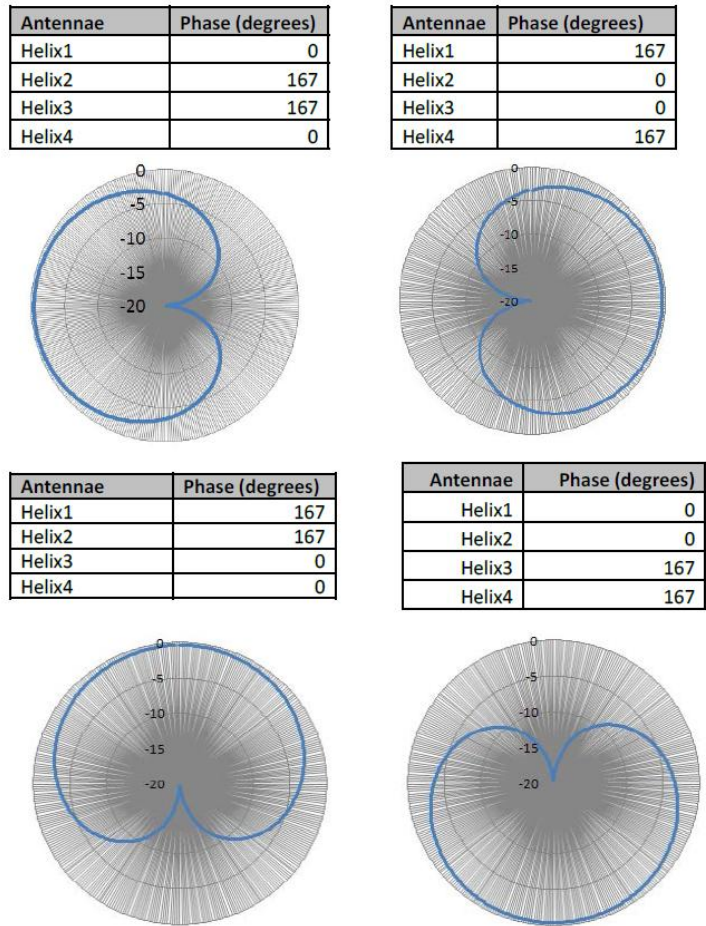


Figure 2. The smart Antenna phase shifts simulation and radiation patterns.

3. Test and Results

The array consists of four NMHA, constructed on an FR-4 PCB, while the array is shown in Figure 3. In order to evaluate the array performance, the Voltage Standing Wave Ratio VSWR (caused by the mutual coupling between the elements and compensated for by rotating the helix) was first minimized for every individual helix. The gain of the four-element circular array relative to the performance of the whip telescopic antenna was evaluated by primarily steering electronically the array towards the direction of the maximum radiation of the incident waves monitored via the spectrum analyzer shown in Figure 4. The monitored radio services are three local channels utilizing 91.6 MHz, 93.3 MHz and 93.7 MHz frequencies. All monitored radio services are broadcasting from the same direction. The spectrum analyzer readings were obtained by utilizing the spectrum analyzer ROVER-DL1. The maximum radiation is illustrated in Figure 4, which reveals the field strength of 93.3 MHz is 33.7 dBuV versus 33.5



Figure 3. The four-element circular array.

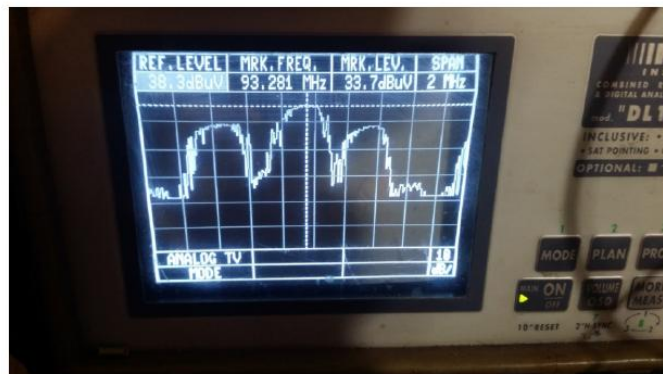


Figure 4. Real conditions spectrum analyzer readings of the circular array.

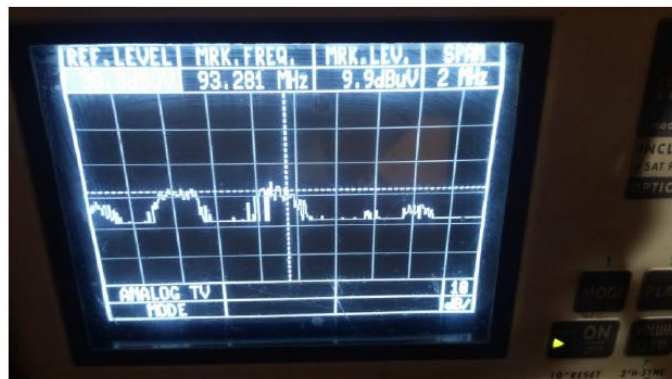


Figure 5. Real conditions spectrum analyzer readings of the circular array.

dBuV obtained for the traditional whip telescopic antenna has been tested previously. As a result, the gain of the four-element array in Band II is very satisfactory. The next highly important test performed as a part of this work aimed to determine the null, created by the arranged phase shift by electronically rotating the array by 180° in the opposite direction of the transmitting point. As a result of this adjustment, the field strength of the strongest radio service (which is 33.7 dBuV) declined to 9.9 dBuV, as illustrated in Figure 5. It is important to note that the field strength of the other two adjacent channels (91.6 MHz and 93.7 MHz, illustrated in the spectrum analyzer in Figure 5), broadcasting from the same transmitting point, was also reduced significantly.

As a result, it can be asserted that the four-element circular array has enabled a reduction in gain of around 24 dB in the opposite direction of the transmitting point, which complies with the radiation patterns simulated in the previous section.

4. Conclusion

Applying the circular array as it has been implemented in this study in Band III (174 to 240 MHz) for Digital Audio Broadcasting (DAB+) will enhance the SNR of digital receivers during motion. Circular array can also be a very important technology for the future mobile digital video broadcasting terrestrial (DVB-T) service that broadcasts television in UHF Band between the channels 21 and 69 (*i.e.* in the 512 - 800 MHz frequency range).

References

- [1] Rabinovich, V. (2011) Direction Finding System for Automotive Applications Using Small Phased Antenna Array. *Microwave and Optical Technology Letters*, 53, 2441-2446. <https://doi.org/10.1002/mop.26275>
- [2] Lee, M. and Kim, Y. (2009) Development of a K-Band FMCW Phased Array Radar Sensor with Low Complexity Receiver Based on Antenna Switching. *Microwave and Optical Technology Letters*, 51, 2848-2850. <https://doi.org/10.1002/mop.24785>
- [3] Howard, J. and Fung, C. Clever Dumb Antenna: Passive Multibeam Antenna for Broadband Wireless Communication.
- [4] Vedula, V., Paladuga, S. and Prithvi, M. (2015) Synthesis of Circular Array Antenna for Sidelobe Level and Aperture Size Control Using Flower Pollination Algorithm. *International Journal of Antennas and Propagation*, 2015, 1-9. <https://doi.org/10.1155/2015/819712>
- [5] Winters, J. (1998) Smart Antennas for Wireless Systems. *IEEE Personal Communications*, 5, 23-27. <https://doi.org/10.1109/98.656155>
- [6] Davies, D. and Rizk, M. (1977) Electronic Steering of Multiple Nulls for Circular Arrays. *Electronics Letters*, 13, 669. <https://doi.org/10.1049/el:19770475>
- [7] Hui, H.T. (2007) Decoupling Methods for the Mutual Coupling Effect in Antenna Arrays: A Review. *Recent Patents on Engineering*, 1, 187-193. <https://doi.org/10.2174/187221207780832200>